Infared magneto-optical spectroscopy of boron nitride encapsulated graphene

Nedoliuk, Ievgeniia

How to cite

NEDOLIUK, Ievgeniia. Infared magneto-optical spectroscopy of boron nitride encapsulated graphene. Doctoral Thesis, 2018. doi: 10.13097/archive-ouverte/unige:114899

This publication URL: https://archive-ouverte.unige.ch/unige:114899
Publication DOI: 10.13097/archive-ouverte/unige:114899

UNIVERSITÉ DE GENÈVE
Département de Physique
de la Matière Quantique

FACULTÉ DES SCIENCES
Directeur de Thèse:
Dr. Alexey B. Kuzmenko

Infrared magneto-optical spectroscopy of boron nitride encapsulated graphene

THÈSE

présenté à la Faculté des Sciences de l'Université de Genève
pour obtenir le grade de docteur ès Sciences, mention physique

par

Ievgeniia Oleksandrivna Nedoliuk

de

Kyiv (Ukraine)

Thèse n° 5274

GENÈVE
Imprimerie Harder
2018

UNIVERSITÉ
DE GENÈVE
FACULTÉ DES SCIENCES

DOCTORAT ÈS SCIENCES, MENTION PHYSIQUE

Thèse de Madame Ievgeniia NEDOLIUK

intitulée :

«Infrared Magneto-Optical Spectroscopy of Boron Nitride Encapsulated Graphene»

La Faculté des sciences, sur le préavis de Monsieur A. KUZMENKO, docteur et directeur de thèse (Département de physique de la matière quantique), Monsieur C. SENATORE, professeur assistant (Département de physique de la matière quantique), Monsieur M. ORLITA, docteur (Laboratoire National des Champs Magnétiques Intenses, Université de Grenoble, Alpes, Centre National de la Recherche Scientifique, Grenoble, France), autorise l'impression de la présente thèse, sans exprimer d'opinion sur les propositions qui y sont énoncées.

Genève, le 22 octobre 2018

Thèse - 5274 -

Le Doyen

N.B. - La thèse doit porter la déclaration précédente et remplir les conditions énumérées dans les "Informations relatives aux thèses de doctorat à l'Université de Genève".

Abstract in English

This work is devoted to experimental investigation of graphene – a novel material which was introduced to a broad scientific community in 2004. Graphene has unique electronic and optical properties which is directly related to its exotic band structure. During the current decade, this material has been intensely investigated in different conditions with various techniques: electron transport measurements, optical spectroscopies, scanning tunneling microscopy, angle-resolved photoemission spectroscopy etc. The method with which a graphene crystal is synthesized and further handling of the crystal largely influence the quality of graphene. Currently, the best quality graphene is produced by scotch-tape exfoliation method, and its quality is maintained by encapsulation of graphene monolayer in between two thin monocrystalline flakes of hexagonal boron nitride (hBN).

The goal of this work is investigation of magneto-optical properties of the best quality graphene crystals. For reasonable technologically achievable values of magnetic field, all spectral features of graphene always lay in the infrared and THz regions of spectrum. Unfortunately, high quality graphene samples mentioned above are so small in size that conventional well-established methods of infrared magneto-optical measurements are not applicable. Therefore we have developed two superconducting magnets and an auxiliary cryostat which are compatible with a commercial infrared microscope already connected to a commercial FTIR spectrometer. This combination of experimental setup has allowed us to perform many magneto-optical measurements which were impossible before when working with small samples: proper normalization of the infrared spectra without overfilling, measuring the Faraday rotation angle. Our setup can produce magnetic fields in the range from 0 to ± 4 Tesla; base temperature in the sample compartment is always fixed at ~ 5 Kelvin.

We have measured transmission and Faraday rotation angle of weekly doped suspended hBN-encapsulated graphene membranes at different magnetic fields in a broad range of spectrum: in the near, middle, and far infrared regions. In addition, Kramers-Kronig constrained fitting of these spectra allowed us to restore magneto-optical conductivity tensor of the hBN-encapsulated graphene as well as absorption in graphene for right- and left-handed circularly polarized light separately. An important discovery of our work is that high quality graphene samples exhibit unprecedentedly strong signatures of both intraband and interband magneto-optical transitions between the Landau levels which form in graphene in magnetic field. These magneto-optical transitions manifest as well separated deep narrow absorption lines in graphene's transmission spectra and large Faraday rotation angle at the corresponding energies. In fact, for the most intensive line, magnitude of graphene's absorption closely approaches 50 % which is the maximally allowed value for ultrathin conducting films. Doped graphene samples also show very strong magnetic circular dichroism.

Apart from that, high quality graphene samples allowed us to register new subtle effects which have not been previously reported: additional absorption lines which do not obey the generally accepted selection rule for magneto-optical transitions, hBN phonon induced magneto-optical splitting of absorption lines, unexpected magnetic field dependent splitting of an interband absorption line, anomalous inflection of Faraday rotation curve at certain energies.

Results of this work represent scientific interest for purely fundamental research and also allow one to re-examen graphene applications from a different perspective.

Résumé en français

Ce travail est consacré à l'étude expérimentale du graphène – un matériau novateur qui dès 2004 a commencé à capter l'intérêt des scientifiques. Ses propriétés électroniques et optiques uniques découlent de son exotique structure de bande. Au cours de la présente décennie, ce matériau a, dans une large gamme de conditions expérimentales, été le sujet d'intenses travaux recouvrant variantes techniques telles que le transport électronique, la spectroscopie optique, la microscopie à effet tunnel, la spectroscopie photoélectrique résolue en angle et bien d'autres encore. La méthode de synthèse des cristaux de graphène et les précautions prises lors de leur manipulation influencent grandement la qualité des échantillons. À ce jour, la méthode d'exfoliation au ruban adhésif produit la meilleure qualité de mono-couches de graphène dont les propriétés sont par la suite préservées par l'encapsulation entre deux couches monocristallines de nitrure de bore hexagonal.

L'objectif du présent travail est l'étude des propriétés magnéto-optiques des meilleurs cristaux de graphène actuels. En raison des restrictions des valeurs de champ magnétique techniquement atteignables, les principales caractéristiques spectrales sont confinées dans la gamme THZ et infrarouge. Malheureusement, la taille très réduite des échantillons de haute qualité rend inadaptées les méthodes conventionnelles d'études magnéto-optiques dans l'infrarouge. Pour y remédier, deux aimants supraconducteurs ainsi qu'un cryostat ont été développés de manière à pouvoir être utilisés sous un microscope infrarouge couplé à un spectromètre à transformée de fourrier. Ce couplage de dispositifs expérimentaux a rendu accessibles des nouveaux mesures magnéto-optiques sur des échantillons de la taille réduite, notamment grâce à une normalisation appropriée du spectre infrarouge (la résolution spatiale atteinte permettant d'éviter les débordements lumineux) et grâce à la mesure de l'ange de la rotation Faraday. Le dispositif peut générer des champs magnétiques dans la gamme de 0 à ± 4 Tesla tout en maintenant la température de la base de l'échantillon à ~ 5 Kelvin.

Nous avons mesuré la transmission et l'angle de la rotation Faraday de membranes suspendues de graphène faiblement dopé encapsulées dans du nitrure de bore hexagonal; ce à différents champs magnétiques et dans une large plage spectrale couvrant l'infrarouge proche, moyen et lointain. De plus, la régression conforme aux relations de Kramers-Kronig appliquée aux spectres mesurés a permis de reconstituer le tenseur de la conductivité du graphène encapsulé de même que la distinction entre l'absorption du graphène pour les polarisations circulaire droite et circulaire gauche. Une découverte majeure de ce travail est que les échantillons de graphène de haute qualité présentent des niveaux d'intensité sans précédent de signatures de transitions magnéto-optiques, à la fois intra et interbandes, entre les niveaux de Landau formés par le champ magnétique. Ces transitions se manifestent par de profondes et distinctes lignes d'absorption dans le spectre de transmission ainsi que par un important angle de la rotation Faraday aux mêmes énergies. La ligne la plus intense d'absorption du graphène présente de façon remarquable une atténuation de près de 50% qui correspond à la valeur maximale admise par les films conducteurs ultraminces. Les échantillons de graphène dopé présentent également un très fort dichroïsme circulaire magnétique.

Ces échantillons de graphène de haute qualité ont également permis de remarquer des effets plus subtils qui n'ont jusqu'à présent pas été rapportés tels que des lignes d'absorption supplémentaires n'obéissant pas aux règles de sélection des transitions magnéto-optiques conventionnelles, la division des lignes d'absorption induite par le photon du nitrure de bore hexagonal, l'inattendue division par champ magnétique d'une ligne d'absorption interbande et l'inflexion anormale de la rotation Faraday à certaines énergies.

Les résultats de ce travail revêtent un intérêt scientifique à la fois pour la recherche fondamentale ainsi que pour les différentes perspectives d'applications du graphène.

Contents

Chapter 1

Introduction

1.1 A black swan of condensed matter physics

The term “graphene” was first introduced in 1986 by Boehm and his colleagues [1] as a combination of the word “graphite” and the suffix “-ene” referring to polycyclic aromatic hydrocarbons. By that time graphene was already long well-known due to earlier theoretical works [2]. However in these works, graphene was considered merely as a building block of graphite. It was also generally accepted that two-dimensional (2D) crystals, including graphene, cannot exist in isolation. Such an opinion was supported both by theoretical calculations and an ample set of experimental observations. Famous works of Landau, Peierls and Mermin [3, 4, 5, 6] argued that strictly 2D crystals are thermodynamically unstable at any nonzero temperature because of pronounced thermal fluctuations in crystalline lattices. Numerous experiments with thin films of different nature showed that their melting temperatures rapidly fall down as these films get thinner. Typically, a thin film becomes unstable when its thickness approaches a few dozen atomic layers: the film decomposes and coagulates into islands to minimize its surface energy, see topical reviews [7] and [8]. Thus scientific discussions were mostly about estimation of the maximal possible size of atomically thin 2D crystalites (also called flat macromolecules) which was calculated to be only a few nanometers.

Over the course of the 20th century there were only several dozen publications about what now would be called graphene related materials − thin films and flakes of graphite. An overview to this early research is given in [9], here I mention only one important date. In 1962 Hanns-Peter Boehm and his colleagues reported [10] about synthesis of a small several micron fragment of reduced graphite oxide which was for the first time identified as an atomic monolayer. Therefore this work could be dubbed as discovery of graphene.

The situation changed a lot after 2004 when a famous paper “Electric Field Effect in Atomically Thin Carbon Films” by Novoselov et al. [11] was published. Graphene emerged in sight of the scientific community as something completely unexpected, a black swan of condensed matter physics. In the following years other 2D crystals were cleaved and characterized [12]. This attracted the attention of a large number of scientists from the condensed matter physics and even high energy physics community. Next, uncommonly soon for current decades, the 2010 Nobel Prize in physics was jointly awarded to Andre Geim and Konstantin Novoselov "for groundbreaking experiments regarding the two-dimensional material graphene". In 2013 the "Graphene Flagship" initiative with a €1 billion budget was launched to fund graphene related research. By that time the yearly number of scientific papers on graphene related topics counted approximately ten thousand [13, 14], and involved specialists not only from condensed matter physics but also from chemistry, engineering, biology, medicine, environmental science, and other interdisciplinary branches. Thus graphene research could be divided into two periods: sporadic, largely disconnected in the 20th century and fashionable, generously funded in the style of "five-year plans" in the 21st century. One may ask why the publication [11] made such a difference.

Firstly, work [11] suggested that micron sized 2D crystals could be fairly robust despite the Landau-Peierls argument. It was shown that graphene crystals do not degrade even under ambient conditions and after contact with other chemicals (whereas typical requirements for surface science research are ultrahigh vacuum, ultraclean chambers and liquid helium temperatures ~ 4 Kelvin). Moreover, graphene crystals could be manufactured and then identified with a more or less reproducible yield using very simple tools such as, a pair of gloves, tweezers, and scotch tape.

The very existence of 2D crystals could be partially explained in hindsight. Infeasibility of growing a 2D crystal from scratch does not actually imply it cannot be created artificially. Indeed, graphene could be grown at high temperature as an inherent part of a 3D system: inside bulk graphite or on top of another crystal with an appropriate lattice. Next, at lower temperatures, graphene could be decoupled from its progenitor 3D system and transfered [15, 16] to another substrate which would also suppress bond-breaking fluctuations in the 2D crystal. For example the dielectric substrate SiO_2 stabilizes graphene and also allows studying its electronic properties. Thus the Landau-Peierls argument seems to be circumvented. Yet another surprise came in 2007 with a publication [17] which reported for the first time a successful suspension of graphene monolayer in midair. Unsupported graphene membrane was deemed impossible, however, it stabilizes due to spontaneous out-of-plane crumpling on the nanometer scale. Graphehe's stability, ground state and melting are still very poorly understood. A priori it is not even clear how to define graphene's melting temperature because of change in dimensionality: a 2D membrane is deemed to melt into a 3D liquid phase [18]. Neither the order of such phase transition nor the value of the melting temperature are known yet. Currently these questions are subject of ongoing discussions and research.

Secondly, publication [11] was not merely observational in contrast to the previous works. Early graphene research conducted in the 20th century solely reported about synthesis of ultrathin graphite films or occasionally even monolayers, however, measurements of graphene's physical properties were not done. A few electrical and optical measurements were performed on optically thin graphite films [19] which were peeled with scotch-tape already back in 1990. However these experiments did not reveal properties of graphene either. Meanwhile work [11] emphasized distinctive properties of graphene: ambipolar field effect and high mobility of graphene's charge carriers even at highest electric-field-induced concentrations and at room temperature. Theses properties were interesting from the point of view of fundamental science as well as showed potential for applications in everyday life: creation of long speculated room-temperature ballistic transistors seemed to be a step closer. Further research revealed all the more peculiar and sometimes unique properties of graphene often described with superlative adjectives [20]. Such followup had not been anticipated even by Andre Geim, Konstantin Novoselov and their colleagues.

1.2 Open questions and motivation of this work

This work is devoted to the extraordinary optical properties of graphene. Graphene is highly transparent in a remarkably broad range of wavelengths: from THz to UV region. This is related to the fact that graphene, unlike many other materials, does not have intensive absorption lines nor bands due to optical phonons. An exceptional property of pristine graphene is that the value of its optical absorption does not depend on the wavelength of light and remains constant almost all the way into the region mentioned above. Moreover, this value does not depend on any parameters which characterize graphene crystal: it is expressed in terms of several fundamental constants.

However, optical properties of graphene could be modified and tuned. In an external magnetic field, absorption lines emerge and at the same time graphene is expected to becomes more transparent in between these lines. Positions of these lines depend on the value of the external magnetic field, thus the magnetic field could be viewed as a knob which allows tuning optical absorption at a given wavelength. In addition, gate voltage applied to a graphene crystal together with a magnetic field allows tuning polarization handedness of the absorbed light and Faraday rotation of transmitted light.

A simple independent electron theory predicts that magneto-optical effects may be very strong in graphene, potentially their magnitude can approach the fundamental limit allowed for ultrathin conducting films. However, in realistic situations there exist many line broadening mechanisms due to disorder and different types of interactions. In the end, the magneto-optical absorption lines are smeared: they become shallower and the tuning of graphene's properties becomes less efficient. Apart from that, there also exist mechanisms which cause less trivial redistribution of spectral weight: shifting of optical absorption lines, their splitting, formation of additional lines, etc. As a result, until now, magneto-optical absorption reported in numerous experiments has been either low or its values could not be properly assessed due to technical issues.

Therefore many questions naturally arise: What are the dominant mechanisms limiting magneto-optical absorption in graphene? To which extent could they be eliminated? How large are the maximal values of magneto-optical absorption which could be reproducibly achieved with current technology? The goal of this work is to shed some light on these questions and understand how far one can go. On the one hand this would give a deeper understanding of conceptual questions like electron-electron interactions and scattering processes which take place in graphene. On the other hand this would allow one to assess potential applications of graphene. Tunability of graphene's magneto-optical properties in the infrared region makes this material promising for development of long speculated Landau level lasers with tunable wavelength, broad range infrared Faraday isolators, etc.

1.3 Structure of the manuscript

Chapter 2 gives introductory information and brief overview of literature about graphene, special emphasis is made on graphene's optical properties in the absence and in the presence of an external magnetic field. We also discuss existing variation in quality of graphene crystals which is very important in the context of spectral line intensity and broadening. At the end we mention some noteworthy results of magneto-optical experiments performed on graphene prior to this work.

Chapter 3 is devoted to description of high quality hBN-encapsulated graphene samples which were manufactured in the University of Manchester especially for our experiments. We also mention currently known benefits as well as side-effects (or emergent phenomena) of hBN-encapsulation. Such detailed description is necessary because graphene's properties depend a lot on the method of its synthesis and preparation. Thus information from this chapter is crucial during comparison of our results to theoretical predictions and experimental results obtained in other groups.

Chapter 4 describes the experimental setup employed during the magneto-optical measurements. Particular attention is given to our home-made devices (a superconducting magnet and its optical cryostat) which have been created during this work in order to enable magneto-optical measurements on small samples in the infrared region of wavelengths.

Chapter 5 describes protocols of magneto-optical experiments which have been performed with the help of our newly-built setup.

Chapter 6 gives important information about optical properties of ultrathin conducting films in the context of our experiments with graphene. Then it describes how we model propagation of light in the hBN-encapsulated graphene. At the end we describe the data treatment algorithms which were developed to extract different physical quantities from the magneto-optical spectra we measured.

Finally, in Chapter 7 we present results of the magneto-optical measurements performed on our three hBN-encapsulated graphene samples in the different subregions of infrared part of spectrum. This includes magneto-optical transmission in unpolarized and linearly polarized light as well as Faraday rotation angle. We comment on the spectral signatures which were registered in the spectra and give our interpretation of different phenomena which have been observed. We also present magneto-optical conductivity and magneto-optical absorption extracted from experimental data with the help of Kramers-Kronig analysis. At the end we make a brief comment of the errors as well as technical problems which we encountered during the measurements.

Chapter 8 summarizes the work which has been done and new phenomena which have been observed in ultrapure hBN-encapsulated graphene. It also talks about future possible experiments in line with our work. Then hypothetical applications of our findings and their feasibility are briefly discussed.

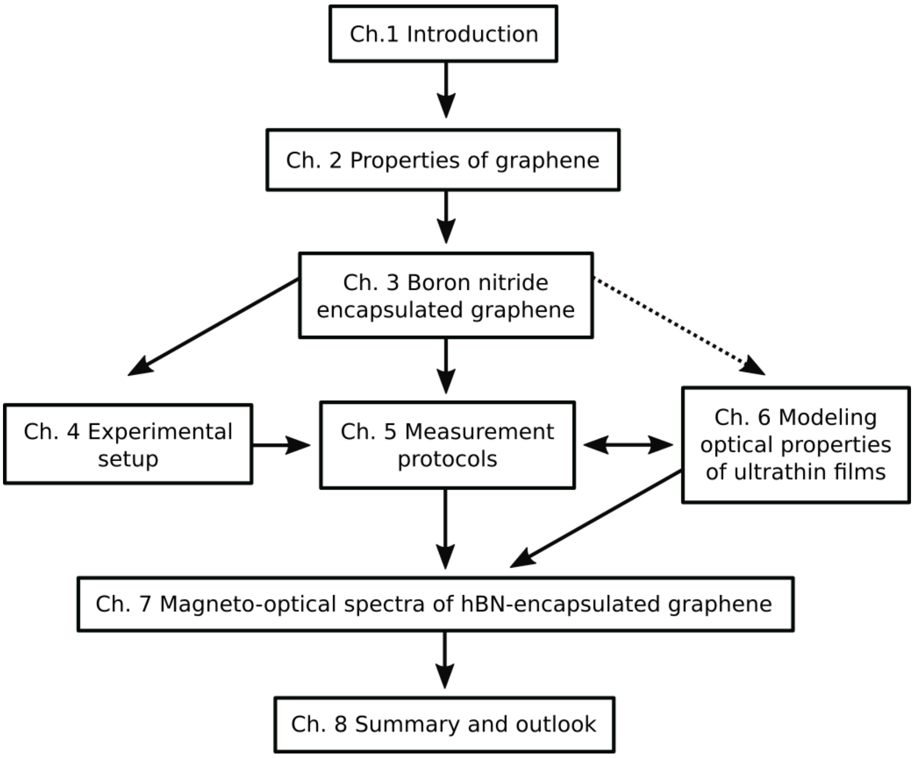

Figure 1.1 – Structure of the manuscript. Arrows show the sequences in which the chapters can be read or omitted without loss of continuity.

Chapter 2

Properties of graphene

A graphene monolayer consists of carbon atoms arranged in a flat honeycomb structure with lattice constant of $a_{\mathrm{Gr}} = 0.246$ nm which corresponds to $a_{\mathrm{Gr}}/\sqrt{3} \approx 0.142$ nm spacing between the neighboring carbon atoms [21, 22, 23], see Figure 2.1. Graphene's lattice is bipartite, i.e. it could be decomposed into two sublattices A and B in such a way that atoms of one sublattice neighbor only with atoms of the other sublattice. In graphene, both A and B sublattices have triangular shape. Graphene's crystalline lattice has the c_{6v} point group symmetry which contains the following elements: rotation by $2\pi/6$ ($\hat{c}_6$), reflection preserving sublattices ($\hat{c}_y$), reflection exchanging sublattices ($\hat{c}_x$). Graphene is a uniaxial crystals due to the honeycomb structure of its lattice. Thus optical properties of flat non-stained graphene are perfectly isotropic in the plane of graphene sheet which is the highest symmetry a 2D crystal can have.

Each carbon atom has six electrons: two electrons from the lowest $1s$ orbital belong to the ionic core meanwhile four remaining electrons are available for chemical bonding. In graphene, $2s$, $2p_x$, and $2p_y$ electrons are hybridized into $2sp$ configuration and form three inplane σ-bonds of crystalline lattice. $2p_z$ electrons result into π-bonds of atypical configuration: they dangle *perpendicularly* to the plane of graphene (i.e. electron density is accumulated perpendicular to the line connecting adjacent atoms) and at the same time π-electrons could be shared sideways across the lattice. Such atypical bonding is rare in nature and is related to the peculiar shape of carbon's atomic orbitals [24].

Graphene's lattice is composed of light atoms with strong bonding which leads to a very high sound velocity [25]. Vibrational properties of graphene have been described in terms of the dynamical matrix. Taking into account atoms from both sublattices and vibrations in all three dimensions leads to a (6×6) dynamical matrix for graphene. Two eigenvalues of this matrix correspond to out-of-plane vibrations: acoustic (ZA) and optical (ZO) phonons. Four remaining eigenvalues correspond to in-plane vibrations: transverse acoustic (TA), transverse optical (TO), longitudinal acoustic (LA), and longitudinal optical (LO) phonons.

2.1 Graphene in the absence of magnetic field

Electronic properties

Electronic properties of graphene are described in a topical review [26]. In graphene, the π-electrons are delocalized free-moving charge carriers and are responsible for most electronic properties of graphene. A standard tight-binding approach allows calculating the band structure of graphene. Taking into account only nearest-neighbor hopping of electrons, see Figure 2.1, one finds two bands: π^*-band and π-band [26]. They cross only in two points of the Brillouin zone: K and K' which are called Dirac points in the literature about graphene. The electron's dispersion is found to be

$$E_{\pi^*}(p) = E_0 + \gamma_1\sqrt{1 + 4\cos^2\left(\frac{p_y a_{\mathrm{Gr}}}{2}\right) + 4\cos\left(\frac{\sqrt{3}p_x a_{\mathrm{Gr}}}{2}\right)\cos\left(\frac{p_y a_{\mathrm{Gr}}}{2}\right)}, \tag{2.1}$$
$$E_\pi(p) = 2E_0 - E_{\pi^*}(p),$$

here E_0 is constant on-site energy, $\gamma_1 \approx 3.2\ eV$ is nearest-neighbor transfer integral which describes hopping of electrons, see Figure 2.1. In pristine (i.e. undoped) graphene, the Fermi level lies right in the Dirac point thus graphene's Fermi "surface" consists of only two point: K and K'. Graphene is classified as a semimetal or a zero-band-gap semiconductor, and phenomena which occur around the Dirac point define many properties of graphene. Existence of the Dirac points is related to the fact that its A and B sublattices are equivalent in graphene i.e. they are occupied by indistinguishable atoms. For comparison, graphene's "sister" compound hBN has very similar structure but the two sublattices are occupied by different atoms in hBN, see Figure 3.1. As a consequence, hBN is a broad band

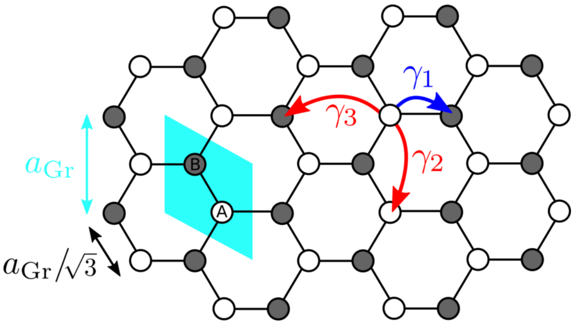

Figure 2.1 – Crystalline lattice of graphene. A unit cell is depicted by light blue rhombus with lattice constant a_{Gr}. Carbon atoms of A and B sublattices are depicted by white and black circles correspondingly. Nearest neighbor hopping (γ_1) of electron from one site to another is shown by deep blue arrow, second (γ_2) and third (γ_3) neighbor hoppings are shown by red arrows.

gap insulator. In the vicinity to the Dirac point, i.e. for energies $|E_{\pi^*,\pi} - E_0| \ll \gamma_1$, the complex shape of the dispersion relation (2.1) could be approximated by a pair of cones called Dirac cones:

$$\varepsilon_{\pm}(k) \approx \pm v_F \hbar |k|, \tag{2.2}$$

here the electrons' energy $\varepsilon_{\pm}$ and momentum $\hbar k$ are measured relative to the K or K' point, i.e. $\varepsilon_{\pm} = E_{\pi^*,\pi} - E_0$ and $k = p - K$, where $\hbar K$ is electron's momentum in the K point or K' point. In (2.2) energy does not depend on the direction of electron's momentum and Dirac cones are rotationally symmetric, see Figure 2.2. Parameter $v_F = \sqrt{3} a_{\text{Gr}} \gamma_1 / (2\hbar)$ has dimension of velocity and provides the value of the Fermi velocity. Typically $v_F \approx 10^6$ m/s in graphene. Many experiments have shown that a linear approximation of ideal cones (2.2) holds fairly well for the energies below $\sim$ 500 meV relative to the Dirac point. In a more general case, several types of deviations from the ideal double-cone shape (2.1) have been described in literature: non-linearity, trigonal warping, and electron-hole symmetry breaking.

Linear character of the dispersion relation (2.2) and the shape of the electrons' wave functions found with the tight-binding approach allow one to draw an analogy between electrons in graphene and massless ultrarelativistic particles like neutrinos in free space. The energy of massless ultrarelativistic particles also has linear dependency on momentum $E(p) = c\sqrt{p^2 + m^2 c^2} = c|p|$, where c is the speed of light in vacuum. Comparing the above mentioned formula to (2.2), one can see that v_F plays the role of "speed of light" for massless Dirac electrons which are low energy excitations in graphene. Thus graphene allows observing some hallmark relativistic phenomena but with a different velocity scale v_F, typically $c/v_F \approx 300$. However one should not forget that relativistic-type dispersion of electrons in graphene is merely a band structure effect. The speed with which interactions propagate in graphene is still related to c and not to v_F.

Gate voltage and/or chemical doping allow shifting the Fermi level in graphene, see Figure 2.2. As a consequence of (2.2), graphene's density of states rises linearly when moving away from the Dirac point:

$$D(\varepsilon_{\pm}) = \frac{|\varepsilon_{\pm}|}{v_F^2} \cdot \frac{g_s g_v}{2\pi\hbar^2}, \tag{2.3}$$

here factors $g_s = g_v = 2$ take into account for the spin and valley degeneracies of electrons. For comparison, in 2D systems with massive particles, density of states is constant [27]. Moreover, graphene's electron-hole symmetry and zero band gap allow ambipolar tuning of doping: graphene could be easily converted into an n-type or a p-type semimetal.

Many unique electronic properties of graphene stem from the fact that it is both a 2D crystal and a Dirac material at the same time. Indeed, currently only silicene, germanene, and a few other materials are deemed to combine these exotic features together [28]. For comparison, majority of the known Dirac materials are

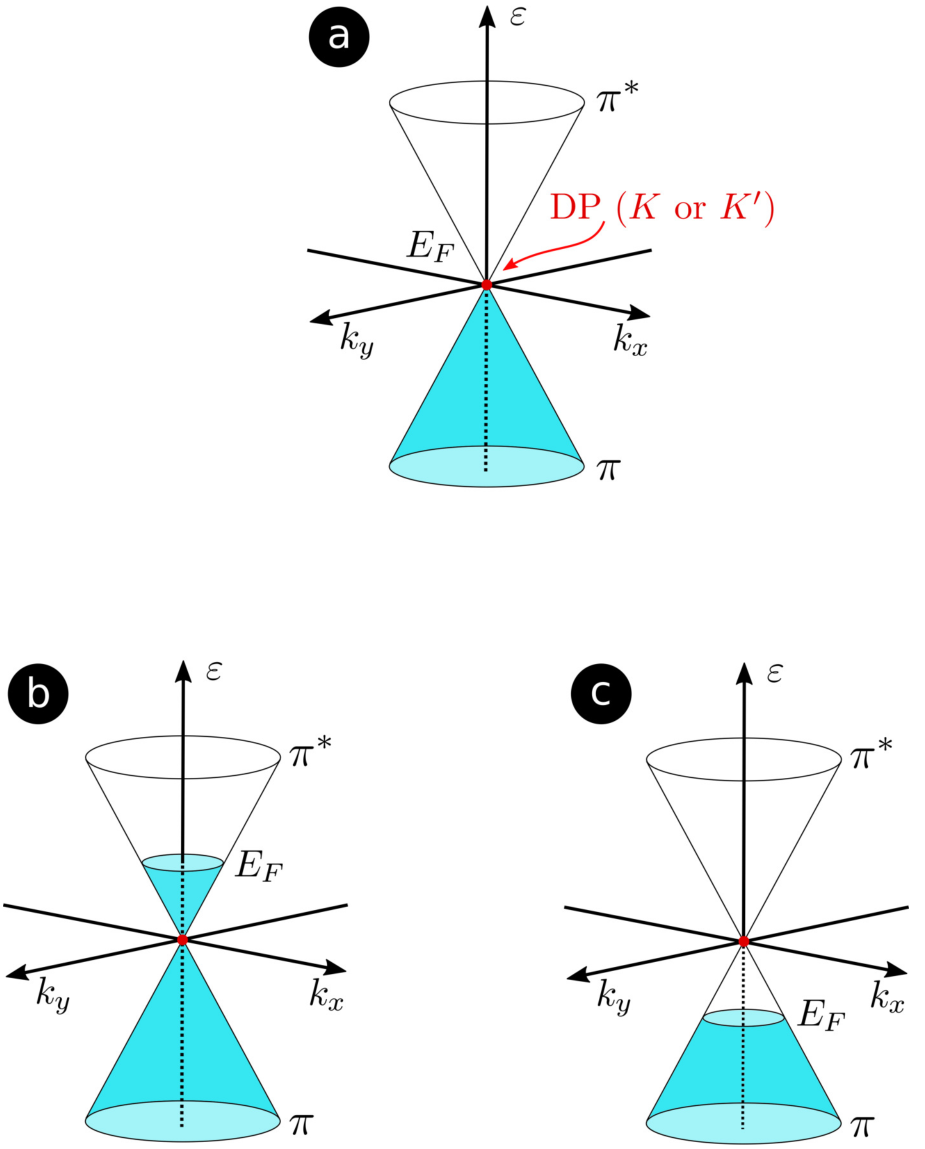

Figure 2.2 – Electrons' dispersion of graphene described by (2.2), two Dirac cones meet in the Dirac point. Blue color designates states occupied by electrons. **Panel a:** Pristine (i.e. undoped) graphene, the Fermi level resides right in the Dirac point. **Panel b:** The Fermi level is above the Dirac point which makes graphene an n-type semimetal. **Panel c:** The Fermi level is below the Dirac point which makes graphene a p-type semimetal.

3D systems (for example bismuth [29], quasicrystals, etc, see topical review [30]). Few-layer graphene crystals are still considered to be 2D systems because their thickness is much smaller than their electrons' de Broglie wavelengths. However, already in bilayer graphene the Dirac spectrum is substituted by a usual quadratic one [31]. The 2D electron gas which emerges at the interfaces of gallium arsenide and oxide [32] heterostructures also has a quadratic dispersion relation of its charge carriers.

Optical conductivity

Electric transport and optical properties of graphene could be understood in terms of its optical conductivity, also called dynamical conductivity. Optical conductivity σ describes current J induced in a solid as a local linear response to the external electric field E (in our experiments, it is electric field of the incident IR radiation):

$$J = \sigma E.$$

Unlike 3D conductivity, units of sheet conductivity do not involve distance: $[\sigma] = \Omega^{-1}$ in SI. In general case σ is a complex function of frequency ω of the external electric field. Optical conductivity of graphene has been calculated for different conditions using different approximations [33, 34, 35, 36, 37, 38, 39, 40]. For pristine graphene with linear dispersion approximation (2.2), the real part of the optical conductivity is found to be independent of frequency and quantities which characterize the material:

$$\operatorname{Re}\sigma(\omega) = \frac{e^2}{4\hbar} \equiv \sigma_0. \tag{2.4}$$

Therefore it is called *universal conductivity* of graphene. Such unusual property is directly related to the fact that graphene is a 2D Dirac crystal. In such a crystal, the density of states depends linearly upon energy (2.3). As optical conductivity is proportional to the density of states and inversely proportional to the frequency $\sigma_0 \sim (1/\omega) \cdot D(\omega)$, in the end the frequency-dependency is canceled out.

However this universality breaks when the Fermi level E_F is shifted away from the Dirac point, see Figure 2.4. In doped graphene, optical conductivity varies with frequency $\sigma = \sigma(\omega)$ and has a pronounced maximum at $\omega = 0$, followed by a step at the frequency $\hbar\omega = 2E_F$, at higher frequencies the conductivity approaches the universal conductivity of graphene $\sigma(\omega \gg 2E_F/\hbar) \to \sigma_0$. The exact shape of the curve $\sigma(\omega)$ depends on many parameters like scattering rate of electrons, their charge density, temperature, etc. It has been calculated for different cases and character of scattering in [41]. In the next subsection we explain the optical conductivity curve on a qualitative level.

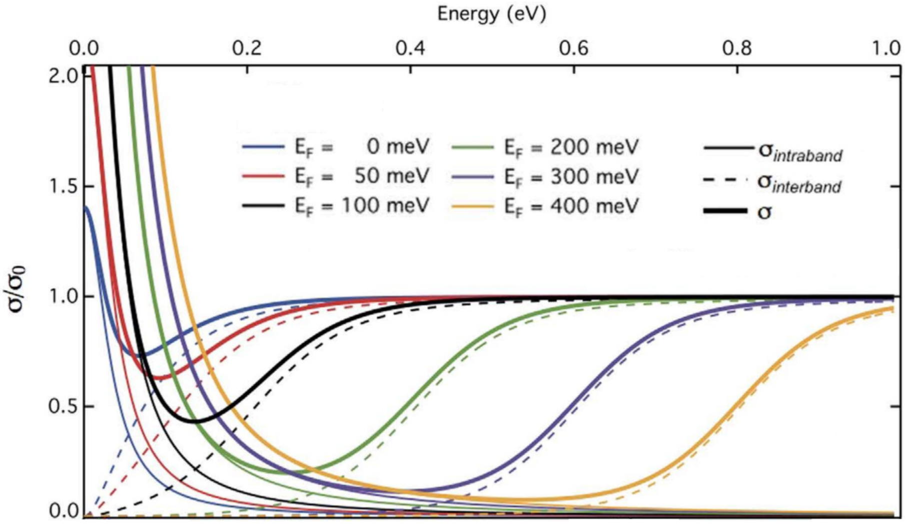

Figure 2.3 – Real part of graphene's optical conductivity in the units of graphene's universal conductivity σ_0. Different colors represent modeling of the conductivity for different values of the Fermi energy and the same value of charge carrier scattering rate $\tau = 20$ fs. Thin solid lines represent contribution to the conductivity from intraband transitions, dashed lines represent contribution to the conductivity from interband conductivity, thick solid lines represent the total conductivity. The figure is made after [42].

Optical properties in the absence of magnetic field

Optical properties of graphene are described in the topical review [27]. Theoretical analysis of the optical properties for different temperatures, carrier densities, and angles of light incidence is given in [43]. Optical properties beyond the usual Dirac-cone approximation are calculated in [44].

Graphene transmits most part of the incident light and absorbs a relatively small fraction of it. It is unusual and remarkable that graphene shows such behaviour in exceptionally broad range of wavelengths: from THz to UV region. Broad range transparency of graphene is related to the fact that it is a purely covalent crystal[1]. Its optical phonons do not interact directly with light and thus do not create any absorption lines or bands so typical for many other materials. Broad range absorption in pristine, i.e. undoped, graphene is related to the fact that graphene does not have any band gap which would block optical absorption at low frequencies of incident light. At the same time, absorption in doped graphene may become very close to zero for some photons from the region $0 < \hbar\omega < 2E_F$. In this case, the exact values of absorption largely depend on the quality of the graphene sample.

Graphene's optical response is mostly defined by interaction of light with elec-

---

[1] This feature is also typical of diamond, another carbon allotrope.

trons. Phonons may influence optical properties of graphene only indirectly[2]: for example via electron-phonon interactions and scattering. Whenever a photon is absorbed an electron is excited to a higher energy level. In this process conservation of energy and momentum laws must hold. Electron transitions could be classified into interband and intraband, see Figure 2.4.

In *interband* transitions, electrons are promoted from the π-band to π^*-band. In this process the photon's energy corresponds to the change of electron's energy:

$$\hbar\omega = E_{\text{f}} - E_{\text{in}}, \tag{2.5}$$

here ω is the frequency of the absorbed photon, E_{in} and E_{f} are the initial and final energies of the excited electron. The photon's momentum is negligible compared to the change of the electron's momentum $\hbar\omega/c \ll \hbar\omega/v_F$ because the Fermi velocity is two orders of magnitude smaller than the speed of light. Thus transitions of electrons across the Dirac point must be "vertical" in the k-space, see panels a and b of Figure 2.4.

For pristine graphene, frequency independent conductivity (2.4) leads to frequency independent optical absorption A_0, reflection R_0, and transmission T_0, at normal incidence of light [33]:

$$\begin{gathered} A_0 = \pi\alpha \approx 2.3\,\%, \\ R_0 = \pi^2\alpha^2 T/4 \ll T \approx 0.01\,\%, \\ T_0 \approx 1 - \pi\alpha \approx 97.7\,\%. \end{gathered} \tag{2.6}$$

Here α is the fine structure constant: $\alpha = e^2/(\hbar c)$ in CGS units and $\alpha \approx 1/137$ in all unit systems. Such frequency independent optical properties are a peculiar feature of graphene and are not typical for other materials. However this universality is only valid as long as the linear dispersion of electrons (2.2) holds. It has been shown in optical measurements [45] that properties of graphene start deviating from universal values (2.6) at short wavelengths of light already within the ultraviolet region of the spectrum. Another reason for deviation from the universal values (2.6) is related to nonlinear phenomena which manifest in graphene at high intensities of light [46, 47].

If the Fermi level is shifted away from the Dirac point then interband optical absorption occurs only for photons with energies $\hbar\omega > 2E_F$ because electron transitions are possible only between occupied and non-occupied states, see panel b of Figure 2.4. Thus graphene becomes more transparent for photons with lower energies $\hbar\omega < 2E_F$ which is sometimes redundantly called the "Pauli blocking regime". The onset of interband transitions at frequencies $2E_F/\hbar$ leads to a pronounced step in the optical conductivity, see Figure 2.3. At higher frequencies $\hbar\omega > 2E_F$, optical transitions occur with almost the same intensities as in pristine graphene and the value of conductivity approaches universal conductivity σ_0.

---

[2] Raman scattering of light involving graphene phonons is a very low probability process.

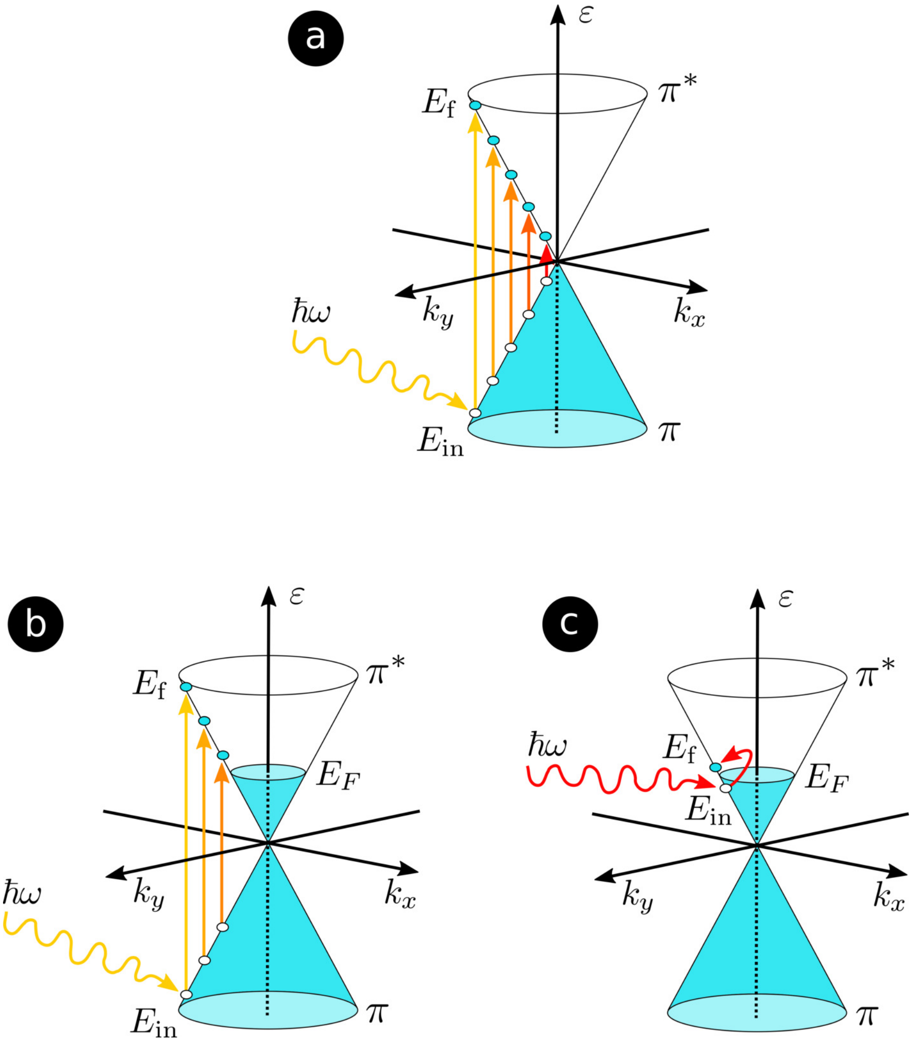

Figure 2.4 – Absorption of light by graphene. **Panel a:** Interband optical transitions in pristine graphene. **Panel b:** Interband transitions in n-doped graphene, the same transitions are allowed in p-doped graphene when the Fermi level is shifted downwards symmetrically relative to the Dirac point, see Figure 2.2. **Panel c:** intraband transition in n-doped graphene, the same transitions are allowed in p-doped graphene due to the electron-hole symmetry.

In *intraband* transitions electrons are promoted to higher energy levels within the same band, see panel c of Figure 2.4. This phenomenon is possible when Fermi level is shifted away from the Dirac point. Moreover, intraband transitions are not "vertical" in the k-space therefore a photon can be absorbed only when the change of the electron's momentum is somehow compensated. The necessary change of momentum could be provided by disorder in the graphene sample. Intraband transitions result in the Drude-like peak in the optical conductivity around $\omega = 0$.

Interaction effects

The above mentioned tight-binding calculations do not take into account interactions between particles in graphene. This approach explains many phenomena on qualitative and often even on quantitative level. However there is a lot of experimental evidence and theoretical considerations showing that single-electron description of graphene is incomplete. For more information about interaction effects in graphene see topical reviews [48, 49, 50].

The importance of the Coulomb interaction could be estimated using the ratio of the Coulomb energy to the kinetic energy of electrons. In graphene, such ratio takes value:

$$\alpha_{\text{Gr}} = \frac{E_C}{E_K} = \frac{e^2}{\kappa \hbar v_F},$$

where κ is effective dielectric constant defined by graphene's environment. As one may notice, α_{Gr} is a quantity analogous to the fine structure constant $\alpha = e^2/(\hbar c)$.

Here are the values of κ for some typical graphene's substrates: for SiC$(000\bar{1})$ $\kappa = 7.26$, for hBN $\kappa = 4.22$, for SiO_2 $\kappa = 1.80$, for a-SiO_2 $\kappa = 2.45$, and for vacuum $\kappa = 1$ (the values are taken from [48]). Thus for suspended graphene in vacuum $\alpha_{\text{Gr}} \approx 2.3$. Meanwhile for graphene laying on a substrate electron-electron interactions are partially screened, for example in the case of SiO_2 substrate $\alpha_{\text{Gr}} \approx 1$ and in the case of hBN substrate $\alpha_{\text{Gr}} \approx 0.6$. These numbers show that interaction between charge carriers is quite pronounced in graphene. In contrast, in quantum electrodynamics $\alpha \approx 1/137$ is considered to be a small parameter.

One of the widely discussed effects of electron-electron interactions is so called renormalization of the Fermi velocity near to the Dirac point [48, 49]. It implies that the electron dispersion relation deviates from linear one (2.2) and Dirac cones acquire some negative curvature already at low energies near to the Dirac point. Theoretical calculations which have been proposed so far predict different character of dependency of the renormalized Fermi velocity on momentum. Renormalization also makes the relation between the observable quantities and calculated quasiparticle properties more complicated. Thus comparison of theoretical predictions to experimental results requires very careful analysis.

Another important presumable effect of electron-electron interactions is opening of a gap Δ at the Dirac point. As a result, the linear dispersion relation (2.2) of graphene is substituted by

$$\varepsilon_\pm(k) = \pm\sqrt{\Delta^2 + v_F^2\hbar^2k^2}. \tag{2.7}$$

Existence of the gap in graphene and mechanisms of the band gap opening are still in debate. Presumable values of the gap which have been reported in the literature are relatively small $\Delta < 1 - 100$ meV. This means that graphene's dispersion relation remains almost the same far from the Dirac point.

2.2 Electronic properties of graphene in magnetic field

Landau levels

Behaviour of massless electrons in external magnetic field perpendicular to graphene's plane is summarized in the topical review [51]. In this work, we consider only this orientation of the magnetic field and avoid phenomena observed in tilted magnetic fields [52].

Magnetic field B introduces new important scales in graphene: magnetic length l_B, magnetic frequency ω_B, and associated magnetic energy E_B:

$$l_B = \sqrt{\frac{\hbar}{eB}} \approx \frac{25.5}{\sqrt{B[\text{Tesla}]}}\ \text{nm},$$

$$\omega_B = \sqrt{2}v_F/l_B,\ \ E_B = \hbar\omega_c = v_F\sqrt{2\hbar eB},$$

It's important to note that these scales are proportional or inversely proportional to the *square root* of the magnetic field. In a nonzero magnetic field the continuous electron density of states (2.3) falls apart into a set of discrete Landau levels which we enumerate by n:

$$E_n = \text{sign}(n)v_F\sqrt{2e\hbar B|n|} = \text{sign}(n)E_B\sqrt{|n|}, \tag{2.8}$$

$$n = ... - 3,\ -2,\ -1,\ 0,\ +1,\ +2,\ +3, ... \ .$$

Non-equidistant positions of the Landau levels and the existence of the zeroth level $n = 0$ just in the Dirac point are peculiar features of graphene, see Figure 2.5. In contrast, particles with a constant density of states have equidistant Landau levels: $E_n^{\text{cl}} = \hbar\omega_c^{\text{cl}}(n + 1/2)$ with $\omega_c^{\text{cl}} = eB/m$ classical cyclotron frequency directly proportional to magnetic field. Each Landau level must accommodate the same number of electrons, therefore in systems with a constant density of states the levels are equidistant. However in graphene the density of states grows with energy (2.3), as a result spacing between Landau levels becomes narrower (2.8) for higher $|n|$. And the existence of the zeroth level $n = 0$ in graphene is related to its nontrivial Berry phase [53, 54, 55].

Within the semiclassical approximation, the cyclotron mass m^* of charge carriers is defined through the area $A(E)$ in k-space enclosed by a cyclotron orbit:

$$m^* \equiv \frac{1}{2\pi}\left[\frac{\partial A(E)}{\partial E}\right]_{E=E_F},$$

thus cyclotron mass of Dirac electrons in graphene is

$$m^* = E_F/v_F^2.$$

Each Landau level has degeneracy of $g_s g_v|B|/(2\phi_0)$ states per unit area where $\phi_0 = h/(2e)$ is the magnetic flux quantum and $g_s = g_v = 2$ are spin and valley

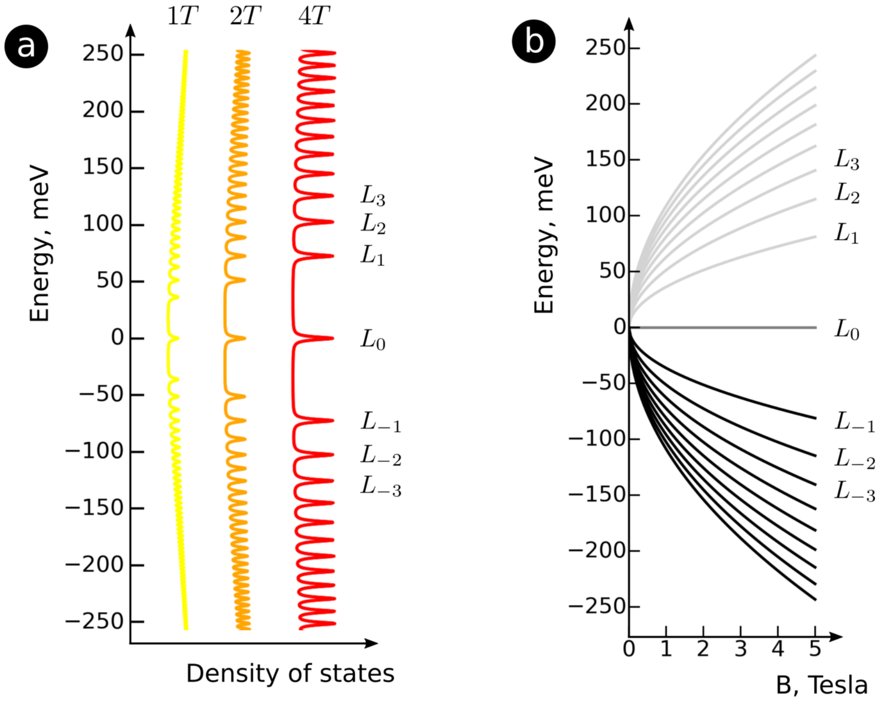

Figure 2.5 – Electronic properties of graphene in a magnetic field, Fermi velocity $v_F = 10^6$ m/s (a typical value found in graphene). **Panel a:** Density of states is plotted with some offset to avoid visual overlap of the curves for three different values of external magnetic field, the width of each level is 1.5 meV (the value was picked haphazardly to create this illustration). As the magnetic field decreases, spacing between the Landau levels shrinks and in the limit of $B \to 0$ the linear dependency (2.3) is recovered. **Panel b:** Landau fan diagram i.e. energies of lowest Landau levels (2.8) plotted as a function of magnetic field. Fully occupied Landau levels are shown in black, half-filled level L_0 is dark gray, and empty Landau levels are shown in light gray. Such filling of Landau levels corresponds to pristine graphene at zero temperature.

degeneracies of states. Strictly speaking the spin degeneracy g_s is lifted in an external magnetic field, however the value of the Zeeman splitting is very small and it could be observed only in extreme conditions of high magnetic fields and low temperatures, therefore in most cases it is neglected.

In pristine graphene the zeroth Landau level is half-filled and characterized by the filling factor $\nu = 2$. Applying a gate voltage to a graphene sample allows adding or removing electrons gradually at a fixed value of magnetic field. At zero temperature, whenever all states at a particular Landau level are occupied or emptied, the Fermi level shifts to a neighboring Landau level. Apart from that, graphene crystals may have some chemical doping introduced on purpose or due to unintended contamination. We denote concentration of charge carriers per unit of area as N. The concentration of the charge carriers N, filling factor ν, and number of the Landau level are related to each other the following way:

$$\begin{aligned} &\nu = \pm(4|n| + 2), \\ &N = \nu\frac{eB}{h} \quad \text{where} \quad \frac{e \cdot 1\text{Tesla}}{h} \approx 24.1 \cdot 10^9 \text{cm}^{-2}, \end{aligned} \tag{2.9}$$

here in the first formula the sign "$+$" describes the case of n-doping, the sign "$-$" describes the case of p-doping, and prefactor 4 takes into account spin and valley degeneracies of each level.

In some optical experiments, including ours, the amount of the extra charge due to the doping is fixed $N = \text{const}$. Applying gate voltage to the sample is not always possible due to technical reasons and only the value of the magnetic field could be tuned. These circumstances are often important to understand and model the phenomena observed in optical experiments. Whenever the value of the magnetic field is changed, the density of states at each Landau level also changes according to the formulas 2.9. Therefore the extra charge must be redistributed and accommodated on the Landau levels in a different way. As a result, position of the Fermi level depends on magnetic field: In the case of n-doping (or p-doping), when the value of magnetic field is increased then the highest filled Landau level becomes emptied (or completely filled), and the Fermi level "jumps" from this Landau level to a neighboring one in the direction towards the Dirac point for both types of doping, see Figure 2.6. In a more general case including nonzero temperatures, the position of chemical potential as a function of magnetic field $\mu = \mu(B)$ could be found for a given concentration N from the following equation:

$$N = \frac{4eB}{h} \sum_{n=-\infty}^{\infty} \left[f(E_n) - \frac{1}{2} \right], \tag{2.10}$$

here the sum goes over all Landau levels, the prefactor takes into account the degeneracy of each Landau level, $f = f(E)$ is the Fermi-Dirac distribution which takes into account the effect of nonzero temperature T:

$$f(E_n) = \frac{1}{\exp\left(\frac{E_n - \mu}{k_B T}\right) + 1}. \tag{2.11}$$

Equation (2.10) defines the total doping charge per unit of area in such a way that $N = 0$ when the chemical potential is in the Dirac point i.e. $\mu = 0$.

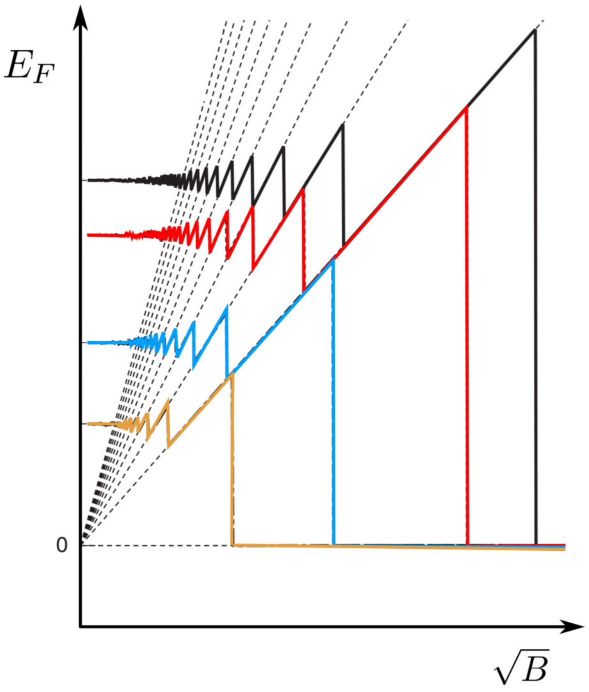

Figure 2.6 – Positions of the Fermi level in n-doped graphene as a function of magnetic field at zero temperature. Lines of different color represent four different charge carrier concentrations. Dotted lines denote the energies of Landau levels. The figure is made after [56].

Structure and properties of magneto-optical conductivity tensor

Magneto-optical response of a solid body is often distinct and more complicated than its optical response in the absence of magnetic field described by $\sigma(\omega)$. In the most general case, magneto-optical conductivity $\hat{\sigma}(\omega, B)$ is a second rank tensor represented by a 3×3 matrix with complex components which depend on magnetic field B. It is important to emphasize that $\hat{\sigma}(\omega, B)$ has nonzero off-diagonal components even in the case of an optically isotropic material. In the case of an optically anisotropic material, $\hat{\sigma}(\omega, B)$ also has nonzero off-diagonal components even if it is written down in coordinate system defined by the principal axes of the crystal. The off-diagonal components of $\hat{\sigma}(\omega, B)$ describe the time-reversal symmetry breaking introduced by an external magnetic field. In particular these components are needed in order to properly describe optical response of a solid to the circularly polarized light of different handedness (right-handed and left-handed circularly polarized rays of light could be viewed as time-reversed versions of each other).

Graphene is a 2D crystal therefore $\hat{\sigma}(\omega, B)$ could be reduced to a 2×2 matrix. Here redistribution of electric charge in the direction perpendicular to graphene's plane is considered to be negligible. Moreover, graphene has uniaxial symmetry i.e. optical properties of graphene remain unchanged after any rotations around any axis perpendicular to the plane of graphene. Due to the above mentioned symmetry and Onsager reciprocity relations [57], only two components of magneto-optical conductivity tensor remain independent and $\hat{\sigma}(\omega, B)$ acquires the following form in the Cartesian coordinates:

$$\hat{\sigma}(\omega, B) = \begin{bmatrix} \sigma_{xx}(\omega, B) & \sigma_{xy}(\omega, B) \\ -\sigma_{xy}(\omega, B) & \sigma_{xx}(\omega, B) \end{bmatrix}. \tag{2.12}$$

Here $\sigma_{xx}(\omega, B)$ is diagonal or longitudinal optical conductivity. Two diagonal components of $\hat{\sigma}(\omega, B)$ are equal due to the uniaxial symmetry of graphene: $\sigma_{xx}(\omega, B) = \sigma_{yy}(\omega, B)$. Onsager relations impose more restrictions on the diagonal components:

$$\sigma_{xx}(\omega, B) = \sigma_{xx}(\omega, -B), \quad (\sigma_{xx}(\omega, B))^* = \sigma_{xx}(-\omega, B).$$

$\sigma_{xy}(\omega, B)$ is the off-diagonal conductivity or the Hall conductivity. The off-diagonal components of $\hat{\sigma}(\omega, B)$ are opposite to each other due to Onsager relations. Here are all the restrictions on the off-diagonal components due to Onsager relations summarized together:

$$\sigma_{xy}(\omega, B) = -\sigma_{yx}(\omega, B),$$

$$\sigma_{xy}(\omega, B) = -\sigma_{xy}(\omega, -B), \quad (\sigma_{xy}(\omega, B))^* = \sigma_{xy}(-\omega, B)$$

Eigenvalues of $\hat{\sigma}(\omega, B)$ tensor correspond to conductivities which describe the response of graphene to right- and left-handed circularly polarized light:

$$\sigma_+(\omega, B) = \sigma_{xx}(\omega, B) + i\sigma_{xy}(\omega, B),$$

$$\sigma_-(\omega, B) = \sigma_{xx}(\omega, B) - i\sigma_{xy}(\omega, B).$$

Thus in the circular basis, $\hat{\sigma}(\omega, B)$ acquires diagonal form with its components equal to right-handed and left-handed circular conductivities. This basis is naturally inherent for description of magneto-optical phenomena in graphene. Indeed, each magneto-optical transition of an electron in graphene is accompanied by absorption of either a right- or a left-handed circularly polarized photon, see the next section. Representation in Cartesian coordinates is more common in the literature about the Hall effect.

As one can see from the above mentioned equations due to Onsager relations, the diagonal components $\sigma_{xx}(\omega, B)$ do not change after magnetic field inversion and off-diagonal components $\sigma_{xy}(\omega, B)$ are antisymmetric with respect to the magnetic field inversion. This implies that the off-diagonal component vanishes in the absence of external magnetic field $\sigma_{xy}(\omega, 0) = 0$ and there remain only equal diagonal components. As a result, the magneto-optical conductivity tensor reduces to the scalar optical conductivity $\sigma(\omega)$ described in the previous section:

$$\sigma_{xx}(\omega, 0) = \sigma_{+}(\omega, 0) = \sigma_{-}(\omega, 0) \equiv \sigma(\omega).$$

Pristine (undoped) graphene represents a very interesting case: the off-diagonal components of its magneto-optical conductivity tensor vanish due to the electron-hole symmetry $\sigma_{xy}(\omega, B) = 0$ even if external magnetic field is not zero. Meanwhile the its diagonal components are equal to each other but distinct from the universal conductivity of graphene:

$$\sigma_{xx}(\omega, B) = \sigma_{+}(\omega, B) = \sigma_{-}(\omega, B) \neq \sigma(\omega).$$

All the above mentioned components of magneto-optical conductivity tensor are causal response functions [58, 59]. Therefore their real and imaginary parts are connected to each other by Kramers-Kronig relations which assume the following form in the case where magneto-optical effects are taken into account [60]:

$$\operatorname{Re}\sigma_i(\omega, B) = \frac{1}{\pi}\mathcal{P}\int_{-\infty}^{\infty} \frac{\operatorname{Im}\sigma_i(\omega', B)}{\omega' - \omega} d\omega', \tag{2.13}$$

$$\operatorname{Im}\sigma_i(\omega, B) = -\frac{1}{\pi}\mathcal{P}\int_{-\infty}^{\infty} \frac{\operatorname{Re}\sigma_i(\omega', B)}{\omega' - \omega} d\omega', \tag{2.14}$$

here the index i designates any of "xx", "xy", "$+$" or "$-$". It is important to remark that integration in (2.13) and (2.14) also includes the negative frequencies.

Magneto-optical conductivity of graphene

Magneto-optical tensor $\hat{\sigma}(\omega, B)$ has been calculated and analyzed in [61, 62]. Here we only summarize results of a simple single-particle model [27] containing a set of phenomenological parameters which could be found only in the framework of more complicated models. This model could be used as a starting point to illustrate some properties of graphene. Linear response approximation leads to the Kubo-Greenwood formula [63] for right-handed and left-handed components of the magneto-optical conductivity tensor:

$$\sigma_{\pm}(\omega, B) = \frac{4ie^3B}{\pi} \sum_{\text{in,f}} \frac{f(E_{\text{in}}) - f(E_{\text{f}})}{E_{\text{f}} - E_{\text{in}}} \frac{|\langle\Psi_{\text{in}}|\hat{v}_{\pm}|\Psi_{\text{f}}\rangle|^2}{\hbar\omega - (E_{\text{f}} - E_{\text{in}}) + i\Gamma_{\text{in}\to\text{f}}}. \tag{2.15}$$

Here indices "in" and "f" designate initial and final states of electrons during magneto-optical transitions between Landau levels, Ψ_{in} and Ψ_{f} are the wave functions which describe these states, E_{in} and E_{f} are energies of the corresponding Landau levels. Values of both indices run through all Landau levels:

$$\text{in, f} = ... - 3,\ -2,\ -1,\ \ 0,\ +1,\ +2,\ +3, ...\ .$$

$f = f(E_n)$ is the Fermi-Dirac distribution given in the formula (2.11). $\hat{v}_\pm = \hbar^{-1}\partial\hat{H}/\partial k_\pm$ is velocity operator, $\hat{H}$ is system's Hamiltonian close to the K point and $k_\pm = k_x \pm ik_y$ describes electrons' momentum. $\Gamma_{\text{in}\to\text{f}}$ is a phenomenological parameter which describes broadening of each transition. The exact values of these parameters could be found from experiment or in the framework of a more complicated theory. The prefactor in the Kubo-Greenwood formula takes into account degeneracy of Landau levels.

In a simple case of non-interacting electrons, the Hamiltonian $\hat{H}$ which takes into account only the nearest neighbor hopping of electrons could be easily diagonalized. Its eigenfunctions Ψ_n and corresponding energies E_n of Landau levels could be found explicitly, see formula (2.8). Next, one can verify that only three groups of matrix elements $|\langle\Psi_{\text{in}}|\hat{v}_\pm|\Psi_{\text{f}}\rangle|^2$ have nonzero values. These matrix elements are divided into three groups regarding the band of the initial and final states of the electrons:

$$\begin{aligned} 1)\ \ \text{mixed transitions}\ \ &|\langle\Psi_0|\hat{v}_+|\Psi_1\rangle|^2 = |\langle\Psi_1|\hat{v}_-|\Psi_0\rangle|^2 = \\ &= |\langle\Psi_0|\hat{v}_+|\Psi_{-1}\rangle|^2 = |\langle\Psi_{-1}|\hat{v}_-|\Psi_0\rangle|^2 = v_F^2/2, \end{aligned} \tag{2.16}$$

$$\begin{aligned} 2)\ \ \text{interband transitions}\ \ &|\langle\Psi_{-j}|\hat{v}_+|\Psi_{j+1}\rangle|^2 = |\langle\Psi_{-j-1}|\hat{v}_-|\Psi_j\rangle|^2 = \\ &= |\langle\Psi_{j+1}|\hat{v}_-|\Psi_{-j}\rangle|^2 = |\langle\Psi_{-j}|\hat{v}_-|\Psi_{-j-1}\rangle|^2 = v_F^2/4, \end{aligned} \tag{2.17}$$

$$\begin{aligned} 3)\ \ \text{intraband transitions}\ \ &|\langle\Psi_{-j-1}|\hat{v}_+|\Psi_{-j}\rangle|^2 = |\langle\Psi_j|\hat{v}_-|\Psi_{j+1}\rangle|^2 = \\ &= |\langle\Psi_{-j}|\hat{v}_-|\Psi_{-j-1}\rangle|^2 = |\langle\Psi_{j+1}|\hat{v}_-|\Psi_j\rangle|^2 = v_F^2/4, \end{aligned} \tag{2.18}$$

here the new index j assumes only positive values $j = 1, 2, 3, \ldots$. Substituting the formulas (2.16), (2.17), and (2.18) into the Kubo-Greenwood formula (2.15) one can obtain the final expression for the right-handed and left-handed magneto-optical conductivities of graphene:

$$\begin{aligned} \sigma_\pm(\omega, B) =\ & 2 \cdot \frac{i\hbar}{\pi}\left[\frac{W_{1\pm}}{\hbar\omega - T_1 + i\Gamma_1} + \frac{W_{1\mp}}{\hbar\omega + T_1 + i\Gamma_1}\right] + \\ & + \frac{i\hbar}{\pi}\sum_{j=2}^{\infty}\left[\frac{W_{j\pm}}{\hbar\omega - T_j + i\Gamma_j} + \frac{W_{j\mp}}{\hbar\omega + T_j + i\Gamma_j}\right] + \\ & + \frac{i\hbar}{\pi}\sum_{j=2}^{\infty}\left[\frac{W'_{j\pm}}{\hbar\omega - T'_j + i\Gamma'_j} + \frac{W'_{j\mp}}{\hbar\omega + T'_j + i\Gamma'_j}\right]. \end{aligned} \tag{2.19}$$

Here the sum goes only over transitions with nonzero probabilities. The three terms (each one is presented on a separate line) take into account mixed, interband, and intraband transitions correspondingly. T_1, T_j and T'_j are energies of these transitions i.e. differences between the energies of initial and final states:

$$T_j = E_B(\sqrt{j} + \sqrt{j-1}), \quad j = 1, 2, 3, \dots ,$$

$$T'_j = E_B(\sqrt{j} - \sqrt{j-1}), \quad j = 2, 3, 4, \dots .$$

Coefficients W_j and W'_j are spectral weights of these transitions:

$$W_{j+} = \frac{e^2 E_B^2}{2\hbar^2} \cdot \frac{f(-E_{j-1}) - f(E_j)}{T_j}, \quad W_{j-} = \frac{e^2 E_B^2}{2\hbar^2} \cdot \frac{f(-E_j) - f(E_{j-1})}{T_j},$$

here $j = 1, 2, 3, \dots$.

$$W'_{j+} = \frac{e^2 E_B^2}{2\hbar^2} \cdot \frac{f(E_{j-1}) - f(E_j)}{T'_j}, \quad W'_{j-} = \frac{e^2 E_B^2}{2\hbar^2} \cdot \frac{f(-E_j) - f(-E_{j-1})}{T'_j}$$

here $j = 2, 3, 4, \dots$.

The widths Γ_j of magneto-optical transitions are defined by different broadening mechanisms: Auger processes as well as scattering of graphene's charge carriers on defects, impurities, and graphene's optical phonons. Therefore the widths can be found only in the framework of a more advanced theory, see [64], and the exact values of Γ_j depend on energy, doping, concentration of the defects and their type, magnetic field, and temperature. In general the widths Γ_j are larger at higher energies and for higher magnetic fields.

The formula (2.19) could be largely simplified in the case of pristine graphene at zero temperature, or in the case when both the chemical potential and the temperature are low compared to the magnetic energy $\mu,\ k_B T \ll E_B$. Indeed, all terms (2.18) corresponding to the intraband transitions become irrelevant. Next, formula (2.19) could be rearranged the following way:

$$\sigma_\pm(\omega, B) = \frac{2}{\pi} \sum_{j=1}^{\infty} W_j \frac{i\hbar(\hbar\omega + i\Gamma_j)}{(\hbar\omega + i\Gamma_j)^2 - T_j^2}. \tag{2.20}$$

where the energies and spectral weights of the remaining transitions are

$$T_j = E_B(\sqrt{j} + \sqrt{j-1}), \quad W_j = \frac{e^2 E_B^2}{2\hbar^2} \cdot \frac{1}{T_j}.$$

As one can see, pristine graphene has a noteworthy property: the product between the energy and the spectral weight of any transition depends only on magnetic field and does not depend on its number j :

$$T_j W_j = \frac{e^2}{2\hbar^2} E_B^2 = \frac{e^3}{\hbar} v_F^2 B. \tag{2.21}$$

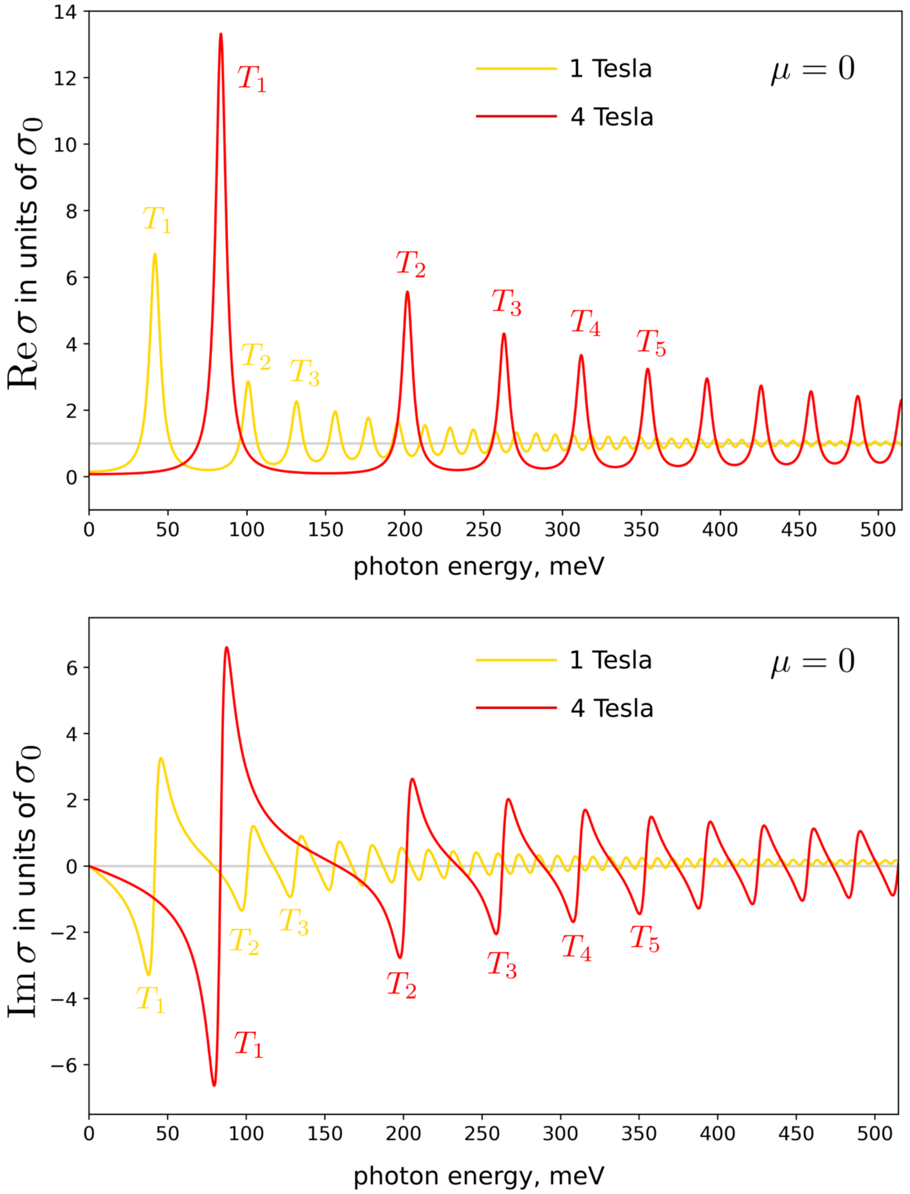

Figure 2.7 – MO conductivity of graphene according to the simple model, see formula (2.19), for the case of zero doping $\mu = 0$, temperature 10 Kelvin, and constant width of the MO transitions $\Gamma_j = 4$ meV. Such narrow widths of MO transitions could be found only in high quality graphene samples. Undoped graphene represents a special case when right- and left-handed conductivities coincide $\sigma_+ = \sigma_- \equiv \sigma$ due to the electron-hole symmetry. Scheme of magneto-optical transitions is shown in panel a of Figure 2.9. In pristine graphene only the mixed MO transition T_1 and interband MO transitions $T_i, i \geq 2$ are active. At high energies far from 0^{th} LL, behaviour of graphene resembles the one of undoped graphene in the absence of magnetic field $\sigma \to \sigma_0$.

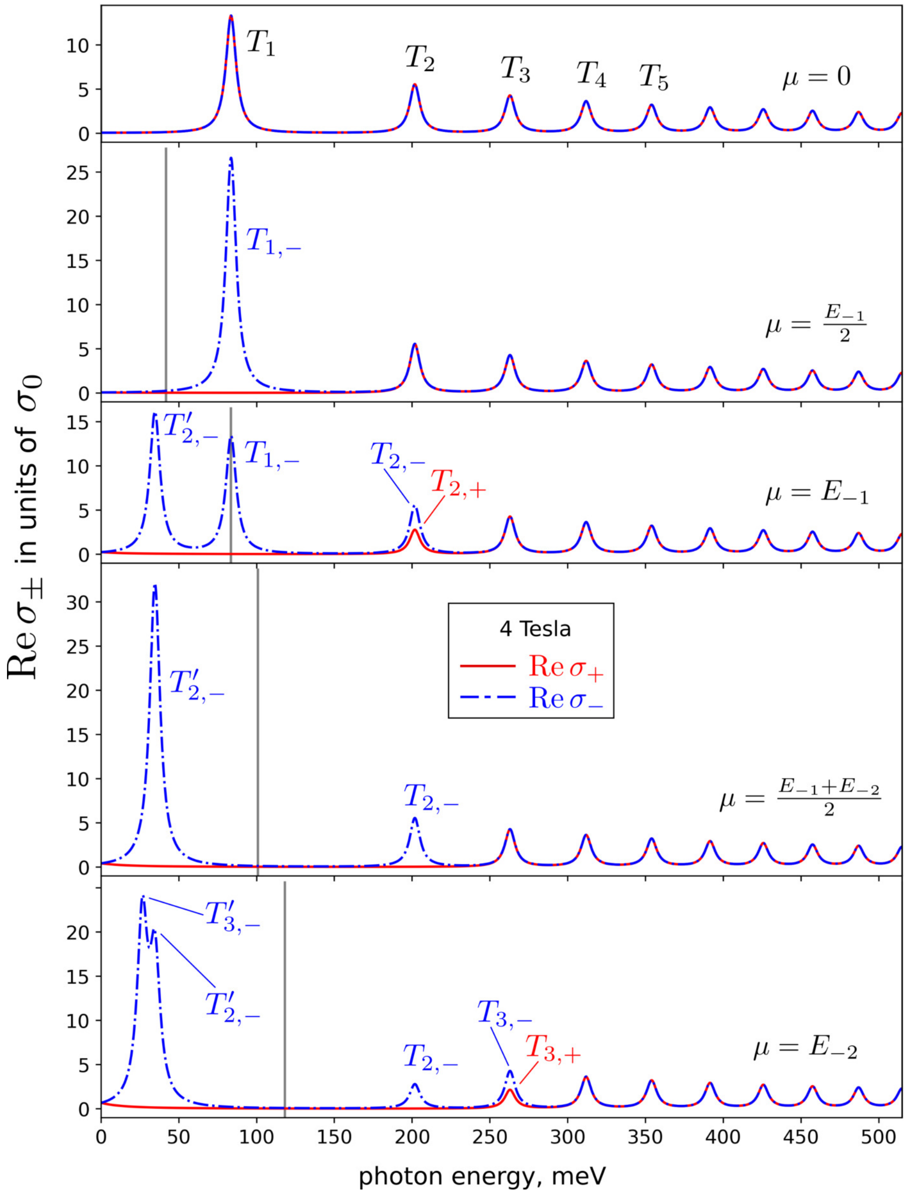

Figure 2.8 – MO conductivity of undoped and p-doped graphene according to the simple model, see formula (2.19), for temperature 10 Kelvin, and constant width of the MO transitions $\Gamma_j = 4$ meV. The color code is the same in all panels. Gray vertical lines indicate the absolute value of the chemical potential $|\mu|$. The values of the chemical potential were chosen to illustrate how different MO transitions acquire and lose their spectral weight as the chemical potential moves down away from the 0^{th} LL and consequently crosses the energies of -1 and -2 LLs, see formula (2.8). Schemes of MO transitions are given in Figure 7.15 and Figure 7.15. At high energies far form $2|\mu|$, behaviour of graphene resembles the one of pristine graphene $\sigma_+ - \sigma_- \to 0$. In the case of n-doping the conductivity curves exchange i.e. $\sigma_\pm \to \sigma_\mp$ when $\mu \to -\mu$.

Effects beyond a simple theory

Interaction effects briefly mentioned in the previous section also influence graphene's properties in the presence of magnetic field. As a result, positions of the Landau levels could be shifted which is sometimes described in terms of different values of effective Fermi velocity (or renormalized Fermi velocity) for each number of a Landau level, see topical review [48]. In contrast, in 2D systems with a parabolic dispersion relation the electron-electron interactions have no impact on the cyclotron resonance energy due to the Kohn's theorem [65, 66]. Another presumable effect of interactions is band gap opening. If a band gap is present, degeneracy of the zeroth Landau level is lifted: it splits in two levels which we denote by $n = +0$ and $n = -0$. The energies of the Landau levels acquire the following values:

$$\begin{aligned} n > 0, \quad E_n &= \Delta/2 + \sqrt{2e\hbar v_F^2 Bn + (\Delta/2)^2}, \qquad (2.22) \\ n = +0, \; E_{+0} &= \Delta/2, \\ n = -0, \; E_{-0} &= -\Delta/2, \\ n < 0, \quad E_n &= -\Delta/2 - \sqrt{2e\hbar v_F^2 B|n| + (\Delta/2)^2}. \end{aligned}$$

In the limit $\Delta \to 0$ these equations coincide with (2.8).

2.3 Magneto-optical properties of graphene

Magneto-optical transitions and absorption lines

Magneto-optical properties of graphene are described in the review [27]. When pristine or doped graphene is exposed to an external magnetic field absorption of light occurs due to transitions of electrons between the discrete Landau levels. During this process three conditions must be satisfied. Firstly, (i) such transitions must be compatible with the following selection rule:

$$|n_\mathrm{f}| - |n_\mathrm{in}| = \pm 1, \qquad (2.23)$$

n_in and n_f are initial and final Landau levels, see Figure 2.9. This selection rule is based on the formulas (2.16) − (2.18) which describe transitions with nonzero probability. Formula (2.23) could be clarified from the point of view of angular momentum conservation: Each time an electron is promoted to a higher level, its orbital angular momentum changes by ± 1. This change is compensated by the angular momentum of the absorbed photon. A photon with left-handed circular polarization carries angular momentum -1 and right-handed one carries $+1$.

Secondly, (ii) the energy conservation law (2.5) defines frequencies of the photons which could be absorbed. Thus using formulas (2.8) and (2.5) one finds energies T of absorption lines in magneto-optical spectrum of graphene:

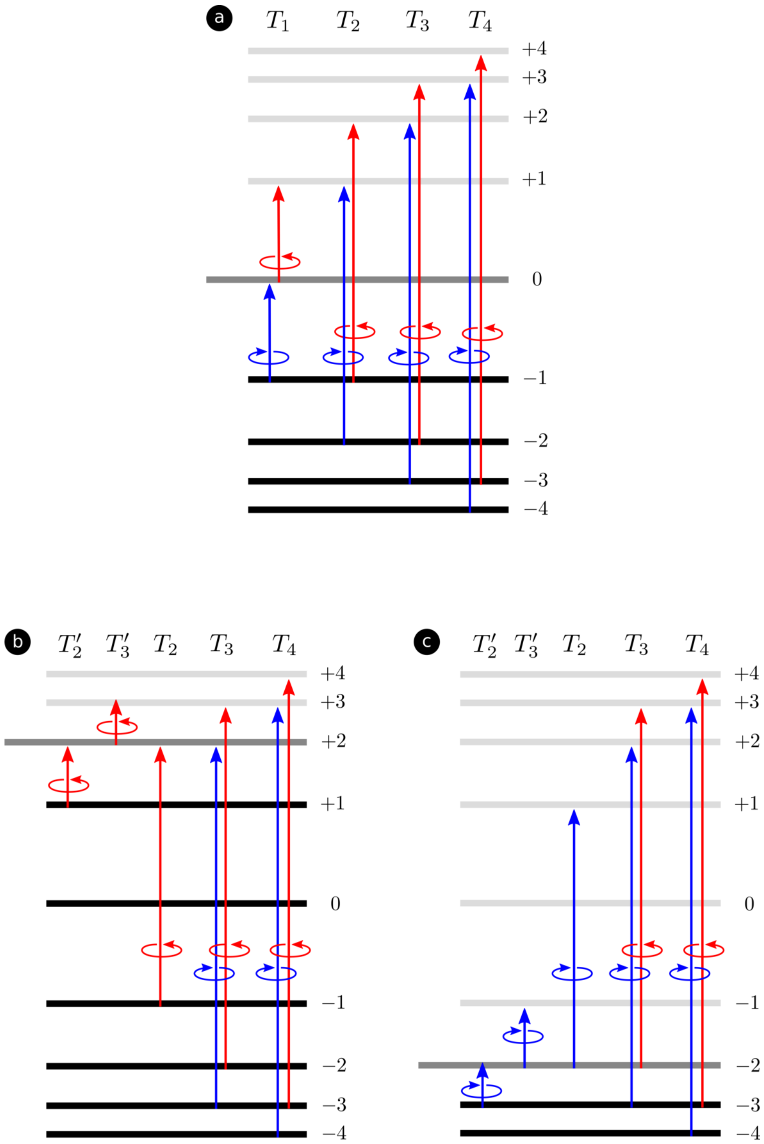

Figure 2.9 – Magneto-optical transitions of electrons in graphene, the three panels depict Landau levels for the same value of external magnetic field but different values of graphene's doping. Black, dark gray and light gray horizontal lines depict fully filled, partially filled, and empty Landau levels correspondingly. Red and blue vertical arrows depict electronic excitations accompanied by absorption of photons with right and left circular polarizations correspondingly. **Panel a:** Pristine graphene, all interband and mixed transitions for both polarizations of photons are active. **Panel b:** n-type doping, only two intraband and some interband transitions are active. **Panel c:** p-type doping, the active transitions have the same energy but opposite handedness of polarization compared to the case of n-type doping.

$$T(n_{\mathrm{in}} \to n_{\mathrm{f}}) = E_B \left(\mathrm{sign}(n_{\mathrm{f}})\sqrt{|n_{\mathrm{f}}|} - \mathrm{sign}(n_{\mathrm{in}})\sqrt{|n_{\mathrm{in}}|}\right). \tag{2.24}$$

And finally, (iii) electron's transition must occur between an occupied and an unoccupied state. If a particular Landau level is partially filled then it could act both as initial or final level for different optical transitions. Thus taking into account all conditions (i), (ii) and (iii), active magneto-optical transitions and corresponding absorption lines could be classified into three groups: interband, intraband, and "mixed" ones.

Interband transitions occur from Landau levels in the π-band to Landau levels in the π^*-band: $-2 \to 1$ and $-1 \to 2$, $-3 \to 2$ and $-2 \to 3$, $-4 \to 3$ and $-3 \to 4$, etc, see Figure 2.9. Due to electron-hole symmetry of band structure near to the Dirac point the interband transitions form pairs. Within each pair, both transitions have the same energy of absorption lines, however these transitions are distinguished by polarization of the absorbed photons. Energies of absorption lines T_i due to interband transitions are given by (2.25). In this manuscript, each line is enumerated by the number $i \geq 1$ of the Landau level to which an electron is promoted during absorption of a photon with right circular polarization, and a supplementary subscript "+" or "$-$" could be added to differentiate between absorption lines of right and left circular polarizations. For example, transition $-2 \to 3$ leads to a spectral line denoted as $T_{3,+}$ and transition $-3 \to 2$ leads to a spectral line denoted as $T_{3,-}$. Both lines have the same energy and could be denoted simply as T_3. Energies of photons absorbed during the interband transitions are always larger than the magnetic energy $T_i > E_B$. Just as in the absence of magnetic field, some of the low energy interband transitions are blocked when the Fermi level is away from the Dirac point.

$$T_i = v_F\sqrt{2e\hbar B}\left(\sqrt{i} + \sqrt{i-1}\right). \tag{2.25}$$

Intraband transitions occur between Landau levels within one band, see Figure 2.9 panels b and c. Transitions in the π-band $-2 \to -1$, $-3 \to -2$, $-4 \to -3$, etc are induced by light with left circular polarization. Transitions in the π^*-band $1 \to 2$, $2 \to 3$, $3 \to 4$, etc are induced by light with right circular polarization and have the same line energies as analogous intraband transitions in the π-band. Lines are enumerated with $i \geq 1$ the same way as described above but with a prime sign. For example, transition $2 \to 3$ leads to a spectral line denoted as $T'_{3,+}$ and transition $-3 \to -2$ leads to a spectral line denoted as $T'_{3,-}$. Both lines have the same energy and could be denoted simply as T'_3. Energies of absorption lines T'_i due to intraband transitions are given in the formula (2.26). Energies of photons absorbed during the intraband transitions are always less than the magnetic energy $T_i < E_B$. Just as in the absence of magnetic field, intraband transitions are observed only when the Fermi level is away from the Dirac point. At zero temperature, only one or two (but not three) intraband transitions could be observed in optical spectra for a particular value of external magnetic field.

$$T_i' = v_F\sqrt{2e\hbar B}\left(\sqrt{i} - \sqrt{i-1}\right). \tag{2.26}$$

“Mixed” transitions involve the zeroth Landau level: $-1 \to 0$ and $0 \to 1$, see Figure 2.9 panel a. The zeroth Landau level belongs both to π^* and π bands therefore formally such transitions could be considered as both interband and intraband transitions. For this reason, we refer to them using the word “mixed” in this manuscript. The absorption lines are denoted with T_1. Energies of absorption lines coincide with the magnetic energy $T_1 = E_B$, both (2.25) and (2.26) formulas are valid in this peculiar case. At zero temperature, mixed transitions are observed when the Fermi level resides at the -1, or 0, or 1 Landau level. This occurs only in the case of low doping or high magnetic field. Both $-1 \to 0$ and $0 \to 1$ transitions are observed simultaneously only when the zeroth Landau level is partially filled. The two transitions are distinguished by polarization of absorbed photons.

Magneto-optical spectra of graphene

In the infrared region of spectrum, magneto-optical properties of both pristine and doped graphene (transmission, reflection, and absorption) may vary significantly with the wavelength of light. Graphene has two distinct types of magneto-optical behaviour: so called quantum and classical regimes.

The **quantum regime** is observed when $\mu \ll E_B$ i.e. at small doping and/or high magnetic fields. In this regime magneto-optical transmission spectrum of graphene has a series of well-separated dips, see Figures 2.10 and 2.11. They correspond mainly to the absorption lines due to the mixed and interband transitions described in the previous subsection. What makes graphene stand out is that *multiple* absorption lines could be simultaneously observed at a given value of magnetic field. Such a distinct magneto-optical property of graphene is directly related to the existence of Landau levels both above and below the Dirac point and also to the non-equidistant spacing between graphene’s Landau levels. In such system, magneto-optical transitions of different energies of photons are simultaneously active.

The number of well-separated lines in graphene’s magneto-optical spectra depends the on line broadening. Naively, one may assume that this number always increases at high magnetic fields because separation between the lines grows as $\sqrt{B}$, see the formulas (2.25) and (2.26). However, the line broadening also changes with the magnetic field and energy of the transition. In the end, the resulting magneto-optical transmission curve, the number of well-separated dips, their intensity and width depend significantly on the type of the dominant scattering mechanisms, some broadening mechanisms may even alter the usual Lorentzian shape of the absorption lines [64]. Thus the linewidths may vary largely from one graphene sample to another.

In pristine graphene, which is a clear-cut example of the quantum regime, the most intense absorption line is due to the mixed magneto-optical transition T_1

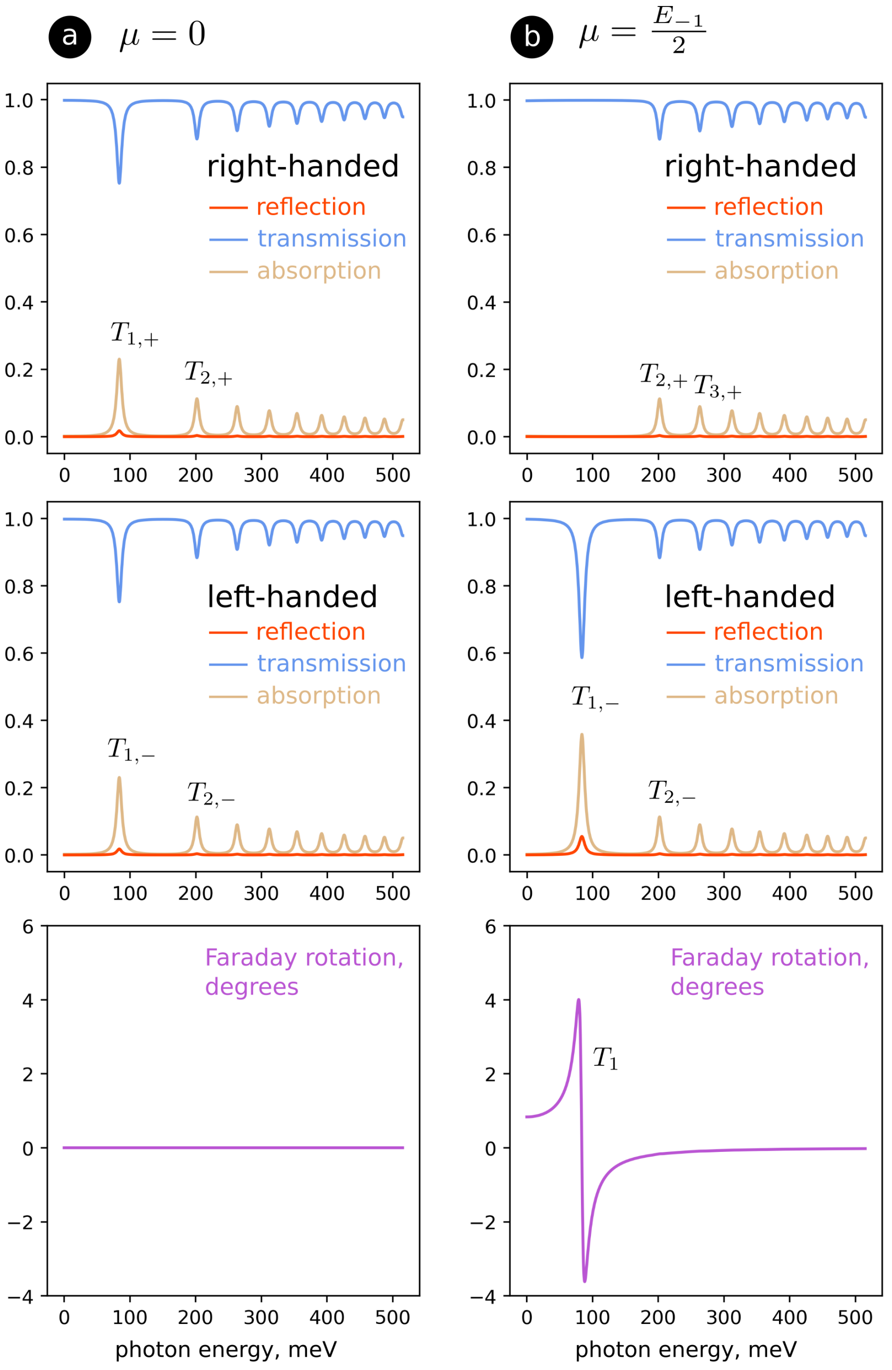

Figure 2.10 – MO properties of free-standing undoped and p-doped graphene at 4 Tesla for circularly polarized light of different handedness as well as FR angle. Each column shows plots for a particular value of doping based on the MO conductivities presented in Figure 2.8, relations between the $\hat{\sigma}$ and the optical properties are given in Section 6.3.

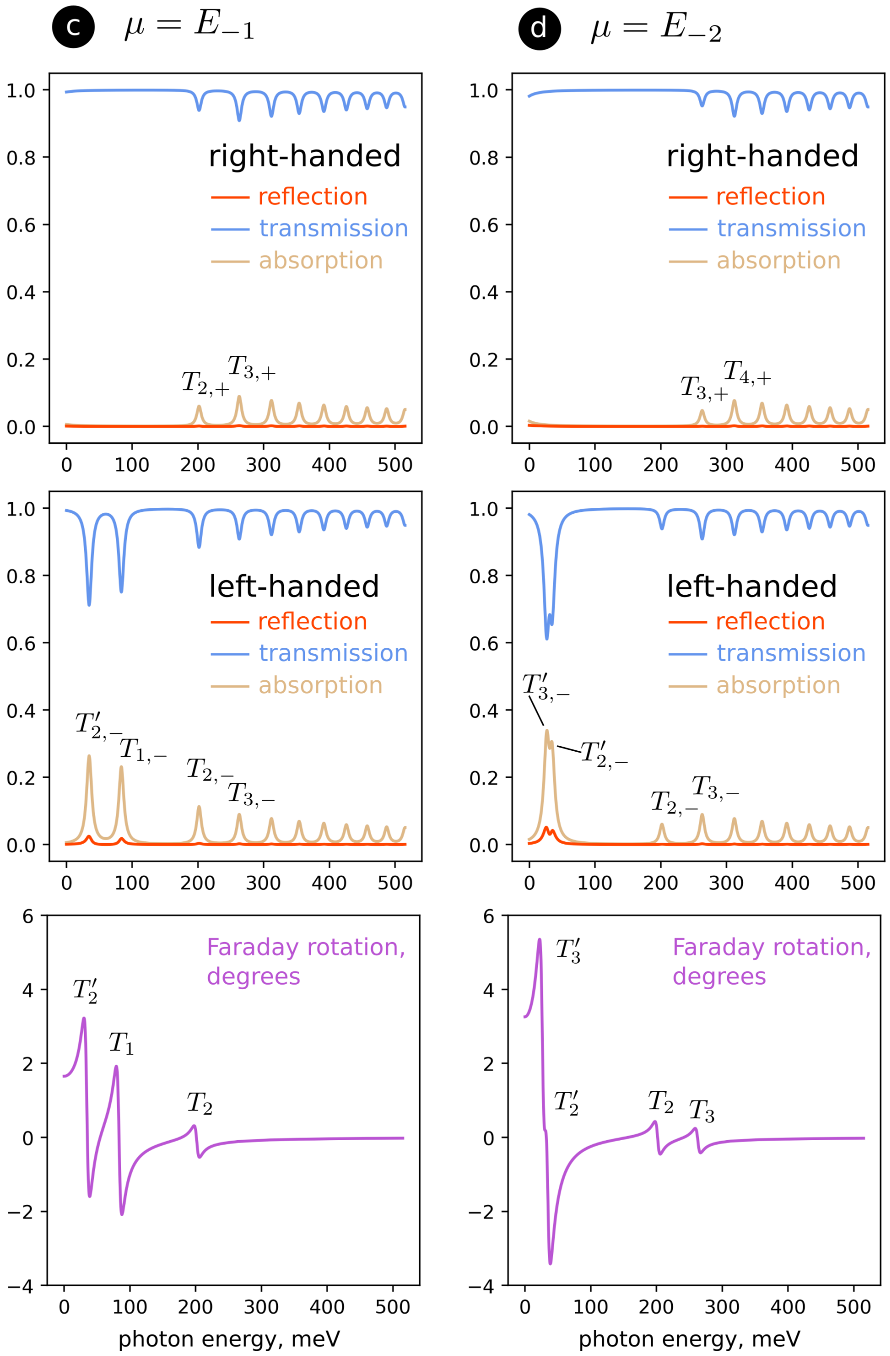

Figure 2.11 – MO properties of free-standing undoped and p-doped graphene at 4 Tesla for circularly polarized light of different handedness as well as FR angle. Each column shows plots for a particular value of doping based on the MO conductivities presented in Figure 2.8, relations between the $\hat{\sigma}$ and the optical properties are given in Section 6.3.

which is the lowest one in such a regime. Intraband transitions are not active. Spectral features due to the interband transitions are less pronounced than the T_1 feature for two reasons: (i) they have smaller spectral weight W_j, see the formula (2.21) and (ii) line broadening Γ_j increases with j. Thus the dips in transmission spectra become shallower as the number of the transition T_i grows. Finally at some high energies of photons $\hbar\omega \gg E_B$, the magneto-optical transmission spectrum of graphene becomes devoid of any marked features i.e. does not depend on the wavelength at all and becomes almost the same as its transmission spectrum in the absence of magnetic field $T(\omega, B \neq 0) \to T(\omega, B = 0) \approx 97.7\%$.

The **classical regime** is observed in graphene when $E_F \gg E_B$ i.e. at strong doping and/or relatively low magnetic fields. In this regime, the magneto-optical transmission spectrum of graphene is dominated by features due to the intraband transitions. At zero temperature, not more than two intraband transitions are simultaneously active at a particular value of magnetic field and doping, see panels b and c of Figure 2.9. For $E_F \gg E_B$, separation between the Landau levels is not large compared to widths of absorption lines. Therefore the two absorption lines (or transmission dips) observed in experiment at a given magnetic field often cannot be properly resolved: they merge together to form a single relatively broad spectral feature. As an example, merging of $T'_{2,-}$ and $T'_{3,-}$ lines could be seen in panel d of Figure 2.11 already at a relatively small doping $\mu = E_{-2} \approx 120$ meV. If amount of the extra charge due to the doping is fixed, see formula 2.10, then the position of the Fermi level glides in between different pairs of adjacent Landau levels as magnetic field decreases. The lower magnetic field the higher the absolute values $|n|$ of these adjacent Landau levels are and the spacing between them is narrower. Thus new lower energy intraband transitions T'_i become active, at the same time former (higher energy) intraband transitions become inactive. As a result, magneto-optical spectra of graphene contain only one feature which moves to lower energies as the magnetic field decreases. This feature is attributed to the classical cyclotron resonance and consists of many different absorption lines merged together. The position of the Fermi level $E_F = E_F(B)$ discussed in the previous section is important to predict the exact energy, broadening, and intensity of the cyclotron resonance. Calculations [61] showed that if the charge carrier concentration in the sample is constant then the cyclotron resonance energy is directly proportional to the value of magnetic field B. Such behaviour mimics conventional and classical systems hence comes the name “classical cyclotron resonance”.

It is important to note that in principle the interband transitions are not at all forbidden in the classical regime. However their energies must be high enough to overcome almost the double of the Fermi energy $T_i > 2E_F \gg 2E_B$. Interband transitions of such high energies have low spectral weight, in addition their absorption lines are subject to pronounced broadening. Therefore they do not lead to any marked features just as it has been already described for the case of pristine graphene.

A **crossover between the quantum and classical regimes** is observed in doped graphene when $E_F \sim E_B$. In this case all types of transitions are accessible for observation: well-separated interband transitions T_i at relatively high energies, pronounced mixed transition T_1 in the middle energies, and several poorly resolved features resulting form the highest intraband transitions T_i' which then merge into a monolith cyclotron resonance feature as the energy of photons decreases.

At finite temperature the occupation of Landau levels changes, in addition some scattering mechanisms, for example the ones which involve phonons, become more pronounced. This leads to the following tendencies: 1) the absorption lines described above become less sharp and less intense 2) at the same time more magneto-optical transitions become simultaneously active (because of the partial occupation of many Landau levels) and their weak signatures could be observed as additional absorption lines together with the main ones.

Magnetic circular dichroism in graphene

Doped graphene shows a peculiar phenomenon of magnetic circular dichroism, which is defined as a property of a material to develop different optical responses to the circularly polarized light of opposite handedness when placed in an external magnetic field. In pristine graphene right-handed and left-handed magneto-optical transitions have the same energies and intensities due to the electron-hole symmetry near the Dirac point, see panel a of Figure 2.9 and column a of Figure 2.10. When pristine graphene is illuminated with unpolarized light the two types of transitions compensate each others selectivity to polarization, and the transmitted light remains unpolarized. However the situation changes for doped graphene: the electron-hole symmetry near the Dirac point is broken. Thus p-doped graphene has some non-compensated absorption lines $T_{i,-}$ and $T_{i,-}'$ which absorb only the left circularly polarized light, see panel c of Figure 2.9, as a result transmitted light acquires partial right circular polarization, see Figures 2.10 and 2.11. N-doped graphene behaves the other way around: it has non-compensated absorption lines $T_{i,+}$ and $T_{i,+}'$ and transmitted light acquires partial left circular polarization.

Magnetic circular dichroism is also observed when absorption lines of the same energies and opposite handedness are active but have different intensities. In this case, they only partially compensate each other. In the end, the question whether the circular dichroism would be pronounced in graphene or not is defined by exact values of Landau level fillings which are in turn defined by the doping and temperature. Discussion of the magnetic circular dichroism in graphene is continued in Section 6.3.

Phenomenon of Faraday rotation in solids

Handedness of circular polarization is important for many magneto-optical phenomena. For historical and practical reasons, these phenomena are often described in terms of linear polarization. However it is merely a change of basis: linearly polarized light could be represented as a linear combination of left- and right-handed circularly polarized rays and vice versa.

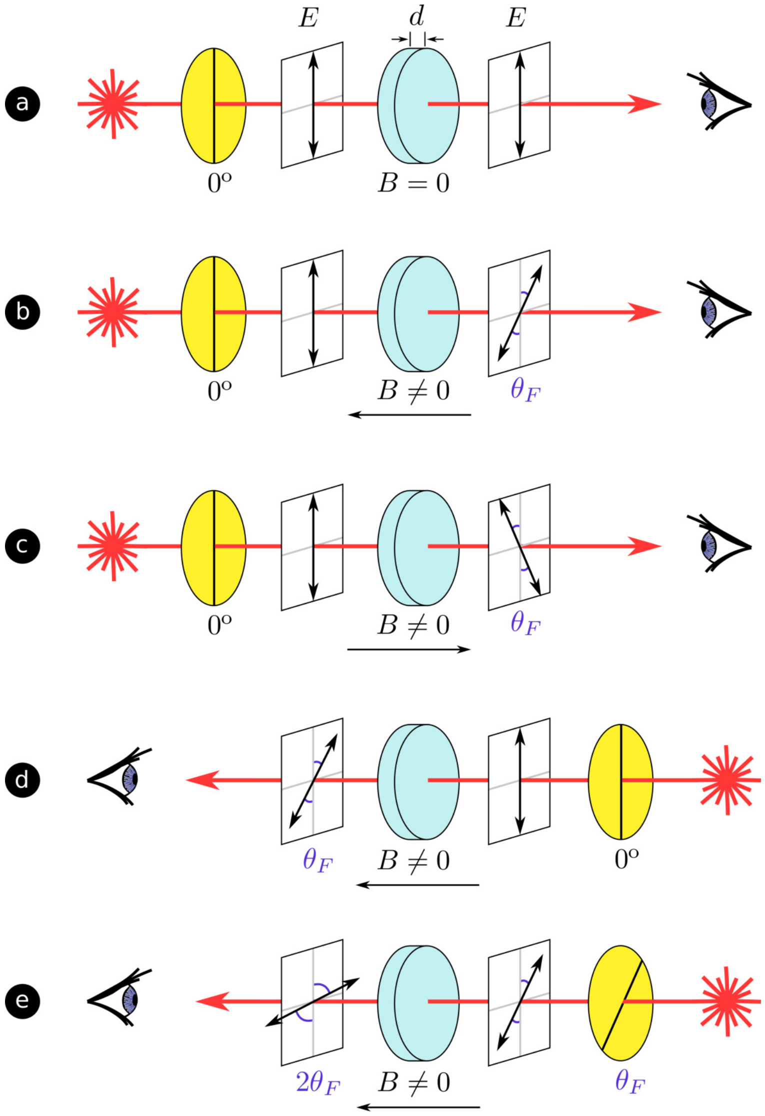

Figure 2.12 – Demonstration of the Faraday rotation effect and convention about the sign of the Faraday rotation angle. Elements of the scheme: a slab (light blue) characterized by positive Faraday rotation angle $\theta_F \geq 0$, a source of light (red), a linear polarizer (yellow circle with a black line indicating its axis), an observer, white squares show polarization i.e. orientation of electric component E of the electromagnetic wave for one particular frequency. **Panel a:** In the absence of an external magnetic field the Faraday rotation angle is zero. **Panels b:** Faraday rotation is clockwise for the observer. **Panels c:** Faraday rotation is anticlockwise for the observer but the sign of θ_F is still considered to be positive according to the convention because here light propagates and magnetic field points in the same direction. **Panels d:** Faraday rotation is anticlockwise for the observer. **Panels e:** Faraday rotation does not unwind back when the direction of the light is reversed, compare to panel b.

When exposed to external magnetic field all materials show a peculiar magneto-optical effect of Faraday rotation in their transmission spectra: When a linearly polarized electromagnetic wave impinges on the material and passes through, then the outgoing electromagnetic wave is also linearly polarized[3], however its polarization plane changes by some angle θ_F called Faraday rotation angle, see Figure 2.12. The Faraday rotation effect is a nonreciprocal phenomenon i.e. the polarization plane is always rotated in the same direction in space relative to the direction of magnetic field and regardless of the direction in which the ray of light propagates, compare panels b and d of Figure 2.12. This is a manifestation of the time-reversal symmetry breaking introduced by the external magnetic field. In this context time-reversal (T) corresponds to inversion of the light path, see panel e of Figure 2.12. The time-reversal symmetry breaking is well illustrated in the following thought experiment: When a ray of light bounces back and forth in a slab, the Faraday rotation angle accumulates and increases during each transition through the slab, i.e. polarization plane is never unwound back to its initial orientation each time the ray goes in the backward direction. Thus in the panel e of Figure 2.12, orientation of the polarization becomes $2\theta_F$ and not 0 which is expected when time-reversal symmetry holds. The Faraday rotation angle changes its direction to the opposite one only when the direction of magnetic field is inverted, compare panels b and c of Figure 2.12.

As a result, an observer who captures incoming light registers different directions of the Faraday rotation depending on whether the magnetic field points parallel or antiparallel to the direction of light propagation, compare panels b, c and d of Figure 2.12. As Faraday rotation is nonreciprocal, the notions of "observed direction" and "sign" of the Faraday rotation angle must be distinguished from each other. By convention accepted in most sources, Faraday rotation angle is considered to be positive for clockwise rotation when light propagates anti-parallel to the magnetic field (i.e. as shown on the panel b of Figure 2.12) as well as for anticlockwise rotation when light propagates parallel to the magnetic field (i.e. as shown on the panels c and d of Figure 2.12). Here the direction of rotation is registered from the point of view of an observer who captures light at the detector i.e. looks in the direction anti-parallel to the propagation of light. In other cases the sign of the Faraday rotation is considered to be negative.

In bulk materials, Faraday rotation is a direct consequence of circular birefringence which is in turn induced by external magnetic field. In circular birefringent materials, left- and right-handed rays propagate at different speeds. In the end, both rays come out from the material and result into a linearly polarized one but with some phase offset θ_F in polarization compared to the incident ray:

$$\theta_F = \frac{\omega}{2c}(n_- - n_+)d, \tag{2.27}$$

---

[3] Phenomenon of Faraday rotation is always accompanied by magnetic circular dichroism. As a result, in general case the outgoing wave could be elliptically polarized. The outgoing wave can remain linearly polarized and acquire some nonzero Faraday rotation only at specific values of wavelength.

where ω is frequency of light, c is speed of light, n_- and n_+ are refractive indices of the material for left- and right-handed circularly polarized light, d is the thickness of the investigated sample of the material.

Some materials exhibit circular birefringence without external magnetic field. This case is distinct from Faraday rotation (which is an inherently magneto-optical effect) and the change or polarization plane is called optical rotation or optical activity. In contrast to Faraday rotation, optical activity is a reciprocal phenomenon, time-reversal symmetry holds, and polarization plane is rotated in opposite directions depending on the direction in which the ray of light propagates through the sample. In the above mentioned thought experiment, rotation of polarization plane does not accumulate after many transitions of light through the slab, in fact the rotation angle is merely wound and unwound when a ray of light bounces back and forth in the slab.

In most cases the value of the Faraday rotation angle is proportional to the thickness d of the material as well as absolute value of external magnetic field and obeys Becquerel's formula:

$$\theta_F = \nu|B|d. \tag{2.28}$$

The coefficient of proportionality ν is called Verdet constant of the material. By convention, ν has the same sign as the Faraday rotation angle. Both Faraday rotation angle and Verdet constant depend on the frequency of the incident light. Description of magneto-optical response of a solid body is more complicated compared to the zero-field case therefore function $\theta_F = \theta_F(\omega)$ yields important information about the investigated material. Nowadays, many materials which show pronounced Faraday rotation are known and various microscopic mechanisms which cause the phenomenon have been uncovered. Theory of the Faraday rotation effect in solids is described in [67, 68, 69, 70].

In transparent insulating magnetic materials the Faraday rotation is related to the Zeeman effect and interaction of electron spins with a magnetic component of an incident electromagnetic wave. In the visible region of spectrum, the highest Verdet constants among crystalline bulk materials is found in terbium gallium garnet (TGG) $Tb_3Ga_5O_{12}$. For example for red light with 632 nm wavelength, its value is $\nu_{TGG} = 134$ rad/(T·m) [71]. Thus a 1 mm thick TGG slab produces $\sim 4^\circ$ Faraday rotation when exposed to a magnetic field of 0.5 Tesla which could be achieved with rare-earth permanent magnets. In the visible region of spectrum Faraday rotation effect has been harnessed to create devices such as Faraday rotators which allow the manipulation of polarization of light, Faraday isolators which act as "optical diodes", etc. However in terbium gallium garnet the values of ν drop quickly at lower frequencies of light and Faraday rotation effect becomes negligible in the IR region of spectrum.

In thin metallic films[4] as well as in many doped semiconductors and semimetals phenomenon of Faraday rotation originates from the interaction of the electric

---

[4] The metal must be thin enough to be transparent.

field component of the electromagnetic wave with the orbital motion of charge carriers [72]. Therefore there is some analogy between magneto-optical experiments and the Hall effect transport measurements: transimissivity curve $T = T(\omega)$ is complemented with Faraday rotation curve $\theta_F = \theta_F(\omega)$ like value of the longitudinal conductivity is complemented with value of the transverse (i.e. Hall) conductivity. Knowledge of the Faraday rotation curve θ_F, just like Hall conductivity, allows one to infer the sign and density of charge carriers if their cyclotron mass is already known. The above mentioned materials have pronounced magneto-optical features in the infrared region of spectrum.

In the infrared, the highest values of the Verdet constant among non-magnetic crystalline bulk materials are found in the indium antimonide $\nu_{\text{InSb}} = 0.2 \cdot 10^3$ rad/(T·m) [73, 74] and in the bismuth selenide $\nu_{\text{Bi}_2\text{Se}_3} = 5 \cdot 10^3$ rad/(T·m) [75] at liquid helium temperatures. The exact values of ν depends a lot on the temperature as well as doping, and in general they could be an order of magnitude higher than those found in visible range of wavelengths in TGG. Nevertheless, currently there are not many devices which have harnessed the Faraday rotation effect in the infrared region of spectrum. This is partly related to the technical issues which arise when cryogenic temperatures are needed in order to achieve the large values of the Verdet constant in InSb, Bi_2Se_3, etc. The second problem is that in the above mentioned material a large Faraday rotation goes hand is hand with large values of magneto-optical absorption which makes these materials very inefficient for real applications. Thus the lack of nonreciprocal optical devices (Faraday rotators and isolators) which operate in the infrared region of spectrum is yet another reason which fuels graphene research [76].

Faraday rotation in graphene

Theory of the Faraday rotation effect in graphene and related 2D materials is described in [77] and [78]. Doped graphene shows both magnetic circular dichroism and Faraday rotation effects. As a result, when a linearly polarized electromagnetic wave impinges on graphene then the transmitted wave acquires elliptical polarization, the major axis of the ellipse is tilted relative to the initial polarization plane. This polarization tilt corresponds to the Faraday rotation angle θ_F, see Figure 2.13.

As graphene is an ultimately thin crystal, the formulas (2.28) and (2.27) are no longer applicable. Before the advent of graphene materials, the thinnest structures investigated for their magneto-optical properties were several-nanometer-thick 2D electron gases at the GaAs/AlGaAs interface [73]. Magneto-optical measurements on monolayer graphene [79] showed remarkably pronounced Faraday rotation in the far infrared region of spectrum: $\theta_F \sim 6^\circ$ at magnetic field of 7 Tesla. In order to compare this number to bulk materials, effective thickness of graphene could be taken as interlayer distance in bulk graphite, then (2.28) yields “effective Verdet constant” of graphene $\nu_{\text{Gr}} = 45 \cdot 10^6$ rad/(T·m). Large values of the Faraday rotation in graphene are attributed to small cyclotron mass of its charge carriers and most importantly to the small effective thickness of graphene.

A distinctive and unique feature of the Faraday rotation phenomenon in graphene (apart from its very large magnitude) is related to the electron-hole symmetry and opportunity of ambipolar doping of graphene samples: In graphene the *sign* of θ_F could be reversed by applying gate voltage and thus shifting the Fermi level symmetrically across the Dirac point $E_F \to -E_F$, see panels a and c of Figure 2.13. This procedure could be viewed as charge conjugation (C). Independently from this, the orientation of θ_F also could be reversed just like in other materials by inverting the direction of the external magnetic field, see panels a and b of Figure 2.13. This procedure could be viewed as parity transformation (P) in graphene. When both doping and direction of magnetic field are inverted the two modifications cancel out and in the end orientation of θ_F does not change. Thus one may summarize that for Faraday rotation effect in graphene CP symmetry is preserved and T symmetry is broken.

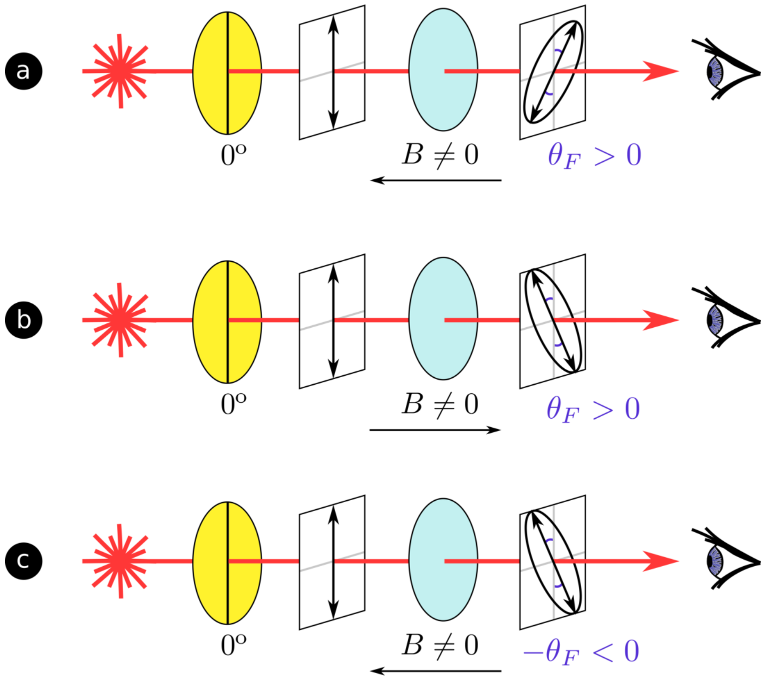

Figure 2.13 – Faraday rotation effect in graphene depicted for one particular frequency. Elements of the scheme: graphene monolayer (light blue), a source of light (red), a linear polarizer (yellow circle with a black line indicating its axis), an observer, white squares show polarization i.e. orientation of electric component E of the electromagnetic wave for one particular frequency. **Panels a, b:** in both cases the sign of the Faraday rotation angle is the same $\theta_F > 0$, consequently the sign of graphene's doping is also the same, however the observed direction of θ_F is different because of the different orientation of magnetic field. **Panel c:** the sign of the Faraday rotation angle is negative because the sample has opposite doping compared to the two previous cases.

Faraday rotation angle $\theta_F = \theta_F(\omega)$ allows identifying the level of doping and the sign of charge carriers in graphene. Transitions with opposite handedness i.e. $T^{(\prime)}_{i,-}$ and $T^{(\prime)}_{i,+}$ have the same energies of absorption lines but opposite signs of the Faraday rotation. A magneto-optical transition which corresponds to a well-separated absorption line at a frequency ω_{sl} has a zigzag-shaped feature centered at the same frequency ω_{sl}, see Figure 2.14. An upward inflection of the zigzag

$$\frac{d\theta_F(\omega)}{d\omega}\bigg|_{\omega=\omega_{\text{sl}}} > 0$$

corresponds to magneto-optical transitions involving light with right-handed circular polarization, for example intraband transitions T'_2 and T'_3 in n-doped graphene, see panel b of Figure 2.9. Meanwhile a downward inflection of the Faraday zigzag corresponds to magneto-optical transitions involving light with left-handed circular polarization, for example intraband transitions T'_2 and T'_3 in p-doped graphene, see panel c of Figure 2.9.

When two intraband absorptions lines T'_i and T'_{i+1} are poorly resolved then their Faraday rotation angles are accumulated together in a single Faraday rotation

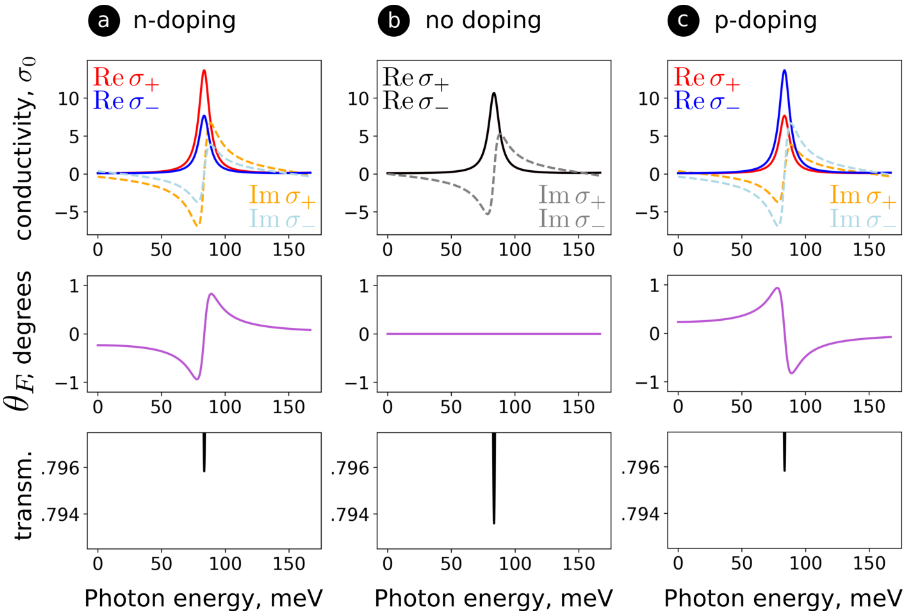

Figure 2.14 – Magneto-optical conductivity in units of σ_0, Faraday rotation angle and transmission of a well-separated spectral line. Three columns describe behaviour of a graphene monolayer for three different values of doping. As one can see, the sign of doping defines the inflection of the Faraday rotation curve but does not influence graphene's transmission for unpolarized light. The graphs are calculated in the framework of the simple model for $\sigma_\pm$ described in the previous section and modeling of ultrathing condcucting films described in Chapter 6.

curve $\theta_F = \theta_F(\omega)$ which has the same type of inflection as the above mentioned lines because all active intraband transitions have the same handedness for a given doping. The situation is somewhat different for the interband transitions $T_{i,-}$ and $T_{i,+}$. They have the same energies and pronounced Faraday rotation of opposite signs. The resulting net Faraday rotation could be large when only one of the above mentioned lines is active for example transition $T_{2,+}$ in the panel b or transition $T_{2,-}$ in the panel c of Figure 2.9. However when both interband transitions $T_{i,+}$ and $T_{i,-}$ are simultaneously active, for example both T_4 in panel c of Figure 2.9, then their contributions to the Faraday rotation partially compensate each other. Thus the resulting net Faraday rotation angle $\theta_F = \theta_F(\omega)$ decreases.

From this point of view pristine graphene is a very special case: both mixed transitions and all pairs of interband transitions are active (see panel a of Figure 2.9) and have exactly the same intensities. As a result, Faraday rotation is fully compensated within each pair of transitions and the net Faraday rotation angle equals to zero for all frequencies $\theta_F(\omega) = 0$. Thus despite the time-reversal symmetry is broken by magnetic field, the Faraday rotation vanishes because charge symmetry is not broken i.e. motion of electrons is fully compensated by the motion of holes.

2.4 Quality and size of graphene crystals

It is well known that physical properties of graphene may vary a lot depending on the method with which it is produced and also the kind of treatment it undergoes afterwards. Previous sections describe behaviour of "idealized" graphene. However in practice, interesting optical features distinctive to graphene are difficult to observe. Some of these difficulties are related to the low quality of graphene, and some are caused by limitations of experimental techniques. Often big graphene crystals are required in order to perform the optical measurements properly. Therefore in our work the most important aspects were quality and size of graphene crystals. As it often happens at the frontiers of science, the best quality graphene samples are small and their size cannot be increased using the same synthesis method, meanwhile large samples produced with other methods typically have worse quality.

Quality

Like in semiconductor physics, quality of a graphene crystal is often described in terms of its charge carrier mobility $\mu = v_d/E$, where v_d is drift velocity of electrons or holes due to an externally applied electric field E. The higher mobility, the better crystalline quality is. Apart from that, graphene's mobility also depends on other factors: it increases as temperature [80] and/or charge carrier concentration N go down. Therefore one should always take mobilities of graphene crystals measured at the same temperatures and doping in order to have an adequate comparison of their quality. Mobilities of different graphene samples have been measured at different conditions in numerous experiments, and the reported values fall into the interval between $\mu \sim 10$ cm^{2}V^{-1}s^{-1} and $\mu \sim 1\ 000\ 000$ cm^{2}V^{-1}s^{-1} [81, 80, 82, 83, 84]. For comparison, the theoretically predicted upper limit for graphene's mobility is $\sim$ 200 000 cm^{2}V^{-1}s^{-1} [85, 86] at room temperature for technologically achievable charge carrier concentrations of $\sim 10^{12}$ cm^{-2}. Mobilities at liquid helium temperatures are often an order of magnitude higher than those at room temperatures.

As one can see, graphene's mobility, and thus quality, may vary several orders of magnitude from one crystal sample to another. Such a large spread of values is directly related to the two-dimensional nature of graphene. Firstly, graphene is ultimately thin so that there remain only two surfaces and no bulk at all in between. In a 3D material, phenomena which take place in the bulk define many properties of the material in a very robust way i.e. these properties do not change much when the surface is altered somehow, for example contaminated or oxidated. In contrast, graphene's properties are very sensitive to contamination of their surface or proximity to another material, for example the substrate on which graphene monolayer resides. Secondly, scattering of charge carriers on defects and charged impurities is more pronounced in 2D phase space than in a 3D one, moreover in a 2D system the screening of charged impurities is less efficient than in 3D. And finally, all 2D crystals are very prone to corrugations because a 2D crystal is not thermodynamically stable when flat. Whether corrugations develop or not and to which extent also depends largely on external conditions and the kind of treatment graphene undergoes.

Relevance of different scattering mechanism limiting graphene's mobility is still a subject of a very intense debate, see topical reviews [89, 90]. Here are the key factors which have been experimentally observed to cause deterioration of graphene's quality:

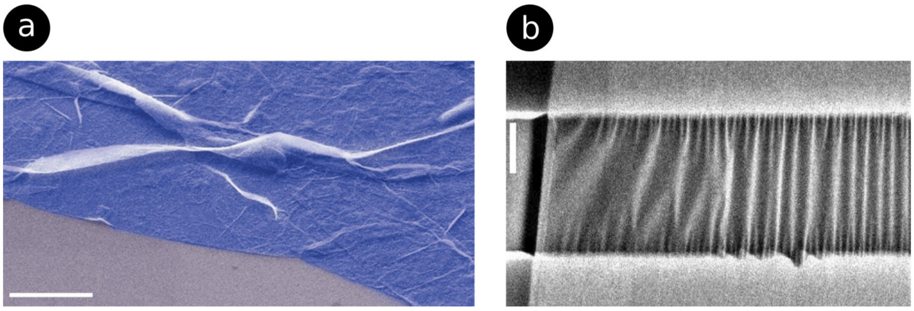

Figure 2.15 – Panel a: STM image of a graphene flake transferred to a new substrate, one can see wrinkles, folds, and so called "collapsed folds" induced by the transfer process, scale bar is 2 μm. The figure is made after [87]. **Panel b:** STM image of a suspended bilayer graphene flake, one can see strain-induced ripples typical for 2D crystals, the scale bar is 1 μm. The figure is made after [88].

- **Surface contamination** [91]. Contaminants adhere to graphene via the van der Waals interaction and graphene's covalent π-bonds. Typical requirements for surface science experiments are working in high vacuum and at low temperature. However the procedures developed so far for manipulations with 2D crystals do not meet these requirements [92]. Thus graphene's surface could be easily inadvertently contaminated early on during graphene's synthesis, later because of exposure to room air and moisture, or even storage in poor vacuum. All the more exposure to contaminating chemicals happens during device fabrication namely transferring graphene to another substrate, suspending or stacking graphene membranes, depositing of electric contacts etc.

- **Inappropriate substrate**. Graphene interacts with its underlying substrate via van der Waals forces. There has been done a lot of research on comparison of different graphene substrates and various nontrivial phenomena which take place at the interface between the two materials [93, 94, 95, 96, 97, 98, 99]. On the one hand, the substrate helps to stabilize graphene and prevent the 2D crystal from scrolling. On the other hand, in most cases the substrate surface is rough on the atomic scale [99] and contains charged impurities (see Figure 3.2) which leads to the deterioration of graphene's quality. Another important effects is interaction of graphene charge carriers with substrate phonons [95].

- **Impurities, point defects and domain walls in graphene's lattice**. Different types of defects and impurities inevitably form during synthesis.

- **Wrinkles, ripples, crumples, and flexural phonons in graphene** [100, 101]. Several types of membrane corrugations have been experimentally observed in graphene. Many different mechanisms of corrugation formation have been proposed so far [102, 103], Figure 2.15 illustrates only one of them. These mechanisms emphasize the importance of graphene lattice defects, regime of graphene growth during synthesis, substrate microstructure and roughness (or absence of substrate in the case of free-standing graphene), substrate-graphene adhesion and mismatch of their thermal expansion coefficients[5], mechanical strain in graphene membrane, etc.

All the above mentioned factors cause scattering of charge carriers and thus reduce mobility in graphene. Scattering mechanisms are often differentiated into long-range scattering on charged impurities and short-range scattering on neutral impurities and defects. It has been shown that certain types of corrugations create a long-range scattering potential and act similar to Coulomb scatterers [101]. For each scattering mechanism scattering rates have peculiar dependencies on temperature, concentration of charge carriers and concentration of scattering centers. For

---

[5] Interestingly enough, graphene has negative thermal expansion coefficient [104]

more details see topical review [26] and theoretical description of these phenomena [105, 106, 107]. The above mentioned problems of quality deterioration are caused by technical issues and potentially could be eliminated therefore they are called *extrinsic*. Here are some factors which already have been shown to improve graphene's quality:

- Using high quality precursors for graphene synthesis;
- optimization of synthesis procedure;
- minimizing amount of contaminants during device fabrication;
- annealing graphene [108, 109];
- suspending graphene membrane;
- using hBN as a substrate [110, 111, 112];
- encapsulation of graphene membrane [83, 84].

In contrast to extrinsic scattering mechanisms, there are *intrinsic* ones: electron-electron and electron-phonon scattering. These scattering mechanisms also reduce mobility however they are inherent to graphene and cannot be eliminated. Therefore, usually they are not considered among the reasons of graphene's quality deterioration but rather viewed as phenomena which set the fundamental upper limit of charge carrier mobility in graphene[6]. Naturally, this limit depends on temperature and charge carrier concentration.

Apart from high mobility, high *spatial homogeneity* is another important attribute of high quality crystals. Charged impurities and membrane corrugations cause the chemical potential to be nonuniform across the graphene crystal. High resolution local probes as STM showed that there could be spatial fluctuation of the Fermi level on relatively short length scales, for example in graphene on SiO_2 they could reach $\varDelta E_r = 30 - 100$ meV [113]. For pristine graphene this leads to formation of so called electron-hole puddles: in some regions of the crystal the Fermi level is above the Dirac point and in other regions it is below the Dirac point [114, 115]. As a result, in practice it is impossible [82] to bring the entire graphene crystal to charge neutrality even if there is an opportunity to fine-tune the positions of its average Fermi level. When graphene's properties are investigated by probes which have lower than STM spatial resolution (for example IR optical spectroscopy, electronic transport measurements etc), the local Fermi level is smeared out. Consequently, one cannot observe the distinct features of Dirac behaviour previous described in Sections 2.1, 2.2, and 2.3. In addition, for temperatures $k_B T \lesssim \varDelta E_r$, electronic properties such as conductivity become independent of temperature [113].

---

[6] Sometimes membrane corrugation and flexural phonons are also considered among intrinsic phenomena which limit graphene's mobility. In this work I number them among extrinsic problems because potentially they could be reduced with the help of strain or proper underlying substrate.

Currently, scotch-tape exfoliation of graphite is a routine way of obtaining the best quality graphene with more or less reproducible yield. Freshly exfoliated graphene flake must be suspended or encapsulated between thin scotch-tape exfoliated hBN flakes. Mobilities of hBN/Gr/hBN stacks may reach $\sim$ 140 000 $\mathrm{cm^2V^{-1}s^{-1}}$ at room temperatures and even $\sim$ 1 000 000 $\mathrm{cm^2V^{-1}s^{-1}}$ at liquid helium temperatures [84]. It has been also reported that high quality graphene flakes could be located on the surface of graphite [116]: sometimes a graphene monolayer is decoupled from its bulk graphite crystal so that its charge carriers acquire Dirac behaviour typical for graphene.

Size

There has been developed more than a dozen graphene synthesis methods so far: scotch-tape exfoliation method, chemical vapor deposition (CVD), epitaxial growth on SiC (hexagonal polytypes 4H and 6H), molecular beam deposition, reduction and further sonication of graphite oxide, unzipping carbon nanotubes, etc. Each method has some advantages and limitations, for more information see review [117].

In this work we consider graphene crystals of $\gtrsim$ 1 mm to be big because it is the minimal size of samples suitable for typical optical spectroscopic measurements. We consider graphene crystals of $\lesssim$ 1 mm to be small because their optical spectra could be measured only with the help of some subsidiary optical elements which focus light directly on the sample: light-pipes, lenses, Cassegrains, etc. Apart from this technical issue, the size of crystals should be larger than the wavelength of light. This may become an important issue in the far infrared region of spectrum. Currently CVD and epitaxial growth on SiC are the only reproducible methods of obtaining big graphene samples.

The CVD synthesis method is easily scalable: it allows growing graphene samples of different sizes. The biggest samples which have been grown so far are about one meter wide [118]. However such samples inevitably contain many domain walls, lacunas, and disconnected islands of graphene bilayer which start growing on top of the monolayer before the monolayer of the intended size has fully formed, see topical review [119].

The CVD procedure could be optimized for growing somewhat smaller but better quality samples so that just after the synthesis their mobility is as good as in mechanically exfoliated graphene. The biggest CVD grown single crystal samples reported so far $\sim$ 10 mm [120]. However CVD graphene is usually synthesized on a metallic surface and for further experiments graphene must be transfered to an insulating substrate or suspended. Transfer methods developed for big samples employ polymers (for example PMMA, polystyrene or polybutadiene) which are deposited in a thin layer on top of graphene before the metallic substrate is etched away. Polymer residues cannot be totally removed which contaminates the graphene. Moreover, drainage of liquid between graphene and the new substrate creates wrinkles in the graphene membrane during the transfer procedure [102]. In the end, the quality of CVD graphene deteriorates and its reported mobilities become $\sim 100 - 30\,000$ cm^{2}V^{-1}s^{-1} [118, 120] at room temperatures. Suspending and annealing of big CVD graphene samples could be problematic[7] and does not allow restoring its best quality. Currently dry transfer and polymer free transfer methods for large-area graphene films are being developed as alternatives to the above mentioned wet transfer method employing both liquid solvents and polymers. It has been shown that graphene's quality could be preserved better resulting in values of mobilities reaching $\sim 60\,000$ cm^{2}V^{-1}s^{-1}. For more information see topical review [122]. An alternative approach which is currently being developed is growing CVD graphene directly on large hBN crystals [123, 124].

Epitaxial graphene on SiC could be grown up to $\sim$ 20 cm in size. Here the limiting factor is the size of the SiC crystals which are used as a precursor. Quality and morphology of the epitaxial graphene largely depend on the regime of growth and on the crystalline face of the SiC sample. Graphene on the silicon terminated face (0001) of SiC is monolayer. The mismatch between the lattice constants of graphene and SiC causes graphene layers to form terraces separated by grain boundaries. This limits the maximal size of graphene's crystal domains to several micrometers. Graphene on the carbon terminated face $(000\bar{1})$ of SiC is multilayer: Many layers of graphene, up to $\sim$ 100, can grow one above the other. Usually these layers are not crystallographically aligned relative to each other (turbostratic orientation) therefore they could be considered as almost independent graphene monolayers. Many experiments with such turbostratic graphene multilayers have shown signatures typical for graphene monolayers for example linear electron dispersion [125]. Reported mobilities of the epitaxial graphene usually fall into the range $\sim 500 - 25\,000$ cm^{2}V^{-1}s^{-1} [126, 127, 128] and in rare cases even reach $\sim 500\,000$ cm^{2}V^{-1}s^{-1} just after the sample fabrication [129, 130, 131]. Typically mobilities of graphene found on the carbon terminated face of SiC are higher compared to those found on the silicon terminated face of SiC [128].

Despite of many efforts and approaches, the quality of large graphene samples remains inferior (or cannot be preserved for a long time) compared to the quality of scotch-tape exfoliated hBN/Gr/hBN stacks. Unfortunately the latter are small in size $\lesssim 100$ μm. Here the limiting factor is the size of bulk hBN crystals which are used as a precursor to create thin hBN flakes. Currently the biggest hBN monocrystals have lateral dimensions of ~ 200 μm.

Scotch-tape exfoliated graphene flakes may have somewhat larger dimensions of $\lesssim 500$ μm. When suspended and annealed at high vacuum they also show good quality approaching the quality of hBN-encapsulated graphene. However, suspended graphene membranes are extremely fragile: they are susceptible to ambient air and moisture, they are difficult to anneal without breaking the membrane, moreover a significant amount of strain is required to suppress flexural modes in a suspended membrane and retain high mobilities [100].

---

[7] The widely flaunted graphene hammock with a cat inside [121] is not viable even though meter-size graphene membranes have been successfully synthesized.

2.5 Probing Landau levels in graphene with FTIR spectroscopy

The first dozen Landau levels above the Dirac point have typical energies $0 - 0.5$ eV for magnetic fields $0 - 10$ Tesla which could be routinely achieved with superconducting electromagnets [132, 133, 134]. Magneto-optical transitions of electrons between these levels lead to signatures in the far and middle infrared regions of transmission, reflection, and absorption spectra of graphene. Fourier transform infrared spectroscopy (FTIRS) [135, 136, 137, 138] allows measuring spectra in a broad range of wavelengths including the far infrared, middle infrared, and near infrared regions which corresponds to the energies of photons from 0.01 to 2 eV. Thus FTIRS allows probing all types of dipole magneto-optical transitions of electrons for different values of chemical potential in a graphene sample.

In FTIRS experiments, investigated materials are illuminated with a broad spectrum infrared light and then intensity of transmitted or reflected light is measured as a function of light frequency ω. At the same time FT spectrometers do not provide a direct access to the phase of the electric field in electromagnetic waves[8]. Therefore one cannot find all components of graphene's magneto-optical conductivity tensor $\hat{\sigma}(\omega, B)$ from a single transmission or reflection spectrum only. Nonetheless, more ample information about magneto-optical response of graphene could be obtained with FTIRS if graphene sample is illuminated with light which has different configurations of polarization, see Sections 5.2 and 6.4. In practice, several additional optical elements are needed for this purpose, for example a pair of motorized linear polarizers. This approach allows measuring the Faraday rotation angel and magnetic circular dichroism of the investigated sample as functions of frequency, in addition, the magneto-optical conductivity tensor $\hat{\sigma}(\omega, B)$ could be fully restored with minimal model assumptions.

In general, the FTIRS method is flexible enough and allows experimental setup of various configurations. Thus FTIR spectrometers combined together with superconducting and hybrid magnets allows probing graphene in a very wide range of stationary magnetic fields up to 35 Tesla [48]. Many configurations of experimental setup allow measuring spectra for different temperatures of the sample: from liquid helium, 2.2 Kelvin, up to the room temperatures and higher. Position of the chemical potential in the sample could be tuned with a gate electrode, in particular transparent conductive materials could be used as a gate electrode when transmission spectra are supposed to be measured. Some commercial FTIR spectrometers are compatible with IR microscopes which allows working with small samples [139].

As one can see, FTIRS provides many opportunities and technical solutions for probing magneto-optical properties of graphene. However not all of them could be easily combined in one configuration of experimental setup, for some more

---

[8] Direct measurement of both intensity and phase is possible with terahertz time-domain spectroscopy (THz-TDS) which is a sister technique of FTIRS.

details see Section 4.1, here we provide only one example of technical problems which may arise. The structure of powerful electromagnets which produce ~ 30 Tesla requires using light pipes to guide the light into the magnet and focus on the samples under investigation. Typical size of the light spot produced in such a way is ~ 1 mm. In a such configuration, an IR detector is placed just behind the sample to ensure that sufficient amount of light would arrive to the IR detector. For this reason, the IR detector is in close proximity to the magnet which influenced the readings of the IR detector which in turn required a more involved normalization of the signal. Moreover, this tight geometry also often hinders measurement of the Faraday rotation angle and the magnetic circular dichroism because when the sample is in the direct vicinity of the IR detector it is difficult to place a polarizer in between.

Magneto-optical spectra of strongly doped and weekly doped graphene have been already measured with FTIRS in many experiments. All regimes of spectral line resolution described in Section 2.3 have been observed: the quantum regime [79, 130, 140, 141, 142, 143], the classical cyclotron resonance regime [143, 144] and the crossover regime [144].

Transmission of monolayer and multilayer epitaxial graphene on SiC was investigated in numerous experiments [142, 143, 79, 144, 130, 131]. The Faraday rotation angle of highly doped epitaxial graphene on SiC substrate was measured in [79]. Sizes of the samples varied in the range $1 - 10$ mm. SiC substrate is opaque for the photon energies between 85 meV and 200 meV. Therefore the spectral range at which epitaxial graphene could be probed in transmission regime is somewhat limited. Here we would like to single out only several interesting and remarkable results, see Figures 2.16 and 2.17. There were also several experiments in which magneto-optical spectra of graphene were measured at small samples produced with the methods involving scotch-tape exfoliation, see Figure 2.18. In the experiment [141], graphene samples were grown with CVD method on the surface of scotch-tape exfoliated hBN flakes. The typical lateral size of such samples is $\sim$ 100 μm. In the experiment [140], graphene samples were scotch-tape exfoliated on the $\mathrm{SiO_2/Si}$ substrate. The typical lateral size of such samples is even smaller $\sim$ 30 μm. Despite ingenious tricks to enable measurements on small samples (light pipes, light cones, apertures deposited as a mask), both above mentions experiments had not completely solved the problem of overfilling i.e. there remained undesired stray light which arrived to the IR detectors bypassing the samples under investigation. Therefore the spectra presented in [141, 140] do not contain definite and precise information about the absolute values of magneto-optical transmission. As a result, only the energies but not the intensities and widths of the absorption lines could be extracted with high degree of certainty.

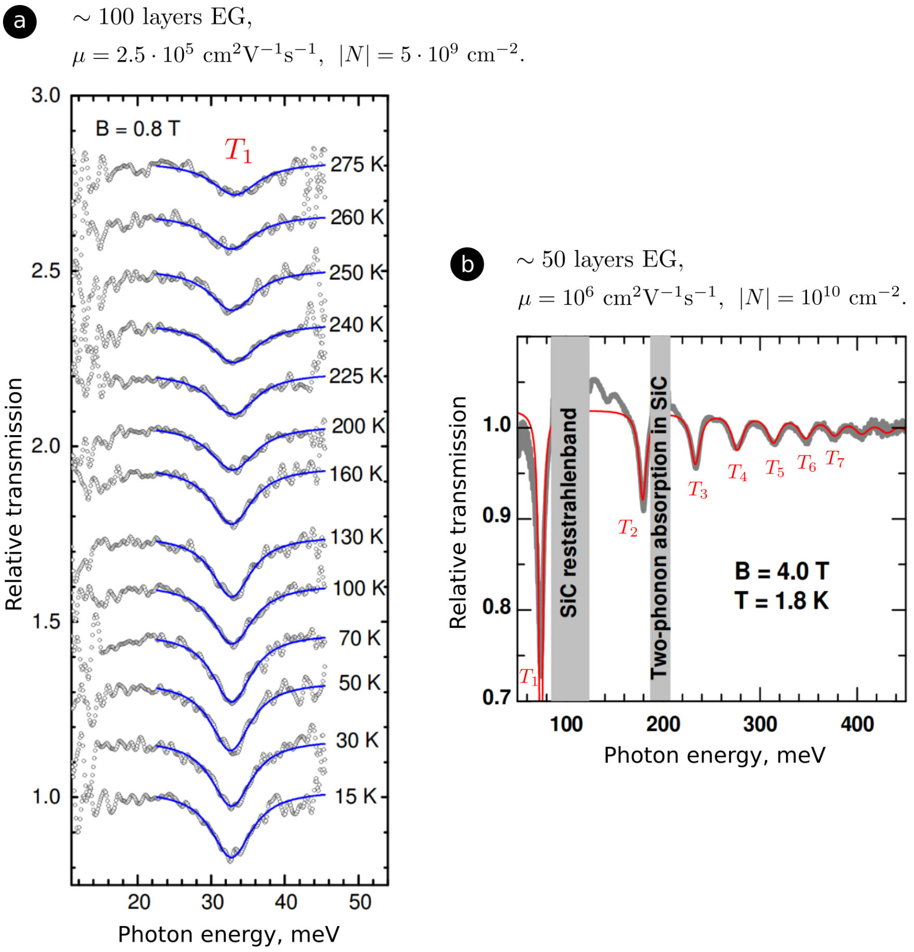

a ~ 100 layers EG, $\mu = 2.5 \cdot 10^5\ \mathrm{cm^2V^{-1}s^{-1}},\ |N| = 5 \cdot 10^9\ \mathrm{cm^{-2}}.$

b ~ 50 layers EG, $\mu = 10^6\ \mathrm{cm^2V^{-1}s^{-1}},\ |N| = 10^{10}\ \mathrm{cm^{-2}}.$

Figure 2.16 – Relative transmission of very high quality multilayer epitaxial graphene on SiC i.e. transmission in nonzero magnetic field normalized by zero field transmission $T(\omega, B)/T(\omega, 0)$. **Panel a:** Plot made made after [131]. Scattering of graphene's charge carriers is more pronounced at high temperature therefore magneto-optical absorption line becomes wider and shallower as the temperature grows. **Panel b:** Plot made after [130]. As one can see, up to 7 magneto-optical absorption lines could be resolved in high quality samples meanwhile not more than 3 or 4 lines are reported in other experiments, see Figures 2.17 and 2.18.

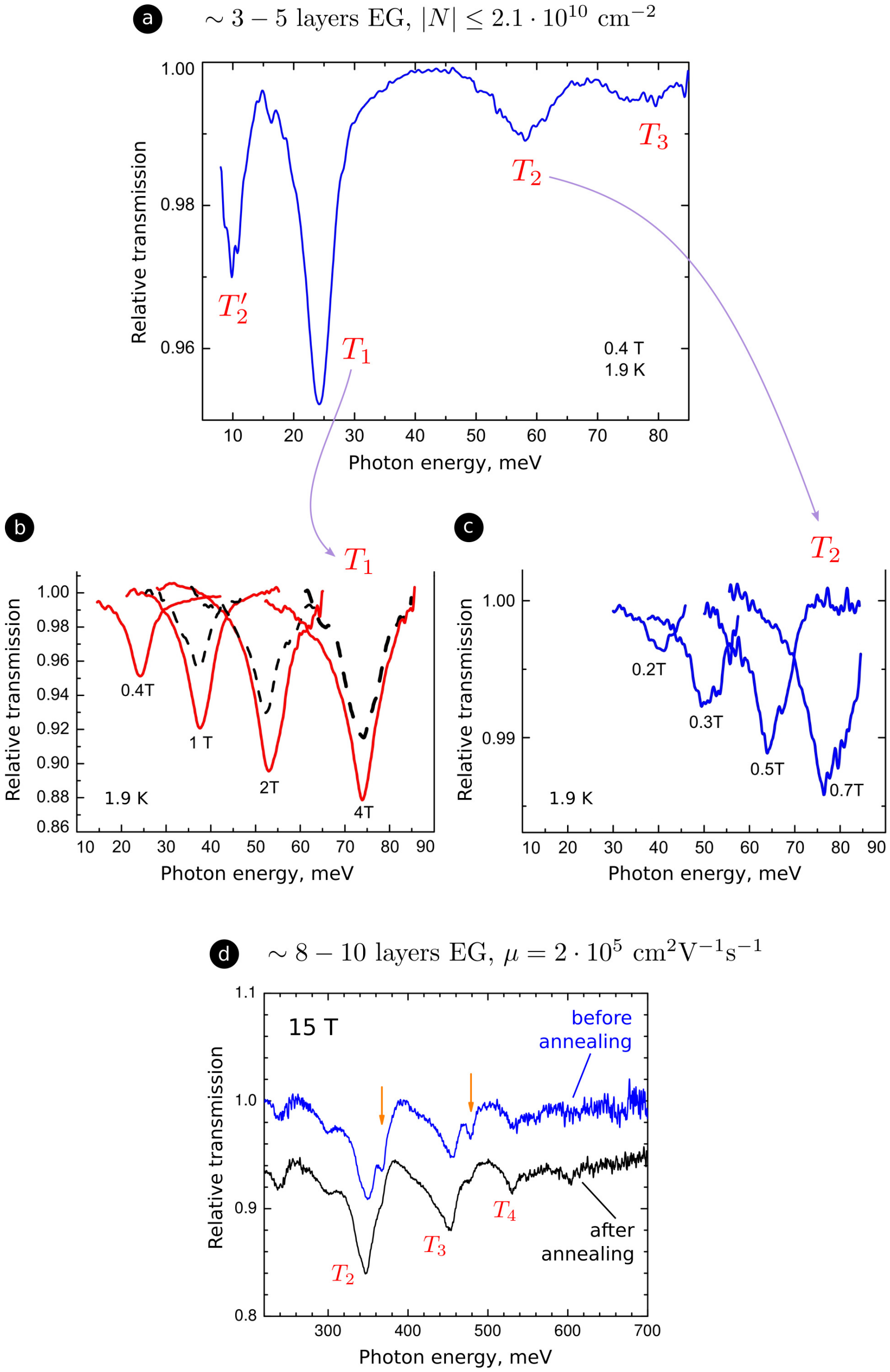

Figure 2.17 – Relative transmission of graphene i.e. $T(\omega, B)/T(\omega, 0)$. **Panels a, b, and c:** Plots made after [142]. Black dashed lines and red solid lines show results obtained on two different samples. **Panel d:** Plot made after [129]. Arrows indicate new magneto-optical absorption lines presumably induced by the disorder in graphene.

a CVD graphene on exfoliated hBN, $\mu = 5 \cdot 10^4\ \mathrm{cm^2V^{-1}s^{-1}}$.

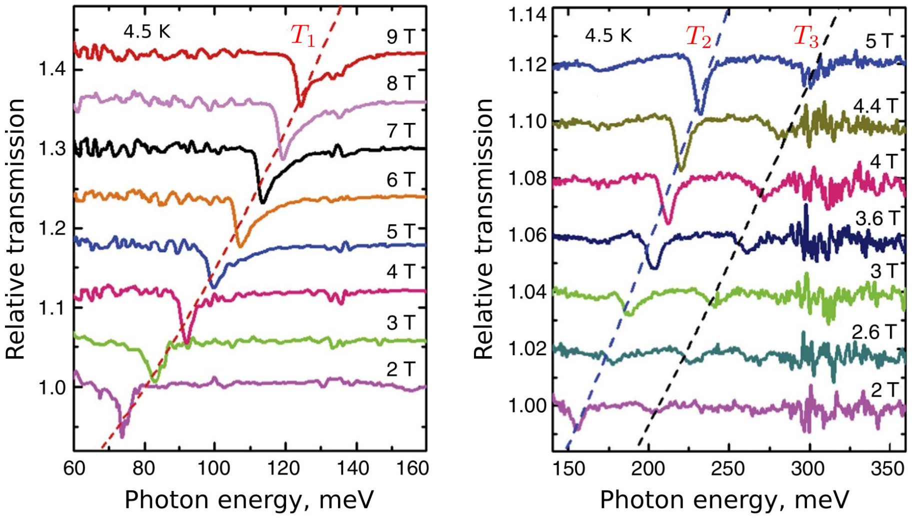

b Exfoliated graphene on Si/SiO$_2$,
$\mu = 3 \cdot 10^3\ \mathrm{cm^2V^{-1}s^{-1}}$, $|N| = 2 \cdot 10^{12}\ \mathrm{cm^{-2}}$.

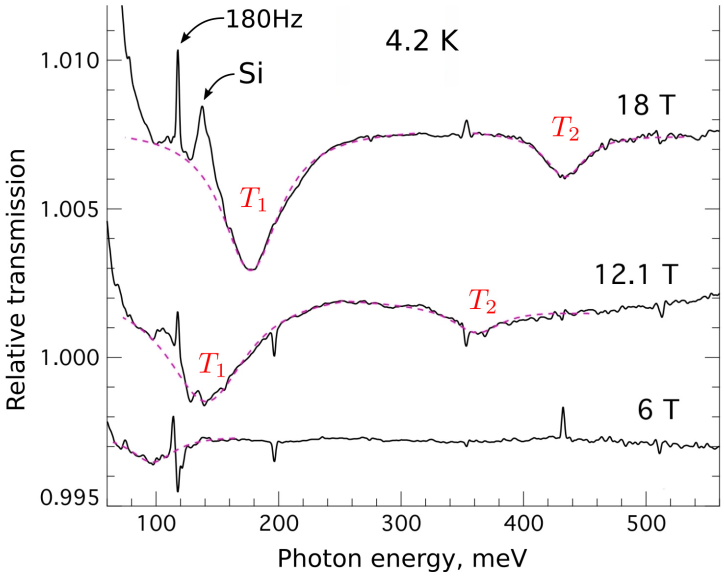

Figure 2.18 – Relative transmission of graphene i.e. transmission in nonzero magnetic field normalized by zero field transmission $T(\omega, B)/T(\omega, 0)$. **Panels a:** Plot made after [141]. **Panel b:** Plot made after [140]. “180 Hz” is an artifact associated with power grid 60 Hz harmonics, “Si” is spectral signature coming from the Si substrate.

Chapter 3

Boron nitride encapsulated graphene

3.1 Graphene/hBN van der Waals heterostructures

Hexagonal boron nitride (hBN) has proven to be very appealing as a graphene substrate compared to many other materials which have been tried so far. Thin hBN flakes obtained with scotch-tape exfoliation were first reported in 2005 [12]. However hBN became popular in graphene device fabrication only six years later after the publications [110, 112] showed its benefits. The next reasonable step was encapsulation i.e. covering *both* sides of a graphene membrane with hBN. Thus hBN has become one of the most studied 2D materials nowadays and even acquired a nickname “white graphene”. Currently hBN is no longer viewed as a subsidiary material for protection of graphene but rather as an important constituent part of van der Waals heterostructures − artificial materials assembled from few-layer or monolayer 2D crystals stacked vertically on top of each other [92].

Properties of hBN

Physical properties of hBN are described in topical reviews [145, 146]. hBN is one of four crystalline BN polymorphs [147]. Structure of hBN [148, 149] somewhat resembles the structure of graphite: hBN crystal also consists of parallel weakly coupled sheets, see Figure 3.1. Each sheet has a honeycomb lattice with boron and nitrogen atoms occupying different bipartite sublattices, which means that boron atoms are only adjacent to nitrogen atoms and vice versa. There exist three different types of stacking of the neighboring honeycomb sheets. We used hBN crystals with polytype 1H stacking, in which hexagons from one sheet are exactly above and below the hexagons from adjacent sheets, see Figure 3.1 panel a. Such crystals are denoted simply by hBN and the staking is denoted by $AA'AA'AA'$..., here prime symbol indicates that boron atoms from one sheet neighbor the nitrogen

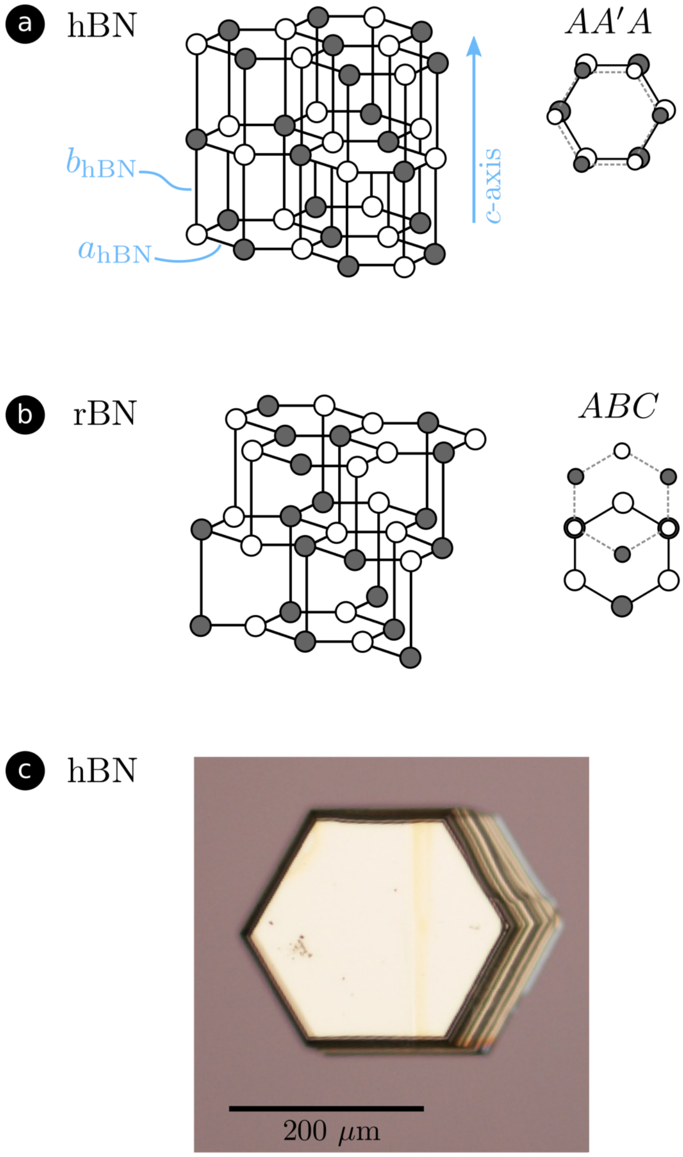

Figure 3.1 – Panel a: crystalline structure of hBN which is used for graphene encapsulation, black and white circles represent boron and nitrogen atoms. Principal axis is referred as c-axis, honeycomb sheets lay in the basal plane of hBN. **Panel b:** crystalline structure of rBN, black and white circles represent boron and nitrogen atoms; this very scheme could be also interpreted as trilayer graphene with ABC stacking, in this case black and white circles represent carbon atoms at two different bipartite sublattices. **Panel c:** High quality hBN monocrystallite which was used to manufacturer our samples, photograph taken with an optical microscope.

atoms from adjacent sheets and vice versa. hBN is a centrosymmetric crystal, i.e. it possesses a point through which a spatial inversion leaves the whole structure invariant.

For comparison, in turbostratic boron nitride (tBN) honeycomb sheets are twisted in random angles relative to each other (this structure is not strictly speaking crystalline), and in rhombohedral boron nitride (rBN) honeycomb sheets have 3R polytype stacking denoted by $ABCABC$... [147] which is the same as in ABC trilayer graphene, see Figure 3.1 panel b. Meanwhile, graphite has polytype 2H stacking also called Bernal stacking and denoted by $ABABAB$... which represents the fact that half of the carbon atoms in graphite do not have matching atoms in adjacent sheets. Graphite with polytype 1H stacking $AAAAAA$... (like in hBN) is not stable.

Values of lattice parameters in hBN are close to those in graphite[1]. Distances between two neighboring boron and nitrogen atoms are $a_{\text{hBN}} = 0.249$ nm and $b_{\text{hBN}} = 0.330 - 0.333$ nm [148, 149, 150, 151] whereas corresponding distances for graphite are $a_{\text{Gr}} = 0.245 - 0.246$ nm and $b_{\text{Gr}} = 0.333 - 0.335$ nm [21, 22, 23]. hBN is easily cleavable owing to weak van der Waals coupling between the neighboring sheets and much stronger in-plane covalent bonding. For this reason hBN powder is traditionally used as a dry lubricant, and also in cosmetic products, dental cements, paints, pencil leads. hBN is a highly anisotropic material: many of its physical properties differ significantly along the c-axis and across the basal plane. Vibrational properties of hBN are described in [152].

In contrast to graphene and graphite, hBN is a wide band gap insulator. This property is directly related to the fact that in hBN the sublattices A and B are occupied by two different types of atoms. The difference between electron's energies when it resides on different sublattices corresponds to the value to the hBN gap. Currently the band structure of hBN is not fully understood and still in debate [153, 154, 155] despite decades of numerous experimental and theoretical studies. Both direct and indirect band gaps have been reported, experimental values ranging from 3.6 eV to 7.1 eV [149, 153, 156, 157, 158, 159, 160, 161] and theoretical values ranging from 2.45 eV to 12.7 eV [154, 161, 162, 163, 164]. These discrepancies are often attributed to the lack of large pure defect-free hBN samples and great variation in electronic properties from sample to sample. Currently, the most reliable value of the gap of high quality hBN is considered to be ~ 6 eV.

hBN has high dielectric breakdown field strength and it is used in electronic equipment as a charge leakage barrier layer because of its good insulating properties. Electrical properties of ultrathin hBN crystals were studied experimentally as a function of the number of layers in [165]. Magnetic properties of hBN were investigated in [166, 167]. It is a diamagnet with magnetic susceptibilities $\chi_{\perp} = 17.3$ μemu/g across honeycomb sheets and $\chi_{\|} = 0.48$ μemu/g along c-axis. The centrosymmetric structure of bulk hBN is incompatible with piezoelectricity [168]. However, few-layer hBN flakes, unlike few-layer graphene flakes, may not have an

---

[1] This fact is nontrivial and represents scientific interest of itself [150].

inversion center [169] leading to piezoelectricity which has been observed [170] and described theoretically [171, 172, 168, 173].

At room temperature, hBN has high thermal conductivity of 400 W/(m·K) in the basal plane which is larger than in many metals and ceramics, meanwhile thermal conductivity along the c-axis is an order of magnitude lower [174, 175, 176]. At liquid helium temperature, the thermal conductivity of hBN drops by three orders of magnitude. The coefficient of thermal expansion is $0.11 \cdot 10^{-6}$ 1/K across honeycomb sheets and $3.1 \cdot 10^{-6}$ 1/K perpendicular to the honeycomb sheets, both values are provided for 10 Kelvin temperature. As temperature grows, the former coefficient decreases and even turns negative at temperature ~ 65 Kelvin [177].

Optical properties of hBN

Optical properties of hBN were investigated in [152, 161, 164, 160]. Being a wide gap insulator, hBN is highly transparent in a broad region of wavelengths from visible to far infrared. hBN reflects and absorbs some substantial portion of incident light only in two narrow regions around the frequencies corresponding to the hBN phonons $\omega_{\text{ph}} = 1367$ cm^{-1} and $\omega'_{\text{ph}} = 767$ cm^{-1}. hBN has uniaxial symmetry with its optical axis along the c-axis: optical properties of hBN are isotropic in the basal plane, meanwhile propagation of light in the perpendicular direction is characterized by a refractive index of a different value. hBN possesses a very rare and extraordinary property: it is a natural hyperbolic material [178] at frequencies of light between the phonon resonances ~770 cm^{-1} and ~1370 cm^{-1}. In this region hBN's dielectric constants obey $\mathrm{Re}\,\varepsilon_{\perp} \cdot \mathrm{Re}\,\varepsilon_{||} < 0$ and hBN shows negative refraction of light in the case of light incidence oblique to the optical axis. In this work, we created a simplified model of the hBN's complex refractive index which is suitable for our optical configuration, see Section 6.2.

hBN synthesis

Thin hBN flakes could be produced with the help of many different methods [179] similar to those of graphene synthesis. Currently, scotch-tape exfoliation of bulk hBN yields the best quality thin monocrystalline flakes [180] however their lateral size is limited to $\lesssim 100$ μm. Here the limiting factor is not only the exfoliation technique itself. Another big problem is that hBN monocrystallites which are used as a precursor for exfoliation cannot be grown larger than ~ 200 μm in size, see Figure 3.1. Thickness of hBN flakes cannot be controlled during exfoliation either. Typically, hBN crystals used in graphene research have thickness ranging from atomic-thin to micron-thick samples. Just as with other 2D materials, properties of ultrathin hBN flakes may depend on the number of honeycomb sheets and may differ from the properties of bulk hBN.

hBN-encapsulation of graphene

Many materials including mica, $SrTiO_3$, pyrolytic BN, parylene, etc were proposed and investigated as substrates for graphene [181]. So far, hBN proved to be the best substrate and encapsulation material from the point of view of preserving graphene's quality. hBN stands out due to coincidence of several factors. Most importantly, hBN crystals could be cleaved into relatively big flakes with atomically flat surfaces which are almost free of dangling bonds and charge traps. Microstructure of graphene on hBN was studied with STM [182] and compared to the microstructure of graphene on SiO_2 which is also a popular graphene substrate due to historical reasons, see Figure 3.2. It was found that hBN flakes are atomically flat and their roughness is 5 times smaller than the roughness of SiO_2. In addition, graphene on hBN showed significant reduction in charge inhomogeneity on microscopic scales which is crucial for observation of excitations in graphene at energies very close to the Dirac point. For comparison, pyrolytic BN has polycrystalline structure and proved to be inefficient for graphene encapsulation [92] presumably because of its rough surface. Another important factor is that hBN is a robust electric insulator which allows gating and efficiently insulating graphene samples from environment. In addition, hBN shows superb thermal and chemical stability. Here are the main benefits of hBN-encapsulation:

- **Protection** of graphene's surface from contamination and mechanical damage. Encapsulated graphene devices are more robust and stable in the long term and do not deteriorate under ambient conditions.

- **Self-cleaning effect.** During encapsulation graphene and adjacent hBN flakes cling to each other tightly because of van der Waals forces. As a result, contaminants which adhered to their surfaces before encapsulation (water, hydrocarbons etc) are squeezed out or agglomerate in micrometre-sized droplets [183] leaving the rest of the Gr/hBN interfaces clean and atomically flat[2].

- **Stabilization** of graphene membrane, reduction of corrugations and flexural phonons.

Currently, many procedures have been developed for thin flake transfer and graphene encapsulation [112]. Some of these procedures involve different polymer coatings and solvents, meanwhile others get by with sticky polymer stamps. In the end the quality of hBN/Gr/hBN stacks depends substantially on how graphene and hBN flakes are handled before and during the assembly of the stack. In general, quality of the flakes is better preserved with so called dry transfer (pick up) techniques in which the contact of 2D flakes with contaminants is minimized.

---

[2] Currently it is the only method of achieving such a fine interface between two crystals, even molecular beam epitaxy gives worse results because of island growth [92].

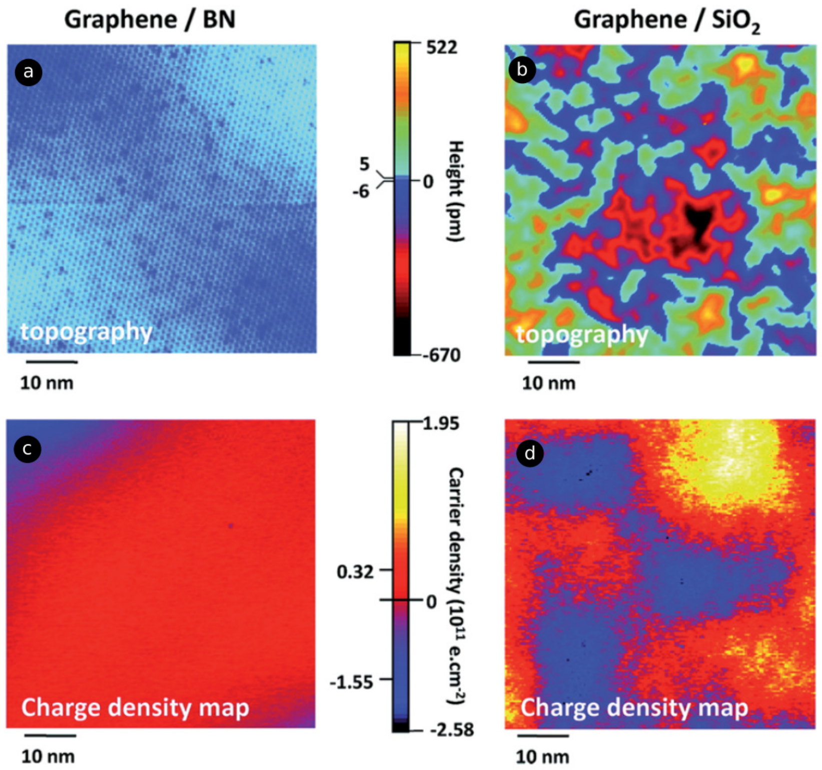

Figure 3.2 – Comparison of graphene on hBN and on SiO$_2$ substances. Topography and charge density maps created with STM clearly demonstrates advantages of hBN as a substrate. **Panels a and c:** Gr/hBN. **Panels b and d:** Gr/SiO$_2$. The picture is based on [182].

Emergent phenomena in hBN/Gr/hBN heterostructure

Apart from the above mentioned benefits, hBN/Gr/hBN stack also exhibits peculiar electronic and structural properties distinct from the properties of its components. The van der Waals interaction between adjacent 2D flakes is relatively weak, nonetheless it affects graphene's charge carriers and lattice. It has been shown [184, 185, 186] that crystallographic alignment of hBN flakes relative to graphene, i.e. angles ϕ between graphene and hBN honeycomb crystallographic axes, is an important factor which defines what new emergent properties could be observed and whether they would be pronounced. Here is a list of emergent phenomena predicted or observed in Gr/hBN and hBN/Gr/hBN stacks:

- screening of Coulomb interactions in graphene;
- moiré superlattice;
- renormalization of the Fermi velocity;

- stretching and adjustment of graphene's lattice to hBN's lattice;
- symmetry breaking and gap opening in graphene (in debate);
- hBN phonons interacting with graphene charge carriers.

Moiré superlattice is a spatial long-period pattern which forms when the graphene honeycomb pattern is overlaid on the crystalline pattern of the substrate. Such moiré patterns [187] were first discovered in STM experiments on graphite [188]: they are caused by misalignment between surface and subsurface honeycomb sheets. Later these patterns were also observed in misaligned few-layer epitaxial graphene on SiC [189] and more rarely in few-layer CVD graphene [187]. Graphene and hBN have very close interatomic spacing $\delta \equiv a_{\text{hBN}}/a_{\text{Gr}} - 1 \approx 1.8\%$ therefore moiré superperiods at Gr/hBN interface may have quite large values just as in the case of Gr/Gr interfaces.

From purely geometric point of view, angle ϕ between graphene's and hBN's lattices defines both the superperiod L which forms at one Gr/hBN interface and orientation of the moiré superlattice ϕ' relative to graphene's lattice [190]:

$$L = \frac{1+\delta}{\sqrt{2(1-\delta)(1-\cos\phi)+\delta^2}} \cdot a_{\text{Gr}}, \quad \operatorname{tg}\phi' = \frac{\sin\phi}{(1+\delta)-\cos\phi}. \tag{3.1}$$

Thus according to the above mentioned formula large values of superperiod are achieved when graphene and hBN flakes are closely aligned i.e. $\phi \to 0$ and the maximal possible superperiod is $L = 57 \cdot a_{\text{Gr}} = 14$ nm. Moiré patterns at Gr/hBN interface have been successfully mapped with the help of STM and C-AFM [182, 190, 191, 192]. However these experiments also revealed that formation of moiré lattices cannot be viewed as a simple geometric superposition of two periodic patterns. For very small angles ϕ, graphene's lattice stretches and readjusts itself to follow a slightly longer period of hBN's lattice. As a result, domains form where graphene and hBN are commensurate, see panel b of Figure 3.3. These domains are separated by domain walls where graphene is compressed to compensate for the accumulated strain due to stretching [191]. However, the resulting overall period of the moiré pattern remains the same as specified in the formula (3.1). For larger angles ϕ graphene exhibits very little adjustment to hBN and their lattices are in so called incommensurate state, see panel a of Figure 3.3. There are still many open questions related to these phenomena: structure and width of domain walls, transition form commensurate to incommensurate states, effect of temperature on the readjustment of the lattice, role of occasional pinning of graphene to hBN by imperfections etc.

The effect of moiré superlattice on the properties of Gr/hBN van der Waals heterostructures are covered in the topical review [184]. The moiré pattern creates a weak periodic potential for charge carriers in graphene. Theoretical studies predict nontrivial effects as formation of a new set of Dirac points and minicones at an energy determined by moiré superperiod [190]. Massless fermions generated at these superlattice Dirac points have a significantly lower Fermi velocity; the local density of states at the minicones is modulated due to the influence of the periodic potential. As a consequence, moiré patterns also modify the optical properties of graphene, these effect were investigated from theoretical point of view in [193] for the case of zero magnetic field. In nonzero magnetic fields, the moiré pattern modifies the set of Landau levels described in Section 2.3 and there forms a beautiful fractal structure of energy levels which is known as Hofstadter's butterfly. These effects emerge only when the superlattice period is larger than the magnetic length $L > l_B$ which is achieved at nearly zero angle of graphene's alignment relative to hBN and in high magnetic fields. Optical properties of systems with Hofstadter's butterfly energy levels were theoretically investigated in [194, 195].

Another important effect predicted theoretically is breaking of sublattice symmetry in graphene: graphene's electrons form A and B sublattices have different on-site energies due to proximity to either boron or nitrogen atoms. This symmetry breaking leads to the band gap opening in the main Dirac point of graphene, predicted values of the gap mentioned in the literature fall into the range $\sim 50 - 500$ meV [196, 185, 186]. Apart from that, the superlattice potential induces warping of the Dirac cones which becomes pronounced already at low energies in the

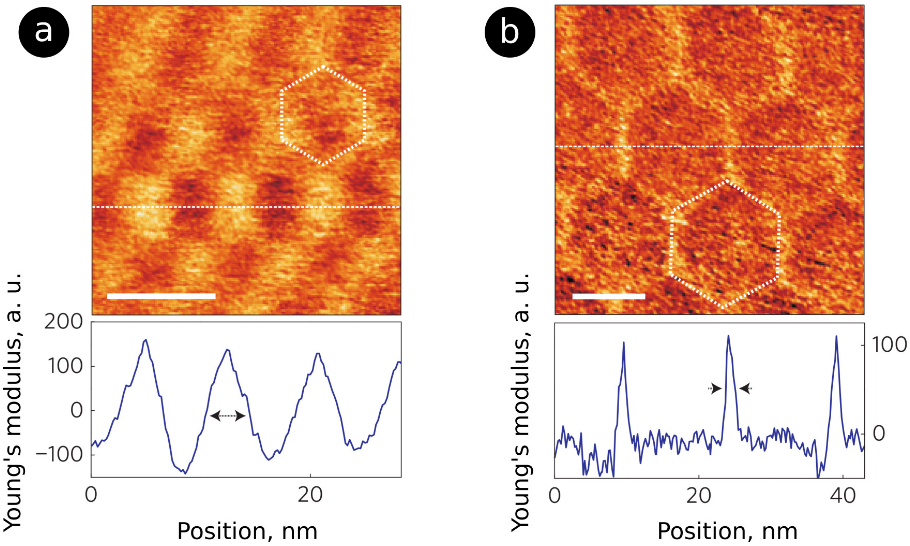

Figure 3.3 – Distribution of the Young's modulus in graphene on hBN substrate, the figure is made after [191]. Colorplots show the moiré patterns in two different samples, both scale bars are 10 nm. Bottom plots show cross sections of the Young's modulus taken along the dashed lines in the corresponding colorplots, and averaged over ten scanning lines which is approximately 2.5 nm. **Panel a:** A 8 nm moiré pattern, tension varies gradually with distance which is a signature of an incommensurate state. **Panel b:** A 14 nm moiré pattern, tension is almost constant between the narrow domain walls whith is a signature of an incommensurate state.

vicinity to the Dirac point. Effects of superlattice potential on the band structure of graphene are systematically investigated from theoretical point of view in [197]. In practice, there exist many factors apart from the stacking angle ϕ which influence the resulting band structure observed in experiments: commensurability of graphene with hBN, lattice defects [198] etc. Experiments in which the gap values were measured give controversial results: both an absence [192] and presence of the gap up to 150 meV [141, 199] were reported.

The superlattice which forms in a hBN/Gr/hBN stack can be more complicated than the one at a single Gr/hBN interface, however the emergent effects due to such superlattice are qualitatively the same. When graphene is exposed to an external periodic potential, such as moiré superlattice, the Fermi velocity of graphene's charge carriers is renormalized even in the framework of a single-particle theory [200, 201]. This phenomenon is not limited only to hBN moiré superlattices and has been reported for other cases of external periodic potentials [202, 203].

In general, van der Waals heterostructures are viewed as a promising approach to creating new metamaterials [92]. The properties of such heterostructures could be engineered with the proper choice of stacking order and relative alignment of different 2D crystals: One may cumulate advantageous features of all 2D crystals in the stack and in some cases also profit from the emergent phenomena on their interfaces. Currently band gap engineering in graphene on hBN is of particular interest in the scientific community. Long term stability, resistance to multiple thermal cycles, and degradation of Gr/hBN van der Waals heterostructures are important issues for potential applications of graphene. To our knowledge, these issues have now been systematically investigated. In most cases, properties of non-encapsulated graphene has been monitored no longer than 6 months [204, 205, 206, 207] and in rare cases up to 18 months [208].

3.2 Our samples: suspended graphene membranes

Graphene samples used in our experiments were fabricated in the University of Manchester Condensed Matter Physics group by Sheng Hu and Marcelo Lozada Hidalgo in collaboration with Andre K. Geim. During design and manufacturing of these samples there were two equally important priorities:

- creating high quality graphene,
- enabling magneto-optical measurements of infrared transmission.

In total five samples have been created: three hBN-encapsulated and two non-encapsulated graphene membranes, all suspended over circular holes. The non-encapsulated samples did not show any spectral features in their transmission spectra. Therefore we assume that most probably these graphene membranes did not survive external conditions and were already broken or highly contaminated during the optical measurements. Further on in this manuscript we always refer to our

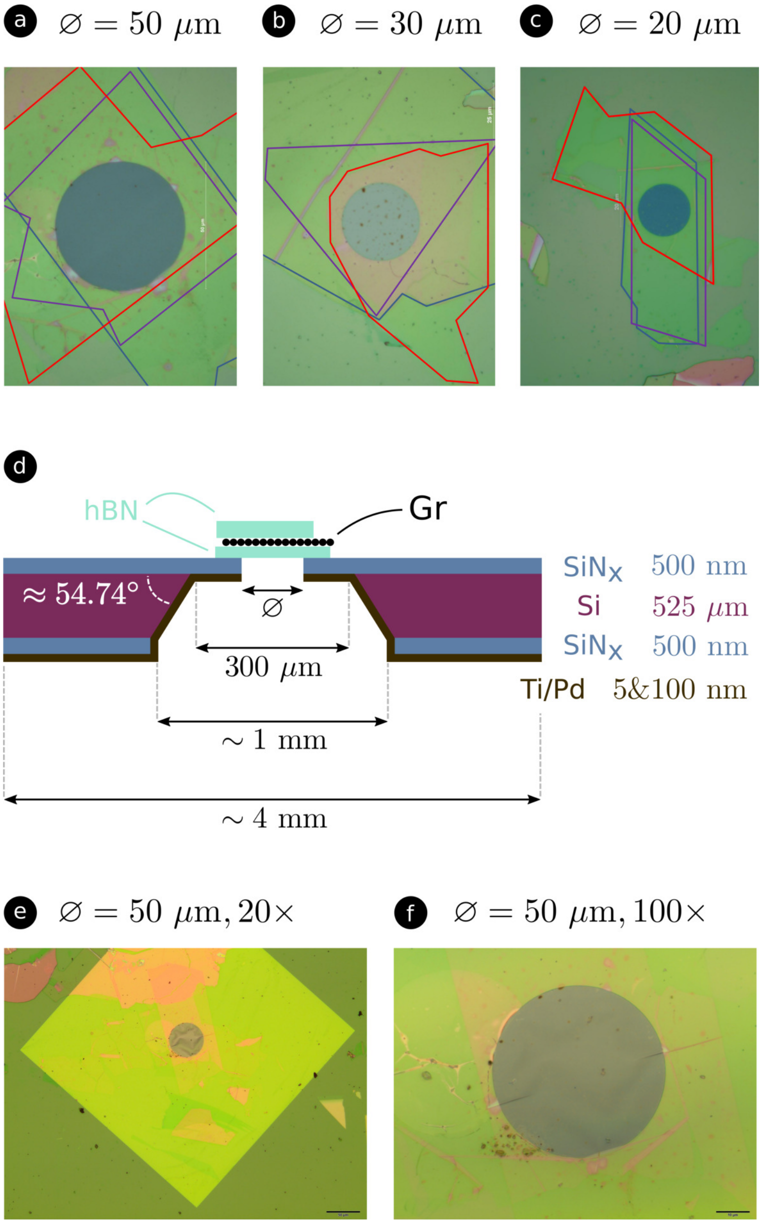

Figure 3.4 – Our hBN/Gr/hBN stacks. **Panels a, b, and c:** Photographs of suspended hBN/Gr/hBN membranes taken with an optical microscope. Color contours roughly outline 2D crystals in the stacks: top hBN flakes (red), bottom hBN flakes (blue) and graphene flakes (purple). **Panels d:** Cross section of hBN/Gr/hBN stack and scaffolding, the scheme does not show real proportions. **Panels e and f:** Photographs of the biggest membrane taken with an optical microscope. Light square in the panel e is the top face of the truncated square pyramid etched in the scaffolding.

encapsulated samples unless something else is explicitly specified. Description of our non-encapsulated samples is given in Appendix A.

Structure

Our three samples have the same structure: graphene monolayer is encapsulated in between two hBN flakes, the whole hBN/Gr/hBN stack rests on a special scaffolding created for measurements of transmission spectra, see Figure 3.4. All graphene and hBN flakes are monocrystalline, hBN flakes are atomically flat i.e. do not have terraces of atomic layers. The scaffoldings are made of a flat ~ 4 mm $\times$ 4 mm pieces of Si/SiN$_\mathrm{x}$ wafer[3]. The wafer consists of 525 μm monocrystalline Si layer, both surfaces of which are covered with thinner 500 nm layers of SiN$_\mathrm{x}$. Roughly in the center of the wafer, there is a hollow which has shape of a truncated square pyramid with edges of 1000 μm at the bottom, 300 μm at the top, side faces make angle of $\arctan\sqrt{2} \approx 54.74°$ with the base. The value of the angle was defined by the orientation of crystallographic planes in the Si wafer. A circular hole is made in SiN$_\mathrm{x}$ right in the center of the pyramid's top face. hBN/Gr/hBN stack is suspended over this hole. The bottom side of the scaffolding was covered with 5 nm layer of titanium and then with 100 nm layer of palladium. This metallic coating acts as a mask and is supposed to block light which bypasses the circular hole in the SiN$_\mathrm{x}$ during optical measurements.

Table 3.1 summarizes geometry which differs for each sample. As one can see the diameters of the suspended membranes correspond to wavelength of far infrared light. Thus they are big enough to enable optical measurements in a broad region of infrared light.

Diameter of suspended membrane, $\varnothing$	hBN thickness		hBN orientation	
	bottom, d_1	top, d_2	bottom, ϕ_1	top, ϕ_2
50 μm	10 nm	5 nm	$< +1°$	$\sim -5°$
30 μm	20 nm	10 nm	$\sim +4°$	$\sim +3°$
20 μm	8 nm	5 nm	$< +1°$	$\sim -2°$

Table 3.1 – Dimensions of hBN/Gr/hBN stacks. Here and later "top" and "bottom" convention is the same as in Figure 3.4. hBN thickness was estimated based on the flakes color and contrast under an optical microscope (for a 30 nm hBN flake the error is $<$ 5 nm). The values of the angles were estimated comparing the angles between the straight edges of the flakes, presumably such edges reveal the orientation of crystallographic axes of the flakes.

---

[3] Here the subscript 'x' indicates that stoichiometry of Si and N atoms is not very well defined.

Orientation of the flakes was chosen to maximize the area of overlap between the flakes in each stack. In the end angles between flakes' crystallographic axes turned out to be relatively small however there was no special intent in it.

Our graphene samples were manufactured from non-doped graphite using only 'clean' procedures and later hBN-encapsulation protected graphene from contamination by charged impurities. Therefore one may assume, that just after the manufacturing, doping of our samples was low and chemical potential laid very close to the Dirac point. An insight into the values of initial doping could be taken from the transport measurements performed on hBN/Gr/hBN samples produced with the same procedure as ours. Publications [83] report charge carrier concentrations of $|N| \sim 10^{10}$ cm^{-1} due to residual extrinsic doping. Further comments about the values of doping and their changes with time are given in Chapter 7.

Manufacturing

First, the scaffolding was created as described in [209] from commercially available Si wafers coated on both sides with SiN$_x$. Figure 3.5 shows the main steps of microfabrication. Reactive ion etching (RIE) is employed to remove a $\sim 1\times1$ mm^2 square of the bottom SiN$_x$ layer. Then the wafer is exposed to a potassium hydroxide (KOH) solution which etches away unprotected Si all the way through to the top SiN$_x$ layer. As a result, there remains a free-standing $\sim 300 \times 300$ μm^2 square section of the top SiN$_x$ layer. Next, RIE is employed again to drill a circular hole in the top SiN$_x$ layer. Finally, titanium and palladium layers were deposited by electron-beam evaporation. Here the titanium layer mainly plays a subsidiary role: it improves adhesion of palladium to the wafer.

To create high quality samples, only scotch-tape exfoliated graphene and hBN were used. Bulk crystals of graphite and hBN (see Figure 3.1 panel c) for exfoliation were commercially supplied by HQ Graphene and NGS Naturgraphit correspondingly. Graphene flakes were encapsulated between a pair of hBN flakes using dry-peel (pick-up) transfer method for assembly of van der Waals heterostructures. The main advantage of this method is that it allows avoiding contamination of graphene by carbohydrates and polymer residues during assembly of the hBN/Gr/hBN stack.

Figure 3.6 shows the main steps of the sample microfabrication. First, top hBN flake was exfoliated on a PMGI/PMMA polymer stack as described in the [181]. Meanwhile, a graphene flake was exfoliated on a SiO$_2$/Si wafer. Next, the graphene flake was picked up by the top hBN using the dry-peeling method described in [210]. Bottom hBN flake was exfoliated on a SiO$_2$/Si wafer and then picked up by the hBN/Gr stack the same way as the graphene flake was picked up by the top hBN flake. Finally, hBN/Gr/hBN stack was transfered to the scaffolding. In all these procedures SiO$_2$/Si wafers were chosen as exfoliation substrate because interference of visible light in thin SiO$_2$ layer allows quick identification of atomically flat crystalline flakes.

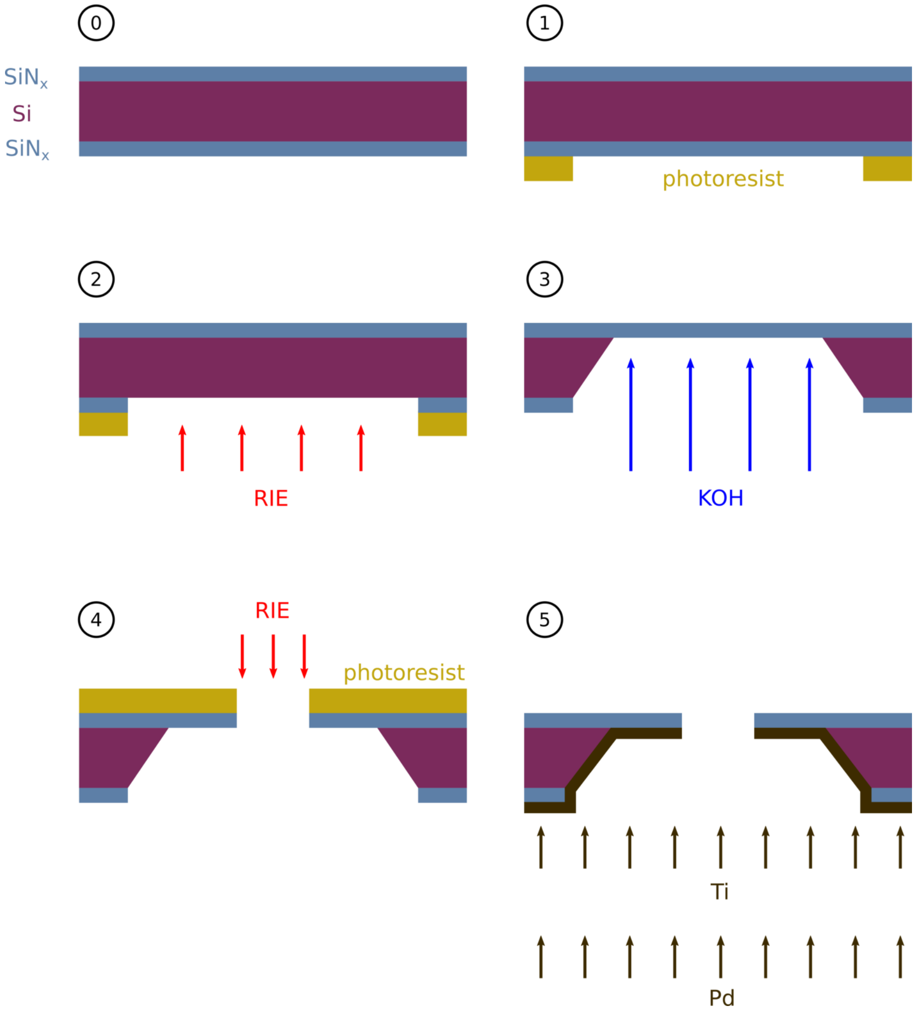

Figure 3.5 – Microfabrication of scaffolding for magneto-optical measurements, more details in the text.

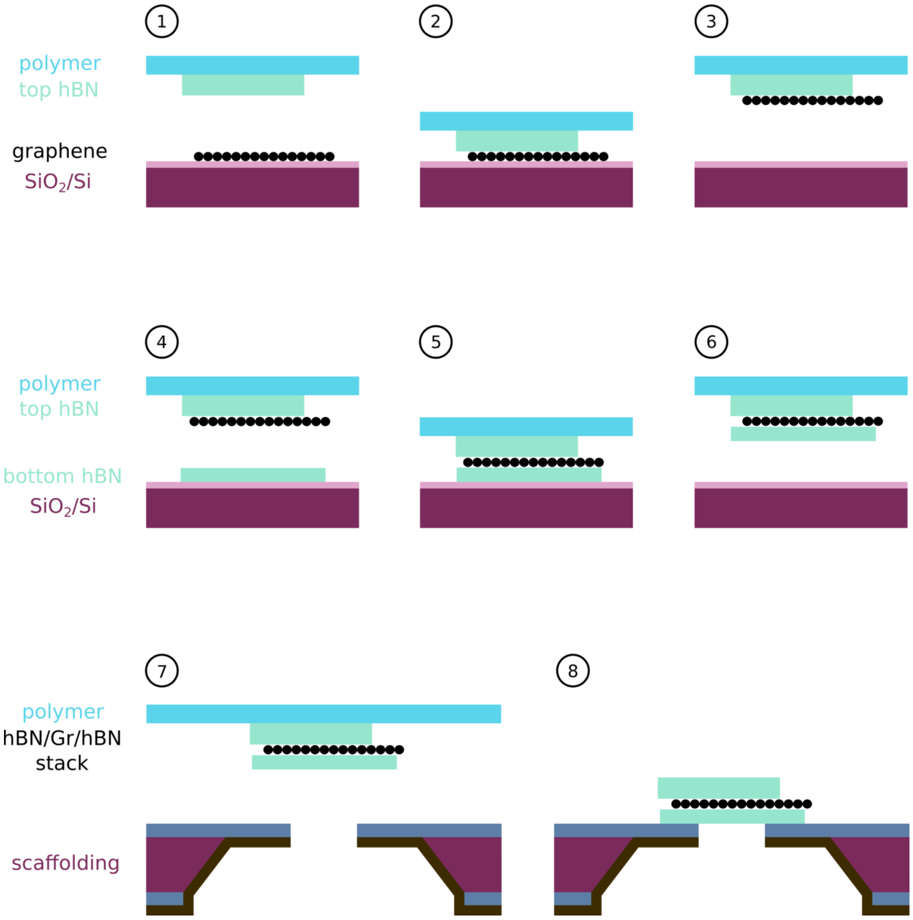

Figure 3.6 – Assembling the hBN/Gr/hBN stack with dry-peel (pick-up) transfer method, more details in the text.

Chapter 4

Experimental setup for magneto-optical microspectroscopy

4.1 Motivation for building new experimental setup

The goal of this work was investigating magneto-optical properties of the highest quality graphene in the infrared (IR) region of spectrum. In practice this meant that we had to perform measurements on small crystals of $\sim 10 - 100$ μm in size produced by scotch-tape exfoliation. Measuring IR magneto-optical spectra of small samples requires setup in which three devices are combined together: an IR spectrometer, an IR microscope and a magnet. These devices must work together as a whole and provide opportunities for typical magneto-optical experiments.

We wanted to investigate transmission (and not reflection) spectra because of two practical advantages. Firstly, graphene's transmission is much higher than its reflection, see sections 2.1, 2.3 and 6.2. Therefore one may profit from better signal-to-noise ratio during the experiments which is especially important when working with small samples. Secondly, transmission of graphene is more sensitive to the changes of magnetic field value than its reflection, see Section 6.2, which also leads to more accurate results. In addition to the transmission spectra, we also wanted to measure the Faraday rotation angle because it gives a deeper insight into magneto-optical transitions in graphene. Combining transmission spectrum together with Faraday rotation angle allows restoring the magneto-optical conductivity of graphene $\hat{\sigma}(\omega, B)$, which is the ultimate goal of a complete linear response optical spectroscopy experiment, see Section 6.4.

Permanent magnets suitable for optical measurements at room temperature can produce fields up to $\sim$ 1.5 Tesla. Achieving higher magnetic fields is feasible with SC electromagnets. Moreover, unlike permanent magnets, SC electromagnets allow easy tuning and inverting of magnetic field, but on the downside they require a cryostat. There are commercial systems which use permanent or SC magnets suitable for spectroscopic measurements at small samples in the visible and infrared

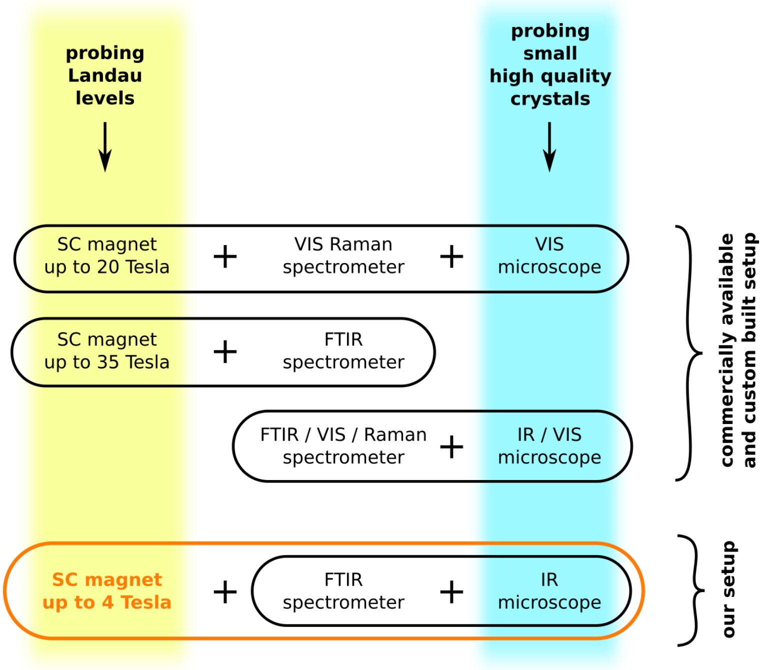

Figure 4.1 – Overview of some experimental setup for optical spectroscopies, ovals encompass pieces of equipment which are compatible with each other and can work together as a whole. *Black:* commercially available and custom built setup predominantly used in graphene research so far. *Orange:* our newly developed SC magnet compatible with a commercial FTIR spectrometer and a IR microscope. The scheme shows which setup allows probing Landau levels (*yellow*) and which allows working with small high quality samples (*blue*).

regions. To our knowledge these are [211] and [212]. Unfortunately, these systems have a number of limitations because they were developed for quite specific types of magneto-optical measurements, in particular they are not compatible with bulky objectives, they do not allow measuring IR transmission but only reflection spectra of the samples under investigation etc.

There exist commercial IR microscopes developed especially for FTIR microspectroscopy [139] i.e. they are compatible with FTIRS and do offer a lot of functionality and opportunities for various spectroscopic experiments, including transmission and Faraday rotation measurements. However, in practice it is difficult to combine a SC electromagnet and its cryostat together with an IR microscope without interfering with the optical path. IR microscopes focus radiation with the help of Cassegrain reflectors because these optical elements have a number of advantages over IR lenses: Reflectors work in a very broad range of wavelengths and they do not have any dispersion. However, unlike lenses, reflectors are bulky, moreover for reasonable magnifications of $10\times - 30\times$ times a typical working distance of a Cassegrain reflector is only several centimeters. All these peculiarities result in a very tight geometry of IR microscopes. Placing the focusing optics entirely inside the magnet's cryostat [213, 140] also leads to a number of problems: the cryostat must have higher cooling power, there is thermal contraction and misalignment of optical elements at low temperatures, changing magnetic field also causes misalignment and makes comparison of spectra measured at different magnetic fields inadequate, etc.

In the visible region of the spectrum these problems have been overcome with the help of optical fibers: the light could be fed and collected inside a SC coil magnet even through narrow passages. Thus optical fibers allowed performing magneto-optical measurements of the Raman shift in the visible range of spectrum on micron sized graphene samples. Unfortunately, currently there are no optical fibers which operate at wavelengths beyond 25 μm (50 meV) i.e. in the far infrared region [214, 215]. Moreover, existing IR fibers usually do not operate in broad regions of wavelengths and the choice of IR polarization-maintaining fibers is even more limited.

Therefore we developed a new experimental setup for FTIR magneto-optical microspectroscopy. It comprises a compact portable cryostat and a superconducting electromagnet in which the sample under investigation is mounted. To perform measurements of magneto-optical spectra this setup is combined with already existing commercial IR microscopes and FTIR spectrometers. Both the cryostat and the SC magnet have been designed as slim as possible and with a wide bore in the center of the magnet to ensure a good passage of light. This makes our setup compatible with IR microscopes even in transmission mode therefore both transmission spectra and Faraday rotation angle could be straightforwardly measured. Despite its small size, our electromagnet is able to produce more than 4 Tesla in the sample compartment. Figure 4.1 compares the functionality of our newly developed setup with functionality of other configurations for optical spectroscopies.

4.2 General overview of our experimental setup

In this work the magneto-optical spectra of graphene were measured using the following equipment combined together:

- FTIR spectrometer "Vertex 70v" manufactured by Bruker;
- IR microscope "Hyperion 2000" manufactured by Bruker;
- continuous flow cryostat based on "ST-100 Optical cryostat" by Janis;
- SC electromagnet (home made);
- detector of IR radiation.

Figures 4.2, 4.3, and 4.4 give an overview of how the key devices are connected together, Appendix B provides information about the commercial equipment. In

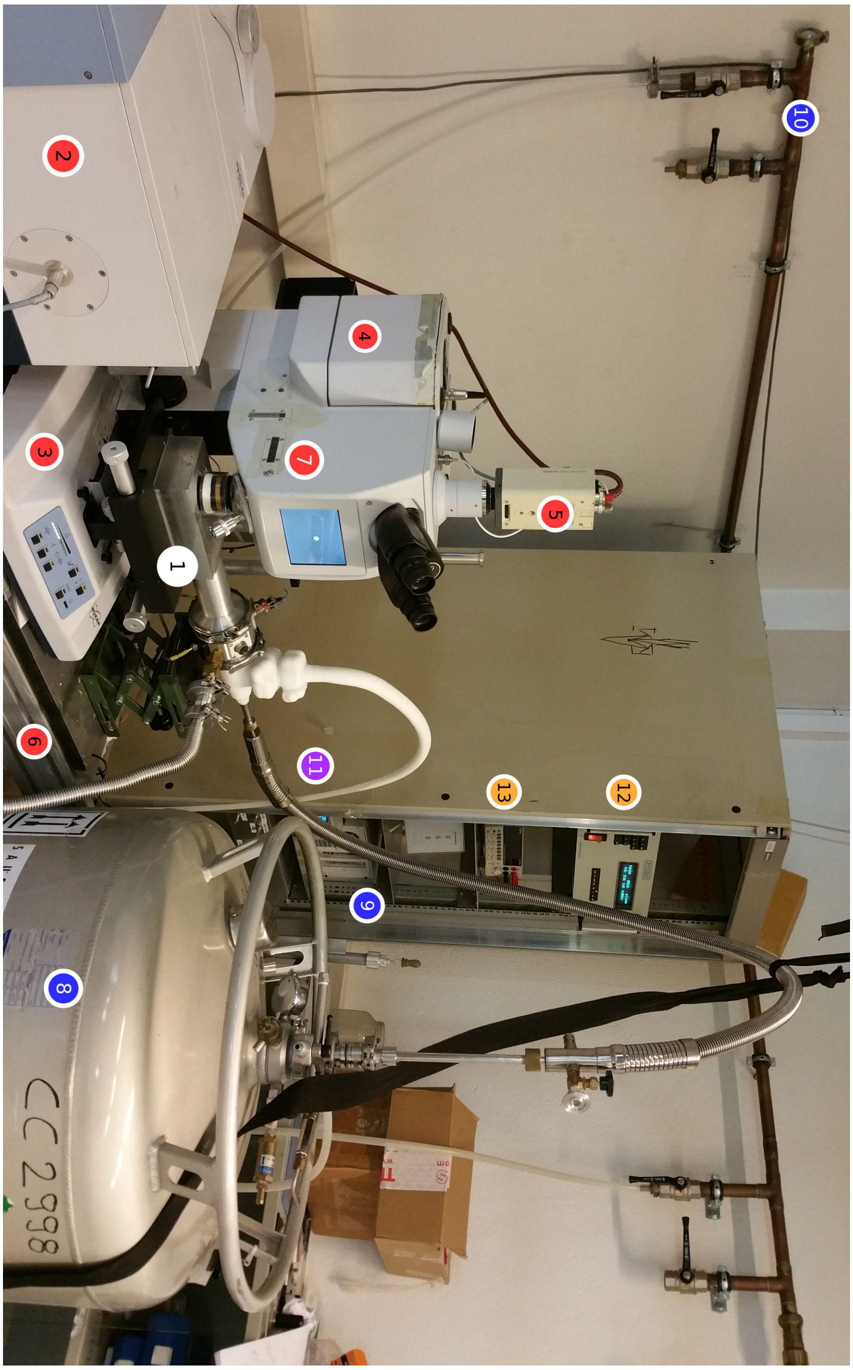

Figure 4.2 – A photograph of the experimental setup at work. More details in the text.

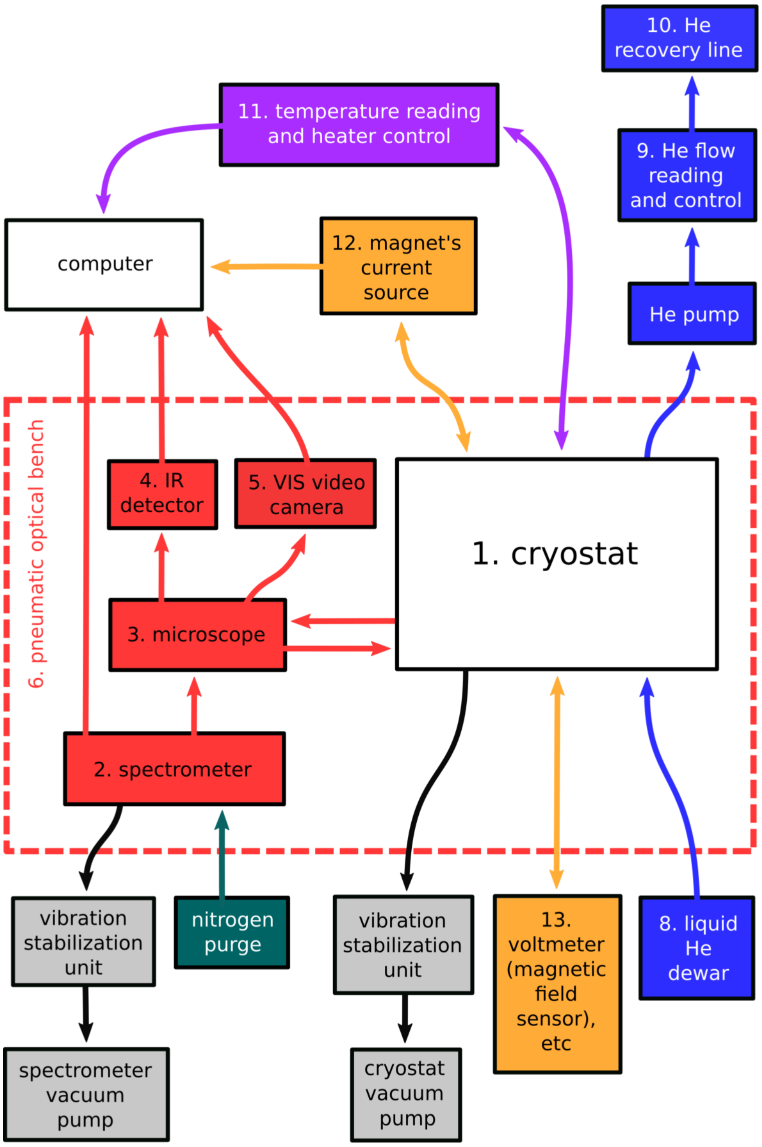

Figure 4.3 – A block diagram of the experimental setup, arrows show the flow of information, electric current, light or matter. More details in the text.

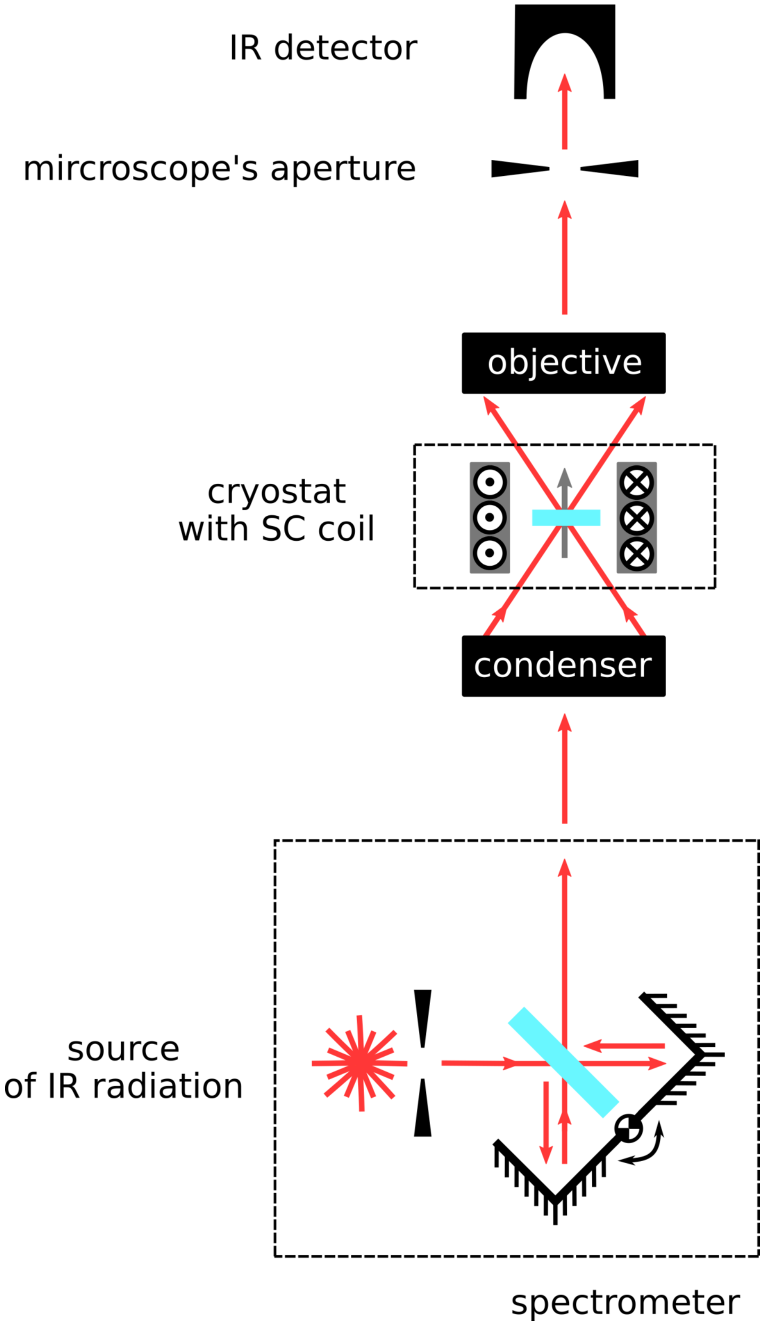

Figure 4.4 – Measurement of magneto-optical transmission spectra: a reductive overview of the optical path and the key devices. Multiple subsidiary mirrors, optical windows etc are omitted in this scheme. More details in the text.

Figure 4.4 optical path begins with a source which emits non-polarized IR light in a broad range of wavelengths. Its intensity could be varied in discrete steps with the help of an aperture placed in front of the source. Rays of light are directed into a Michelson-type interferometer where they impinge onto a beamsplitter. Some part of the light is transmitted and impinges on a corner reflector (the one at the right side in Figure 4.4). Meanwhile some part of the light is redirected by the beamsplitter to another corner reflector (the one at the bottom in Figure 4.4). Next, both portions of light turn back to the beamsplitter, the first portion is reflected while the second portion is transmitted by the beamsplitter and finally they interfere with one another. Both corner reflectors and the beamsplitter are arranged in so called RockSolid configuration [216]: the corner reflectors are permanently fixed relative to one another and can revolve as a single whole relative to the immobile beamsplitter. During such rocking motion, optical path length of each beam changes with time. Optical path difference of the two beams is defined by geometry of the setup and ever changing position x of the corner reflectors relative to the beamsplitter[1]. Thus a beam with time-dependent intensity is created at the exit from the interferometer.

This beam is directed into the microscope equipped with two identical Cassegrain reflectors: a condenser and an objective. The cryostat with the SC electromagnet inside is squeezed in between the two Cassegrains. The electromagnet has toroidal shape with a rectangular cross section. The sample under investigation (light blue in Figure 4.4) is mounted in the center of the electromagnet. Magnetic field produced by the coil (gray arrow in Figure 4.4) is perpendicular to the plane of the sample, signs $\odot$ and $\otimes$ denote the direction of electric current flowing through the depicted cross section of the magnet when the direction of magnetic field is upward. The condenser focuses light on the sample under investigation and its surroundings, and the objective collects all the light which passes through. Next, the microscope's knife-edge aperture defines a rectangular field of view and blocks the rays of IR light streamed by the condenser past the field of view. Finally, the beam of light is guided to an IR detector. The detector registers a signal $s = s(x)$ as a function of mirrors' position x relative to the beamsplitter during many cycles of to and fro motion of the mirrors. Spectrum $S = S(\omega)$ of this signal is calculated as a Fourier transform the interferogram $s(x)$.

Exact shape of the curve $S(\omega)$ depends not only on the sample under investigation but also on the IR light source, IR detector and all the intermediate optical elements: windows, mirrors, apertures etc. If one needs to obtain information about the sample's transmission spectrum $T(\omega)$ then the signal $S(\omega)$ must be normalized one way or the other, see Appendix E. Normalization procedures which we used in this work are valid only when detector's response $s(x)$ or $S(\omega)$ is linearly proportional to the intensity of the impingent light. Such linear regime is achieved when

---

[1] As one can see this way of creating the optical paths difference is a bit different from the one used in the classical scheme of Michelson interferometer where only one mirror is shifted to and fro relative to the beamsplitter.

the detector is illuminated with IR light of reasonably low intensity. Therefore during our measurements we adjusted the amount of the IR radiation coming from the source so that the detector could operate in the linear response regime.

The interferometer, SC coil and IR detector operate under vacuum, each one in a separate box with optical window(s). However the microscope is not airtight and part of the optical path remains exposed to atmospheric gases. Gaseous CO_2 and H_2O have many intense absorption lines in the infrared region. Therefore during the measurements the microscope is continuously purged with pure nitrogen which helps to reduce and stabilize the concentration of atmospheric CO_2 and H_2O in the optical path. Nevertheless, some signatures of these gases may be present in the registered spectra.

The basic principles of FT spectroscopy are universal and hold in a broad range of wavelengths. However not all of the above mentioned optical components can operate across the entire infrared region[2]. Therefore magneto-optical spectra were measured step by step in three narrower regions which we denote the following way: far infrared (FIR), middle infrared (MIR) and near infrared (NIR). Each time the key devices were arranged as depicted in Figure 4.4 meanwhile Table 4.1 summarizes three different sets of optical equipment which we interchanged to enable measurements in each region of wavelengths. The three regions overlap, thus we could verify reproducibility of the spectra, and “stitch” the data together into a more comprehensive picture.

Region / Optical element	FIR 120 – 700 cm^{-1} 0.015 – 0.085 eV 80 – 14.5 μm	MIR 550 – 6000 cm^{-1} 0.07 – 0.75 eV 18 – 1.66 μm	NIR 2500 – 14000 cm^{-1} 0.3 – 1.74 eV 4 – 0.71 μm
Source of IR radiation	globar	globar	tungsten lamp
Beamsplitter	mylar	KBr	quartz
IR detector	bolometer	MCT	MCT
Cryostat windows	PP	ZnSe	CaF_2
Spectrometer window	PE	KBr	KBr

Table 4.1 – Optical equipment which we used in different spectral regions of IR light.

The globar is a silicon carbide rod resistively heated to $\sim$ 1300 K. The NIR source is a tungsten filament light bulb heated to even higher temperatures. Both globar and tungsten lamp produces IR light close to the black-body radiation spec-

---

[2] This problem is actually one of the reasons which fuel graphene research. Graphene is considered to be a promising material for developing detectors, light sources etc which operate in very broad regions of wavelengths, hypothetically from THz to UV [76].

trum. The sensitive element of the bolometer is made of silicon and is cooled with liquid helium during operation. The sensitive element of the MIR detector is made of MCT photoconductor and is cooled with liquid nitrogen during operation. All equipment mentioned in Table 4.1 is commercially available and routinely used in FTIRS, more information about each element could be found in [135, 136].

4.3 Cryostat

The main purpose of our cryostat is cooling the SC magnet down to liquid helium temperatures. We constructed our cryostat around a cold finger from a commercial continuous flow cryostat by Janis “ST-100 Optical cryostat”. While designing our cryostat our prime concerns were the following:

- optimization of geometry, i.e. the cryostat must not block the optical path, must not interfere with the operation of microscope’s optical table;
- minimization of temperature in the cryostat, this allows to profit from better critical field and current of SC wires and produce higher magnetic fields.

When fully assembled, the outer shell of our cryostat consists of four custom-built pieces: a box, a pair of box covers with optical windows, and a tube. These pieces are mounted to the Janis cold finger, see Figures 4.5 and 4.6. The inner shell of the cryostat is a custom-built cold shield which is mounted in the middle of the cold finger. It shields the SC magnet and part of the cold finger from surrounding IR blackbody radiation to improve the cryostat performance at low temperatures. Finally, the SC magnet is mounted to the coldest extremity of the cold finger by means of a connector and the graphene sample under investigation is placed in the middle of the SC coil with the help of a sample holder, see Figure 4.8.

From the outside, the cold finger is equipped with several electric sockets for different purposes: 2 contacts feed current into the SC magnet; 8 contacts for a pair of temperature sensors which monitor the temperature in the cryostat; 2 contacts for a heater installed inside the cold finger; 10 supplementary contacts which could be used for any purpose, for example monitoring magnetic field in the cryostat with a Hall sensor (requires 4 contacts). For practical purposes, we created internal sockets inside the cryostat close to the SC magnet and connected them to the external sockets. Thus one does not have to disassemble the whole cryostat when connecting or disconnecting a sensor.

The whole cryostat has the following dimensions: 106 mm $\times$ 172 mm $\times$ 50 mm and its total weight is 5.1 kg. Thus it is fairly compact and light enough to be compatible with “Hyperion 2000” microscope. The cryostat is mounted to the microscope’s optical table with screws. The top and bottom covers of the outer shell have circular optical windows which allows IR light to pass inside the cryostat and thus measuring the spectra. These windows are placed just above and below the sample under investigation. The thickness of the cryostat in the region around

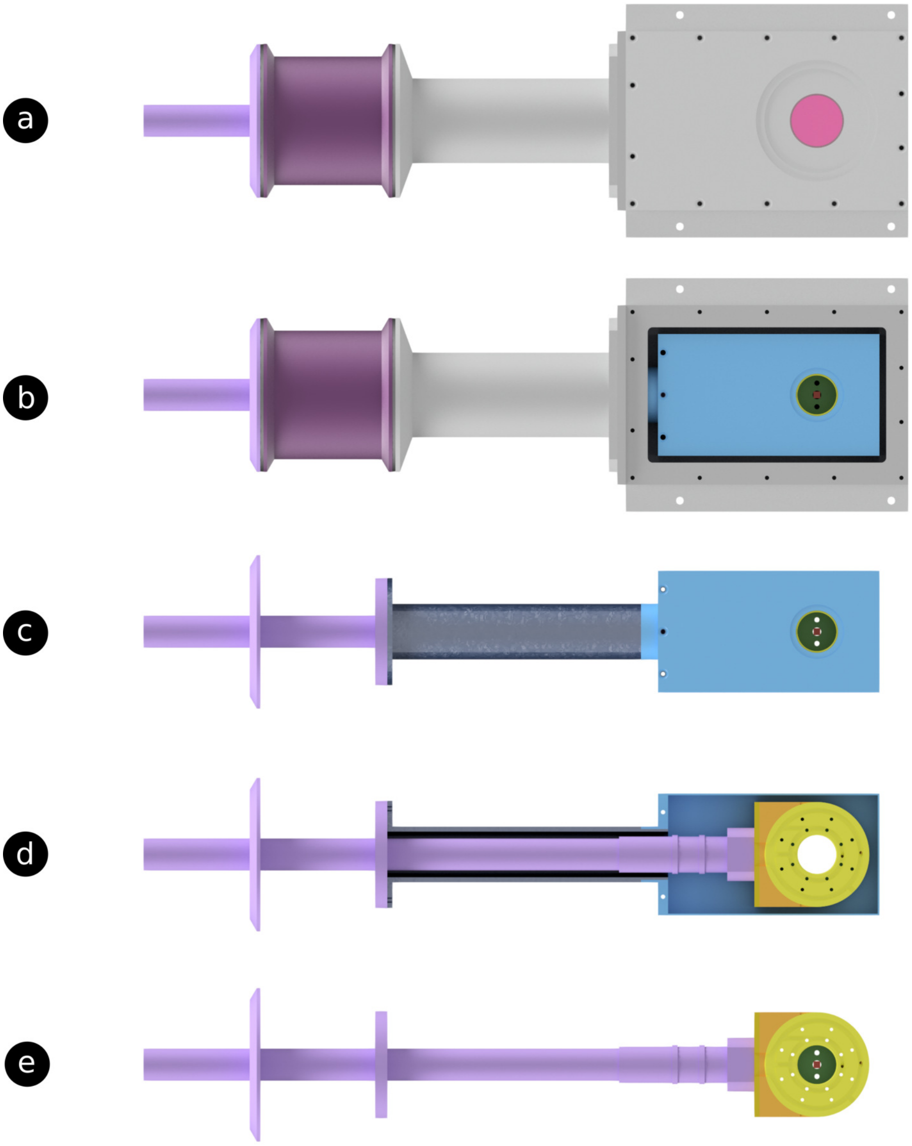

Figure 4.5 – Outer and inner shells of the cryostat. **Panel a:** The cryostat is fully assembled, two parts were taken from the Janis "ST-100 Optical cryostat" (purple and light purple), other parts were designed and manufactured especially for our purposes (gray), an optical window (pink) is glued to the top cover. **Panel b:** The top cover is removed and one can see part of the cold shield (light blue), the sample holder (dark green) and the sample itself (red). **Panel c:** Outer hermetic shell is completely removed, one can see two top parts of the cold shield (dark and light blue). **Panel d:** Both top parts of the cold shield are removed, one can fully see the Janis cold finger (light purple) and the SC magnet (yellow and orange). In this panel the sample holder is also removed. **Panel e:** The cold shield is completely removed, only the cold finger and the SC magnet with the sample holder inside.

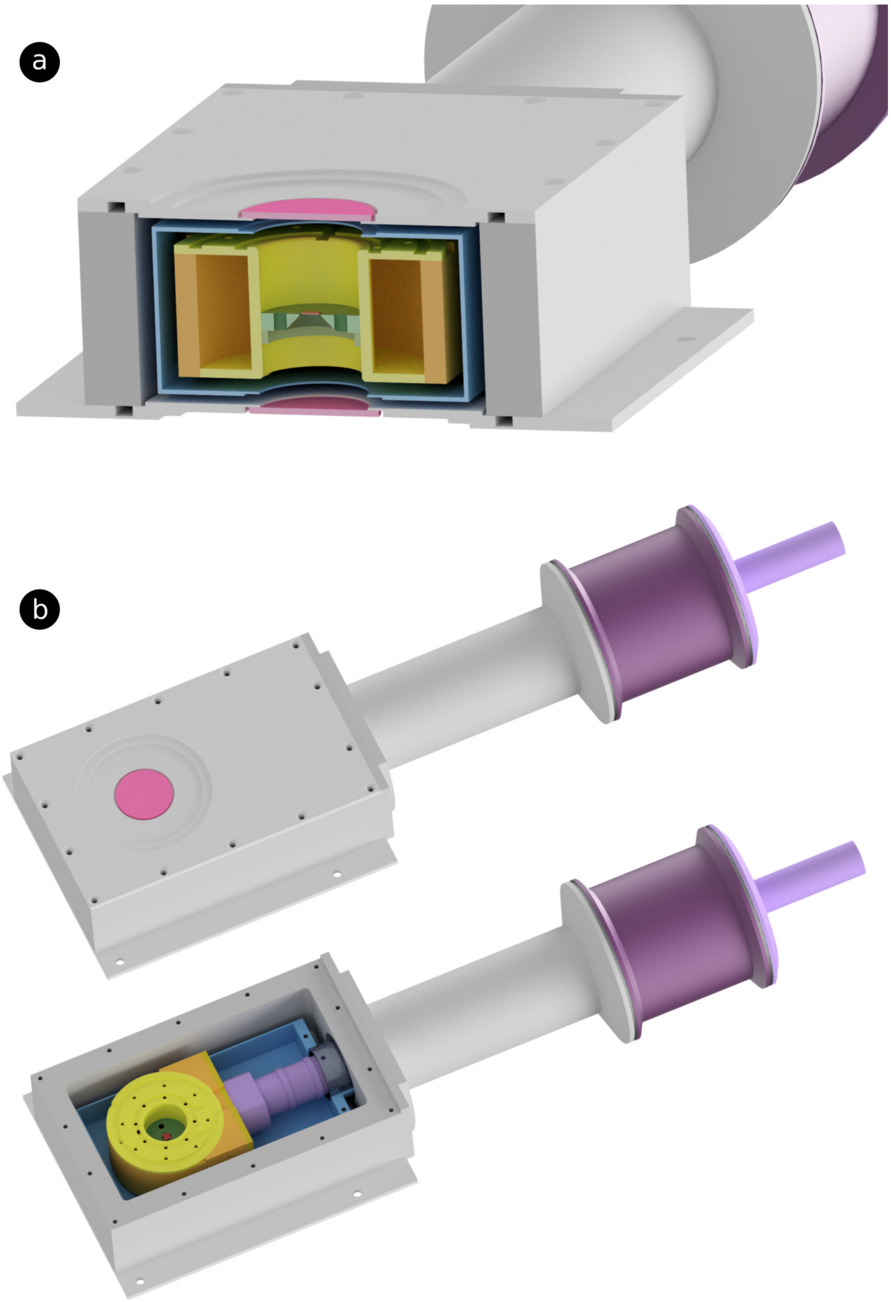

Figure 4.6 – Outer and inner shells of the cryostat. Color code is the same as in Figure 4.5. **Panel a:** Cross section of the fully assembled cryostat along the axis of the magnet. **Panel b:** Closed cryostat and open cryostat with partly assembled cold shield.

the optical windows is 46 mm which is smaller than the above mentioned value owing to the special shape of the covers. This allows placing the cryostat inbetween the optical elements of the microscope which have working distance of 48 mm. We designed a set of interchangeable top and bottom covers which could be easily mounted and unmounted from the cryostat. Each pair of covers has optical windows made of different materials to ensure the best transmission of light in a particular range of wavelengths, see Table 4.1. The strength of magnetic field produced by our magnet drops quickly with the distance from the coil, see Figure 4.11, and does not disrupt the operation of nearby sensitive equipment as IR detectors, the micromotors of the optical table, microscope's video camera, etc.

The SC magnet is cooled with a continuous flow of liquid helium, a pump is required to establish this flow. To achieve the most efficient cooling and lowest possible temperatures in the cryostat we evaporated liquid helium in a forced regime at low pressures of $\sim 0.2 - 0.3$ bar. This allows cooling the system down to ~ 5 Kelvin. During operation the consumption of liquid helium is $1 - 1.5$ liters per hour. Temperatures at the outside surface of the SC magnet and at the coldest extremity of the cold finger were constantly monitored with a pair of sensors. Typically temperature at the cold finger was 3.8 Kelvin and the temperature of the SC magnet was $5.0 - 5.5$ Kelvin.

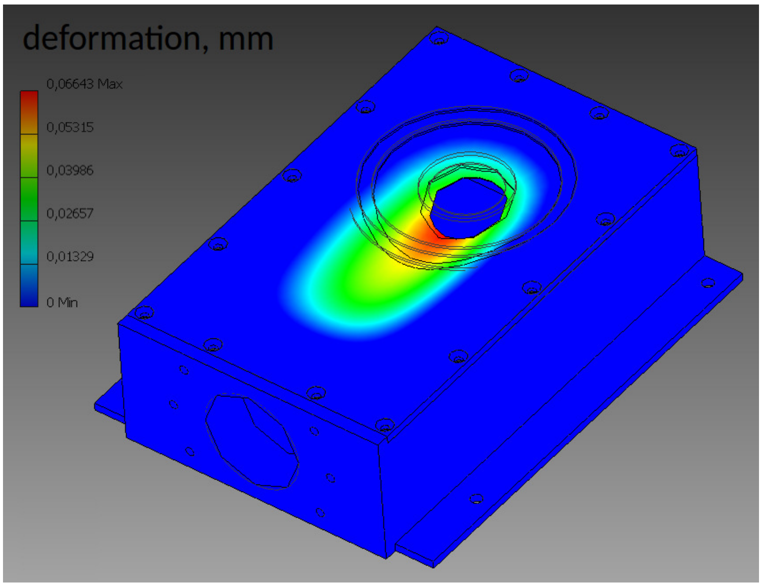

Figure 4.7 – Mechanical deformations which appear in the cryostat under atmospheric pressure when the cryostat is sealed and pumped to vacuum. The deep blue color corresponds to zero deformation and red color corresponds to the maximal displacement of ~ 0.07 mm which occurs in cryostat covers near to the optical windows. This result has been obtained with a help of computer simulation performed with "Inventor" by Autodesk.

The cold shield plays a crucial role in the performance of our cryostat at low temperatures. It consists of four pieces which must be assembled together with the help of screws, see Figure 4.5. Profiles of these pieces were tailored in such a way that the cold shield follows closely the cold finger and the SC magnet. This assures compact dimensions of the setup. To simplify manufacturing, each piece was made of several parts milled separately and then soldered together with silver to ensure a good thermal contact. All pieces of the cold shield are made of oxygen-free high thermal conductivity copper (OFHC) because of the good thermal conductivity and non-magnetic property of this material. We used copper braids to enhance the thermal contact between different pieces of the cold shield. One end of each braid is soldered into a piece mounted to the cold finger and the other end is pressed against the pieces which shield the SC magnet. The surface of the pieces is electroplated with a $\sim 8 - 12\ \mu$m layer of nickel to improve their ability to reflect IR blackbody radiation coming from the outer shell of the cryostat.

As one can see, in our setup the temperatures of the cold finger, SC magnet and graphene crystal are always linked, i.e. they cannot be set or changed independently from one another. When the cold finger reaches its lowest temperature, all fluxes of heat gradually stabilize and there a stationary distribution of temperature forms in the cryostat. We wanted to make this distribution as even as possible across the bulk of the SC magnet and the sample holder. For this purpose all the pieces enclosed by the cold shield were made of a material with high thermal conductivity. We also created a jam nut which presses the sample holder against the SC magnet's spool to ensure a good thermal contact between these pieces. Apart from that, all the above mentioned pieces were gold plated[3] to improve their ability to reflect blackbody radiation coming from the cold shield.

The cryostat operates in vacuum and was constantly pumped during our experiments. Its outer shell is fairly hermetic and withstands atmospheric pressure, see Figure 4.7. All the pieces of the outer shell are milled from aluminum which has been chosen for its non-magnetic nature and lightness. These pieces are sealed with rubber o-rings when the cryostat is assembled together. The inner surfaces of the pieces are smooth which makes degassing quick. We used a turbomolecular pump and achieved $10^{-5} - 10^{-6}$ mbar vacuum when the cold finger was at ~ 5 Kelvin. This base pressure value is measured by a gauge installed in the pump which operates at room temperature. The pressure in the sample compartment of the cryostat is expected to be lower due to the much lower temperature of the cold finger and effect of cryotrapping of gases in the cryostat. When not pumped and at room temperature, the cryostat can keep $10^{-2} - 10^{-3}$ mbar vacuum for many days. For this reason it could be also used as a desiccator for storage or transportation of graphene samples.

---

[3] To improve adhesion of gold, surfaces of the pieces were covered with $\sim 10\ \mu$m nickel-plating before the deposition of gold.

4.4 Superconducting magnet

Our goal was developing a SC magnet specially for IR magneto-optical microspectroscopy. While designing the SC magnet our prime concerns were the following:

- the SC magnet must fit into our cryostat and must not block the optical path of the IR microscope;
- the SC magnet should produce magnetic fields as high as possible in the tight geometry of our cryostat.

We developed a computer simulation of the magnetic field distribution produced by an electric coil. This gave us a better understanding of its critical characteristics such as the maximal magnetic field and current compatible with our SC coil. The simulation also allowed choosing the best suitable SC wire. A description of this simulation is given in Appendix C, in this section we only present some results of the simulation.

We made two SC magnets compatible with our cryostat and the IR microscope. All magneto-optical measurements of graphene spectra were done with the help of our bigger and more powerful SC magnet. Therefore further on in this manuscript expression “SC magnet” would always refer to our bigger SC magnet. Description of our smaller SC magnet is given in Appendix D.

Structure and size

Our SC magnet is made of two coaxial metallic pieces, see Figure 4.8. The inner piece has a shape of a cylindric spool on which loops of SC wire are wound. The outer piece is a casing which protects loops of the SC wire and allows mounting the spool to the cold finger with the help of a connector, see panels d and e of Figure 4.5. The SC magnet has the following dimensions: 62 mm $\times$ 65 mm $\times$ 30 mm. Space dedicated to the loops of SC wire is encompassed by two cylindric surfaces with radii $R_{\text{in}} = 14$ mm and $R_{\text{out}} = 26$ mm and height $H = 26$ mm. As one can see the SC magnet is very compact.

In general an electromagnet coil can produce high magnetic fields if its outer radius R_{out} as well as its height H are big and its inner radius R_{in} is small. However the geometry of our setup is very tight and we had to compromise the dimensions of our SC magnet. Its height was chosen small enough in order to accommodate the working distance of the IR microscope. The objective and condenser are separated only by 48 mm from one another. The SC magnet together with the cold shield, box covers and optical windows of the cryostat had to fit within this space, see Figure 5.1. The inner diameter of the spool was chosen wide enough so that light from the condenser would fully pass to the sample under investigation and would not be blocked by the inner sides of the spool, see Figure 5.2. The outer diameter of the magnet was chosen small enough to avoid deformation of the cold finger under the weight of the magnet and to minimize the heat load on the cold finger.

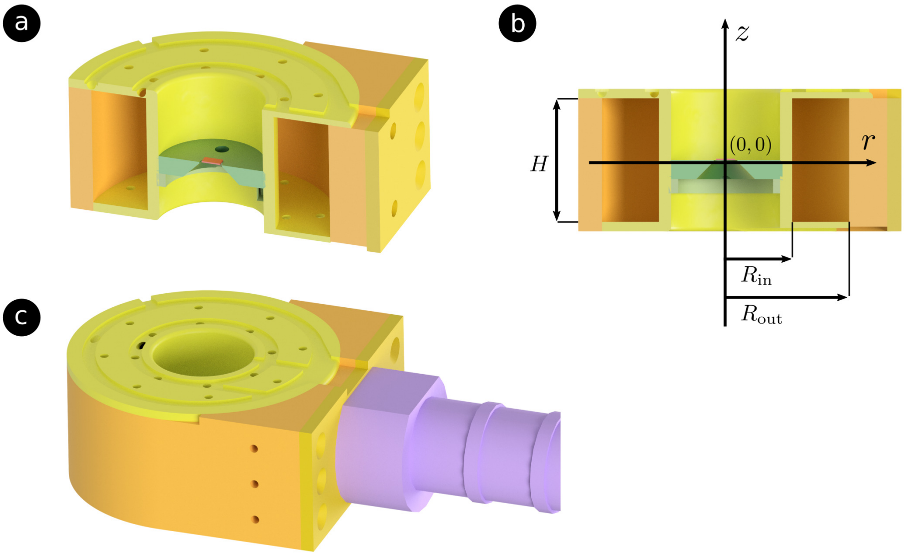

Figure 4.8 – Superconducting magnet. **Panel a:** Cross section of metallic pieces without the SC wires: spool (yellow), casing (orange), connector (dark yellow), sample holder (green), jam nut (light green). **Panel b:** Dimensions of the area occupied by the SC wire. **Panel c:** SC magnet mounted to the cold finger (light purple).

Magnetic field produced by the SC coil

The magnetic field in the sample compartment could be varied continuously from 0 to ± 4.11 Tesla when electric current fed into the SC coil is varied from 0 to ± 19.8 Amperes. These values were verified with a precise magnetic field Hall sensor and are consistent with the values calculated in our magnetic field simulation. The magnetic field distribution inside and around the SC magnet is a complicated function of coordinates $\mathbf{B}(r, z, I)$, here z-axis corresponds to the symmetry axis of the coil, the beginning of coordinates is in the center of the magnet, see Figure 4.8. However the sensor we used does not allow probing magnetic field with high spatial resolution. Therefore all further figures and considerations about magnetic field distribution are based on our computer simulation. Figures 4.9, 4.10, 4.11 and 5.2 show the magnetic field distribution $\mathbf{B}_{\mathrm{max}}(r, z)$ with the highest possible fields produced by our SC magnet i.e. $\mathbf{B}_{\mathrm{max}}(r, z) = \mathbf{B}(r, z, I_{\mathrm{max}})$. For other values of the current I, magnetic field configuration $\mathbf{B}(r, z, I)$ is qualitatively similar: the directions of magnetic induction vector $\mathbf{B}(r, z, I)$ are the same and their absolute values are directly proportional to the current I circulating in the coil: $\mathbf{B}(r, z, I) = I/I_{\mathrm{max}} \cdot \mathbf{B}_{\mathrm{max}}(r, z)$.

A sample under investigation is placed in the center of the magnet. Thus the sample is exposed to the magnetic field $\mathbf{B}(0, 0, I)$ which is a saddle point of the absolute value of magnetic field. The direction of magnetic field is perpendicular to the plane of the sample. Special geometry of the spool allows high homogeneity of

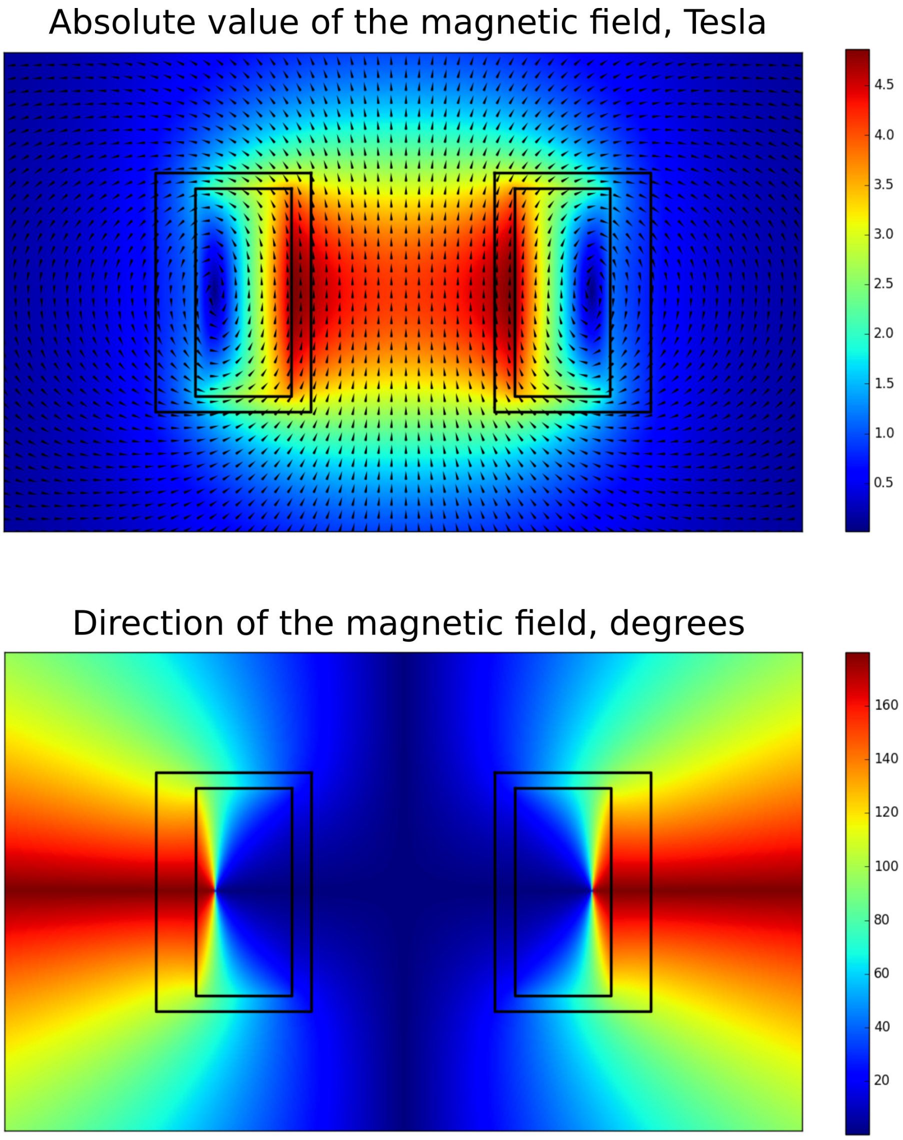

Figure 4.9 – Distribution of magnetic field produced by our SC magnet when $I_{\text{max}} = +19.8$ Ampere current is fed into the coil and the maximal field of $+4.11$ Tesla is achieved in the sample compartment. Black lines show the cross section of the SC magnet: the outer rectangles designates the outline of the magnet and the inner rectangles encompass the area occupied by the SC wire. **Upper panel:** Color shows the absolute value of the highest magnetic field, $|\mathbf{B}_{\text{max}}(r, z)|$, possible to achieved with our SC magnet; arrows show direction of the magnetic field. **Lower panel:** Color shows the angle of magnetic field vector $\mathbf{B}_{\text{max}}(r, z)$ relative to a vertical line in degrees: deep blue corresponds to $0°$ i.e. $\mathbf{B}_{\text{max}}(r, z)$ points upwards; deep red corresponds to $180°$ i.e. $\mathbf{B}_{\text{max}}(r, z)$ points downwards.

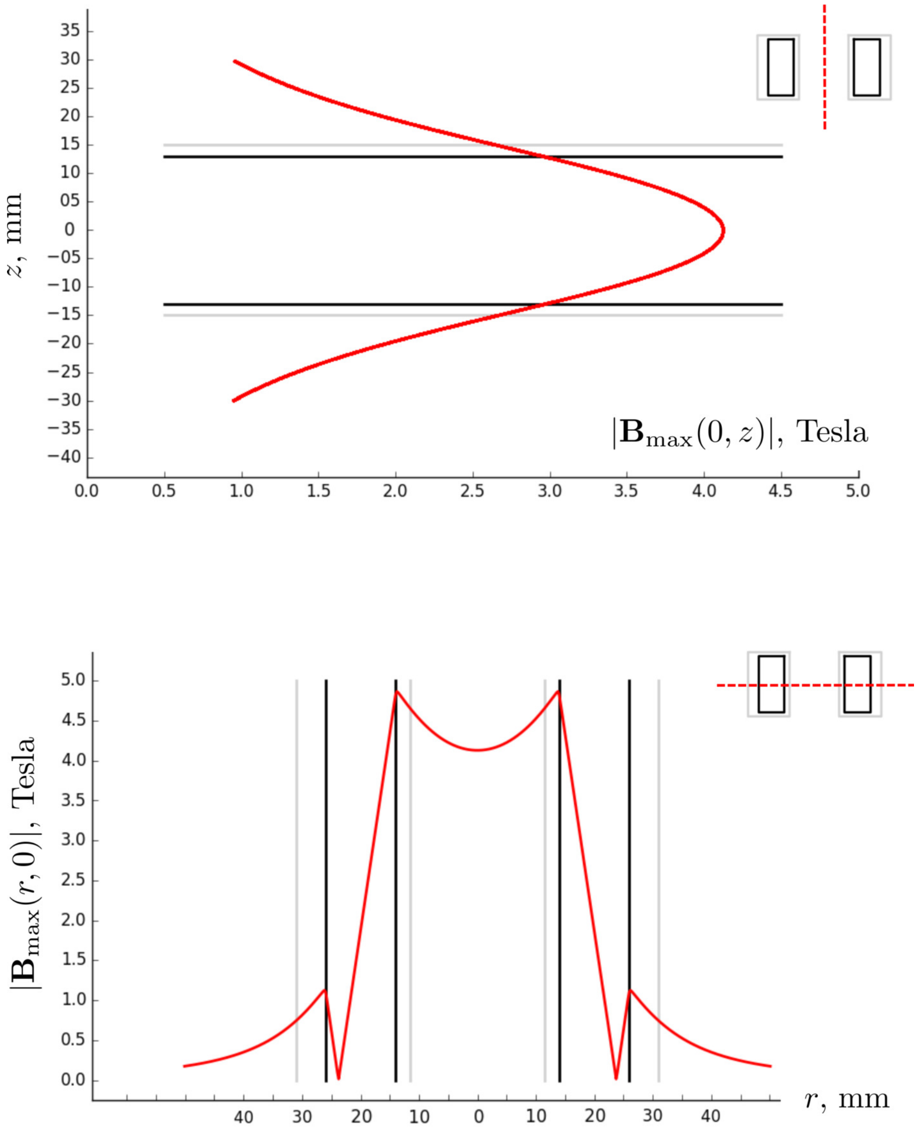

Figure 4.10 – The highest magnetic field possible to achieved with the SC magnet. In the graphs and in the insets, gray lines show the cross section outline of the magnet and black lines encompass the space occupied by the SC wire. **Upper panel:** red curve shows absolute value of the magnetic field $|\mathbf{B}_{\max}(0, z)|$ along the z-axis (symmetry axis of the magnet, designated by a red dotted line in the inset) i.e. above and below the sample under investigation. **Lower panel:** red curve shows absolute value of the magnetic field $|\mathbf{B}_{\max}(r, 0)|$ along the r-axis (designated by red dotted line in the inset) i.e. sideways relative to the sample.

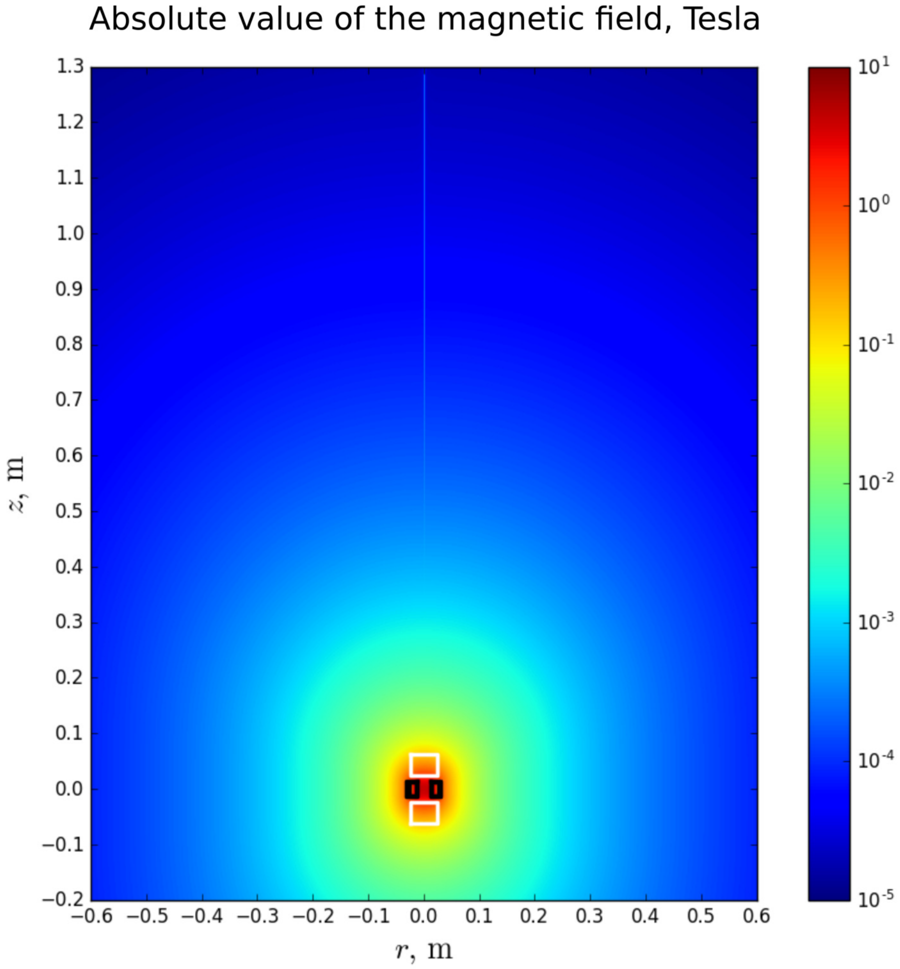

Figure 4.11 – Distribution of magnetic field $|\mathbf{B}_{\text{max}}(r, z)|$ produced by the SC magnet in the vicinity of the cryostat. Black contours designate cross section of the SC magnet, white contours designate cross section of the Cassegrain reflectors mounted on the microscope. The values of magnetic field are color coded in logarithmic scale.

magnetic field in the optically accessible region of the magnet's bore. This is best illustrated in Figures 4.10 and 5.2. According to our simulation, inhomogeneity of the absolute value of magnetic field δ_B takes the following value:

$$\delta_B \equiv (B_1 - B_2)/B_1 = 0.7\%,$$

here B_1 is maximal and B_2 is minimal fields in the entire optically accessible region of the magnet's bore. In practice, inhomogeneity of magnetic field to which a sample under investigation is exposed is much lower. This is due to the fact that our setup has been developed for investigation of small samples which do not occupy the entire optically accessible region. Thus for a $\sim$ 50 μm sample (which is the size of our biggest sample) magnetic field inhomogeneity is only

$$\delta_B < 0.01\%.$$

Magnet quench

Quench is a rapid transition of a SC magnet from superconducting state to the normal resistive state in the case when there is some electric current I in the coil. Energy stored in a SC magnet before a quench is $E = \frac{1}{2}LI^2$, where L is coil's self-inductance. Self-inductance of our coil is estimated to be $L \sim 3$ Henrys [217]. Thus corresponding energy of magnetic field is $E \sim 600$ J for the maximal electric current I_{max} compatible with our magnet. As the SC wire becomes resistive, the energy of magnetic field is rapidly converted into heat which causes an abrupt rise of temperature in the SC magnet. Here are typical situations when quenches occurred in our setup:

- too fast ramp rate of the current fed into the coil;
- unexpected rise of temperature at the cold finger;
- approaching maximal current I_{max} compatible with our SC coil.

The first two problems are easily avoidable if one follows a certain protocol of work with the setup. The third problem is a limitation from which all SC magnets suffer, and in our case quench of the SC magnets occurs in the following way. As one can see in Figures 4.9 and 4.10, the highest magnetic field in our SC magnet is always at the spots in the middle of the coil situated close to its inner side i.e. at the spots with coordinates ($r = R_{\text{in}},\ z = 0$). In particular, for the highest current compatible with our magnet the highest magnetic field is $|\mathbf{B}_{\text{max}}(R_{\text{in}}, 0)| =$ 4.9 Tesla. We make an assumption that temperature is the same across the whole magnet. When one increases the current I fed into the coil beyond I_{max} then the magnetic field increases everywhere in the magnet. As a result parts of the SC wire in the above mentioned spots cannot withstand the new value of current I any longer because it is higher than the critical current $I > I_c$(4.9 Tesla). Thus the above mentioned spots become resistive, next the other parts of the SC magnet heat and also become resistive.

In general, a quench may lead to permanent damage of a SC magnet because of overheating, mechanical strain or inductive voltage spikes caused by a rapid drop of supercurrent. Therefore we avoided quenches as much as possible after we fully installed and tested the SC magnet. In our setup the electric current is switched off automatically when a quench is detected. After a quench, temperature in the magnet does not rise above 30 Kelvin because of a good thermal contact with the cold finger and high thermal conductivity of the spool, casing, and magnet's connector. Additionally, we overlaid loops of the SC wire with thin copper foils to increase thermal conductivity inside the spool. In total, our SC magnet has already survived more than 50 quenches.

Usually unexpected quenches did not pose serious problems during the measurements of spectra: the temperature in the cryostat turns back to 5 Kelvin in ~ 30 minutes after a quench and magneto-optical measurements can be resumed.

Choice of superconducting wire

We used a commercially available SC wire made of niobium-titanium (Nb-Ti) alloy. Nb-Ti alloys are low-T_c type II superconductors with upper critical field $H_{c2} \sim 15$ Tesla and critical temperature $T_c \sim 10$ Kelvin. Nb-Ti wires have been widely utilized already for several decades because they have supremely high values of critical field and critical supercurrent density which allows manufacturing powerful SC magnets.

In the very tight geometry of our setup, the right choice of the SC wire's diameter, D, is very important for maximization of the highest magnetic field produced by the SC coil. Using small diameter wires allows more loops to be wound which is an advantage because each new loop increases the final magnetic field. However in elevated magnetic fields fine wires cannot withstand high currents which leads to a quench of the whole SC magnet. The situation is the other way round for thick SC wires: They can operate at higher currents but it is impossible to wind as many loops as in the case with the fine wires. What makes the choice difficult is that even for a SC magnet with a well fixed geometry there remain interdependent parameters: the wire's critical current depends on the external magnetic field $I_c = I_c(B, D)$, meanwhile this very magnetic field is produced by the SC magnet and depends on the current fed into the above mentioned SC wire $B = B(I, D)$, and both I_c and B depend on the wire's diameter.

We ran the magnetic field simulation for our coil's geometry to choose the best wire among commercially available insulated[4] Nb-Ti and Nb-Sn wires we could find. It turned out to be monofilamentary Nb47%Ti wire in a copper matrix provided by Supercon Inc (product number T48B-M). Its diameter with Formvar

---

[4] In principle SC wires in a copper matrix do not require electric insulation for the loops inside the coil. The insulation is needed only for the parts of the SC wire in contact with the spool and the casing as well as the outside the magnet.

insulation is $D = 203\ \mu$m and bare diameter is $178\ \mu$m, copper to superconductor ratio is $(1.5 \pm 0.2) : 1$.

Table 4.2 summarizes values of the wire's critical currents. The numbers in bold indicate regime around which our SC magnet quenches, more precisely, it quenches at 4.9 Tesla. In our case, "external magnetic field" corresponds to the highest field in the magnet i.e. at the spots in the middle of the coil situated close to its inner side ($r = R_{\text{in}},\ z = 0$). However our SC magnet operates at ~ 5 Kelvin therefore its maximal current I_{max} is somewhat lower than 25 Amperes indicated in the table.

External magnetic field, B, Tesla	3	**5**	7	9
Critical current, I_c, Amperes	40	**25**	15	5

Table 4.2 – Critical current of the SC wire we used in our SC coil as a function of external magnetic field at 4.2 Kelvin. The values are provided by the manufacturer.

Manufacturing of the SC magnet

Both the spool and casing were milled from OFHC copper, a non-magnetic material with high thermal conductivity. After the milling, the pieces were annealed which improved copper's thermal conductivity even further but made the metal softer. Next, both pieces were plated with nickel and then gold.

Further steps of manufacturing are shown in Figure 4.12. SC wire was wound onto the spool with a commercial winding machine "Bobifil". Neighboring layers of loops were mostly arranged in a triangular lattice to achieve the most efficient packing and thus higher density of current. In two places, a layer of loops was overlaid with punctured copper foils to improve thermal conductivity across the magnet. The foils also simplified winding and made arrangement of loops more regular: smooth surface of a foil allowed winding new loops in a perfectly triangular arrangement regardless of previous irregularities of winding which accumulated after many layers of loops.

Then the SC magnet was vacuum impregnated with an epoxy resin to ensure mechanical stability at high magnetic fields. We used a low viscosity epoxy Araldit CY 223 and its reactant hardener Aradur HY 842 by Huntsman Advanced Materials. First, the epoxy was mixed with the hardener and degassed at low pressure, see the panels 9 and 10 of Figure 4.12. Next, a container with the epoxy was placed in the bottom of a vacuum chamber specially created in our group for impregnation of magnets. The spool with SC wire was mounted on a sliding holder just above the epoxy container. Then the vacuum chamber was closed and slowly evacuated. When the lowest pressure was achieved, the spool was plunged into the container and submerged under the surface of the epoxy. Next, compressed air with pressure

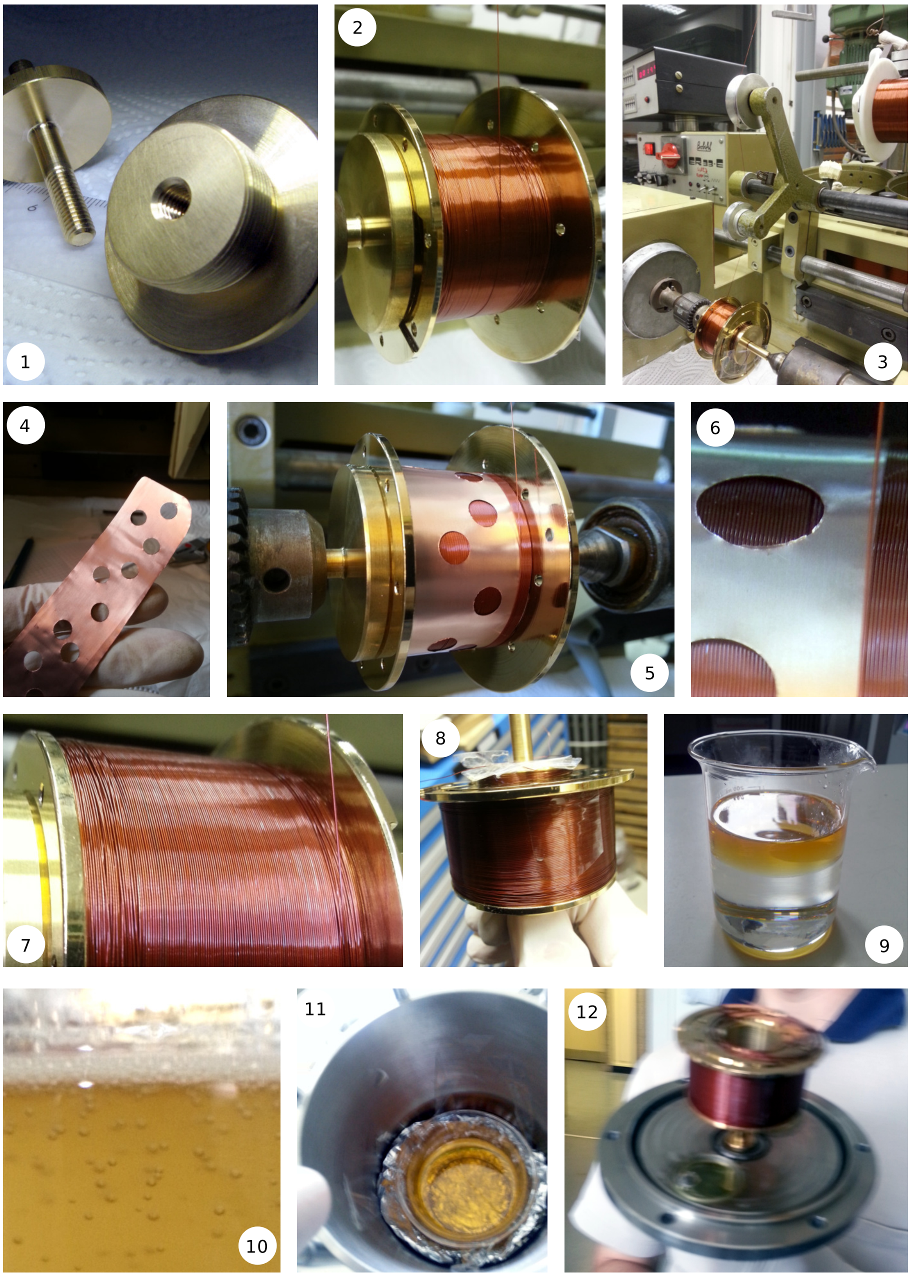

Figure 4.12 – Photographs of superconducting magnet manufacturing. **1:** Pieces for fixation of the spool during winding. **2, 3, and 7:** Winding of the spool. **4:** A punctured copper foil. **5 and 6:** Winding of the SC wire over the copper foils. **8:** Fully wound spool. **9:** Epoxy and its reactant hardener before mixing. **10:** Degassing of the epoxy. **11:** Impregnation chamber. **12:** The spool mounted on a sliding holder at the top cover of the impregnation chamber.

of several atmospheres was allowed into the chamber to push the resin inside the coil. At this stage, little holes provided on the top and bottom surfaces of the spool allowed the epoxy to fill the free space between the loops of SC wire. Next, the spool was removed from the holder, put inside the casing and cleaned from epoxy residues. Finally, the whole SC magnet was dried at a moderate temperature during 24 hours.

Installation and tests

We use a commercial power supply which is designed especially for SC magnets and has an automatic quench protection. Electric current is fed into the cryostat from the power supply via thick copper wires. We wanted to avoid as much as possible both Joules heating of these wires and conduction of the room heat through these wires into the cryostat. Therefore thin high-T_c SC strips made of copper clad YBCO were placed in the middle of the cold finger. One pair of ends of these strips is connected to the resistive copper wires, the other pair of ends is connected to the low-T_c SC Nb-Ti wire of the SC coil. This allowed creating a fully superconducting path starting from the middle of the cold finger right to the SC magnet and we avoid excessive heating inside the cryostat when high currents of ~ 20 Amperes are sent into the coil.

During the tests the magnetic field in the sample compartment of the SC magnet was monitored with a packaged cryogenic Hall effect sensor, model HSP-T, by Cryomagnetics Inc. The SC magnet was "trained" with a dozen quenches to improve it's critical characteristics. The magnetic field in the sample compartment was calibrated as a function of the current fed into the SC magnet: $B = k \cdot I$ where $k = 0.2075$ Tesla/Ampere. After the calibration, magnetic field sensor was removed from the cryostat because it blocked the optical path of the IR microscope. During the magneto-optical measurements values of magnetic field were set and controlled with the current fed into the SC coil. In principle our setup allows constant monitoring of the magnetic field created at the surface of the SC magnet where the sensor does not block the optical path. However we did not use this opportunity.

4.5 Limitations

While designing the experimental setup we had to make some features a priority and compromise other ones. Therefore there are a number of limitations as well as issues which increase errors during the measurement of spectra with our setup.

Temperature in the sample compartment

An important limitation of our setup is that sample's temperature cannot be changed during magneto-optical measurements. The sample holder is always in a thermal contact with the SC magnet which must operate at liquid Helium temperatures.

Heating the sample would directly lead to a quench of the SC magnet. Thus our setup does not allow performing many potentially interesting experiments: for example measuring magneto-optical properties of materials at room temperature and investigating how spectral features depend on temperature.

Temperature measured at the side of the SC magnet is ~ 5 K. Therefore we assume this value to be the *base temperature* of our setup. However real temperature of the samples under investigation could be much higher than the base temperature which is a typical problem when working with small samples.

Mechanical stability of our setup

Mechanical stability of the optical setup is very important for high reproducibility of results and normalization of spectra. Unfortunately, our cryostat does not have efficient passive stabilization (i.e. damping) against vibrations and drifts. Usually cryostats designed for microscopy have such stabilization but it occupies space, moreover it may reduce the effective cooling power of the cryostat. Therefore we compromised stability of the setup to provide more space to the SC magnet and achieve higher magnetic fields.

Sometimes during magneto-optical measurements we observed 1) abrupt random shifts as well as slow drifts of the sample *away* from the axis of the Cassegrain reflectors; 2) high frequency vibrations and slow drifts of the sample *along* the axis of the Cassegrain reflectors. Drifts along the axis were correlated with abrupt changes of the magnetic field. The stability was defined predominantly by the helium evaporation regime at the cold finger and varied a lot on different days of measurements: $\sim 0.1 - 20$ μm per minute.

4.6 Summary and outlook

In the current decade scientific community has been investigating various physical properties of 2D crystals. Experimental setup which is routinely used in the laboratories is not suitable for IR magneto-optical measurements on small 2D crystals produced by scotch-tape exfoliation technique. This is unfortunate because scotch-tape exfoliated 2D crystals often have much superior quality compare to the 2D crystals produced by other methods of synthesis. Therefore we have developed new versatile experimental setup for FTIR magneto-optical microspectroscopy. It comprises an easily portable helium flow cryostat and a compact superconducting electromagnet, see Figures 4.5 and 4.6. Our setup is compatible with existing commercial IR microscopes and FTIR spectrometers, see Appendix B, and thus allows one to measure transmission and reflection spectra of small samples ~ 10 μm in the infrared region of wavelengths. During the measurements a sample under investigation is positioned in the bore of the magnet. Infrared (and visible) light is streamed to the sample and then collected form the sample by a pair of confocal Cassegrain reflectors which make part of the IR microscope, see Figure 5.1. Our setup has been tested with different 2D crystals and in a broad range of wavelengths including the far infrared, middle infrared and near infrared regions. The magnet has already survived many quenches and more than 70 thermal cycles from room temperature to liquid helium temperature.

Here are some new opportunities which our setup made possible when working with small samples: proper normalization of detector's signal without overfilling, measuring the Faraday and Kerr rotation angles, investigating the magnetic circular dichroism, taking pictures and monitoring the sample under investigation during the spectral measurements. At the same time our setup also has some limitations: unfortunately the temperature of the sample under investigation cannot be changed during the magneto-optical measurements. Apart form that mechanical stability of our cryostat is inferior compared to the stability of cryostats specially dedicated to microscopy.

Additional opportunities

While designing the cryostat we also envisaged many opportunities for experiments which have not been tested or presented among the results in this manuscript. Our setup allows one to perform some additional experiments and compliment the magneto-optical data often without unmounting the investigated sample. One can applying gate voltage and perform transport measurements on the sample under investigation simultaneously with the magneto-optical measurements of spectra. Currently 10 contacts could be connected to the sample with the help of a spare socket situated at the side of the cryostat. Wide bore of the magnet allows one using various prefabricated sockets for microscopic electric contacts created on top of the sample which makes handling the sample much more comfortable.

Our cryostat allows one working at magnification higher than $15\times$ in reflection (but not transmission) regime. For this purpose one should use $36\times$ Cassegrain reflector objective from the standard kit of the "Hyperion 2000" IR microscope. This objective has a short working distance of only 10 mm. Therefore the sample under investigation must be mounted closer to the Cassegrain reflector and not in the very center of the magnet's bore. In this configuration the maximal magnetic field to which the sample is exposed equals ~ 2.5 Tesla, see panel a of Figure 5.2. Apart form that, the investigated sample could be also mounted on a skew sample holder in the magnet's bore. This is another useful and interesting configuration for magneto-optical measurements in transmission regime which gives an opportunity to investigate behaviour of the sample in a tilted magnetic field.

As our setup is light and compact it is easily transportable and compatible with many existing optical systems. In particular it could be used at the SLS infrared microscope beamline in the Paul Scherrer Institute (PSI) when standard IR light sources do not produce enough power for a certain experiment with a small sample. Another opportunity is using our setup with a microscope connected to a Raman spectrometer in order to measure magneto-Raman spectra of small samples.

Total weight (cryostat & SC magnet)	5.1 kg
Base temperature in the sample compartment	$\sim$ 5 Kelvin only
Consumption of liquid helium	$1-1.5\,\mathrm{L/h}$
Resistance of the coil at room temperature	$1160\,\Omega$
Resistance of the coil at 5.5 Kelvin	$0.4\,\Omega$
Magnetic field in the sample compartment	from 0 to ±4.1 Tesla
Maximal electric current	19.8 Ampere
Magnetic field inhomogeneity in the optically accessible region of the magnet's bore	0.7 %
Microscope magnification	$15\times$
Numerical aperture	0.4
Angles of incidence of IR light	$12.0^\circ - 23.6^\circ$
Field of view due to the Cassegrain reflectors	1.2 mm
Total field of view allowed by the cryostat	4 mm
Depth of view allowed by the cryostat	$\lesssim$ 2 mm

Table 4.3 – Main characteristics of our experimental setup. Optical characteristics are defined by the "Hyperion 2000" IR microscope (Bruker). For more information about the spectral range see Table 4.1 presented in Section 4.2.

Chapter 5

Measurement protocols

5.1 Relative magneto-optical transmission

The goal of this experiment is to investigate how the magneto-optical transmission of a hBN/Gr/hBN membrane depends on the of external magnetic field B in a broad range of wavelengths. In general, the transmission spectrum of a hBN/Gr/hBN membrane is similar to the transmission spectrum of bare pure graphene. However there are some important differences which are discussed in Sections 3.1 and 6.2.

To enable measurements on our small membranes, we used an IR microscope with two identical Cassegrain reflectors, see Appendix B. The reflectors provide a 15 fold magnification which is reasonable values for our purposes. During the measurements our setup is arranged in such a way that optical axes of both reflectors are perpendicular to the hBN/Gr/hBN membrane, coincide with each other as well as with the symmetry axis of the SC magnet and direction of magnetic field to which the membrane is exposed, see Figures 5.1 and 5.2. The condenser focuses the incoming IR light on the membrane, the objective collects outgoing light transmitted through the membrane and redirects it further to the IR detector. Rays of IR light impinge on the membrane at different angles of incidence determined by the structure of the condenser. In our case, these are all angles between 12.0° and 23.6°.

Our IR light source is extended in space, i.e. it is not a point-like source. Cassegrain reflectors are imaging optical elements and illuminate with IR light the entire 1.2 mm field of view which includes both hBN/Gr/hBN membrane and some part of the Si/SiN$_x$ substrate, see Figure 5.3. Our samples are much smaller than the total field of view, therefore we have to ensure that the resulting beam which arrives to the detector does not contain any spectral signatures of the substrate. For this reason the scaffolding has metallic coating which reflects the light back. In addition, we can adjust the position of microscope's knife-edge aperture, see Figure 4.4, to reduce the size to the field of view.

As it has been already mentioned, the resulting signal on the IR detector de-

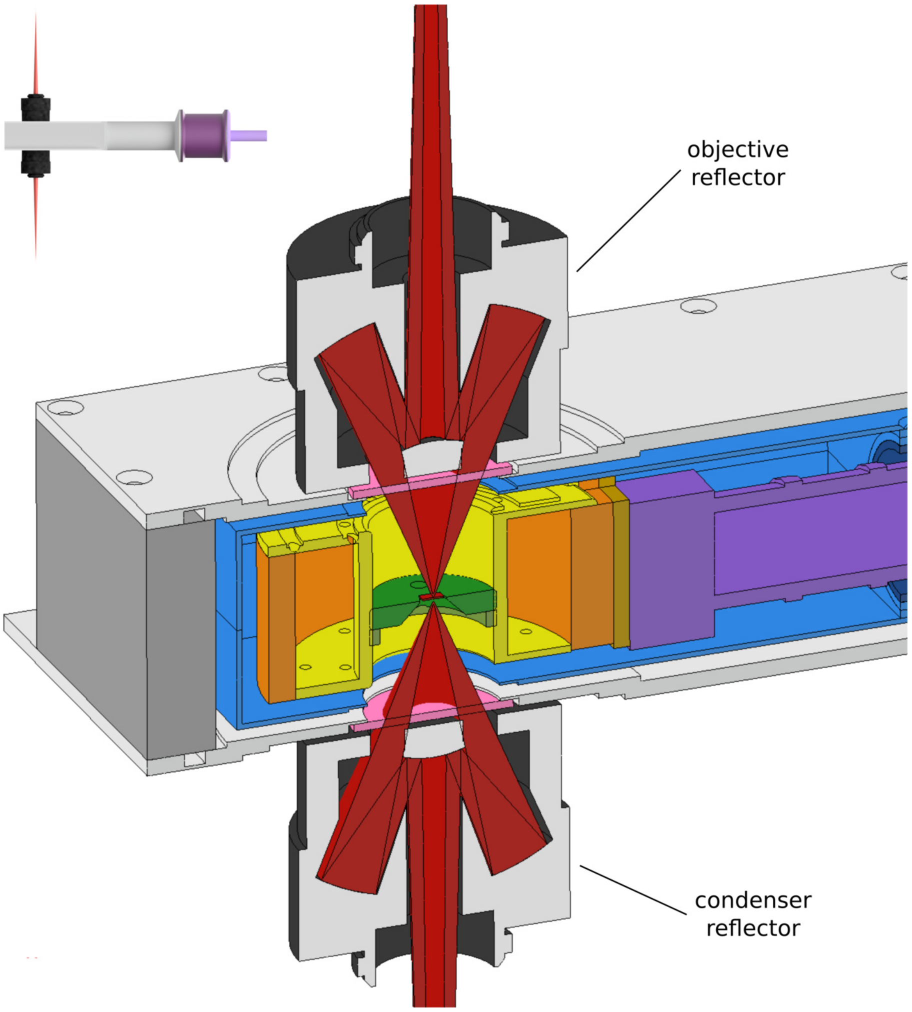

Figure 5.1 – Cross section of the cryostat, the SC magnet and the Cassegrain reflectors during measurement of magneto-optical transmission. Color code is the same as in Figures 4.5 and 4.8. The two Cassegrain reflectors (black/gray) have the same structure and shape: each one has two spherical mirrors which redirect, stream, and focus IR light (red), see also Appendix B. Condenser focuses IR light on the sample under investigation (little red square) and objective collects the IR light transmitted through an optical window (pink) and redirects it further to the IR detector. The distance between the two reflectors is 48 mm. In this illustration only rays from a point-like source are shown to better clarify the optical path in the reflectors. In reality our IR light source is extended in space therefore the whole sample is illuminated with IR light. Inset in the upper left conner demonstrates full focal length of the Cassegrain reflectors.

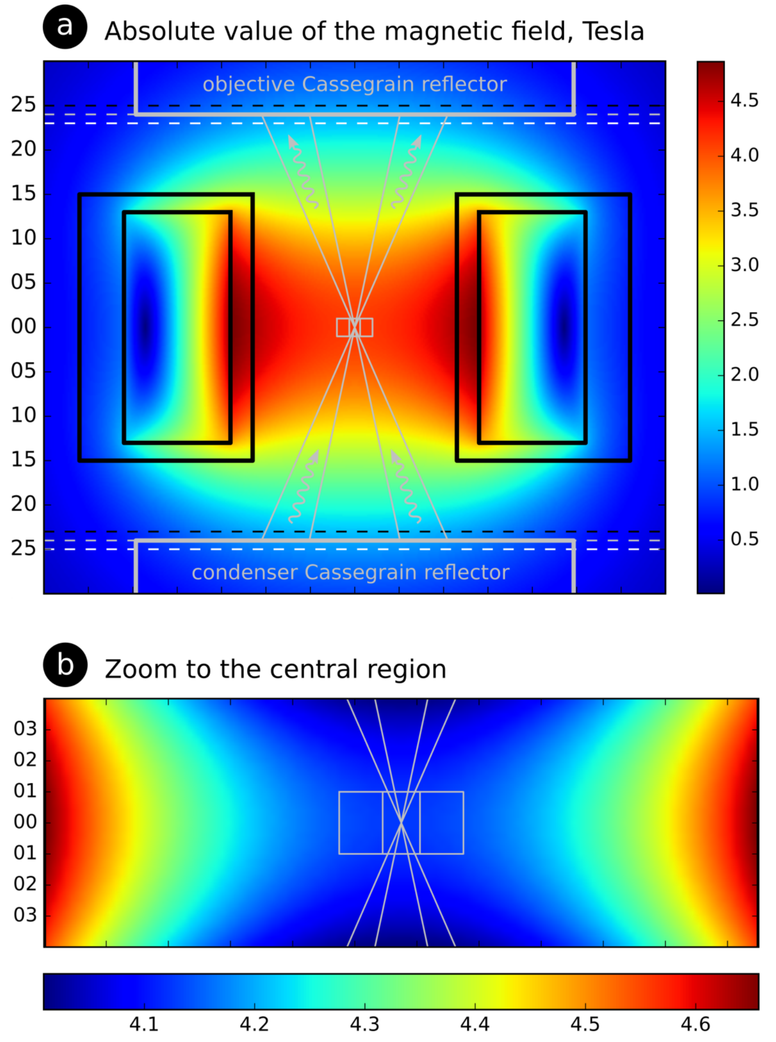

Figure 5.2 – Scheme of the optical path during measurement of magneto-optical transmission superimposed on the magnetic field distribution $|\mathbf{B}_{\text{max}}(r,z)|$ around the SC magnet. In both panels vertical scales on the left show the distance from the center of the magnet in mm. The two panels have different color code for the magnetic field. **Panel a:** Black solid lines show the cross section of the SC magnet; gray solid lines and wavy arrows show the cross section of incoming and outgoing IR light cones; horizontal dashed lines show the margins where the cryostat with the SC magnet could be moved up or down relative to the Cassegrain reflectors; thee gray rectangles in the center of the SC magnet show the optically accessible region of the magnet's bore. **Panel b:** Zoom to the optically accessible region of the magnet's bore. The central gray rectangle is the field of view of the reflectors (1.2 mm); right are left gray rectangles are the regions which become optically accessible when the cryostat is moved horizontally left or right correspondingly. The hight of the optically accessible region is defined by opportunity of moving the cryostat up or down.

pends on many factors unrelated to the properties of the investigated sample. Therefore this signal must be normalized, i.e. compared to a reference signal, so that information about optical properties of the hBN/Gr/hBN membrane could be extracted. Discussion about the different ways of signal normalization is given in Appendix E. In this work, we compared transmission signals of the membrane $S_{\mathrm{SUI}}(\omega, B)$ measured at zero and nonzero magnetic fields, see Figure 5.3. This allowed us to identify *relative* transmission $\widetilde{T}(\omega, B)$ of the hBN/Gr/hBN sample:

$$\widetilde{T}(\omega, B) = S_{\mathrm{SUI}}(\omega, B)/S_{\mathrm{SUI}}(\omega, B = 0). \tag{5.1}$$

Thus $\widetilde{T}(\omega, B)$ yields information about the hBN/Gr/hBN membrane regardless of the other components of the experimental setup. Now transmission spectra of the membrane $T(\omega, B)$ could be easily found provided its transmission spectrum $T(\omega, B = 0)$ at zero magnetic field is known from other experiments or theoretical calculations:

$$T(\omega, B) = T(\omega, B = 0) \cdot \widetilde{T}(\omega, B). \tag{5.2}$$

In any case, relative transmission $\widetilde{T}(\omega, B)$ is an observable quantity of itself and it provides important information about magneto-optical properties of graphene through the equation (5.2).

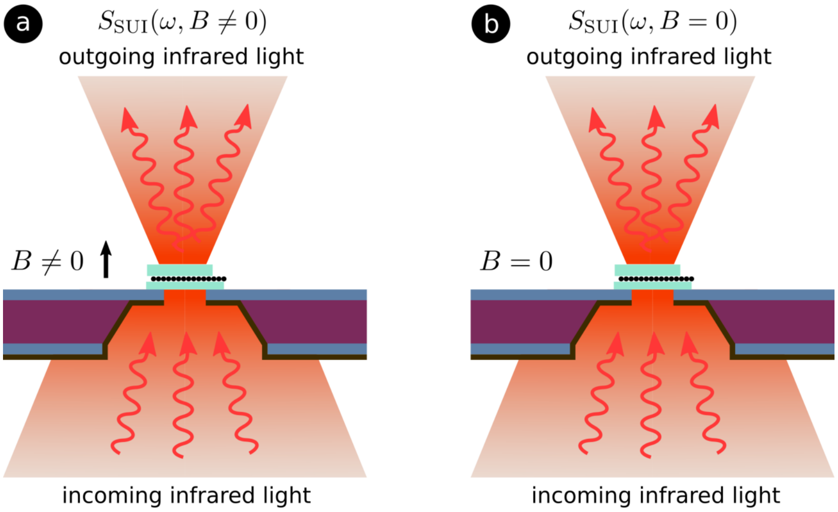

Figure 5.3 – Cross section of hBN/Gr/hBN membrane during measurement of magneto-optical transmission. Metallic coating at the lower side of the scaffolding blocks the IR light which bypasses the sample under investigation. We compared the spectra measured at zero and nonzero magnetic fields to normalize the detector's signal. The scheme is not to scale, the color code is the same as in the previous figures including Figure 3.4.

Measuring IR spectra of small samples of $20 - 50$ μm in diameter is difficult even with an IR microscope because size of these samples is comparable with the wavelength of IR radiation. An approximation of geometrical optics is not valid on this scale and IR light does not come in sharp focus but rather forms broad light spots of complicated shapes depending on the fine adjustment of the optical elements. These diffraction patterns should not pose problems if signal normalization (5.1) is done properly: both signals $S_{\mathrm{SUI}}(\omega, B)$ and $S_{\mathrm{SUI}}(\omega, 0)$ must be measured in exactly the same position of the sample relative to the Cassegrain reflectors. There is a more serious issue related to the diffraction limit: IR light transmitted through the $\mathrm{SiN_x}$ hole with the membrane diverges in all directions in the upper half-plane. The objective collects only some portion of this outgoing light thus resulting signal measured by the IR detector is low and noisy. Naturally, effects of diffraction are more pronounced in the FIR region than in the MIR region. For this reason we could not measure transmission spectra of our smaller 20 μm and 30 μm samples in the FIR region.

As one can see in Figures 5.1 and 4.2, in our setup all optical elements of the microscope remain outside the cryostat. This arrangement gives a number of advantages. Firstly, optical elements always remain at room temperature and do not shift or change their shape because of thermal contraction. Secondly, one can use all the functionality offered by a commercial IR microscope just during the operation of the SC magnet without any need of opening the cryostat and unmounting the investigated sample. Our IR microscope allows using a knife-edge aperture; quick switching between transmission and reflection modes[1]; working with IR light, visible light or both simultaneously (visible light follows the optical path of IR light in the Cassegrain reflectors), see Appendix B. All optical windows of the cryostat are quite transparent in the visible region of wavelengths. This allowed us constant monitoring the sample with a camera or microscope's binocular and taking pictures of the sample in real time during magneto-optical measurements.

5.2 Faraday rotation angle and magnetic circular dichroism

Right-handed and left-handed circularly polarized waves are a convenient basis to describe magneto-optical phenomena in graphene. However performing experiments with circularly polarized light is challenging from technical point of view because currently it is difficult to generate circularly polarized light in a broad range of frequencies. An alternative approach is investigating how graphene behaves when illuminated with linearly polarized light which could be easily generated for example with the help of a broad band linear polarizer. Such magneto-optical experiments do not always yield physical quantities with straightforward interpretations because the Faraday rotation effect is always accompanied by mag-

---

[1] In reflection mode the sample is illuminated and observed from above, see Appendix B.

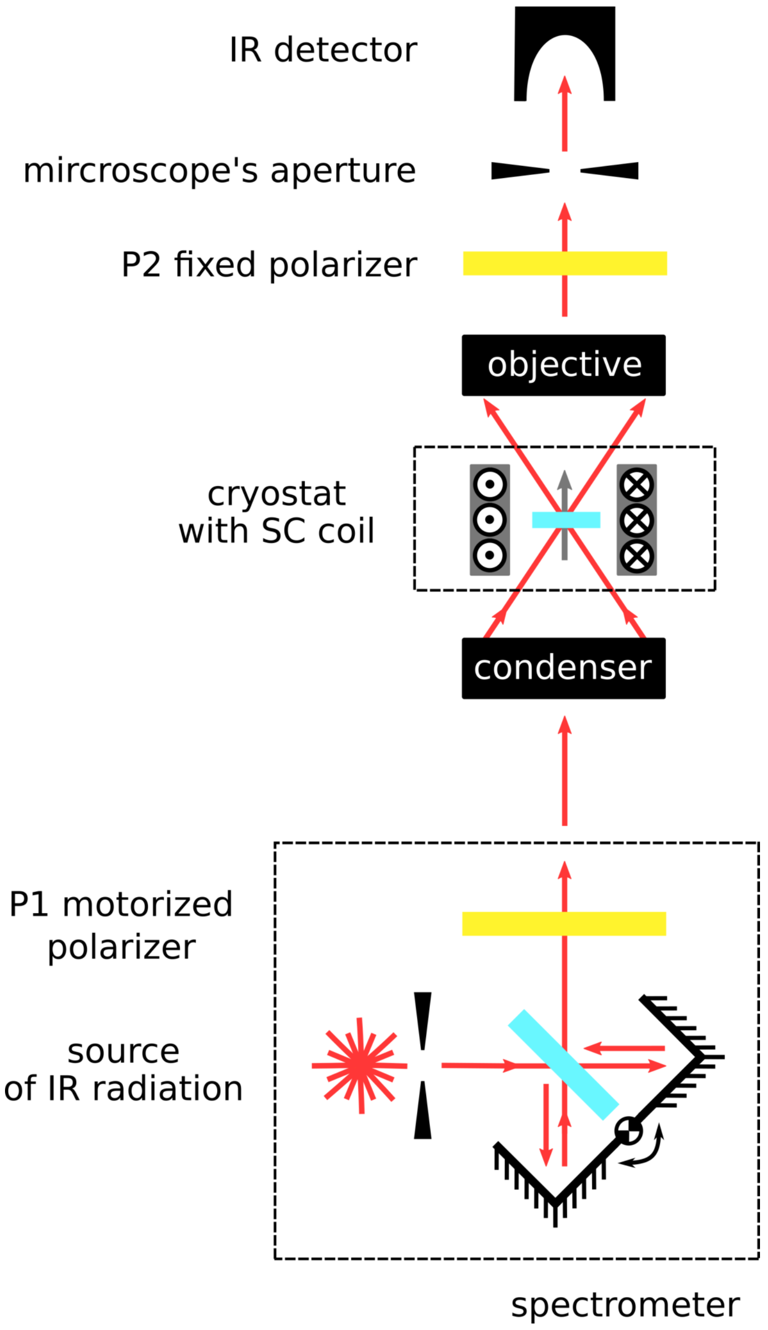

Figure 5.4 – Measurement of Faraday rotation angle: schematic overview of the optical path and key devices. Essentially it is the same scheme as for measurement of transmission but supplemented with two linear polarizers, compare to Figure 4.4. More details in the text.

netic circular dichroism. Nevertheless, signatures of the two effects could be told apart from each other with some minimal assumptions about the nature of the samples under inversion. Thus the goal of this experiment is finding Faraday rotation of a hBN/Gr/hBN membrane at some nonzero values of external magnetic field B in a broad range of wavelengths, i.e. finding $\theta_F = \theta_F(\omega, B)$ curve. Magneto-optical effects are very weak in hBN, apart from that hBN flakes are very thin. As a result of both these circumstances, $\theta_F(\omega, B)$ is very close to the Faraday rotation of bare pure graphene, the differences are discussed in Section 6.3.

Optical path

We used a classical straightforward approach to measure the Faraday rotation angle: our experimental setup for measurements of transmission spectra, see Figure 4.4, was supplemented with two broad range IR linear polarizers, see Figure 5.4. The first polarizer (P1) was mounted inside the spectrometer on the optical path between the source of IR radiation and the sample under investigation to ensure that the light which impinges on the sample is linearly polarized. The second polarizer (P2) was mounted inside a specially dedicated slot of the IR microscope on the optical path between the sample and the IR detector. Table 5.1 summarizes information about two pairs of polarizers which we used to enable measurements in the MIR and FIR regions of wavelengths. Both FIR polarizers were made of free-standing wire grid gold membranes, both MIR polarizers were made of grid metallic coating supported by a KRS-5 substrate.

In our experiments, P1 could be oriented at any angle with a help of a high precision rotation stage with a stepper motor (NR360S by Thorlabs), resolution and precision of positioning $< 1''$. Meanwhile P2 could be rotated manually with a help of gear wheels which gave much worse precision and reproducibility of positioning of $\sim \pm 2°$. Therefore during one series of measurements, P2 always remained in the same orientation and P1 was rotated in order to investigate how the signal at the IR detector changes with the magnetic field B and the angle α between the polarizers' axes.

Region Polarizer	FIR 120 – 700 cm^{-1} 0.015 – 0.085 eV 80 – 14.5 μm	MIR 550 – 5000 cm^{-1} 0.07 – 0.62 eV 18 – 2.0 μm
P1 (motorized)	free-standing gold	Al on KRS-5
P2 (fixed)	free-standing gold	Al on KRS-5

Table 5.1 – Wire gird linear polarizers which we used in different regions of IR light.

Signal at the detector

Both graphene and hBN have uniaxial symmetry. Therefore the exact orientation of the P1 axis relative to the hBN/Gr/hBN stack should not have any influence on the polarization and spectral composition of light transmitted through the hBN/Gr/hBN stack. Consequently, it is not the exact orientations of P1 and P2 axes but the angle α between their axes which matters. Validity of this assumption is discussed in Section 5.4. Propagation of light all the way from the IR source to the IR detector is described in full details in Appendix E, here we only give the final result for the signal registered at the IR detector:

$$S(\omega, \alpha, B) = \kappa(\omega, \alpha) \cdot T(\omega, B) \left[\frac{1}{2} + \frac{\sqrt{D(\omega, B)}}{1 + D(\omega, B)} \cos\left[2\alpha - 2\varphi(\omega, B)\right] \right],$$

$$D(\omega, B) \equiv T_-(\omega, B)/T_+(\omega, B). \tag{5.3}$$

Here $T(\omega, B)$ is transmission of the hBN/Gr/hBN membrane for linearly polarized light. In our case, the transmission $T(\omega, B)$ is the same as membrane's transmission for unpolarized light measured in the previous section because we work at nearly normal incidence of light and our sample has uniaxial symmetry. Next, $D(\omega, B)$ is transmission circular dichroism ratio defined with transmission $T_-(\omega, B)$ of left-handed and transmission $T_+(\omega, B)$ of right-handed circularly polarized light. Angle $\varphi(\omega, B)$ is a change of polarization after the light passes through the hBN/Gr/hBN membrane. It coincides with the Faraday rotation angle up to the sign i.e. $\varphi(\omega, B) = \pm\theta_F(\omega, B)$. Such uncertainty in the sign is related to the fact that light undergoes full handedness inversion after each reflection from multiple subsidiary mirrors on its optical path. The sign of $\theta_F(\omega, B)$ should be found in a separate procedure described below. Finally, $\kappa(\omega, \alpha)$ is a coefficient determined by the spectrum of the IR source, all intermediate elements in the optical path between the source and the IR detector (apart from the sample under investigation), and sensitivity of the IR detector to different frequencies of light. In our experimental setup $\kappa(\omega, \alpha)$ does not depend on B because magnetic field does not alter the performance of any optical elements. However we assume that $\kappa(\omega, \alpha)$ may have some dependence on the orientation of the polarizers P1 and P2 because of their spatial imperfections.

Light transmitted through the sample under investigation is elliptically polarized, the major axis of the ellipse traced by its electric field component is tilted by φ relative to the P1 axis. Thus formula (5.3) has a simple geometrical interpretation: The signal at the detector is maximized when $\alpha = \varphi$ i.e. when axis of P2 is oriented the same way as the major axis of the above mentioned ellipse. In addition, when circular dichroism is negligible then $D \approx 1$ and formula (5.3) takes the familiar form of the Malus law:

$$S(\omega, \alpha, B) = \kappa(\omega, \alpha) \cdot T(\omega, B) \cos^2\left[\alpha - \varphi(\omega, B)\right]. \tag{5.4}$$

Extracting magneto-optical quantities

According to the most rigorous approach, in order to find the Faraday rotation at one value of magnetic field, P1 must be given a full rotation by small equidistant steps. At each step, one must register the transmission spectra and also some reference spectra in order to normalize the signal of the above mentioned transmission spectra. In the end, the angle $\varphi = \varphi(\omega, B)$, dichroism $D = D(\omega, B)$, and possibly[2] even transmission $T = T(\omega, B)$ of hBN/Gr/hBN stack could be found from a set of normalized signals (5.3) measured at different α, see Appendix E. A great disadvantage of such approach is that it is very time consuming because the signal must be measured for many angles. Therefore we had to pick out only a few angles α at which the signal was registered.

We followed a traditional scheme and measured the Faraday rotation with polarizers oriented at $\alpha = \pi/4$ relative to each other. Such orientation gives a lot of advantages when the unknown Faraday rotation angle is reasonably small $|\theta_F(\omega, B)| \leq \pi/8$. Firstly, when $(\pi/4 - \pi/8) < (\alpha - \varphi) < (\pi/4 + \pi/8)$ the intensity of transmitted light is much higher compared to the configuration when the polarizers are crossed[3] i.e. $(\pi/2 - \pi/8) < (\alpha - \varphi) < (\pi/2 + \pi/8)$. Therefore one has a good signal to noise ratio at the detector. Secondly, when $\alpha - \varphi = \pi/4$ the signals in (5.3) and (5.4) have the steepest descent in φ. Thus even a slight deviation of $(\alpha - \varphi)$ from $\pi/4$ due to nonzero Faraday rotation in the sample would lead to a big change of the signal which allows high precision measurements of φ. The same argumentation and advantages also hold for the configuration with the angle $\alpha = -\pi/4$.

Coefficients $\kappa(\omega, \alpha)$ and transmission of hBN/Gr/hBN stack $T(\omega, B)$ are considered to be unknown. Therefore the signal given in the formula (5.3) must be normalized i.e. compared to a reference spectrum. In our case the best choice of the reference is a transmission spectrum measured at magnetic field with the same absolute value but opposite direction compared to the spectrum to be normalized. In this normalization procedure, we make reasonable assumptions that when the direction of magnetic field is inverted then transmission of hBN/Gr/hBN stack remains the same i.e. $T(\omega, B) = T(\omega, -B)$, the absolute value of Faraday rotation angle also remains the same and only the sign of the Faraday rotation angle changes to the opposite i.e. $\theta_F(\omega, B) = -\theta_F(\omega, -B)$ and correspondingly $\varphi(\omega, B) = -\varphi(\omega, -B)$.

Measuring the Faraday rotation for two orientations of the polarizers $\alpha = \pm\pi/4$ and taking the average of the two results allows reducing systematic errors caused by parasitic depolarization of light on the optical path. Thus according to our protocol, we had to measure four spectra in order to investigate Faraday rotation and circular dichroism in a hBN/Gr/hBN stack for one particular absolute

---

[2] It depends on the choice of the optical configuration for the reference spectra.

[3] Configuration of linear polarizers when their axis are crossed i.e. oriented at $\alpha = \pi/2$ is widely used in educational literature to illustrate the phenomenon of Faraday rotation. But such orientation is hardly ever convenient in real experiments.

value of magnetic field. These were transmission spectra $S(\omega, \alpha, B)$ registered by IR detector in the following configurations of polarizers and magnetic field:

- $\alpha = +\pi/4$ and $+B$;
- $\alpha = +\pi/4$ and $-B$;
- $\alpha = -\pi/4$ and $+B$;
- $\alpha = -\pi/4$ and $-B$.

In order to obtain a physical quantity which characterizes the sample under investigation and does not depend on the components of our experimental setup, the four spectra should be combined the following way:

$$\Phi(\omega, B) = \frac{1}{8}\left[\frac{S(\omega, \pi/4, +B)}{S(\omega, \pi/4, -B)} - \frac{S(\omega, -\pi/4, +B)}{S(\omega, -\pi/4, -B)}\right]. \tag{5.5}$$

Indeed, using the formula (5.3) one can see that the coefficients $\kappa(\omega, \pm\pi/4)$ as well as $T(\omega, \pm B)$ cancel out and one obtains

$$\Phi(\omega, B) = \frac{\sqrt{D(\omega, B)}(1 + D(\omega, B)) \sin[2\varphi(\omega, B)]}{(1 + D(\omega, B))^2 - 4D(\omega, B)\sin^2[2\varphi(\omega, B)]}. \tag{5.6}$$

The resulting curve $\Phi(\omega, B)$ yields important information about magneto-optical properties of the hBN/Gr/hBN membrane. However $\Phi(\omega, B)$ does not have a simple and straightforward physical interpretation because it depends in a non-trivial way both on the dichroism ratio $D(\omega, B)$ and the angle $\varphi(\omega, B)$ which is equal to the Faraday rotation angle up to the sign. In a special case when the dichroism is negligible and Faraday rotation angle is small, one may simplify the formula (5.6) using the approximation for small angles which leads to

$$\Phi(\omega, B) = \varphi(\omega, B) \tag{5.7}$$

$$\text{when } D(\omega, B) \approx 1 \text{ and } \sin[2\varphi(\omega, B)] \approx 2\varphi(\omega, B),$$

and one can see that the curve $\Phi(\omega, B)$ coincides with the Faraday rotation angle as usual up to a sign. This gives a better insight into the physical meaning of the $\Phi(\omega, B)$ curve, discussion of the errors induced by the approximation (5.7) is given in Section 5.4.

Sign of the Faraday rotation angle

As it has been mentioned in Section 2.3, the definition of the sign of the Faraday rotation angle involves the direction of the magnetic field and the direction of the light propagation. However modifying the experimental setup and measurement protocol in order to meet this definition is not always convenient or even technically feasible. In our case, we are not able to invert the direction of the IR light propagation each time we invert the magnetic field. Moreover, the angle of polarization changes its sign to the opposite one upon each reflection from the multiple subsidiary mirrors which guide the ray of light through our setup. This also alters the sign of $\varphi(\omega, B)$ or $\Phi(\omega, B)$. Here we would like to point out that both $\varphi(\omega, B)$ and $\Phi(\omega, B)$ always have the same sign even if approximation of small angles and negligible dichroism does not hold.

There are two approaches to finding the true sign of the Faraday rotation angle. According to the first approach, one should meticulously count all the mirrors on the optical path, take into account directions of the magnetic field and light propagation at all steps of the measurement protocol. Based on that, one can assess whether the sign of $\varphi(\omega, B)$ coincides with the sign of $\theta_F(\omega, B)$ or should be changed to the opposite one. According to the second approach, one should use a reference sample with known Faraday rotation (or any other type of optical activity) to “calibrate” the experimental setup in the context of a particular Faraday rotation measurement protocol. This means that one should measure the Faraday rotation of the reference sample following the same protocol as with the hBN/Gr/hBN membrane. If the result coincides with the true value of the Faraday rotation in the reference sample then $\theta_F(\omega, B) = \varphi(\omega, B)$ for the hBN/Gr/hBN membrane. If the result has opposite sign compared to the true value of the Faraday rotation in the reference sample then $\theta_F(\omega, B) = -\varphi(\omega, B)$ for the hBN/Gr/hBN membrane.

We followed the second approach. However for practical reasons we used a linear polarizer (P3) as a reference sample instead of a sample which exhibits magneto-optical activity and Faraday rotation. In this case deviation of P3 axis relative to P1 axis imitates the Faraday rotation effect[4]. Such choice of the reference sample gives several advantages: we did not have to apply any magnetic field, all measurements were done at room temperature without the cryostat and we could easily imitate different angles and signs of Faraday rotation in the reference sample simply rotating the P3 axis by hand. During our manipulations P3 was mounted on a rotating stage with a goniometer. Inversion of magnetic field direction was imitated by inversion of the sign of the angle between P3 and P1 axes.

Transmission measurements

Each measurement of Faraday rotation angle was supplemented the same day with a measurement of the relative transmission spectrum of a hBN/Gr/hBN membrane. We did this to ensure that both curves were obtained in the maximally similar conditions: the same doping level of graphene, temperature of hBN/Gr/hBN membrane, magnetic field etc. Transmission measurements were performed with po-

---

[4] In reality a linear polarizer cannot fully imitate magneto-optical activity because the polarizer does not rotate the plane of polarization but rather projects the electric field vector on the P3 axis. Thus in the case of a linear polarizer, apart from the polarization rotation there must be also some attenuation of light described by the Malus law. This attenuation is weak for reasonably small angles ($\sim 10^\circ$) of polarizer rotation i.e. angles between P1 and P3 axes. Therefore we conclude that a linear polarizer could be used as a reference sample and imitate Faraday rotation effect for small angles.

larizers P1 and P2 oriented parallel to each other i.e. for $\alpha = 0$. This orientation allows maximizing the signal and therefore improving the signal-to-noise ratio. Signal normalization was done the same way as in the previous section i.e. with the help of transmission spectrum measured at zero magnetic field, see Appendix E. Thus we obtained a physical quantity $\Theta(\omega, B)$ which characterizes the sample under investigation and does not depend on the components of our experimental setup:

$$\Theta(\omega, B) = \frac{S(\omega, \alpha = 0, B)}{S(\omega, \alpha = 0, B = 0)}. \tag{5.8}$$

We find the detector's signal $S(\omega, \alpha = 0, B = 0)$ using the general formula for the signal (5.3) and taking into account that at zero magnetic field the sample does not show any optical activity i.e. $D(\omega, B = 0) = 1$ and $\varphi(\omega, B = 0) = 0$. Thus we find that

$$\Theta(\omega, B) = \frac{T(\omega, B)}{T(\omega, B = 0)} \cdot \left[\frac{1}{2} + \frac{\sqrt{D(\omega, B)}}{1 + D(\omega, B)} \cos[2\varphi(\omega, B)] \right]. \tag{5.9}$$

The last factor in the formula (5.9) depends on dichroism and Faraday rotation. One may neglect this dependence and assume that the above mentioned factor is equal to one which is a plausible approximation when the dichroism and the Faraday rotation angle are small. Here another advantage of the parallel orientation of the polarizers $\alpha = 0$ becomes clear: values of $\cos[2\varphi(\omega, B)]$ in (5.9) change slowly around zero as the angle $\varphi(\omega, B)$ grows which reduces the error when the Faraday rotation is neglected. In this approximation

$$\Theta(\omega, B) \approx \frac{T(\omega, B)}{T(\omega, B = 0)} = \widetilde{T}(\omega, B) \tag{5.10}$$

$$\text{when } D(\omega, B) \approx 1 \text{ and } \cos[2\varphi(\omega, B)] \approx 1.$$

Thus the spectrum $\Theta(\omega, B)$ coincides with the relative transmission $\widetilde{T}(\omega, B)$ measured in the previous section and errors induced by such approximation are discussed in Section 5.4. On the whole, the formula (5.10) always underestimates the real value of the relative transmission $\widetilde{T}(\omega, B)$.

In the general case, if the dichroism $D(\omega, B)$ and the angle $\varphi(\omega, B)$ are not small, then optical properties of the sample could be restored with the help of Kramers-Kronig constrained fitting of magneto-optical spectra, see Section 6.4. To this purpose, experimental data $\Phi(\omega, B)$ given in the formula (5.6) and experimental data $\Theta(\omega, B)$ given in the formula (5.9) both measured in a broad range of frequencies must be supplemented with information about zero field transmission $T(\omega, B = 0)$ of the sample.

5.3 Verifying linearity of the optical response

In general, the optical response of a material is linearly proportional to the intensity of the incident radiation provided the its intensity is relatively low. Therefore experiments which probe non-linear optical phenomena often involve powerful light sources such as lasers. Different non-linear optical effects have been reported in graphene [218]. The light source (globar) which we used to investigate the Landau level transitions in graphene is usually not powerful enough to observe the onset of the non-linear phenomena in the semimetals and semiconductors [219]. However in order to have more ample information about our samples, we verified whether the linearity holds in the MIR region for the range of light intensities accessible with our setup. We estimate the upper limit of intensity to which graphene was exposed as ~ 1 W/cm^2 (this number stands for sum of intensities of all MIR wavelengths).

Thus the goal of this experiment is comparing magneto-optical transmissivities of a hBN/Gr/hBN stack measured when the stack is illuminated with IR light of different intensities.

We could change the intensity of the IR light impinging on the hBN/Gr/hBN stacks with the help of apertures of different diameter situated in the spectrometer just in front of the IR light source, see Figure 4.4. We measured relative transmissivities $\widetilde{T}_1(\omega, B)$ and $\widetilde{T}_2(\omega, B)$ as described in Section 5.1 for two different intensities of light which we label with the indices "1" and "2". Then we took the ratio between the two transmissivities to verify the linearity of the optical response:

$$L(\omega) = \frac{S_1(\omega, B)/S_1(\omega, B=0)}{S_2(\omega, B)/S_2(\omega, B=0)} = \frac{\widetilde{T}_1(\omega, B)}{\widetilde{T}_2(\omega, B)}. \tag{5.11}$$

$L(\omega) = 1$ corresponds to a perfectly linear response of the sample under investigation. It is important to mention that direct comparison of the signals $S_1(\omega, B)$ and $S_2(\omega, B)$ is inappropriate without normalization by the corresponding zero-field signals. It is related to the fact that the apertures not only modify the total intensity of light but also slightly distort the distribution of energy in the spectrum of light which reaches the IR detector. Our setup allowed measuring relative transmissivity $\widetilde{T}(\omega, B)$ of hBN/Gr/hBN only at three different intensities of incoming light. Here the main limiting factor was related to the MCT infrared detector which we used in the experiments. The detector is not supposed to be illuminated with high intensity IR light. Otherwise the detector itself has a nonlinear response to the impinging radiation, as a result comparison of the signals (5.11) and signal normalization become inadequate.

5.4 Systematic errors

Undesired depolarization of light

Light interacts with many subsidiary optical elements as beamsplitter, mirrors, and anisotropic optical windows on its way from the source to the sample and finally to the IR detector. Subsidiary elements introduce undesired parasitic changes into the polarization stated of light. This phenomenon is called depolarization. Thus during the transmission measurements described in Section 5.1, unpolarized light form the IR source acquires some partial polarization. Such change of polarization state does not pose significant problems for measurements because our samples have uniaxial symmetry. However during the Faraday rotation measurements described in Section 5.2, undesired depolarization may induce systematic errors in the level of signal up to 10% if not handled properly.

To minimize these errors, we pay attention not only to the relative but also to the absolute orientation of the polarizers P1 and P2. Ideally, one expects total attenuation of light when the axes of polarizers are crossed i.e. $\alpha = \pi/2$. However in practice $\alpha = \pi/2$ is not enough to achieve the total attenuation because of the undesired depolarization. Therefore before starting the measurements, we first find a special absolute orientation of P2 at which we observe maximal attenuation of the signal provided P1 is oriented at $\alpha = \pi/2$ relative to P2. Later on P2 always remains fixed during the measurement of Faraday rotation. Presumably, such orientation of P2 corresponds to the axis of the optical element which gives the largest contribution into the depolarization in our setup.

Measuring the Faraday rotation angle at two opposite orientations of the polarizers $\alpha = \pm\pi/4$ as described in Section 5.2 also partially cancels the systematic errors due to the depolarization of light. Performing measurements at two opposite values of magnetic field is especially important for reducing the errors caused by the depolarization in the optical windows of the cryostat. As the optical windows are situated in between the polarizers P1 and P2, their effect on the polarization state of light cannot be easily distinguished from the Faraday rotation in the sample under investigation. We assume that the depolarization effects do not depend on the direction of magnetic field, meanwhile Faraday rotation angle does, therefore systematic errors are partially canceled when Faraday rotation is measured according to the protocol described in Section 5.2.

Approximation of negligible dichroism and small Faraday rotation angle

Here we analyze the errors in the values of Faraday rotation angle and relative transmission when these quantities are found using the approximations 5.7 and 5.10 correspondingly. We define the error δ_φ as difference of between the real value φ and the approximate value Φ of the Faraday rotation angle:

$$\delta_\varphi \equiv \varphi - \Phi,$$

here the value of Φ is given in the the formula (5.6). We define the error δ_T as the ratio between the real value $\widetilde{T}$ and the approximate value Θ of the relative transmission:

$$\delta_T \equiv \Theta/\widetilde{T},$$

thus δ_T coincides with the second factor on the right hand side of the formula (5.9). The values of both errors δ_φ and δ_T are plotted in Figures 5.5, 5.6 and 5.7 in three different scales as functions of transmission dichroism ratio D and real Faraday rotation angle φ.

As one can see, for relatively small values of the dichroism ratio, approximation $\Phi \approx \varphi$ overestimates the absolute value of the Faraday rotation angle. Meanwhile for larger values of the dichroism ratio, approximation $\Phi \approx \varphi$, underestimates the absolute value of the Faraday rotation angle. Generally, as φ deviates from zero, the error δ_φ grows. However there exist special cases in which D and φ combine in such a way that the resulting error δ_φ becomes zero or almost zero despite the real Faraday rotation angle φ is relatively large and D is not negligibly small either. One can also notice that for any values of φ and D, one has $0.5 \leq \delta_T \leq 1$ thus the approximation $\Theta \approx \widetilde{T}$ always underestimates the real value of the relative transmission $\widetilde{T}$. The error δ_T always grows as φ deviates from zero and D deviates from one.

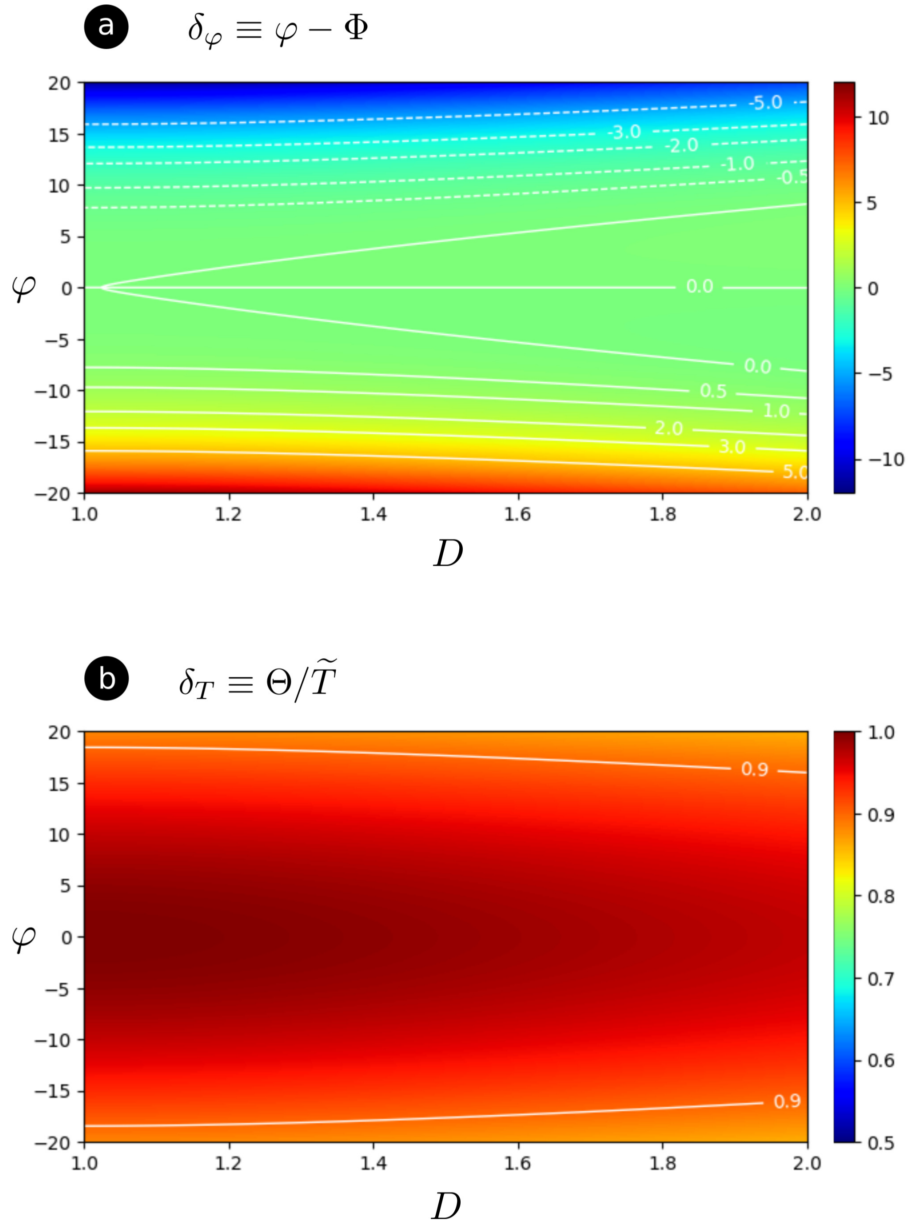

Figure 5.5 – Systematic errors δ_φ and δ_T induced by the approximation of negligible transmission dichroism ratio D and small Faraday rotation angle φ.

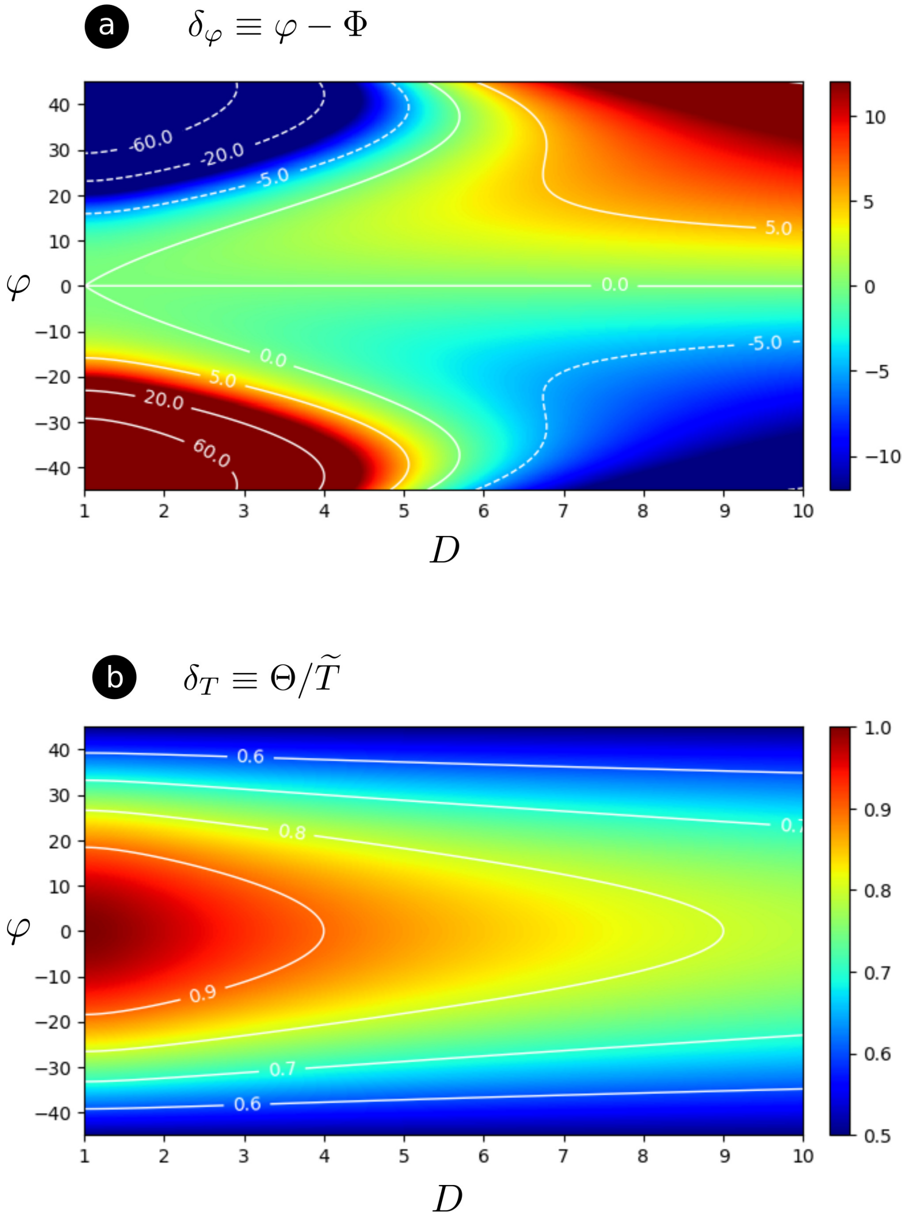

Figure 5.6 – Systematic errors δ_φ and δ_T induced by the approximation of negligible transmission dichroism ratio D and small Faraday rotation angle φ.

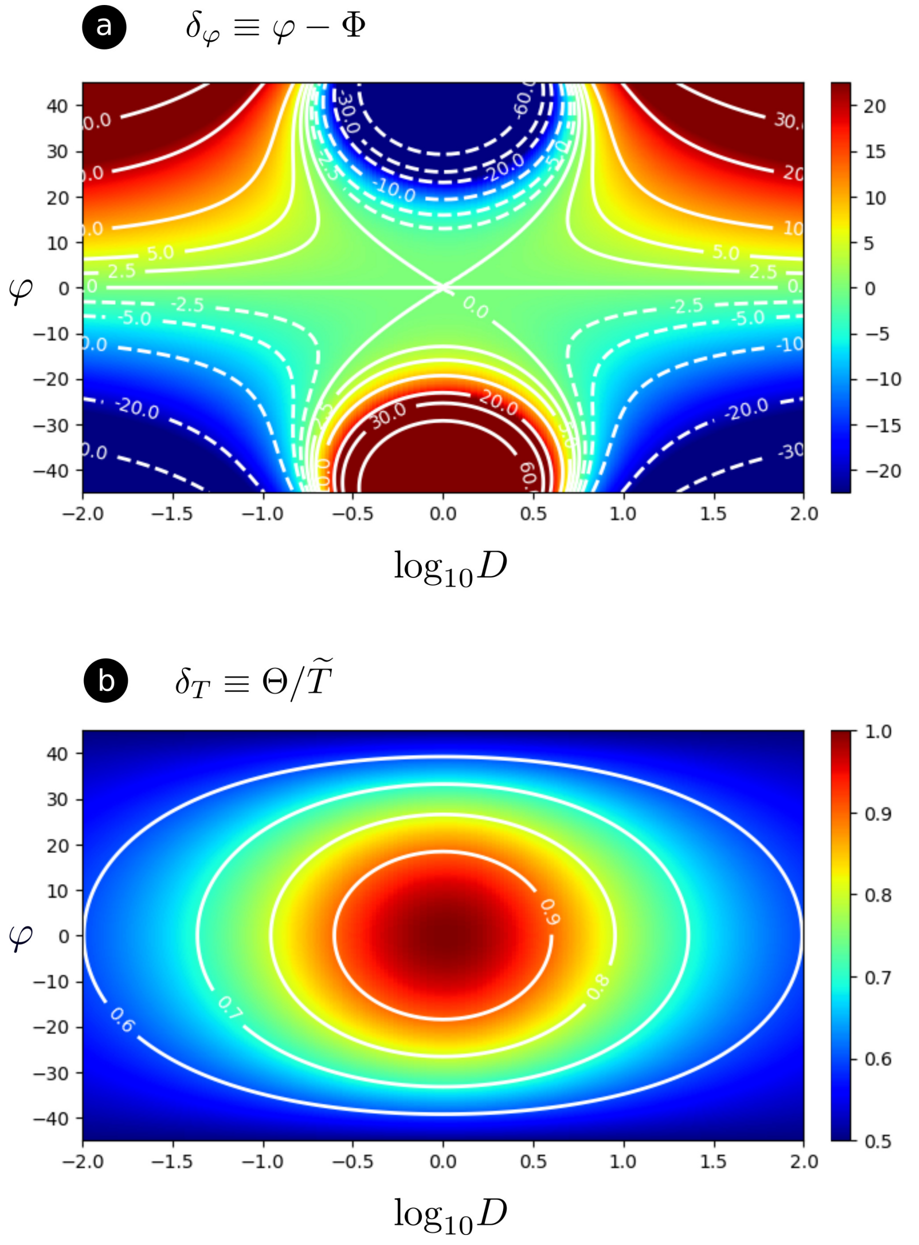

Figure 5.7 – Systematic errors δ_φ and δ_T induced by the approximation of negligible transmission dichroism ratio D and small Faraday rotation angle φ.

Chapter 6

Modeling optical properties of ultrathin films

6.1 Optical properties of ultrathin conducting films

From an optical point of view, graphene is an ultrathin conducting (metallic) film because its thickness is much smaller than the wavelength of light $d \ll \lambda$. In literature, there exist two approaches to describing the optical properties of graphene: 1) in some simulation software as Lumerical FDTD, effective thickness and effective 3D dielectric permittivity should be ascribed to graphene in order to model propagation of light; 2) graphene is considered as a conducting interface between two different or same media and classical methods of thin film optics [220, 221] could be applied. In this work we follow the second approach. Optical properties of ultrathin conducting films were investigated in [222, 223] and in this section we summarize their peculiar features in the context of graphene.

Let us consider the following configuration: an ultrathin film with conductivity σ is placed at the interface of two media with refractive indices n_1 and n_2 and light falls normally on the interface, see Figure 6.1. In this section and in the next section, we do not consider explicit dependency of the conductivity on frequency. Therefore σ could be interpreted either as conductivity in the absence of magnetic field, or as right-handed conductivity σ_+ or as left-handed conductivity σ_- in the presence of magnetic field, here we omit the indices for simplicity. Boundary conditions for electric and magnetic field vectors yield two equations which connect the complex amplitudes of incident, reflected and transmitted electric field vectors (as we consider the normal incidence of light, components of electric field parallel and perpendicular to the plane of incidence are described with the same pair of equations):

$$E_{\text{inc}} + E_{\text{refl}} = E_{\text{tr}}, \quad n_1(E_{\text{inc}} - E_{\text{refl}}) = n_2 E_{\text{tr}} + E_{\text{tr}}\sigma/Y_0,$$

this in turn leads to modified Fresnel coefficients which take into account σ:

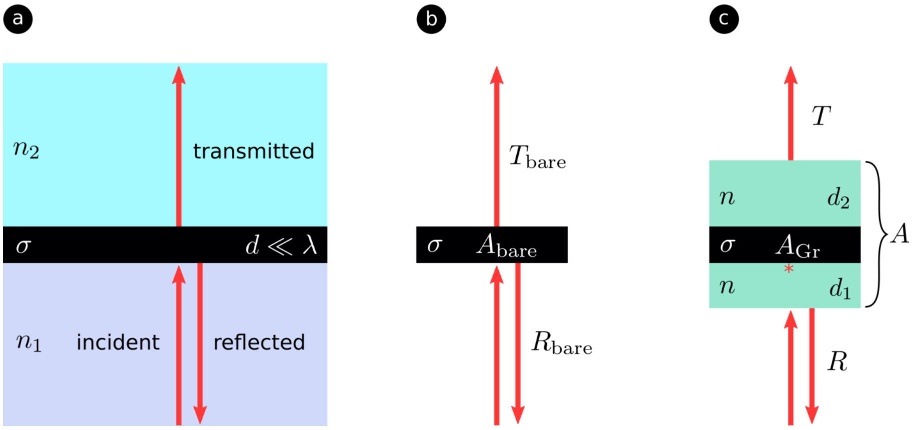

Figure 6.1 – Different configurations of ultrathin conducting films. **Panel a:** An ultrathin film with conductivity σ and thickness d at the interface between two media with different refractive indices n_1 and n_2. **Panel b:** Bare graphene in vacuum. **Panel c:** Graphene encapsulated in between two layers of hBN with refractive index n and different thicknesses d_1 and d_2; amount of light A_{Gr} absorbed in graphene is different from the total amount of light A absorbed by the hBN/Gr/hBN stack.

$$r_{1\to 2} \equiv \frac{E_{\mathrm{refl}}}{E_{\mathrm{inc}}} = \frac{n_1 - n_2 - \sigma/Y_0}{n_1 + n_2 + \sigma/Y_0}, \quad t_{1\to 2} \equiv \frac{E_{\mathrm{tr}}}{E_{\mathrm{inc}}} = \frac{2n_1}{n_1 + n_2 + \sigma/Y_0}, \tag{6.1}$$

where $Y_0 = 1/Z_0 \approx 2.65 \cdot 10^{-3}\ \Omega^{-1}$ is admittance of free space which is a reciprocal of the impedance of free space $Z_0 \approx 377\ \Omega$. Admittance of free space has the same dimension as sheet conductivity and represents an important scale for optical properties of ultrathin films.

When an ultrathin conducting film is suspended in vacuum (which is the case of bare i.e. non-encapsulated suspended graphene) then $n_1 = n_2 = 1$, formulas (6.1) simplify and one obtains the following reflection, transmission and absorption of an ultrathin film in vacuum:

$$r_{\mathrm{bare}} = -\frac{\sigma/(2Y_0)}{1 + \sigma/(2Y_0)}, \quad t_{\mathrm{bare}} = \frac{1}{1 + \sigma/(2Y_0)}, \tag{6.2}$$

$$R_{\mathrm{bare}} = |r_{\mathrm{bare}}|^2 = \frac{|\sigma/(2Y_0)|^2}{|1 + \sigma/(2Y_0)|^2}, \tag{6.3}$$

$$T_{\mathrm{bare}} = |t_{\mathrm{bare}}|^2 = \frac{1}{|1 + \sigma/(2Y_0)|^2}, \tag{6.4}$$

$$A_{\mathrm{bare}} \equiv 1 - R_{\mathrm{bare}} - T_{\mathrm{bare}} = \frac{\mathrm{Re}(\sigma)/Y_0}{|1 + \sigma/(2Y_0)|^2}. \tag{6.5}$$

Optical properties R_{bare}, T_{bare} and A_{bare} depend on the values of complex optical conductivity σ and do not have any explicit dependency on the frequency of light, their plots are given in the first column of Figure 6.4. As one can see, all properties R_{bare}, T_{bare} and A_{bare} are symmetric relative to the real axis of the optical conductivity $\operatorname{Im}\sigma = 0$. Moreover, minimal reflection as well as maximal absorption and transmission are achieved on this axis. A simple model of graphene's magneto-optical conductivity described in Section 2.2, see formula (2.19), suggests that $\operatorname{Im}\sigma_{\pm} \neq 0$ for the most values of frequencies in the electromagnetic spectrum, and special case when $\operatorname{Im}\sigma_{\pm} = 0$ occurs only for the frequencies corresponding to the magneto-optical absorption lines and for one frequency in between each pair of the absorption lines. The values of R_{bare}, T_{bare} and A_{bare} are plotted in Figure 6.5 as functions of $\operatorname{Re}\sigma$ for the case when $\operatorname{Im}\sigma = 0$. One can immediately see several important features. Firstly, for small values of σ/Y_0 the absorption increases and transmission decreases almost linearly with σ. Secondly, for small values of σ/Y_0 the reflection changes slowly meanwhile absorption and transmission are very sensitive to slight increases in σ/Y_0. Thirdly, absorption has a smooth maximum which is an important property of ultrathin conducting films: they cannot absorb more than half of the incident light. The maximal absorption

$$A_{\text{max}} = \frac{1}{2} \tag{6.6}$$

occurs when optical conductivity matches exactly the double of the admittance of free space $\operatorname{Re}\sigma = 2Y_0$, $\operatorname{Im}\sigma = 0$. Maximal absorption is accompanied by quarter reflection and quarter transmission of the film. In the case when $\operatorname{Im}\sigma = 0$, formulas (6.3), (6.4) and (6.5) could be simplified which in the end allows expressing one optical quantity through another unambiguously. For example $\operatorname{Re}\sigma/Y_0$, R_{bare} and A_{bare} which we do not measure in our experiment could be found from graphene's transmission T_{bare}:

$$\begin{aligned} \operatorname{Re}\sigma/Y_0 &= \frac{1}{\sqrt{T_{\text{bare}}}} - 1, \\ R_{\text{bare}} &= (1 - \sqrt{T_{\text{bare}}})^2, \\ A_{\text{bare}} &= 2\sqrt{T_{\text{bare}}}(1 - \sqrt{T_{\text{bare}}}), \end{aligned} \tag{6.7}$$

it is important to remember that the formulas mentioned above describe properties of graphene only at frequencies of magneto-optical absorption lines and at some frequency in between the lines where imaginary part of σ also turns to zero.

The limit (6.6) is derived from very general assumptions as Maxwell equations and boundary conditions. Therefore it holds for any homogeneous ultrathin conducting film regardless of its nature and composition. However the limit (6.6) is related only to the *intrinsic* ability of a bare ultrathin film to absorb the light. In practice, absorption may become more than 50 % because of light interference when a conducting film rests on a half-transparent substrate of certain thickness [223] or inside an optical cavity [224]. Absorption also could be increased with the help of resonance phenomena in plasmonic and metamaterial structures patterned ontop of ultrathin films which has been shown for graphene in [225, 226].

Usual metals like aluminum, gold, titanium, etc cannot exist in atomically thin form. However formally one may calculate their sheet conductivity σ_{2D} for metallic films of unit-cell thickness: $\sigma_{2D} = a\sigma_{3D}$ where a is size of a unit cell and σ_{3D} is usual bulk conductivity. For example, unit-cell thin aluminum has $\sigma_{2D} \sim 15 \cdot 10^{-3}\ \Omega^{-1}$ at room temperature. And sheet conductivity becomes even higher for thicker[1] metallic films and at lower temperatures. Thus for usual metals $\sigma_{2D} \gg 2Y_0$ and values of optical absorption are low compared to A_{max} because most part of the incident light is reflected.

The universal conductivity of graphene is $\sigma_0 \approx 0.061 \cdot 10^{-3}\ \Omega^{-1} \approx 2Y_0/87$, see formula (2.4). This value also results in a relatively low absorption of about two percent (2.6). The only difference is that now $\sigma_0 \ll 2Y_0$ i.e. the value of graphene's conductivity lays on the other side of the $A_{\text{bare}} = A_{\text{bare}}(\operatorname{Re}\sigma)$ slope compared to the conductivity of usual metallic films, see Figure 6.5. Therefore most part of the light is transmitted through and not reflected by graphene. However magnetic field allows tuning graphene's properties. Indeed, in external magnetic field at the frequencies corresponding to the magneto-optical transitions, both graphene's conductivities $\sigma_\pm$ increase and may become much closer to $2Y_0$ especially when resonance width Γ_j of the transitions is small, see Figures 2.7 and 2.8. Thus maximal real part of the left-handed conductivity which we routinely obtained in our experiments for T_1 magneto-optical line around 4 Tesla is $\sigma_{\text{max}} = 58\sigma_0 = 4Y_0/3$. This in turn leads to a dramatic increase in light absorption and drop of transmission which we observed, the results are shown in Chapter 7.

Optical properties of graphene are highly tunable because the universal conductivity of graphene σ_0 has a relatively low value. Indeed, σ_0 from which the tuning starts lays in the region well below $2Y_0$. In this region R_{bare}, T_{bare} and A_{bare} are very responsive to changes of σ. In contrast, on the other side of the $A_{\text{bare}} = A_{\text{bare}}(\operatorname{Re}\sigma)$ slope, i.e. for conductivity $\sigma > 2Y_0$ optical properties of a thin film change very slowly as $\operatorname{Re}\sigma$ increases or decreases because of some external influence. Even more opportunities arise when magnetic field and gate voltage[2] are applied to graphene simultaneously: the former allows tuning values of $\sigma_\pm$ across the infrared region and the later allows tuning the balance between σ_+ and σ_-. Thus not only the magnitude of infrared light absorption but also magnetic circular dichroism could be continuously modulated from one handedness of light to another which could be viewed as an optical analogue of the ambipolar field-effect.

---

[1] Usually metallic films of $\sim$ 10 nm are already thermodynamically stable and their thickness still remains in the ultrathin-film approximation.

[2] Unfortunately, our samples were manufactured in such a way that we could not attach a gate electrode to them, nevertheless we could measure graphene spectra for different levels of doping because the doping changed its value uncontrollably on the time-scale of months.

6.2 Optical properties of an hBN/Gr/hBN stack

In our experiments graphene was not bare but encapsulated. Optical properties of the whole hBN/Gr/hBN stack could be calculated using standard computational techniques for multilayers as matrix method [221] or iterative incorporation of layers [220, 221].

In our microscope IR light impinges on the samples at all angles between 12.0° and 23.6° which is needed to focus the light. Meanwhile all rays of light impinging at angles between 0° and 12.0° are blocked by the secondary mirrors of the Cassegrains, see Figures 5.1 and 4. However in our calculations we approximate such oblique propagation of light by normal incidence. This approximation largely simplifies the analysis of spectra at the same time it does not lead to significant errors. Indeed, the values of Fresnel coefficients change slowly as the angle increases in the vicinity to 0° [44] and absorption is almost independent of the angle of incidence for the angles $\lesssim 45^\circ$ [227]. As we consider only normal incidence of light, the out-of-plane anisotropy of the hBN's refractive index automatically drops out from our description. Consequently, our model does not grasp the hyperbolic properties of hBN.

An hBN/Gr/hBN stack has two layers of hBN and three interfaces: from vacuum to hBN, from hBN to hBN through graphene and from hBN to vacuum, see panel c of Figure 6.1. Propagation of light within each hBN layer is governed by the complex refractive index of hBN $n = n(\omega)$ and layer's thickness which we denote as d_1 and d_2. Thus the first and the last interfaces are described by usual Fresnel coefficients and transition from hBN to hBN through graphene is described by the modified Fresnel coefficients given in the formulas (6.1). In the end, Fresnel coefficients of the whole hBN/Gr/hBN stack for normal incidence of light are:

$$r = \frac{r_{\text{hBN}} - c_1 \cdot \sigma/Y_0 - c_2 \cdot (\sigma/Y_0)^2}{(1 + c_3 \cdot \sigma/Y_0)(1 + c_4 \cdot \sigma/Y_0)}, \quad t = \frac{t_{\text{hBN}}}{1 + c_3 \cdot \sigma/Y_0}. \tag{6.8}$$

Here r_{hBN} and t_{hBN} are reflection and transmission Fresnel coefficients of an hBN film which has $d_1 + d_2$ thickness:

$$r_{\text{hBN}} = \frac{(n^2-1)(\tau_1^2\tau_2^2 - 1)}{(n+1)^2 - \tau_1^2\tau_2^2(n-1)^2}, \quad t_{\text{hBN}} = \frac{4n\tau_1\tau_2}{(n+1)^2 - \tau_1^2\tau_2^2\,(n-1)^2}, \tag{6.9}$$

and c_1, c_2, c_3, c_4 are subsidiary complex coefficients which do not depend on graphene's conductivity σ:

$$c_1 = \frac{1}{2n} \cdot \frac{n-1}{n+1} \cdot \frac{2(n+1)^2 + (n^2-1)(\tau_1^2 + \tau_2^2)}{(n+1)^2 - \tau_1^2\tau_2^2(n-1)^2} + \frac{\tau_1^2}{2n},$$

$$c_2 = \frac{\left[n^2 - 1 + 2(n^2+1)\tau_1^2 + (n^2-1)\tau_1^4\right]\left[n + 1 + (n-1)\tau_2^2\right]}{(2n)^2(n+1)\left[(n+1)^2 - \tau_1^2\tau_2^2(n-1)^2\right]},$$

$$c_3 = \frac{(n+1)^2 + \left(n^2-1\right)\left(\tau_1^2+\tau_2^2\right) + \tau_1^2\tau_2^2\,(n-1)^2}{2n\left[(n+1)^2 - \tau_1^2\tau_2^2\,(n-1)^2\right]},$$

$$c_4 = \frac{\tau_1^2(n-1)+n+1}{2n(n+1)}, \qquad \tau_{1,2} = \exp(i\omega n d_{1,2}/c).$$

In the case of bare graphene $n = \tau_{1,2} = 1$, subsidiary coefficients take values

$$r_{\text{hBN}} = 0, \quad t_{\text{hBN}} = 1$$

$$c_1 = c_3 = c_4 = 1/2, \quad c_2 = 1/4, \quad \tau_{1,2} = 1 \tag{6.10}$$

and formulas (6.8) transform into the formulas (6.2).

For normal incidence of light reflection, transmission and absorption of the whole hBN/Gr/hBN stack are found with

$$R = |r|^2, \quad T = |t|^2, \quad A = 1 - R - T. \tag{6.11}$$

Absorption of encapsulated graphene

The amount of light A_{Gr} absorbed in the graphene monolayer alone differs from the absorption A of the whole hBN/Gr/hBN stack. Absorption A_{Gr} is due to the energy dissipated in graphene because of the current $J = \sigma E_{\text{loc}}$ induced in graphene by the local electric field E_{loc} to which the monolayer is exposed. The red asterisk in the panel c of Figure 6.1 shows the place where E_{loc} is defined. E_{loc} is equal to the sum of two electric fields: the first one corresponds to an electromagnetic wave propagating towards graphene's bottom side from below and the second corresponds to an electromagnetic waves propagating downwards from graphene's bottom side. Thus absorption in the graphene monolayer alone is

$$A_{\text{Gr}} = \frac{\text{Re}(J^* \cdot E_{\text{loc}})}{Y_0 |E_{\text{inc}}|^2}.$$

Ratio of the local field to the incident field could be calculated with the above mentioned methods for multilayers. Thus absorption in a graphene monolayer when it makes part of a hBN/Gr/hBN stack is

$$A_{\text{Gr}} = \text{Re}(\sigma)/Y_0 \cdot |l|^2\,, \tag{6.12}$$

$$l \equiv \frac{E_{\text{loc}}}{E_{\text{inc}}} = \frac{l_{\text{hBN}} + c_5 \cdot \sigma/Y_0}{(1 + c_3 \cdot \sigma/Y_0)(1 + c_4 \cdot \sigma/Y_0)},$$

$$l_{\text{hBN}} = -\frac{2\tau_1\left(n + \tau_2^2\,(n-1) + 1\right)}{\tau_1^2\tau_2^2\,(n-1)^2 - (n+1)^2},$$

$$c_5 = -\frac{\tau_1\left[n + \tau_1^2\,(n-1) + 1\right]\left[n + \tau_2^2\,(n-1) + 1\right]}{n\,(n+1)\left[\tau_1^2\tau_2^2\,(n-1)^2 - (n+1)^2\right]}.$$

Complex quantity l could be interpreted as a Fresnel coefficient because it is defined as a ratio of complex amplitudes of two electric fields. However in contrast to the usual Fresnel coefficient, these electric fields are taken in the points separated from each other by a *finite layer* of dielectric material (in our case it is the bottom hBN layer) and not an interface. l_{hBN} is a complex quantity to which l reduces when conductivity of graphene is formally set to zero. c_5 is yet another subsidiary complex coefficient which does not depend on graphene's conductivity σ. In the case of bare graphene $n = \tau_{1,2} = 1$, subsidiary coefficients take values

$$l_{\text{hBN}} = 1, \quad c_5 = 1/2$$

and coefficient l transforms into t_{bare} given in the (6.2). Thus both absorptions A and A_{Gr} reduce to the absorption of bare graphene A_{bare} given in (6.5).

Modeling refractive index of hBN

We approximate the propagation of light through hBN/Gr/hBN stacks by normal incidence. Therefore we develop only a simplified model of hBN's refractive index which does not take into account neither out-of-basal-plane optical anisotropy of hBN nor its hyperbolic properties. The frequency dependency $n = n(\omega)$ of hBN's complex refractive index could be modeled the following way:

$$n^2 = \epsilon_\infty + \frac{\Omega_{\text{ph}}^2}{\omega_{\text{ph}}^2 - \omega^2 - i\omega\gamma_{\text{ph}}}. \tag{6.13}$$

Here $\epsilon_\infty = 4.95$ is high-frequency dielectric function of hBN to which we assign the value found in [152]. The remaining parameters $\Omega_{\text{ph}} = 2200\ \text{cm}^{-1}$, $\omega_{\text{ph}} = 1367\ \text{cm}^{-1}$ (169.5 meV) and $\gamma_{\text{ph}} = 12\ \text{cm}^{-1}$ (1.5 meV) describe the intensity, frequency and width of the optically active phonon in hBN. We found the values of these parameters from the absolute signal at the detector during measurements of hBN/Gr/hBN transmission at zero magnetic field, see Appendix E. The second optically active phonon at 767 cm^{-1} (95.1 meV) is not as pronounced as the first one. We have not detected any of its effect on the transmission spectra of the hBN/Gr/hBN stacks therefore we do not include any term corresponding to this phonon to the equation (6.13). Result of our modeling of hBN's refractive index is shown in the panel a of Figure 6.2.

Knowledge of $n = n(\omega)$ allows understanding optical properties of thin hBN flakes without graphene, see panel b of Figure 6.2. At frequencies away from ω_{ph}, hBN is highly transparent and its properties vary very slowly with frequency. At frequencies in the direct vicinity to ω_{ph}, transmission of hBN drops almost to zero because of a sharp increase in reflection and absorption of light by hBN.

Effect of encapsulation on the optical properties

It is important to mention that formulas (6.8)−(6.12) take into account only wave optics phenomena like multiple reflections and interference in a hBN/Gr/hBN stack.

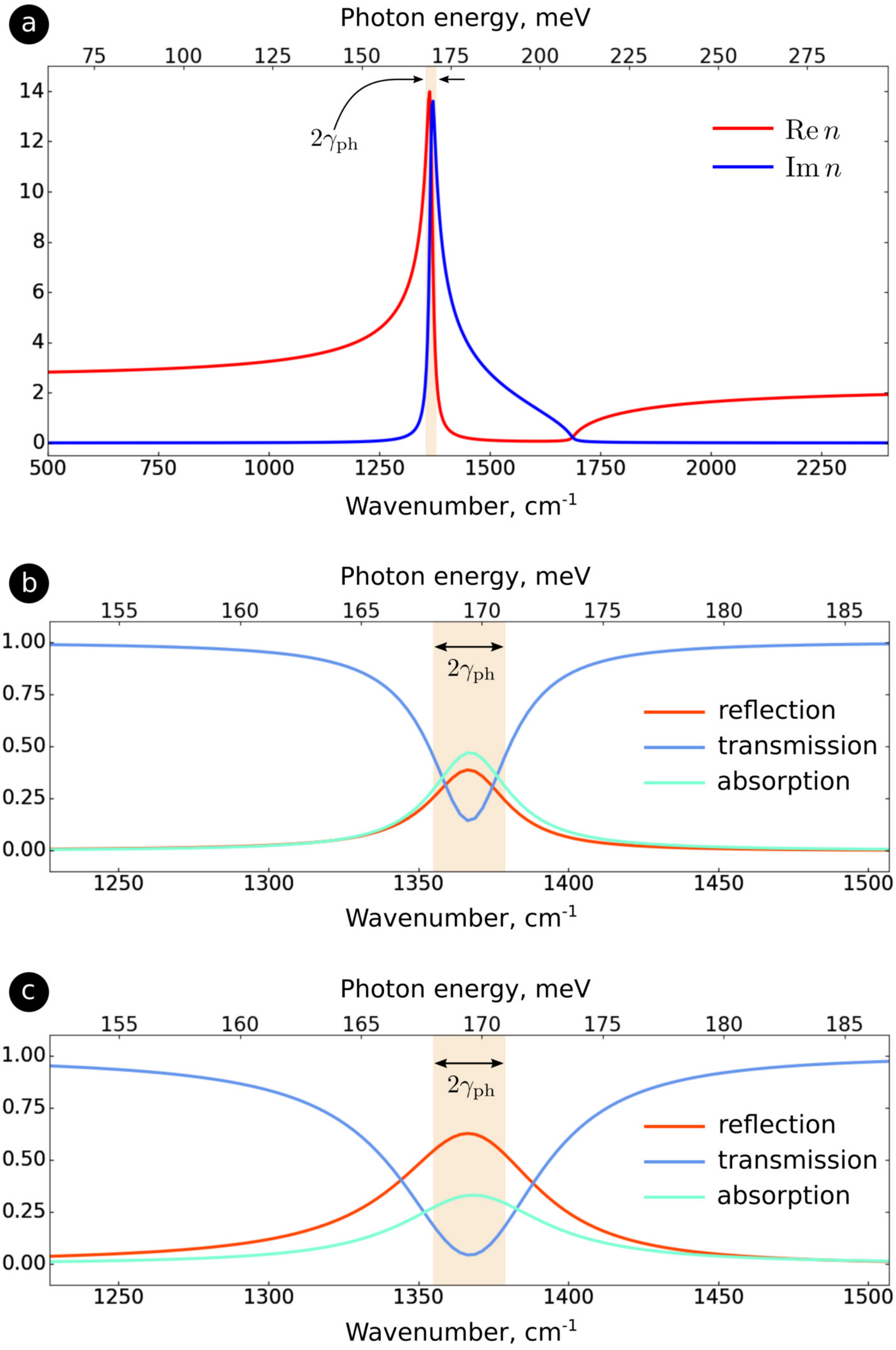

Figure 6.2 – Optical properties of hBN as a function of frequency. The ivory bar is centered at the phonon's frequency ω_{ph} and has width $2\gamma_{\mathrm{ph}}$. **Panel a:** Real and imaginary parts of hBN's refractive index, see formula (6.13). **Panel b:** Optical properties of a 13 nm thick hBN flake (as thick as our thinnest $\varnothing = 20\ \mu$m hBN/Gr/hBN membrane), see formulas (6.9). **Panel c:** Optical properties of a 30 nm thick hBN flake (as thickness as our thickest $\varnothing = 30\ \mu$m hBN/Gr/hBN membrane), see formulas (6.9).

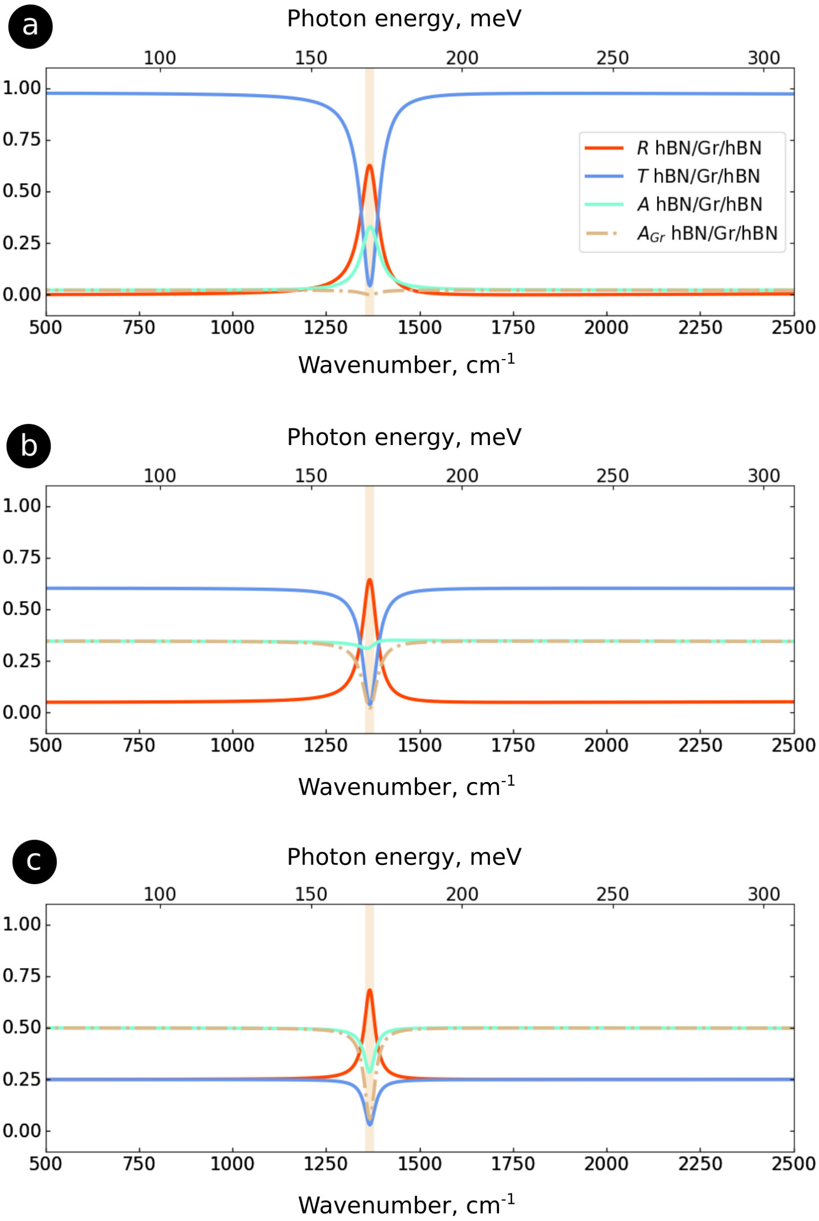

Figure 6.3 – Optical properties of a hBN/Gr/hBN stack as a function of frequency. R, T, A and A_{Gr} are given in the formulas (6.11)−(6.12) and plotted for the case when $\operatorname{Im}\sigma = 0$, $d_1 = 10$ nm and $d_2 = 20$ nm. Ivory bar is centered at the phonon's frequency ω_{ph} and has width $2\gamma_{\mathrm{ph}}$. One can see how the hBN phonon influences the total absorption of the stack for different values of graphene's optical conductivity. **Panel a:** $\operatorname{Re}\sigma = \sigma_0$, which is similar to the case of an hBN flake without graphene, see panel b of Figure 6.2. **Panel b:** $\operatorname{Re}\sigma = 29\sigma_0$ value which we routinely obtained in our experiments. **Panel c:** Hypothetical case $\operatorname{Re}\sigma = 2Y_0$.

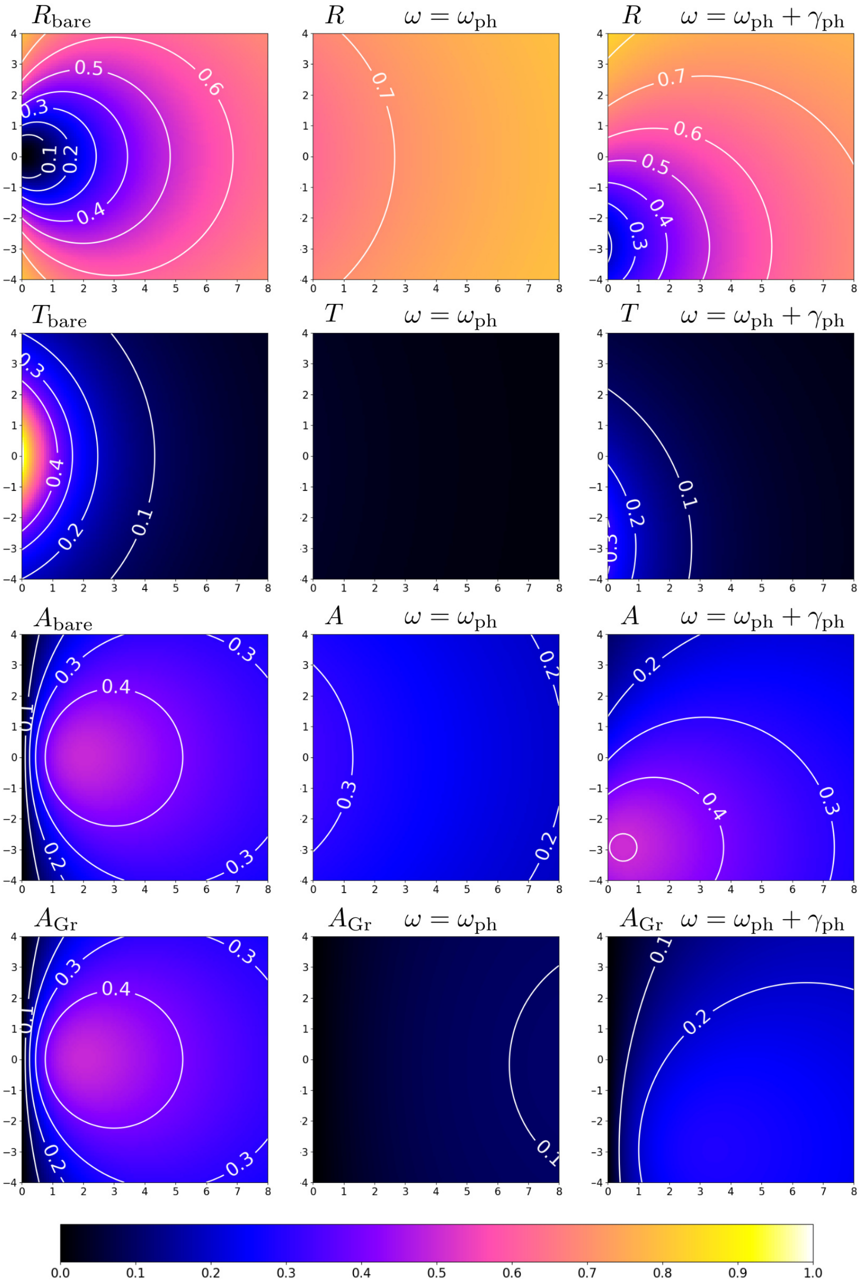

Figure 6.4 – Optical properties of bare and encapsulated ultrathin conducting films plotted as functions of their $\mathrm{Re}\,\sigma/Y_0$ (horizontal axis) and $\mathrm{Im}\,\sigma/Y_0$ (vertical axis). hBN layers have thicknesses $d_1 = 10$ nm and $d_2 = 20$ nm. **1st column:** Properties of a bare film, see formulas (6.3)−(6.5). Properties of an encapsulated film are similar to those of a bare film for frequencies far from the hBN phonon therefore we do not plot them here. **2nd and 3rd columns:** Properties of the encapsulated film, see formulas (6.11)−(6.12), for the frequencies in the direct vicinity to the hBN phonon ω_{ph}.

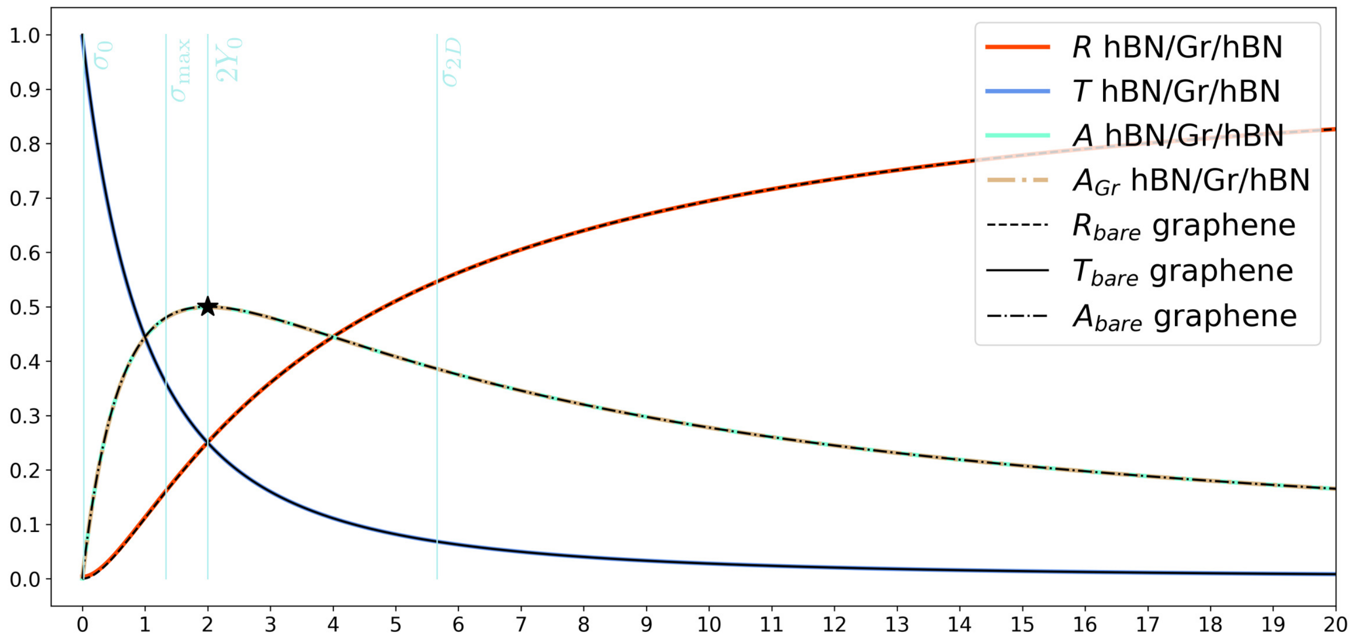

Figure 6.5 – Optical properties of ultrathin conducting films as a function of their conductivity $\mathrm{Re}\,\sigma/Y_0$ for the case when $\mathrm{Im}\,\sigma/Y_0 = 0$. Properties of bare films R_{bare}, T_{bare}, and A_{bare} are given in the formulas (6.3)−(6.5). Properties of encapsulated films R, T, A, and A_{Gr} are given in the formulas (6.11)−(6.12), hBN layers have thicknesses $d_1 = 10$ nm and $d_2 = 20$ nm which correspond to our thickest hBN/Gr/hBN membrane ($\varnothing = 30\ \mu$m). Frequency of light is much lower than frequency of the hBN phonon ω_{ph}. Blue vertical lines indicate some typical values of sheet conductivities.

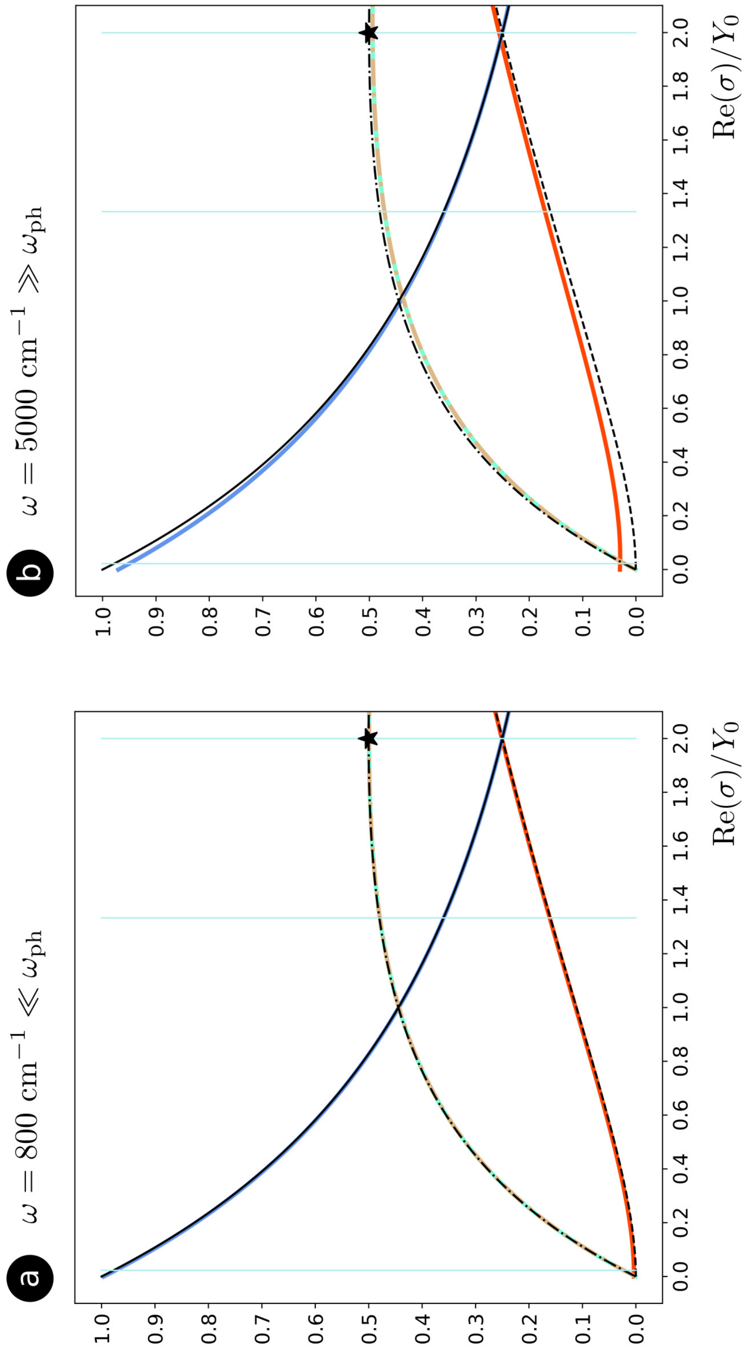
a
$\omega = 800\ \mathrm{cm}^{-1} \ll \omega_{\mathrm{ph}}$
b
$\omega = 5000\ \mathrm{cm}^{-1} \gg \omega_{\mathrm{ph}}$
1.0
0.9
0.8
0.7
0.6
0.5
0.4
0.3
0.2
0.1
0.0
0.0
0.2
0.4
0.6
0.8
1.0
1.2
1.4
1.6
1.8
2.0
$\mathrm{Re}(\sigma)/Y_0$

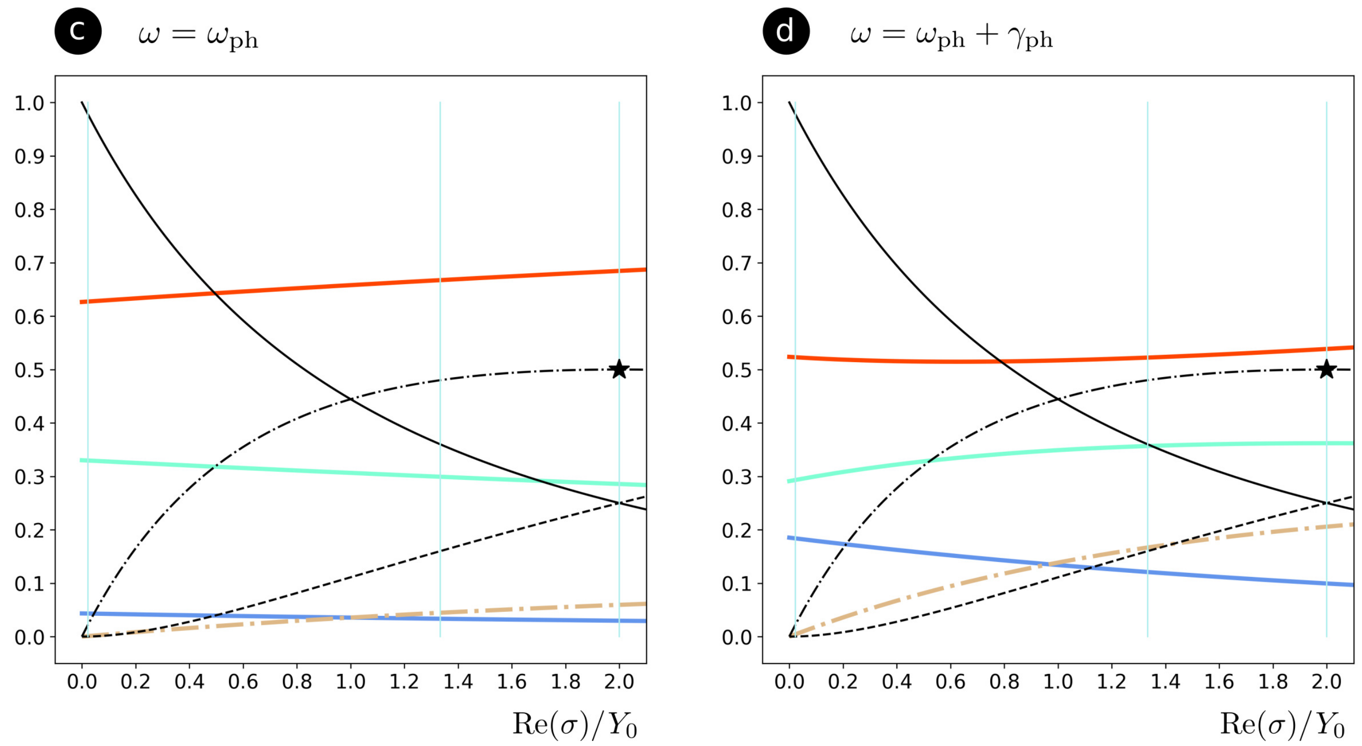

Figure 6.6 – Optical properties of bare and encapsulated ultrathin conducting films. The same physical quantities (and color code) as in Figure 6.5 calculated for various frequencies of the incedent light. **Panels a and b:** Frequency is far from the hBN phonon $\omega_{\rm ph}$. **Panels c and d:** Frequency is in the direct vicinity to the hBN phonon $\omega_{\rm ph}$.

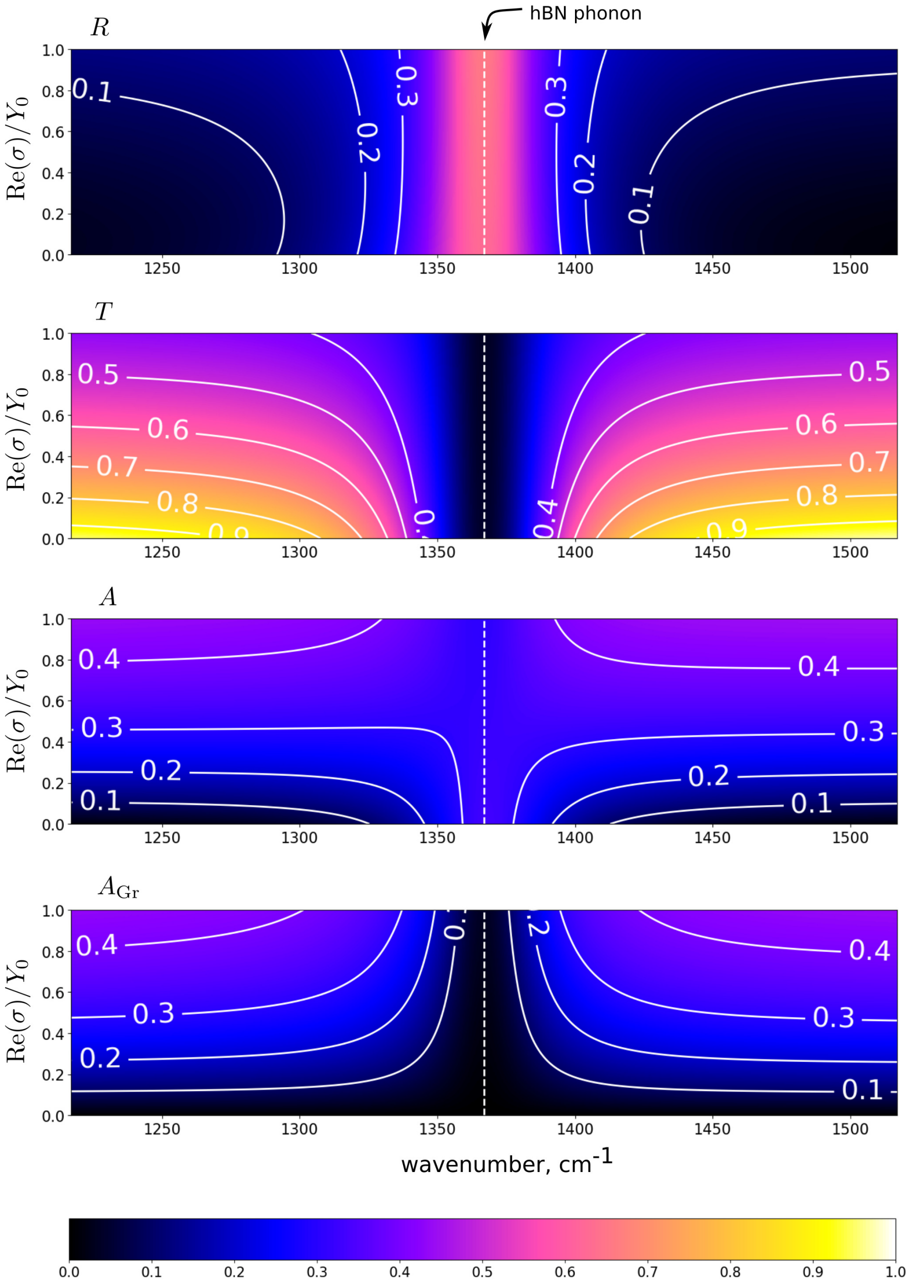

Figure 6.7 – Optical properties of encapsulated ultrathin conducting film, see formulas (6.11)–(6.12), plotted as functions of frequency (horizontal axis) and its $\mathrm{Re}\,\sigma/Y_0$ (vertical axis) for the case when $\mathrm{Im}\,\sigma/Y_0 = 0$. hBN layers have thicknesses $d_1 = 10$ nm and $d_2 = 20$ nm which corresponds to our thickest hBN/Gr/hBN membrane ($\varnothing = 30$ μm). One can see a non-symmetric variation of absorption A as one approaches ω_{ph} from different sides.

It has been already indicated in Section 3.1 that hBN-encapsulation also modifies behaviour of charge carriers in graphene. Therefore strictly speaking optical conductivity σ of encapsulated graphene in the formulas (6.8) and σ of bare graphene in the formulas (6.2) $-$ (6.5) are different functions of frequency. Developing a theoretical model which describes how encapsulation modifies frequency dependency of σ is far beyond the scope of this work. Here we only discuss the wave optics phenomena in a hBN/Gr/hBN stack at normal incidence of light. In order to make an adequate comparison of bare and encapsulated graphene, in the current section we consider σ as an independent variable regardless of any underlaying mechanisms which formed its final value. Such approach is justified because the values of optical conductivity are not fixed exclusively by the values of frequency: the position of Fermi level, external magnetic field, temperature, mechanisms of charge carriers scattering, substrate, etc influence the resulting value of σ.

Figures 6.4 $-$ 6.7 visualize how optical properties of bare graphene and an hBN/Gr/hBN stack depend on three independent variables: frequency, real and imaginary parts of the optical conductivity. In the most parts of the infrared region, optical properties of an hBN/Gr/hBN stack are almost the same as those of bare graphene (see panels a and b of Figure 6.6). This is because hBN is highly transparent and also because it is very thin compared to the wavelength of infrared light thus the interference effects in an hBN/Gr/hBN stack are not pronounced. However for the frequencies in the vicinity to the hBN phonon $\omega_{\text{ph}} = 1367\ \text{cm}^{-1}$, optical properties of the whole hBN/Gr/hBN stack may differ significantly from those of bare graphene (see panels c and d of Figure 6.6) as well from those of an hBN flake which has the same thickness as the whole hBN/Gr/hBN stack (compare Figure 6.3 to the panel b of Figure 6.2). Optical properties of an hBN/Gr/hBN stack reduces to those of an hBN flake when $\sigma \to 0$, thus Figure 6.7 shows how optical properties of an hBN/Gr/hBN stack change in most part of the spectrum as σ grows and remain almost the same around phonon's frequency. The 2nd column of Figure 6.4 also shows that when light frequency coincides with the phonon's frequency, optical properties of hBN/Gr/hBN stack almost do not depend on the optical conductivity of graphene. The 3d column of Figure 6.4 shows that when light frequency is close but does not coincide with the phonon's frequency, the minima of R and T as well as maximum of A are shifted away from the real axis $\operatorname{Im}\sigma/Y_0 = 0$ where they all reside in the case of a bare film. Maximal value of A exceeds A_{max} a little bit. However we could not explore these new minima and maximum in our experiments because applying a magnetic field does not allow tuning the values of conductivity that far away from the real axis $\operatorname{Im}\sigma/Y_0 = 0$.

One can also notice another interesting tendency: absorption of light in the encapsulated graphene A_{Gr} at the hBN phonon frequency is always lower compared to the case of bare graphene (compare the 1st and the 2nd columns of Figure 6.4, see panel c of Figure 6.6) and to the case of encapsulated graphene in the other regions of spectrum (see Figures 6.3 and 6.7). Such behaviour is partly explained by the fact that large fraction of the incident light is reflected by the hBN layer.

hBN thickness d_1 and d_2 enters symmetrically into the formulas for Fresnel coefficients r_{hBN}, t_{hBN}, t. However r and l depend on d_1 and d_2 in a non-symmetric way. This means that for $d_1 \neq d_2$ absorption and reflection of a hBN/Gr/hBN stack as well as absorption right in graphene monolayer change when one or the other side is exposed to the incident light (hBN layer exposed to the incident light is denoted by d_1).

6.3 Magnetic circular dichroism and Faraday rotation

In a magnetic field, Fresnel coefficients (6.2) and (6.8) acquire dependency on polarization of incident light and are described by matrices which have the same symmetry as magneto-optical conductivity of graphene (2.12). Thus for reflection and transmission:

$$\hat{r} = \begin{bmatrix} r_{xx} & r_{xy} \\ -r_{xy} & r_{xx} \end{bmatrix}, \quad \hat{t} = \begin{bmatrix} t_{xx} & t_{xy} \\ -t_{xy} & t_{xx} \end{bmatrix}. \tag{6.14}$$

In a magnetic field, optical conductivities of graphene $\sigma_\pm = \sigma_\pm(\omega, B)$, Fresnel coefficients $\hat{r} = \hat{r}(\omega, B)$, $\hat{t} = \hat{t}(\omega, B)$ and all related optical quantities depend on the values of frequency ω and magnetic field B, however we omit these arguments to simplify notation.

Matrix $\hat{r}$ has two eigen values r_+ and r_- which are reflection Fresnel coefficients for right-handed and left-handed circularly polarized light; similarly, matrix $\hat{t}$ has two eigen values t_+ and t_- which are transmission Fresnel coefficients for right-handed and left-handed circularly polarized light:

$$r_\pm = r_{xx} \pm i r_{xy}, \quad t_\pm = t_{xx} \pm i t_{xy}.$$

Fresnel coefficients $r_\pm$ and $t_\pm$ could be found with a help of substitution $\sigma \to \sigma_\pm$ in the formulas (6.8) for usual Fresnel coefficients calculated in the absence of magnetic field. Thus in the case of normal incidence, we obtain the following Fresnel coefficients of an hBN/Gr/hBN stack in a magnetic field:

$$r_\pm = \frac{r_{\text{hBN}} - c_1 \cdot \sigma_\pm/Y_0 - c_2 \cdot (\sigma_\pm/Y_0)^2}{(1 + c_3 \cdot \sigma_\pm/Y_0)(1 + c_4 \cdot \sigma_\pm/Y_0)}, \qquad t_\pm = \frac{t_{\text{hBN}}}{1 + c_3 \cdot \sigma_\pm/Y_0}, \tag{6.15}$$

here all subsidiary coefficients r_{hBN}, t_{hBN}, c_1, c_2, c_3, c_4 and $\tau_{1,2}$ have the same values as before because optical properties of hBN do not change in an external magnetic field. Following the formulas (6.11), reflection, transmissions and absorption of an hBN/Gr/hBN stack for right-handed and left-handed circular polarizations are:

$$R_\pm = |r_\pm|^2, \quad T_\pm = |t_\pm|^2, \quad A_\pm = 1 - R_\pm - T_\pm. \tag{6.16}$$

Similarly to the Fresnel coefficients, absorption in graphene only is also described by the substitution $\sigma \to \sigma_\pm$ in the formula (6.12):

$$A_{\text{Gr}\pm} = \text{Re}(\sigma)/Y_0 \cdot |l_\pm|^2, \tag{6.17}$$

$$l_{\pm} = \frac{l_{\text{hBN}} + c_5 \cdot \sigma_{\pm}/Y_0}{(1 + c_3 \cdot \sigma_{\pm}/Y_0)(1 + c_4 \cdot \sigma_{\pm}/Y_0)}.$$

In different experiments, we illuminated graphene sometimes with linearly polarized light and sometimes with unpolarized light. Reflection and transmission of linearly polarized light can be found as a sum of corresponding right-handed and left-handed components with equal amplitudes. Graphene possesses uniaxial symmetry therefore the exact orientation of the in-plane component of the linear polarization relative to the crystalline lattice of graphene is not important. This also implies that graphene's reflection and transmission of unpolarized light are expressed by the same formulas as graphene's reflection and transmission of the linearly polarized light:

$$R_{\text{non pol}} = R_{\text{lin pol}} \equiv R = \frac{R_+ + R_-}{2}, \qquad T_{\text{non pol}} = T_{\text{lin pol}} \equiv T = \frac{T_+ + T_-}{2}.$$

Thus absorption of linearly polarized or unpolarized light is $A = 1 - T - R$ from which follows that

$$A = \frac{A_+ + A_-}{2}.$$

When $\sigma_+ \neq \sigma_-$ absorptions of oppositely handed circularly polarized light are different. This phenomenon of circular dichroism is often quantified as

$$\Delta_A \equiv \frac{A_- - A_+}{A_- + A_+}, \quad -1 \leq \Delta_A \leq 1. \tag{6.18}$$

If an ultrathin conducting film is not encapsulated then it cannot absorb more that half of the impinging light i.e. its values of absorption $A_+, A_-, A \leq 1/2$. However the ultimate values of absorption dichroism $\Delta_A = \pm 1$ could be still achieved when $A_+ = 0$ and at the same time $A_- = 1/2$ or vice versa.

In our experiments, we measured transmission properties of graphene. For this reason we also use the transmission circular dichroism *ratio* defined as

$$D \equiv T_-/T_+.$$

Transmissions T_+ and T_- are real numbers and do not contain any information about arguments of Fresnel coefficients t_+ and t_-, see (6.16). Values of Fresnel coefficients given in the equations (6.15) could be rewritten in the polar form as:

$$t_{\pm} = \sqrt{T_{\pm}} \exp(i\theta_{\pm}).$$

Moduli and arguments of $t_{\pm}$ could be expressed in terms of optical conductivities $\sigma_{\pm}$ using the equation (6.15) the following way:

$$|t_{\pm}| = \sqrt{T_{\pm}}, \qquad T_{\pm} = \frac{|t_{\text{hBN}}|^2}{|c_3\sigma_{\pm}/Y_0|^2 + 2\,\text{Re}\,(c_3\sigma_{\pm}/Y_0) + 1}, \tag{6.19}$$

$$\text{Arg}(t_{\pm}) = \theta_{\pm} = \text{Arg}(t_{\text{hBN}}) - \text{Arg}(1 + c_3\sigma_{\pm}/Y_0).$$

Faraday rotation angle θ_F contains useful information about the arguments θ_+ and θ_- of transmission Fresnel coefficients:

$$\theta_F = \frac{\theta_- - \theta_+}{2}.$$

Faraday rotation angles of encapsulated and bare graphene in terms of optical conductivities $\sigma_\pm$ are

$$\theta_F = \frac{1}{2}\operatorname{Arg}\left(\frac{1 + c_3\sigma_+/Y_0}{1 + c_3\sigma_-/Y_0}\right), \tag{6.20}$$

$$\theta_{F\,\mathrm{bare}} = \frac{1}{2}\operatorname{Arg}\left(\frac{1 + \sigma_+/(2Y_0)}{1 + \sigma_-/(2Y_0)}\right). \tag{6.21}$$

Plots of $R_\pm$, $T_\pm$, $A_\pm$, and θ_F are shown in Figures 2.10 and 2.11 for the case of bare graphene with MO conductivities $\sigma_\pm$ calculated in the framework of the simple theory (2.19), values of the subsidiary coefficients are given in (6.10).

Maximal Faraday rotation angle

Formula (6.21) allows understanding the maximal possible value of Faraday rotation angle for an ultrathin conducting film. First we rewrite (6.21) as a difference of arguments of two complex numbers z_+ and z_-:

$$\theta_{F\,\mathrm{bare}} = \frac{1}{2}\left(\operatorname{Arg} z_+ - \operatorname{Arg} z_-\right), \quad z_\pm = 1 + \frac{\operatorname{Re}\sigma_\pm}{2Y_0} + i\frac{\operatorname{Im}\sigma_\pm}{2Y_0}.$$

Imaginary parts of both optical conductivities $\operatorname{Im}\sigma_\pm$ can take on both positive or negative values depending on the frequency, position of Fermi level etc. But their real parts can only be positive $\operatorname{Re}\sigma_\pm \geq 0$ because negative values are incompatible with energy conservation. Therefore $-\pi/2 < \operatorname{Arg} z_\pm < \pi/2$ and we conclude that maximal possible value of the Faraday rotation angle is $|\theta_{F\,\mathrm{max}}| < \pi/2$ regardless of the nature of an ultrathin conducting film. This simple reasoning also allows us making another conclusion: The existence of the upper limiting value implies that dependency of the Faraday rotation angle on the magnetic field $\theta_F = \theta_F(B)$ cannot be linear.

The above mentioned reasoning is very general and does not take into account that in real materials including graphene, $\operatorname{Re}\sigma_\pm$ and $\operatorname{Im}\sigma_\pm$ cannot assume any values from their allowed regions independently from one another. Thus in the framework of the simple model of $\sigma_\pm$ described in Section 2.2, see formula (2.19), exact values of the Faraday rotation angle depend significantly on the widths Γ_j but at any circumstances cannot exceed the limiting value

$$|\theta_{F\,\mathrm{max}}| < \pi/4.$$

In practice, Faraday rotation of bare graphene can be increased beyond (6.21) by placing graphene inside or on the surface of a Fabry-Perot cavity. These opportunities were investigated in [228]. When a ray of light performs multiple round trips inside the cavity, Faraday rotation angle increases at each passage because of the the non-reciprocal nature of Faraday rotation effect. However in our case the thicknesses d_1 and d_2 of hBN layers are much smaller than the wavelength of IR light. As a result, the Faraday rotation angle of encapsulated graphene (6.20) is almost the same as Faraday rotation angle of bare graphene (6.21)[3]

Kramers-Kronig relations

Magnetic circular dichroism and Faraday rotation are inherently related phenomena: quantities $D(\omega)$ and $\theta_F(\omega)$ taken at a particular value of magnetic field cannot be two arbitrary and independent functions of frequency. This has been explained in Section 2.3 from the point of view of magneto-optical transitions between the Landau levels. From a more general point of view, there exists a deep connection between $D(\omega, B)$ and $\theta_F(\omega, B)$ due to causality.

In the case of zero magnetic field, it has been shown [229, 230] that one can introduce an auxiliary complex function $\Omega = \Omega(\omega)$ the following way

$$\Omega(\omega) \equiv \ln t(\omega) = \sqrt{T} + i\theta(\omega)$$

and apply the Kramers-Kronig relations to this function provided $\ln t(\omega)$ does not have any poles or other singularities in the upper complex semiplane of its argument ω:

$$\theta(\omega) = -\frac{1}{\pi}\mathcal{P}\int_{-\infty}^{\infty} \frac{\ln\sqrt{T(\omega')}}{\omega' - \omega} d\omega' + \pi = -\frac{\omega}{\pi}\mathcal{P}\int_{0}^{\infty} \frac{\ln T(\omega')}{\omega'^2 - \omega^2} d\omega' + \pi, \quad (6.22)$$

here parity relation $T(\omega) = T(-\omega)$ is used to change the integration range.

In the case of non zero magnetic field, one has two equations similar to (6.22):

$$\theta_\pm(\omega) = -\frac{\omega}{\pi}\mathcal{P}\int_{0}^{\infty} \frac{\ln T_\pm(\omega')}{\omega'^2 - \omega^2} d\omega' + \pi, \quad (6.23)$$

Moreover, another complex auxiliary function $\Omega'(\omega)$ could be introduced:

$$\Omega'(\omega) \equiv \ln\left(\frac{t_-(\omega)}{t_+(\omega)}\right) = \frac{1}{2}\ln D(\omega) + 2i\theta_F(\omega),$$

and provided both $\ln t_\pm(\omega)$ are analytic functions, the Kramers-Kronig relations yield equation which connects transmission circular dichroism ratio and Faraday rotation angle:

$$D(\omega) = \exp\left[\frac{8\omega}{\pi}\mathcal{P}\int_{0}^{\infty} \frac{\theta_F(\omega')}{\omega'^2 - \omega^2} d\omega'\right]. \quad (6.24)$$

---

[3] Just as before, (6.20) and (6.21) must be compared for the same values of conductivities $\sigma_\pm$ regardless of frequency etc because formula (6.20) takes into account only wave optics phenomena and not the influence of hBN-encapsulation on charge carriers in graphene.

6.4 Kramers-Kronig analysis of magneto-optical spectra

Ultimate goal of magneto-optical spectroscopy is finding magneto-optical conductivity tensor $\hat{\sigma}(\omega, B)$ which could be then compared to theoretical predictions or used as a starting point for further analysis: for example modeling and predicting magneto-optical properties of graphene which have not been directly measured in the magneto-optical experiment which allowed finding $\hat{\sigma}(\omega, B)$ in first place. In practice this means that four real functions of frequency must be found: both real and imaginary parts of both $\sigma_+(\omega, B)$ and $\sigma_-(\omega, B)$ components. For comparison, in the absence of magnetic field only two functions must be found: real and imaginary parts of $\sigma(\omega)$. The whole procedure of restoring $\hat{\sigma}(\omega, B)$ must be done for each value of magnetic field separately.

Thus knowledge of the transmission curve $T = T(\omega, B)$ solely for unpolarized light at a particular value of magnetic field is not enough for restoring $\hat{\sigma}(\omega, B)$ unambiguously or without any supplementary model assumptions. Naively, one should perform experiments with circularly polarized light: investigate magneto-optical response of a solid body to each handedness of light separately and then apply well established zero-field methods for extracting the optical conductivities $\sigma_+(\omega, B)$ and $\sigma_-(\omega, B)$ separately. However, as it has been already mentioned in Section 5.2, generating circularly polarized light in a broad range of frequencies is challenging from technical point of view.

In this work, we performed FTIRS experiments with a pair of broad band linear polarizers in transmission regime, the protocol is described in Section 5.2. Such approach allows measuring physical quantities which are complicated function of the sample's relative transmission[4] $\widetilde{T} = \widetilde{T}(\omega, B)$, Faraday rotation $\theta_F = \theta_F(\omega, B)$ and transmission dichroism ratio $D = D(\omega, B)$, see formula (5.3). Even if transmission of the system is measured for many different positions α of the polarizers, only three above mentioned physical quantities could be found from the data obtained in the experiment. This is still not enough to restore the magneto-optical tensor $\hat{\sigma}(\omega, B)$.

Therefore in this work we profit from the Kramers-Kronig relations in order to obtain all components of $\hat{\sigma}(\omega, B)$. Indeed, Kramers-Kronig relations impose constraints on causal response functions including the magneto-optical response of a solid. As a result one physical quantity could be derived from another without any additional magneto-optical measurements. The Kramers-Kronig analysis has been already widely used for a long time to restore complex conductivity σ form an optical spectrum in the absence of magnetic field. However applying the Kramers-Kronig analysis in the case of magneto-optical spectra is not straightforward. Here is an example of such an approach: both optical conductivities $\sigma_\pm(\omega, B)$ could be obtained from equations (6.19) if four curves $T_\pm = T_\pm(\omega)$ and $\theta_\pm = \theta_\pm(\omega)$ are previously found from the experimental data and the Kramers-Kronig relations.

---

[4] A different signal normalization procedure potentially allows measuring transmission $T = T(\omega, B)$ instead, see Appendix E.

However using the Kramers-Kronig relations (6.23) and (6.24) for this purpose is not straightforward and leads to computational difficulties. Moreover, in some optical configuration the functions $\Omega(\omega)$ and $\Omega'(\omega)$ introduced at the end of the previous section do not have regular analytical behavior in the upper complex half plane of frequency. Therefore the Kramers-Kronig relations are no longer valid. In order to overcome these difficulties we approach the problem from a different perspective and use Kramers-Kronig constrained analysis similar to the one described in [231, 232].

Kramers-Kronig constrained fitting of spectra

Here we describe how to fully restore the magneto-optical conductivity tensor $\hat{\sigma}(\omega, B)$ from a minimum of two independent magneto-optical quantities measured in the experiment. In a simple case these two quantities could be for example transmission $T = T(\omega, B)$ together with Faraday rotation angle $\theta_F = \theta_F(\omega, B)$. In a more general case of transmission regime measurements these two quantities could be any combinations of $T_+(\omega, B)$, $T_-(\omega, B)$, and $\theta_F(\omega, B)$. Here the Faraday rotation angle is always involved because FTIRS experiments allow measuring only the difference but not the explicit values of the phases $\theta_\pm$.

Let us denote the two quantities measured in the FTIRS experiment by P and Q. In order to proceed with the analysis, both P and Q should be expressed in terms of Fresnel coefficients, in our case these are $t_\pm$. Next, equations (6.15) allow to relate the experimental quantities to the right- and left-handed optical conductivities and one can obtain the following expressions:

$$P = f_P(\omega, \sigma_+(\omega), \sigma_-(\omega)), \quad Q = f_Q(\omega, \sigma_+(\omega), \sigma_-(\omega)). \tag{6.25}$$

Here and later we omit the magnetic field argument to simplify the notation.

The main idea of our method is to profit from the Kramers-Kronig relations (2.13), (2.14) imposed on the real and imaginary parts of the optical conductivities $\sigma_\pm(\omega)$ which are *supposed to be found* in the end and not from the Kramers-Kronig relations as (6.23) imposed on the Fresnel coefficients nor from the Kramers-Kronig relations as (6.24) imposed on the optical quantities which are potentially available from an experiment. For this purpose, we introduce a set of complex functions of real frequency $s_j = s_j(\omega)$ which we call basis functions. These functions must be chosen in such a way that real and imaginary parts of each $s_j(\omega)$ are Kramers-Kronig consistent, explicit form of these functions is discussed later. Next, we represent conductivities $\sigma_\pm(\omega)$ as a sum of the basis functions the following way:

$$\sigma_+(\omega) = \sum_{j=1}^{N} R_j \left[s_j(\omega) + (s_j(-\omega))^* \right], \tag{6.26}$$

$$\sigma_-(\omega) = \sum_{j=1}^{N} L_j \left[s_j(\omega) + (s_j(-\omega))^* \right].$$

The terms $(s_j(-\omega))^*$ are added to ensure that optical conductivities satisfy the Onsager relations $(\sigma_\pm(\omega))^* = \sigma_\pm(-\omega)$, see Section 2.2. R_j and L_j where $j = \overline{1, N}$ are real numbers which do not depend on ω. They represent some unknown amplitudes, free parameters which must be found in order to restore $\sigma_\pm(\omega)$. First one should obtain expressions for the experimental quantities in terms of the amplitudes R_j and L_j simply substituting the formulas (6.26) into (6.25):

$$P = F_P(\omega, R_1, \, ... \, , R_N, L_1, \, ... \, , L_N), \tag{6.27}$$

$$Q = F_Q(\omega, R_1, \, ... \, , R_N, L_1, \, ... \, , L_N).$$

Now all amplitudes R_j and L_j could be found based on the experimental data and equations (6.27) with the help of various existing numerical optimization routines. We used the classical least-square minimization for this purpose. Our experimental data consists of three sets of data points: values of frequencies $\{\omega_i\}$, values of the optical quantities $\{P_i\}$ and $\{Q_i\}$ both measured at the above mentioned set of frequencies. We denote the number of data points in one set by M, thus $i = \overline{1, M}$. One should start with some reasonable initial guesses $R_j^{(\text{guess})}$ and $L_j^{(\text{guess})}$ for all amplitudes. Next, one should calculate two sets of values $\{P_i^{(\text{guess})}\}$ and $\{Q_i^{(\text{guess})}\}$ using the equations (6.27) at frequencies $\{\omega_i\}$ for the tentative values $R_j^{(\text{guess})}$ and $L_j^{(\text{guess})}$. We define the sum of squared residuals the following way:

$$\chi^2 \equiv \sum_{i=1}^{M} \left(P_i - P_i^{(\text{guess})}\right)^2 + \sum_{i=1}^{M} \left(Q_i - Q_i^{(\text{guess})}\right)^2 .$$

Minimization of χ^2 allows finding plausible values of the amplitudes $R_j^{(\text{fit})}$ and $L_j^{(\text{fit})}$. It is important to mention that χ^2 must contain at least two sets of data points corresponding to the optical quantities carrying independent physical information about the system. Otherwise, an adequate convergence of the fit would be impossible i.e. one could obtain $\chi^2 \to 0$ for different sets of values of the amplitudes $R_j^{(\text{guess})}$ and $L_j^{(\text{guess})}$ and it will not be clear which of the aforementioned sets describes magneto-optical response of the sample under investigation. Knowledge of all $R_j^{(\text{fit})}$ and $L_j^{(\text{fit})}$ allows restoring both components of the magneto-optical conductivity tensor $\hat{\sigma}(\omega, B)$:

$$\sigma_+^{(\text{fit})}(\omega) = \sum_{j=1}^{N} R_j^{(\text{fit})} \left[s_j(\omega) + (s_j(-\omega))^*\right], \tag{6.28}$$

$$\sigma_-^{(\text{fit})}(\omega) = \sum_{j=1}^{N} L_j^{(\text{fit})} \left[s_j(\omega) + (s_j(-\omega))^*\right].$$

Now knowledge of both conductivities $\sigma_\pm^{(\text{fit})}(\omega)$ gives an opportunity to calculate and plot as a function of frequency various physical quantities which have been introduced in the previous section: these are reflection, transmission, absorption of a hBN/Gr/hBN stack and absorption right in graphene for different handedness separately as well as for both handedness together, absorption dichroism, transmission dichroism ratio, Faraday rotation angle, etc. Thus Kramers-Kronig constrained fitting of spectra allows a better insight into the sample's behaviour without performing numerous magneto-optical experiments and most importantly without actually generating the circularly polarized light. In addition, if experimental curves P and Q do not have a straightforward and simple physical interpretation i.e. represent complicated combinations of $T_+(\omega)$, $T_-(\omega)$, and $\theta_F(\omega)$, then Kramers-Kronig constrained fitting of spectra allows "disentangling" them into more meaningful and habitual ones.

Choice of the basis functions

As it has been mentioned above, the real and imaginary parts of $s_j(\omega)$ must be Kramers-Kronig consistent. Therefore we start with some analytic functions of complex variable $S_j = S_j(z),\ z = \omega + i\omega'$ which does not have any singularities in the upper semiplane $\omega' \geq 0$. Next, the basis functions $s_j(\omega)$ correspond to the values of $S_j(z)$ on the real axis $\omega' = 0$. Convergence of the fit and precision of the result depend significantly on the exact shape and number N of the basis functions $s_j(\omega)$. In order to achieve a high precision of the fit, we introduce a large number of basis functions which coincides with the number M of the data points. One way of improving convergence of the fit in such a large parameter space, is to choose basis functions so that each $s_j(\omega)$ is well localized and centered around one frequency ω_j from the set of experimental data points. This approach allows fitting virtually any spectrum with high level of precision and minimal model assumptions about the nature of $\hat{\sigma}(\omega)$. At the same time special precautions possibly would be needed in order to avoid overfitting. Here is a possible choice of $S_j = S_j(z)$ which satisfies all the above mentioned requirements:

$$S_j(z) = \frac{i}{z - \omega_j + i\Gamma_j},$$

and corresponding basis functions take form of Lorentzians:

$$s_j(\omega) = \frac{i}{\omega - \omega_j + i\Gamma_j} = \frac{\Gamma}{(\omega - \omega_j)^2 + \Gamma_j^2} + i\frac{\omega - \omega_j}{(\omega - \omega_j)^2 + \Gamma_j^2}.$$

Here the frequencies $\{\omega_j\}$ around which the Lorentzians are centered are the same as frequencies of experimental data points $\{\omega_i\}$. The Lorentzians' widths $\{\Gamma_j\}$ should be assigned fixed values several orders of magnitude smaller than the frequency resolution of the spectra measured in the experiment. Thus the free parameters which remain to be found from the fit are the amplitudes $\{R_j\}$ and $\{L_j\}$. Other choices of the basis functions are discussed in [232].

Fit convergence and validity of the result

Strictly speaking, one can profit from the Kramers-Kronig relations only when behavior of the causal response functions is known at all values of frequency. However in reality, optical quantities are always measured in a finite region of electromagnetic spectrum. Thus, in the fitting procedure described above, the values of the conductivities $\sigma_{\pm}^{(\mathrm{fit})}(\omega)$ are found based only on the values of the optical quantities from a finite region of frequencies. This may lead to an incorrect result for $\sigma_{\pm}^{(\mathrm{fit})}(\omega)$ even if χ^2 is successfully minimized i.e. if at the end of the fitting procedure χ^2 becomes smaller than the sum of the squared errors of the optical quantities measured in the experiment. In order to mitigate this problem, both P and Q must be measured in a broad range of frequencies which contains all the key spectral features and/or both P and Q must be supplemented with reasonable extrapolations into the regions of spectrum where no experimental data is available.

For practical purposes, one may also develop a simple model of the material's magneto-optical conductivity $\sigma_{+}^{(\mathrm{sm})}(\omega, a_{\mathrm{R}})$ and $\sigma_{-}^{(\mathrm{sm})}(\omega, a_{\mathrm{L}})$ which contains a sum of relatively small number of Lorentzians, each one corresponding to a well defined resonance in the investigated material, a_{R} and a_{L} stand for all unknown free parameters of the simple model. In a proper model, each term would be Kramers-Kronig consistent and would satisfy the necessary symmetries due to the Onsager relations. An example of such a model is described in Section 2.2 in formula (2.19). Values of all unknown free parameters a_{R} and a_{L} should be found using the Kramers-Kronig constrained fitting procedure described in the previous subsection. In practice, the least-square fitting to a simple model could be made highly robust because such model contains a relatively small number of free parameters with well defined physical meaning. Once the values of a_{R} and a_{L} are found from the fit one can obtain components of the magneto-optical conductivity tensor in the approximation of the simple model $\sigma_{\pm}^{(\mathrm{sm\ fit})}(\omega)$. It is clear that a simple model cannot cover all pronounced spectral features without distortion and it cannot at all grasp subtle features which are not envisaged in its framework. Still, there are two practical advantages of having such a model before starting a "full scale" model independent fitting procedure described in the previous subsection:

- it provides reasonable extrapolations of $\sigma_{\pm}(\omega)$ beyond the spectral range accessible in the experiment;
- it simplifies the choice of the tentative values $R_j^{(\mathrm{guess})}$ and $L_j^{(\mathrm{guess})}$.

Now model independent Kramers-Kronig constrained fitting procedure should be performed the following way. The magneto-optical conductivities $\sigma_{\pm}(\omega)$ should be expressed as a combination of the simple model conductivities $\sigma_{\pm}^{(\mathrm{sm\ fit})}(\omega)$ and expansions with the basis functions $s_j(\omega)$:

$$\sigma_{+}(\omega) = \sigma_{+}^{(\mathrm{sm\ fit})}(\omega) + \sum_{j=1}^{N} R_j \left[s_j(\omega) + (s_j(-\omega))^* \right], \qquad (6.29)$$

$$\sigma_-(\omega) = \sigma_-^{(\text{sm fit})}(\omega) + \sum_{j=1}^{N} L_j \left[s_j(\omega) + (s_j(-\omega))^*\right].$$

In this approach $\sigma_\pm^{(\text{sm fit})}(\omega)$ gives a rough description of $\sigma_\pm(\omega)$ meanwhile expansion with the basis functions provides a fine adjustment of $\sigma_\pm(\omega)$ and ensures that the final result is largely independent from the assumptions made in the simple model. The amplitudes R_j and L_j are supposed to have small values in the representation of the magneto-optical conductivities (6.29). This leads to a reasonable choice of the tentative values for the amplitudes $R_j^{(\text{guess})} = L_j^{(\text{guess})} = 0$ which largely improves convergence of the fit and validity of the final results. In contrast, the amplitudes R_j and L_j in the representation of the magneto-optical conductivities (6.26) may have any values. Our experience shows that the wrong choice of $R_j^{(\text{guess})}$ and $L_j^{(\text{guess})}$ may lead to that fact that the fit converges to an apparently wrong unphysical result.

In general, validity of the whole approach described in this section has not been proven with full mathematical rigor. In fact it is well known that recovery of an analytic in the upper half-plane function from experimental data on the real axis is an ill-posed task and contains a number of problems [233]. Nevertheless, in our case such an approach has given a plausible physical result. Successful convergence of the fit largely depends on the proper choice of $\sigma_\pm^{(\text{sm})}(\omega)$ which is supposed to push the convergence of the fit in the proper direction.

Chapter 7

Magneto-optical properties of hBN-encapsulated graphene

7.1 Overview

In this chapter we present infrared magneto-optical transmission and Faraday rotation spectra of three high quality suspended hBN-encapsulated graphene membranes. Our graphene membranes have the same structure but different dimensions and twist angles between graphene and hBN crystals, see Section 3.2 for more details. All magneto-optical measurements presented in this work have been performed with the Fourier transform infrared (FTIR) spectroscopy [135, 136, 137, 138]. A graphene membrane was illuminated with broad spectrum infrared light which was either non-polarized or linearly polarized in different experiments. Intensity of the light transmitted through the membrane was measured as a function of frequency ω and external magnetic field B. The values of magnetic fields applied to graphene during the experiment fall into the range between 0 and 4.1 Tesla. All optical measurements were performed at the same *base* temperature of $\sim$ 5 Kelvin. However temperature of the graphene membranes could not be directly measured[1]. Modeling of the thermal fluxes and temperature distribution shows that the actual temperature of the graphene crystals could be up to several tens Kelvin higher than the base temperature in the sample compartment.

Magneto-optical properties of hBN/Gr/hBN stacks were probed in a broad range of energies from 14 meV to 1.74 eV i.e. in the far, middle and near infrared regions of light wavelengths. For energies below 400 meV, we observed pronounced absorption lines and large angle of Faraday rotation due to magneto-optical transitions between the Landau levels. At the same time there were not any clearly discernible spectral features at photon energies higher than 400 meV.

---

[1] It is a typical problem when working with small samples which have relatively poor thermal contact with the cold finger.

Most of the spectral features were reproduced in all three hBN/Gr/hBN samples, however there are some noteworthy differences which are discussed in the next sections. Many of the experiments were repeated on different days with large time intervals in between, the largest time interval for the same sample was 15 months. This allowed us to verify the reproducibility of results and also monitor the evolution of hBN/Gr/hBN membranes with time. All hBN/Gr/hBN membranes proved to be robust, survived ambient air, more than a dozen cycles from room temperature down to cryogenic temperatures, annealing at 200°C and even withstood deposition of ice on the hBN surface. In between the procedures the samples were stored in a desiccator in 10^{-3} mbar vacuum. In the end, we observed pronounced signatures of magneto-optical transitions even more than 18 months after the sample fabrication. This demonstrates once again the usefulness of hBN-encapsulation for preservation of graphene's quality.

In contrast, our non-encapsulated suspended graphene membranes quickly degraded. Their MIR spectra did not contain any discernible signatures of magneto-optical transitions. Therefore we conclude that most probably the non-encapsulated suspended membranes did not survive ambient conditions and were already damaged during the first magneto-optical experiment.

At the same time, we also noticed some sign of degradation of our hBN/Gr/hBN membranes, for example, slight broadening of magneto-optical absorption lines and change of their shape many months after the sample fabrication. We also noticed some uncontrollable increase of doping with time which influenced the magneto-optical spectra as well.

The most important experiments and the hBN/Gr/hBN samples with which they have been performed are listed in Table 7.1. We provide the exact dates of the experiments so that comparison of the results obtained on different days would be more adequate. Apart from that, we also performed Kramers-Kronig constraint fitting of the spectra which allowed restoring the magneto-optical conductivity tensor $\hat{\sigma}(\omega, B)$ for several values of magnetic fields. Based on $\hat{\sigma}(\omega, B)$ we calculated the magneto-absorption of graphene for circularly polarized light.

Evolution of doping

Presumably, graphene had low residual extrinsic doping just after the hBN/Gr/hBN stacks were assembled. The exact value of doping was not measured then, however its order of magnitude could be inferred from transport measurements performed on similar hBN/Gr/hBN samples assembled with the same method. Thus, [83] report charge carrier concentration $|N| \sim 10^{10}$ cm^{-1} due to residual extrinsic doping.

Magneto-optical spectra allow finding the value of charge carrier concentration. "Pauli blocking" of the T_1 magneto-optical transition (or higher transitions $n \geq 2$ in the case of strong doping) is a clearcut optical signature which depends on the position of the chemical potential. This allowed us to find the charge carrier concentration $|N| \sim 10^{11}$ cm^{-1} from the FIR spectra measured on the 50 μm

Experiment and/or physical quantity	**Diameter $\varnothing$ of the hBN/Gr/hBN membrane and date**
MIR transmission	50 μm – 2015 Sep 23, 2016 Jun 11–12, 2016 Dec 21, 2017 Jan 12 30 μm – 2015 Aug 29, 2015 Nov 10 and 12 20 μm – 2015 Sep 4
FIR transmission	50 μm – 2015 Dec 11, 2016 Jul 21–25, 2016 Nov 7–8
NIR transmission	50 μm – 2015 Dec 12 30 μm – 2015 Nov 12
MIR Faraday rotation & transmission	50 μm – 2016 Dec 20 30 μm – 2015 Nov 25, 2015 Dec 2
FIR Faraday rotation & transmission	50 μm – 2016 Nov 9
MIR non-linearity	50 μm – 2016 Dec 21
$\hat{\sigma}(\omega, B)$ and $A_{\pm}$ obtained from the KK constraint fit (data of MIR Faraday rotation & transmission)	50 μm – 2016 Dec 20

Table 7.1 – List of the magneto-optical experiments. hBN/Gr/hBN membranes were fabricated in June 2015.

sample on 2016 Nov 7 and 8. We also registered some spectral signatures which imply in a less direct way that the doping of graphene increased with time. Namely, the depth of the T_1 absorption line registered in the MIR region slightly decreased with time which is most likely explained by the increase of the doping and subsequent redistribution of the spectral weight in favor of the intraband magneto-optical transitions by the cost of the T_1 transition.

The reason why the doping increased is not fully clear. Presumably the membranes became covered with a thin layer of polar carbohydrates after some exposure to air between the multiple procedures they underwent and many thermal cycles of cooling down to cryogenic temperatures. Apart from that, our biggest 50 μm membrane was contaminated on 2016 Jun 4 by a droplet of some unknown condensate which formed on it when the sample was in the cryostat. Then the sample was soaked in water, ethanol, acetone and annealed in the argon and hydrogen gas blend (the highest temperature was 200°C) to remove the droplet. Presumably, the accident and the cleaning procedures could have shifted position of the chemical potential in an uncontrollable way.

We assume that during one day of measurements the doping remained constant. It is important to mention that in our samples it is the charge carrier concentration which remained constant, at the same time position of the chemical potential moved in response to the changes of the external magnetic field, see Sections 2.2 and 7.3.

7.2 Middle infrared transmission: interband transitions

We performed many series of MIR relative transmission measurements with unpolarized light on all three hBN/Gr/hBN membranes we had. All the measurements were done as described in Section 5.1, the results are shown in Figures 7.2 – 7.7, 7.9, 7.11, and 7.12. As one can see, transmission spectra contain a series of pronounced lines which move to higher energies as magnetic field grows. They correspond to the interband magneto-optical transitions between the Landau levels $T_i,\ i \geq 2$, see Figure 7.1 (for a more ample description and labeling of the magneto-optical transitions see Section 2.3). At high magnetic fields > 3 Tesla, yet another line becomes visible in the low region of the MIR energies: it is T_1 due to the mixed transitions. In the MIR region, the energies of photons are much higher than temperature of the samples $k_B T < \hbar\omega_{\text{MIR}}$. Apart from that, for charge carrier concentration $|N| \sim 10^{11}$ cm^{-1}, chemical potential resides at energies which correspond to the photons from the lowest part of the MIR region $\mu \lesssim \hbar\omega_{\text{MIR}}$. As a result, the transmission spectra of our samples cannot have any signatures of intraband transitions in the MIR region. In fact, our MIR transmission spectra resemble those of pristine graphene at zero temperature.

A remarkable finding of our experiments is that the absorption lines are very deep and sharp compared to what has been reported so far, see Section 2.5. In our samples, the quantum regime of magneto-optical excitations (i.e. the lines remain well separated) persists even at low magnetic fields ~ 1 Tesla, see panel b of Figure 7.3. At medium and high magnetic fields $2-4$ Tesla, we could routinely discern up to 7 absorption lines $T_i,\ 1 \leq i \leq 7$ in all three hBN/Gr/hBN samples, see panel a of Figure 7.2 and Figure 7.9. Moreover, in the case of 30 μm hBN/Gr/hBN membrane we could clearly discern even 10 absorption lines $T_i,\ 1 \leq i \leq 10$ in the spectra measured about two month after the sample was manufactured. However two and a half months later we could not reproduced this result and only 7 absorption lines remained, see Figure 7.9, which is most probably related to a slight degradation of the hBN/Gr/hBN sample with time. For comparison, in the previously reported works a maximum of 3 well-separated lines were usually observed in FTIRS experiments, more lines were resolved only in exceptional cases, see Section 2.5. Such a difference cannot be fully explained by the problem of overlighting in the previous experiments. In fact this is a direct signature that the line broadening mechanisms are much weaker in hBN/Gr/hBN heterostructures compared the unprotected graphene crystals. The low scattering rate of the charge carriers is in turn related to the high purity and supreme quality of the hBN/Gr/hBN membranes. The lifetime of an electron in its excited state could be estimated from the line's

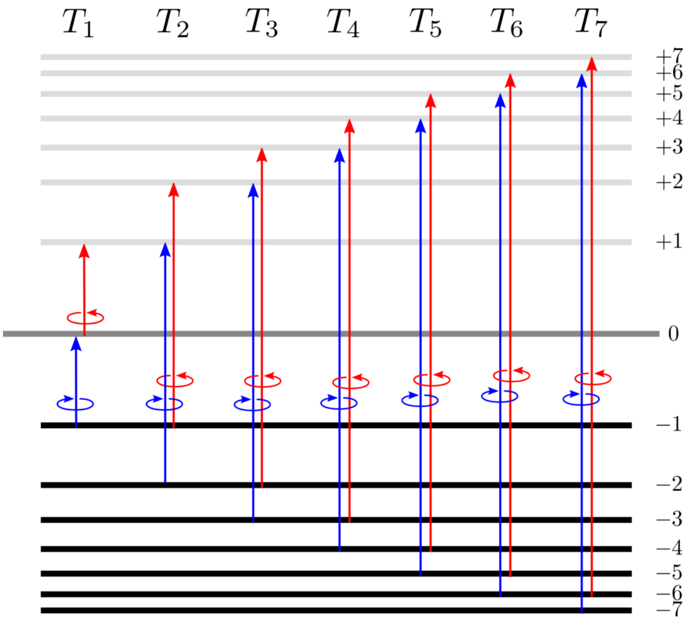

Figure 7.1 – Mixed and interband magneto-optical transitions which give rise to the absorption lines in the MIR spectra of hBN/Gr/hBN membranes presented in this section. Black, dark gray and light gray horizontal lines depict fully filled, partially filled and empty Landau levels correspondingly. Red and blue vertical arrows depict electronic excitations accompanied by absorption of photons with right and left circular polarizations correspondingly. Landau levels' fillings depicted in this figure correspond to pristine or weakly doped graphene at zero temperature.

width at half minimum. For example for T_1, the full width is $\gamma_1 = 3.6$ meV at 3.92 Tesla, see Figure 7.2, which yields lifetime $\tau = 2\hbar/\gamma_1 \approx 0.4$ ps.

Interestingly, the number of clearly discerned lines remains the same in a large range of magnetic fields, $1.5 - 4$ Tesla, despite the fact that in higher magnetic fields the lines stand further away form each other (the spacing between the lines grows with magnetic field as $\sqrt{B}$). In fact less lines could be discerned only when they become very weak in low magnetic fields. A constant number of lines has been noticed in the previous magneto-optical experiments on graphene and especially investigated in [234] with a help of an experimental method which allows to increases apparent contrast of the lines. The constant number of absorption lines is related to the fact that scattering mechanisms and consequently the line broadening become more pronounced as magnetic field grows [64]. Thus determining the maximum possible number of clearly discerned absorption lines is an interesting conceptual question.

The deepest absorption line is observed at our highest magnetic fields of ~ 4 Tesla and corresponds to the T_1 magneto-optical transition: relative transmission falls down to 0.6 in the narrow region of energies around T_1. Such large value of magneto-absorption is directly related to the narrow width of the line. Transmission dips corresponding to the higher magneto-optical transitions $T_i,\ 2 \leq i$ are also noticeable but less intense $\widetilde{T}(\omega, B) \gtrsim 0.9$. At photon energies > 480 meV, the relative transmission of hBN/Gr/hBN stacks becomes equal to unity within the error of measurement even at our highest magnetic field of ~ 4 Tesla. This means that at these energies the optical properties of graphene are no longer influenced by the magnetic field and its transmission $T(\omega, B)$ is almost the same as in the absence of magnetic field.

The relative transmission becomes greater than unity at photon energies which lay in between the discernible T_i transitions, see Figures 7.2, 7.3 and 7.4. This means that in an external magnetic field, a graphene monolayer becomes more transparent in between the absorption lines compared to the case of zero magnetic field i.e. $T(\omega, B) > T(\omega, 0)$ for $\hbar\omega$ not matching T_i. This effect is easily explained by the redistribution of the spectral weight in the $\mathrm{Re}\,\sigma_{\pm}(\omega, B)$ in favor of the absorption lines T_i on the cost of the nearby regions in between the lines. Such an effect is rarle reported despite its apparent triviality. Most probably, overfilling, lack of proper normalization procedure, or proper baseline correction were the main obstacles for registering $T(\omega, B) > T(\omega, 0)$ in many previous magneto-optical experiments, see Section 2.5.

In general, the main spectral features were fairly reproduced in all three samples, see Figure 7.9.

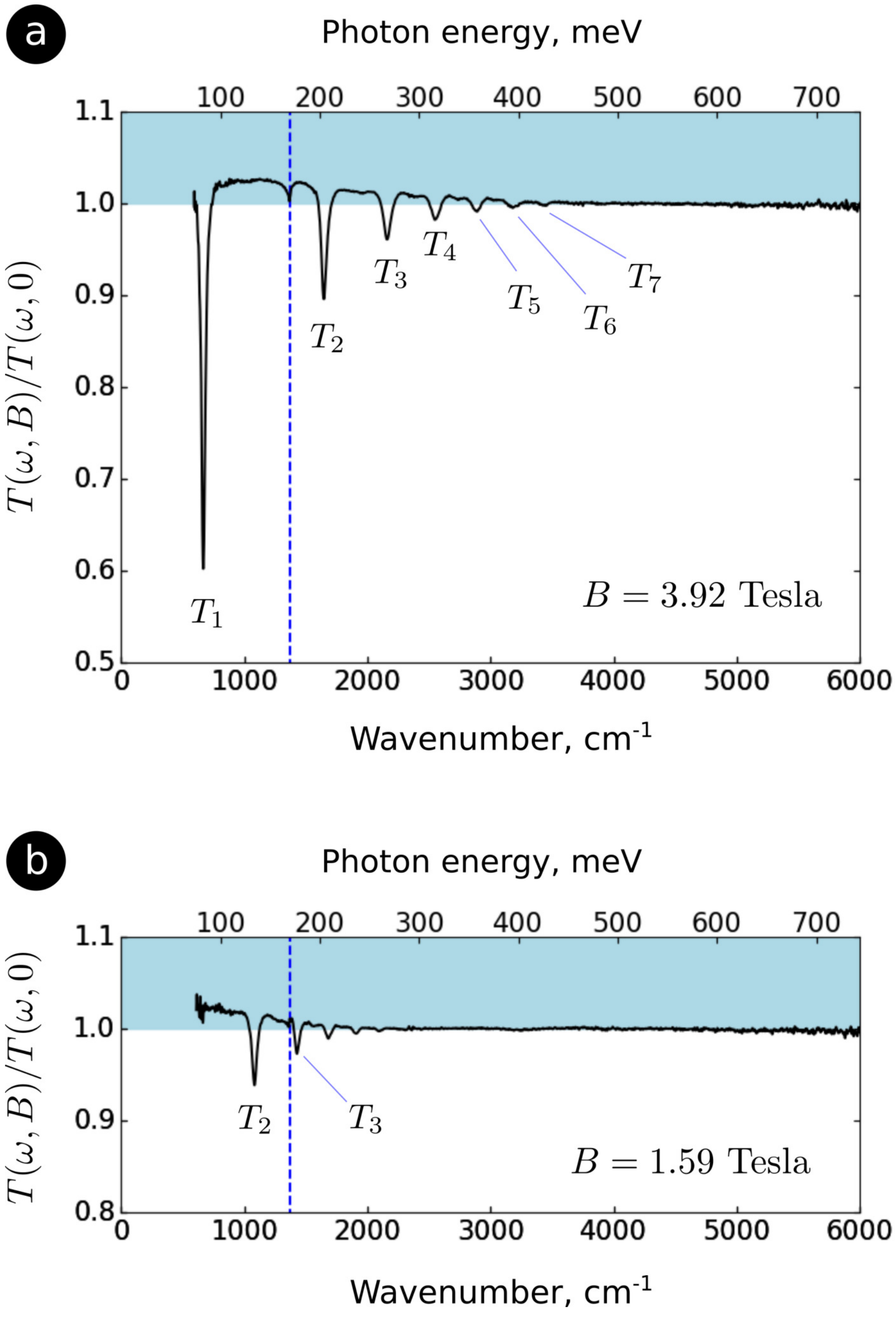

Figure 7.2 – MIR relative transmission spectra $T(\omega, B)/T(\omega, 0)$ of the 50 μm hBN/Gr/hBN membrane, measurements performed on 2015 Sep 23. The two panels have the same scales of both axes to simplify comparison of the curves. The blue dotted line designates energy of optically active hBN phonon. Data presented in the panel b is also plotted in the panel a of Figure 7.3 but in a different scale which allows to see more details. Resolution 5 cm^{-1}.

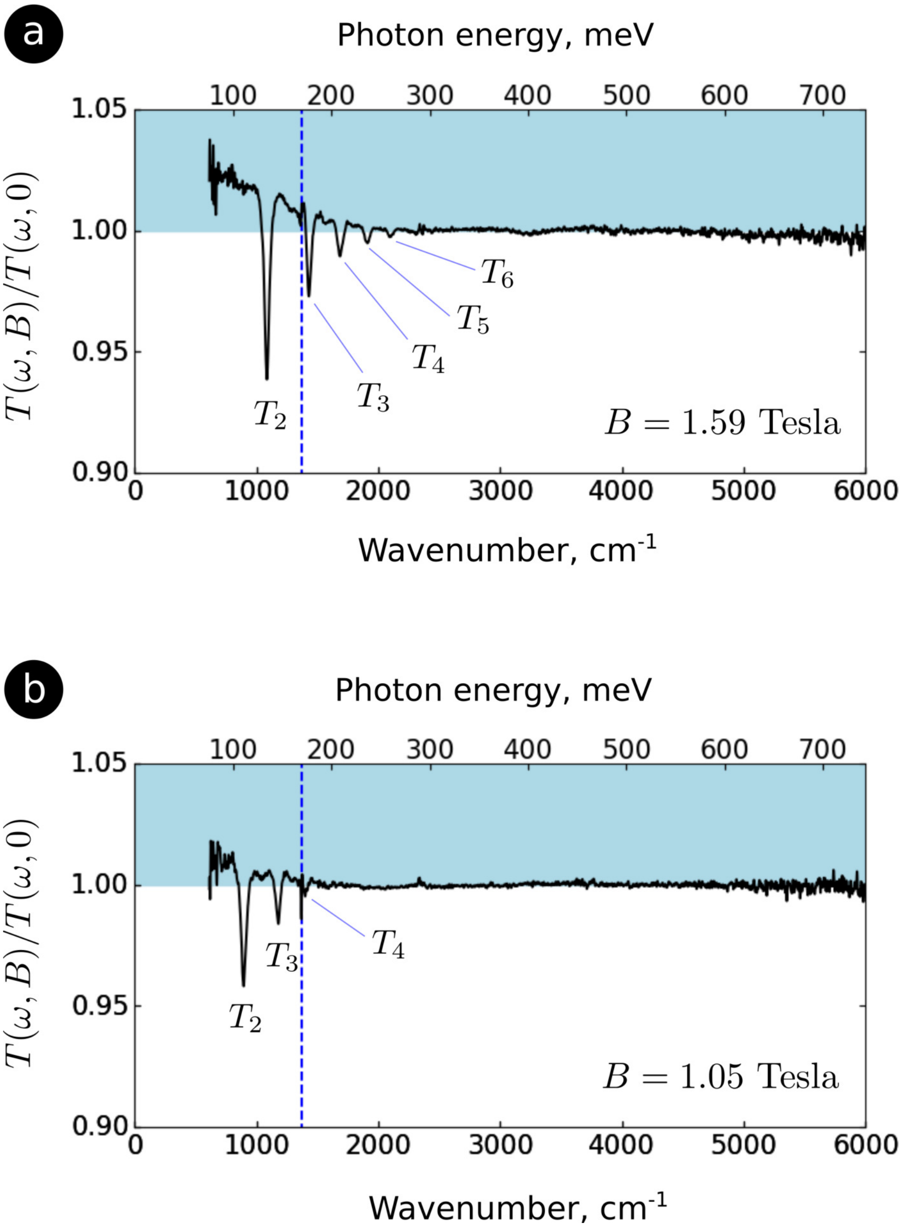

Figure 7.3 – MIR relative transmission spectra $T(\omega, B)/T(\omega, 0)$ of the 50 μm hBN/Gr/hBN membrane, measurements performed on 2015 Sep 23. The two panels have the same scales for both axes to simplify comparison of the curves. Blue dotted line designates energy of optically active hBN phonon. Resolution 5 cm^{-1}.

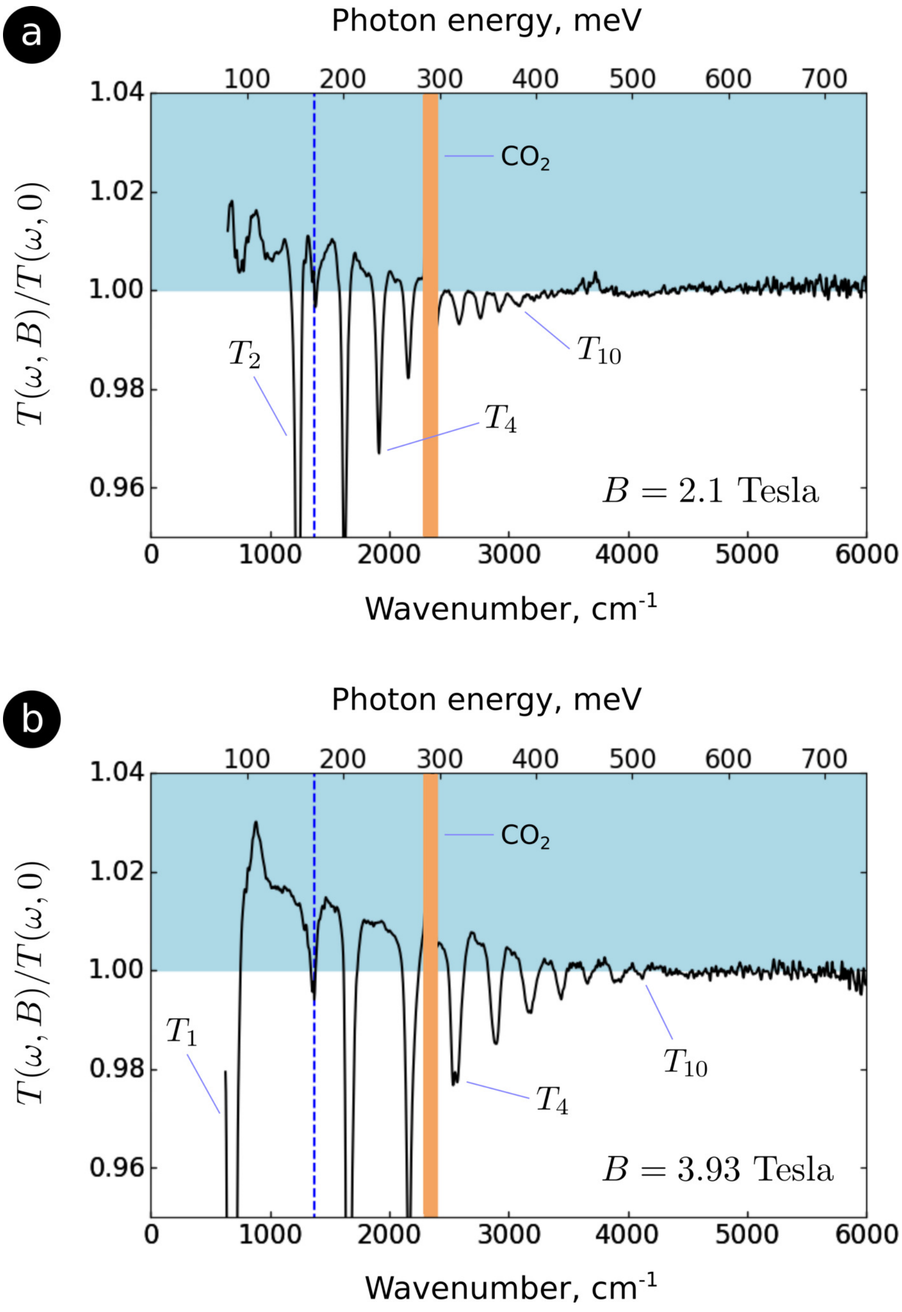

Figure 7.4 – MIR relative transmission spectra $T(\omega, B)/T(\omega, 0)$ of the 30 μm hBN/Gr/hBN membrane, measurements performed on 2015 Aug 29. Up two 10 absorption lines could be told apart. T_4 absorption line has a peculiar two-humped shape in high magnetic field. Blue dotted line designates energy of optically active hBN phonon. Resolution 10 cm^{-1}.

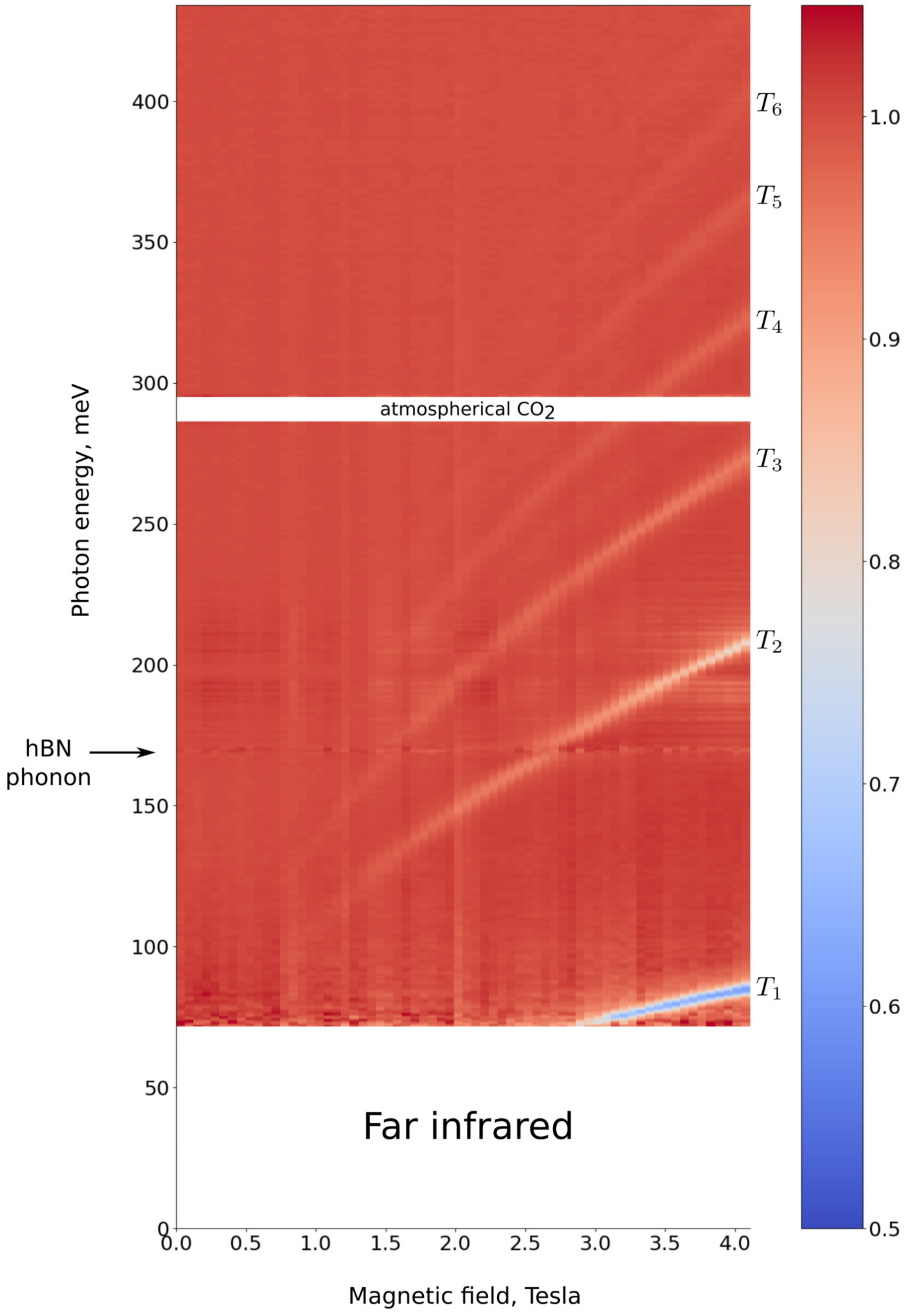

Figure 7.5 – Colorplot of MIR relative transmission spectra $T(\omega, B)/T(\omega, 0)$ of the 50 μm hBN/Gr/hBN membrane, measurements performed on 2017 Jan 12. Resolution 8 cm^{-1}, step in magnetic field 0.06 Tesla.

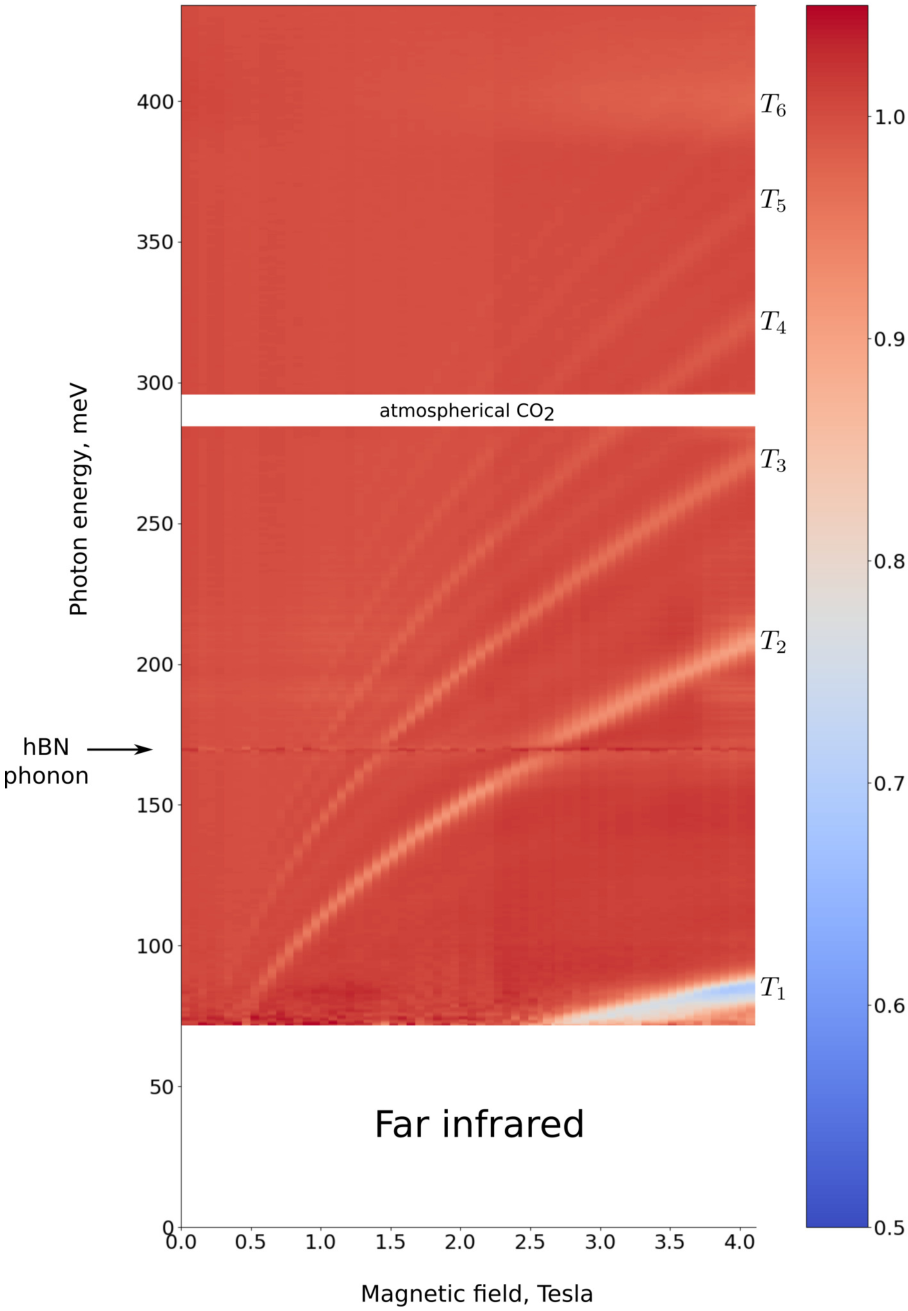

Figure 7.6 – Colorplot of MIR relative transmission spectra $T(\omega, B)/T(\omega, 0)$ of the 30 μm hBN/Gr/hBN membrane, measurements performed on 2015 Nov 10 and 12. Resolution 8 cm^{-1}, step in magnetic field 0.06 Tesla.

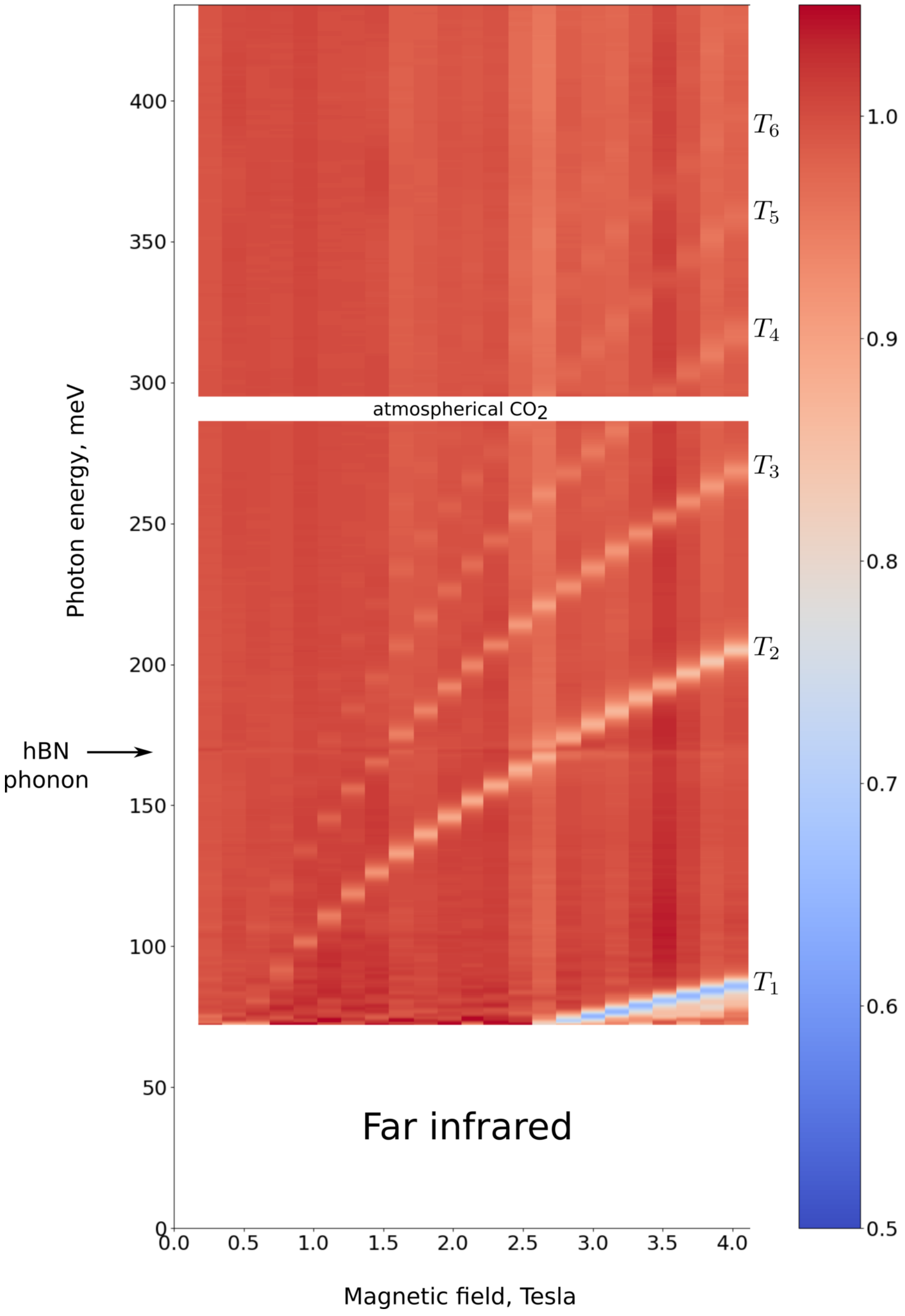

Figure 7.7 – Colorplot of MIR relative transmission spectra $T(\omega, B)/T(\omega, 0)$ of the 20 μm hBN/Gr/hBN membrane, measurements performed on 2015 Sep 4. Resolution 10 cm^{-1}, step in magnetic field 0.17 Tesla.

Energies of absorption lines

We find characteristics of the absorption lines observed in the relative transmission spectra by fitting each line with an upside-down Lorentzian:

$$L(\omega) = C - I \frac{\gamma/2}{(\omega - \omega_{\text{sl}})^2 + (\gamma/2)^2}, \tag{7.1}$$

here we have four free parameters: γ is full width of the line, ω_{sl} is wavenumber of the line, I is line's intensity, and C is some vertical offset which compensates for the contributions coming from the other spectral lines to the final value of relative transmission around the frequency ω_{sl} (subscript "sl" stands for "single line"). We extracted energies of absorption lines with the help of a Lorentzian fit described above, the result is shown in Figure 7.8.

In the framework of a simple theory, the energies of the lines are given by the formula (2.25) which we rewrite here the following way:

$$T_i^{\text{(theory)}} = v_F \sqrt{2e\hbar B} \left(\sqrt{i} + \sqrt{i-1} \right), \quad i \geq 1. \tag{7.2}$$

The Fermi velocity v_F is a constant defined by the band structure of graphene monolayer. A priori the exact value of v_F is not known. In order to simplify comparison of the actual line energies T_i found in the experiment with the prediction $T_i^{\text{(theory)}}$ of a simple theory, we introduce the reduced line energies

$$T_i^{\text{(reduced)}} \equiv \frac{T_i}{\sqrt{2e\hbar B} \left(\sqrt{i} + \sqrt{i-1} \right)} = v_F \frac{T_i}{T_i^{\text{(theory)}}}. \tag{7.3}$$

Comparing the formulas (7.2) and (7.3), one can see that for our graphene samples the reduced line energy T_i^{reduced} has meaning of an "effective Fermi velocity" if one wants to stick with terminology of the single-particle nearest neighbor tight-binding model. The reduced energies are plotted in the middle panel of Figure 7.8. There is a clearly visible trend that deviations of the line energies from prediction of the simple theory depend of magnetic field as well as on the number i of the absorption line.

Such deviations have been already reported in the infrared [141] and Raman [235] spectra as well as STS experiments [48] on graphene. Many theoretical works attribute these deviations to the renormalization of the Landau level energies by the Coulomb interactions, however currently there is not any clear consensus about this problem [48, 49]. In the lowest panel of Figure 7.8, we plot the reduced energies in yet another scale to simplify comparison with the existing theoretical predictions which suggest a linear dependency of $T_i^{\text{(reduced)}}$ on $\ln \sqrt{B/B_o}$, here we choose $B_o = 1$ Tesla. Apart from interaction effects, renormalization of the Fermi velocity has also been attributed to the moiré superlattice in the framework of a single-particle theory [200, 201].

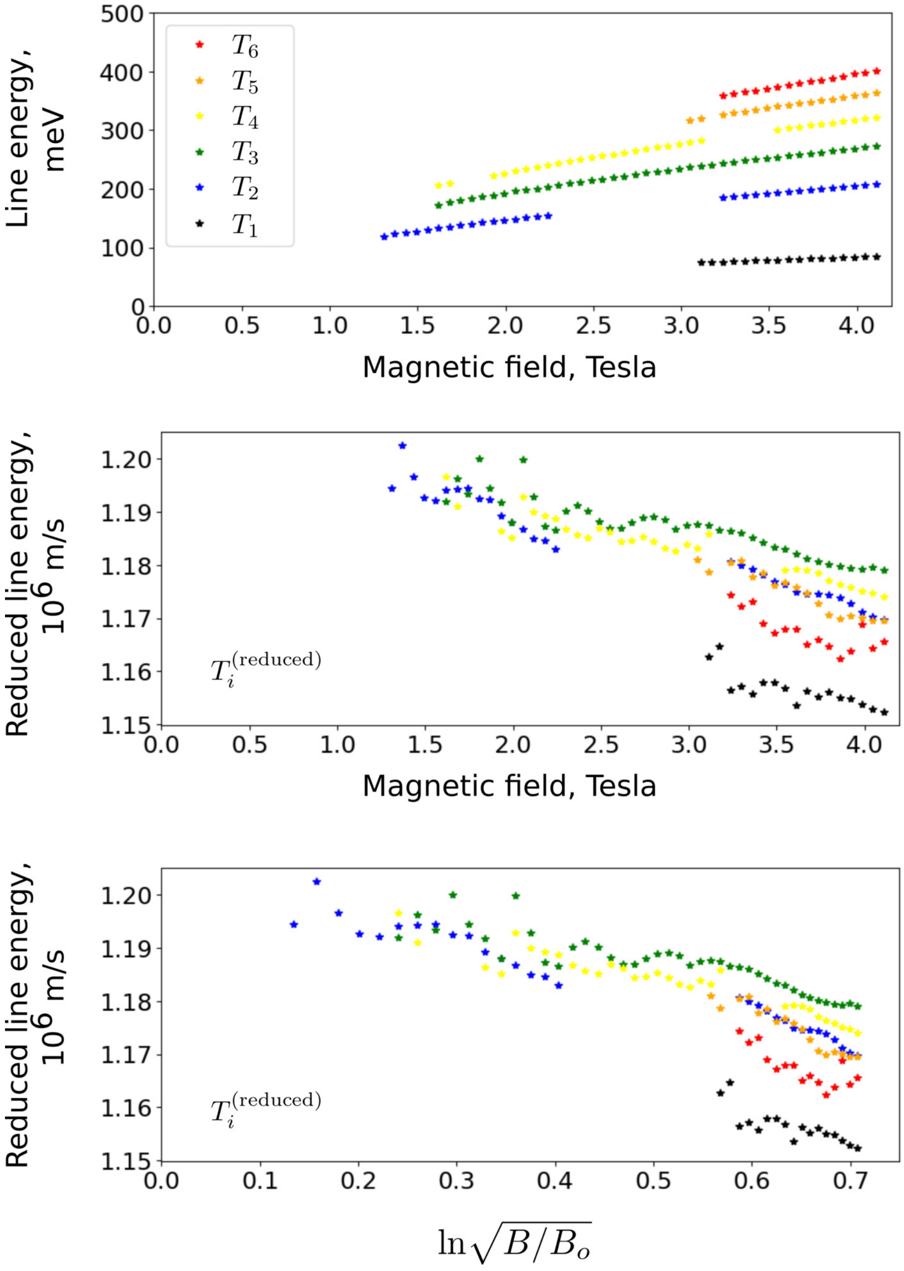

Figure 7.8 – Energies of absorption lines extracted from the magneto-optical relative transmission spectra measured on the 50 μm hBN/Gr/hBN membrane on 2017 Jan 12, see Figure 7.5. The three panels present the same data about line energies in three different ways. Definition of the reduced energy is given in the formula (7.3). In the lowest panel $B_o = 1$ Tesla. All three panels have the same color code.

“Forbidden” magneto-optical lines

Apart from the T_i lines, the magneto-optical spectra contain additional lines of smaller intensity which we denote F_i, $1 \leq i \leq 5$, see Figure 7.9, slight traces of F_i could be also spotted in Figures 7.5, 7.6, 7.7 however their color scheme is not optimal for this purpose. F_i lines are present in the spectra of all three hBN/Gr/hBN samples, their signatures are most pronounced in the 30 μm sample. Each F_i is always situated in between the usual lines T_i and T_{i+1} and they all move to higher energies without changing their order as magnetic field increases. The lines F_i cannot be identified with any kind of magneto-optical transition described in Section 2.3. Thus it seems that F_i do not satisfy the usual magneto-optical selection rule valid for T_i i.e. for the F_i absorption lines

$$\Delta_n \equiv |n_{\mathrm{f}}| - |n_{\mathrm{in}}| \neq \pm 1. \tag{7.4}$$

Selection rule $\Delta_n = \pm 1$ for graphene monolayer has been derived in the framework of ideal Dirac cones approximation. In general, selection rules and absorption rates of magneto-optical transitions are defined by the crystalline symmetry and characteristics of the electron wave functions. As an example, bilayer and trilayer graphene as well as bulk graphite have different symmetries, as a result, each of the above mentioned materials has a peculiar magneto-optical behaviour distinct from graphene's despite all of them belong to the same family of carbon allotropes. Theoretical work [236] showed that taking into account trigonal warping in graphene bilayer leads to unlocking of additional magneto-optical transitions which obey the selection rule $\Delta_n = \pm 2$. Apart from that, disorder in graphene also unlocks magneto-optical transitions of different type which violate the usual selection rule $\Delta_n = \pm 1$. Thus, theoretical work [237] predicts emergence of interband transitions symmetric relative to the Dirac point: $-1 \to +1$, $-2 \to +2$, $-3 \to +3$ etc which obey the following selection rule $\Delta_n = 0$, see panel b of Figure 7.10. Other disorder-induced transitions, including mixed and intraband transitions, with selection rules $\Delta_n = \pm 2, \pm 3$, ... have lower intensities compared to the symmetric ones, see panel d of Figure 7.10.

Phenomenon similar to our “forbidden” lines has been reported in the magneto-optical spectra of multilayer epitaxial graphene[2] on SiC [129]. Moreover, it has been shown that the “forbidden” lines become weaker after annealing – a procedure which usually reduces the disorder in samples. The last observation confirms scenario [237]. Meanwhile, in our samples the F_i lines had different intensities on different days of cooling down to liquid helium temperatures and measurements which makes it difficult to draw any final conclusions.

Energies of F_i lay in the MIR region therefore we suppose that if F_i are caused by a special class of magneto-optical transitions then these must be mixed and/or interband transitions and not the intraband transitions. Unfortunately, knowledge

---

[2] Interestingly, this type of graphene often also has a moiré superlattice due to the neighboring layers of graphene.

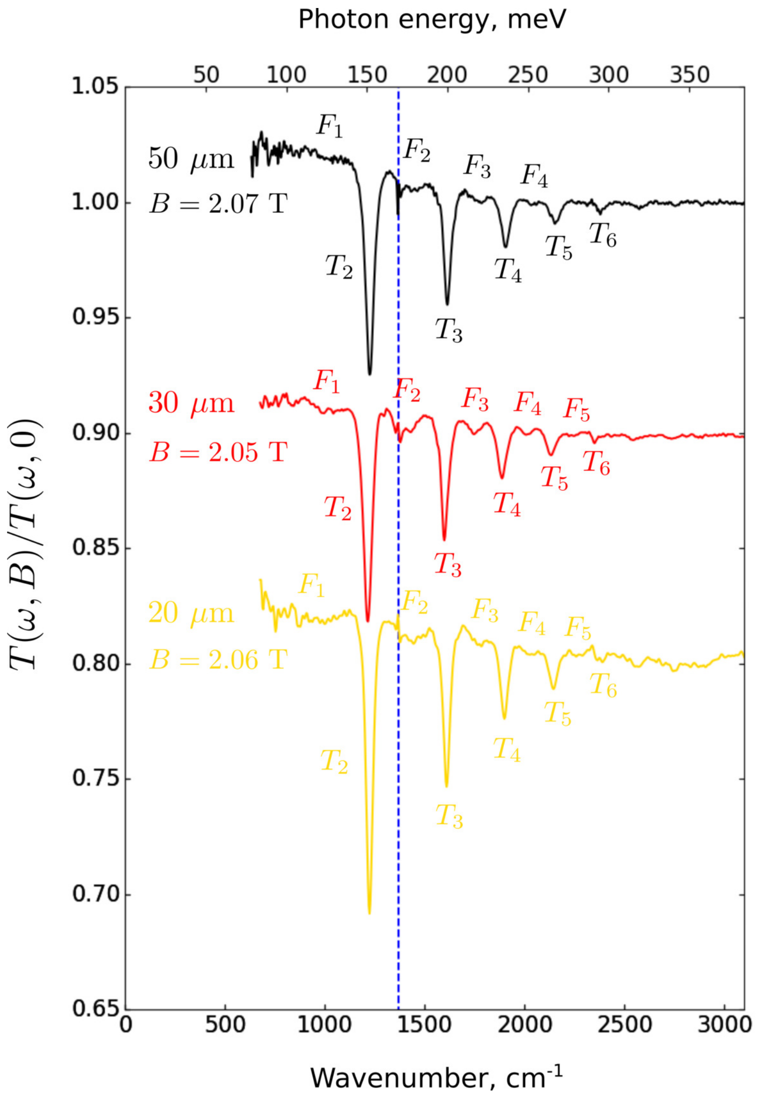

Figure 7.9 – MIR relative transmission spectra $T(\omega, B)/T(\omega, 0)$ of the three hBN/Gr/hBN membranes measured at almost the same values of magnetic field ≈ 2 Tesla. The main spectral features are reproduced in all three samples. "Forbidden" absorption lines F_i have low intensity and reside in between the main absorption lines T_i which have much higher intensity. F_i are most pronounced in the spectra of the 30 μm hBN/Gr/hBN membrane. The spectra were measured on 2015 Sep 23 for the 50 μm membrane with resolution 5 cm^{-1}, on 2015 Nov 10 and 12 for the 30 μm membrane with resolution 8 cm^{-1}; on 2015 Sep 4 for the 20 μm membrane with resolution 10 cm^{-1}.

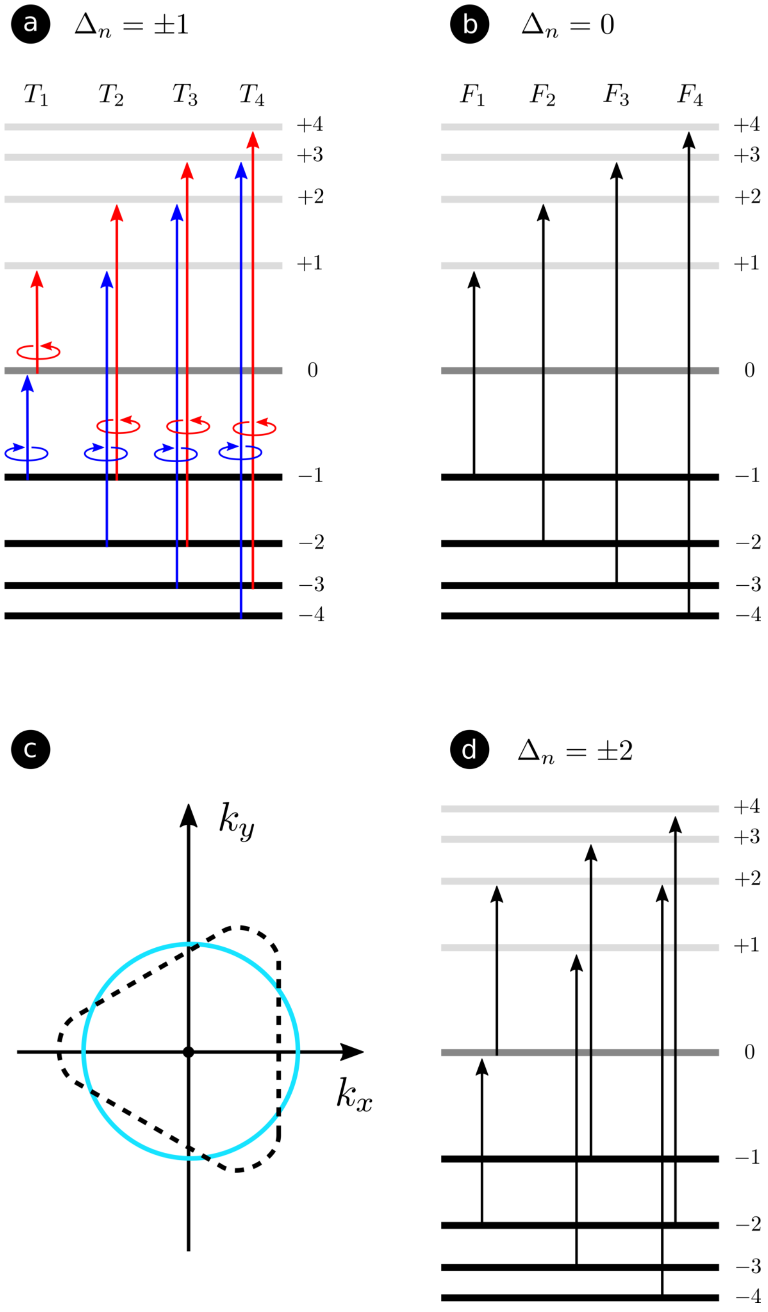

Figure 7.10 – Panel a: Magneto-optical transitions T_i compatible with the simple theory. **Panels b and d:** Hypothetical magneto-optical transitions to which the F_i lines could be attributed. **Panel c:** Schematic illustration of the trigonal warping in 2D crystals. Blue circle shows constant energy cross section of a dispersion relation which neglects the trigonal warping, dashed black line shows the same energy cross section when the trigonal warping is not neglected.

of exact positions of the F_i does not help to straightforwardly reveal the selection rule which these transitions obey. Presumably energies of the Landau levels are renormalized (see the previous subsection) which makes analysis much more complicated compared to the case of the single electron theory. Thus, the nature of the "forbidden" lines is not clear and requires more investigations. Faraday rotation curves presented in the next sections do not clarify the origin of F_i lines either. As so little is known about the F_i lines, currently one cannot exclude other than the $\Delta_n \neq \pm 1$ explanations of their emergence.

In the end, we would like to emphasize that "forbidden" absorption lines F_i have been registered in the linear response regime because in the FTIRS experiments the samples are illuminated with infrared light of relatively low intensity. In our case absorption of photons during magneto-optical transitions is an elastic process. Magneto-optical transitions which obey the $\Delta_n = 0$ selection rule have been also reported and described from theoretical point of view in the magneto-Raman spectra of graphene [238, 239]. However Raman shift is a non-linear and non-elastic phenomenon which could be observed only when graphene is illuminated by a powerful light source. In a typical magneto-Raman experiment, graphene is illuminated with a monochromatic light of a laser. Thus magneto-optical transitions $\Delta_n = 0$ active in Raman spectra must not be confused with F_i.

Splitting of the T_4 absorption line

We observed an interesting effect in the 30 μm hBN/Gr/hBN membrane which cannot be explained in the framework of a simple single-particle approach. At magnetic fields 3.93 Tesla and higher, T_4 absorption line has a peculiar two-humped shape, see Figures 7.11, 7.12 and 7.4. Meanwhile at magnetic fields 3.15 Tesla and lower, T_4 has a simple quasi-Lorentzian shape. All other absorption lines $T_i, i \neq 4$ which are properly visible in the MIR region have simple quasi-Lorentzian shapes for all magnetic fields at which the hBN/Gr/hBN sample was probed. The magnitude of the T_4 splitting is $\sim$ 4.3 meV. As the magnetic field grows, this value remains almost unchanged, at the same time there develops a clearly visible asymmetry between the two "shoulders" of the T_4 line.

Such a phenomenon was not reproduced in the other two hBN/Gr/hBN samples we had. Two and a half month later, T_4 splitting was no longer present even in the spectra of the 30 μm hBN/Gr/hBN membrane where it was observed in first place, i.e. T_4 acquired a usual quasi-Lorentzian shape for all values of magnetic field accessible with our setup. Such a change of the magneto-optical spectra could be attributed to the uncontrolled change of the sample's doping and/or slight degradation of the membrane with time. The latter is also confirmed by the fact that less absorption lines could be resolved in the spectra of the 30 μm hBN/Gr/hBN membrane.

The nature of T_4 splitting is not clear and could be related to the Coulomb interactions.

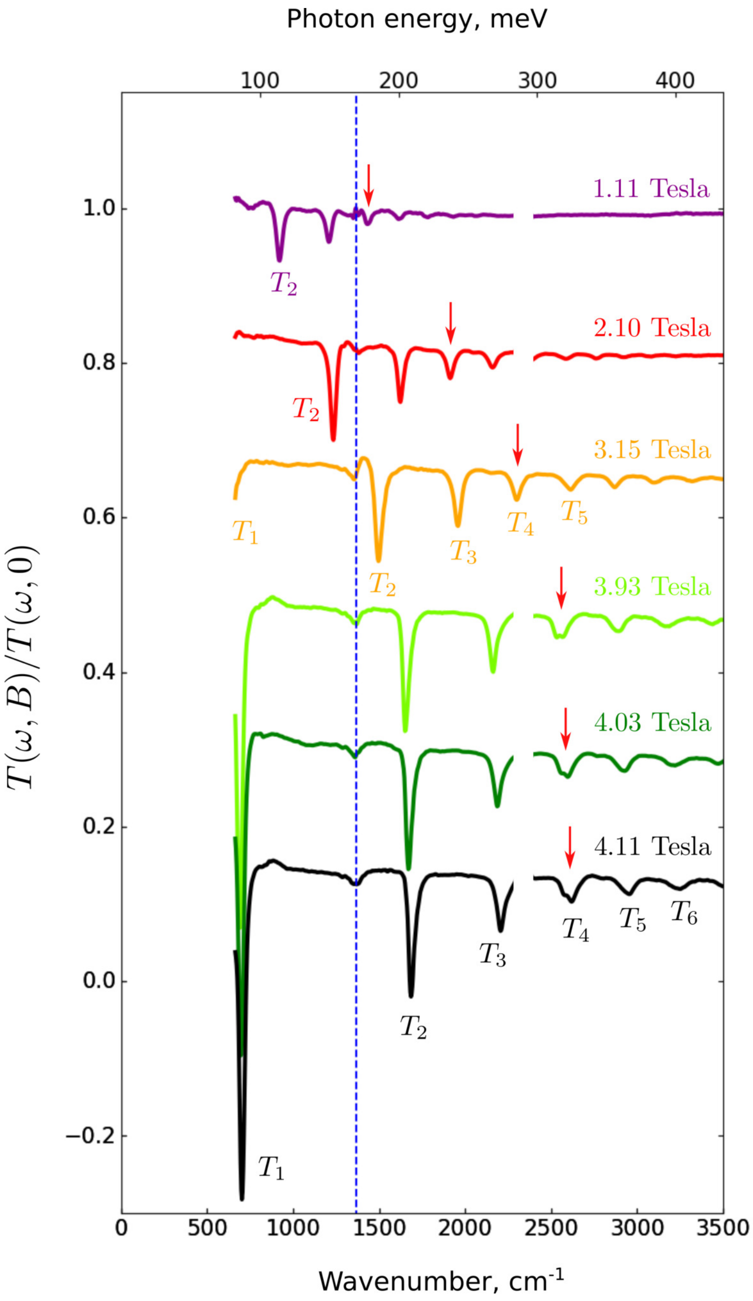

Figure 7.11 – MIR relative transmission spectra $T(\omega, B)/T(\omega, 0)$ of the 30 μm hBN/Gr/hBN membrane, measurements performed on 2015 Aug 29, resolution 8 cm^{-1}. At high magnetic fields the T_4 line acquires a two-humped shape. Parts of the spectra influenced by the atmospherical CO$_2$ are removed.

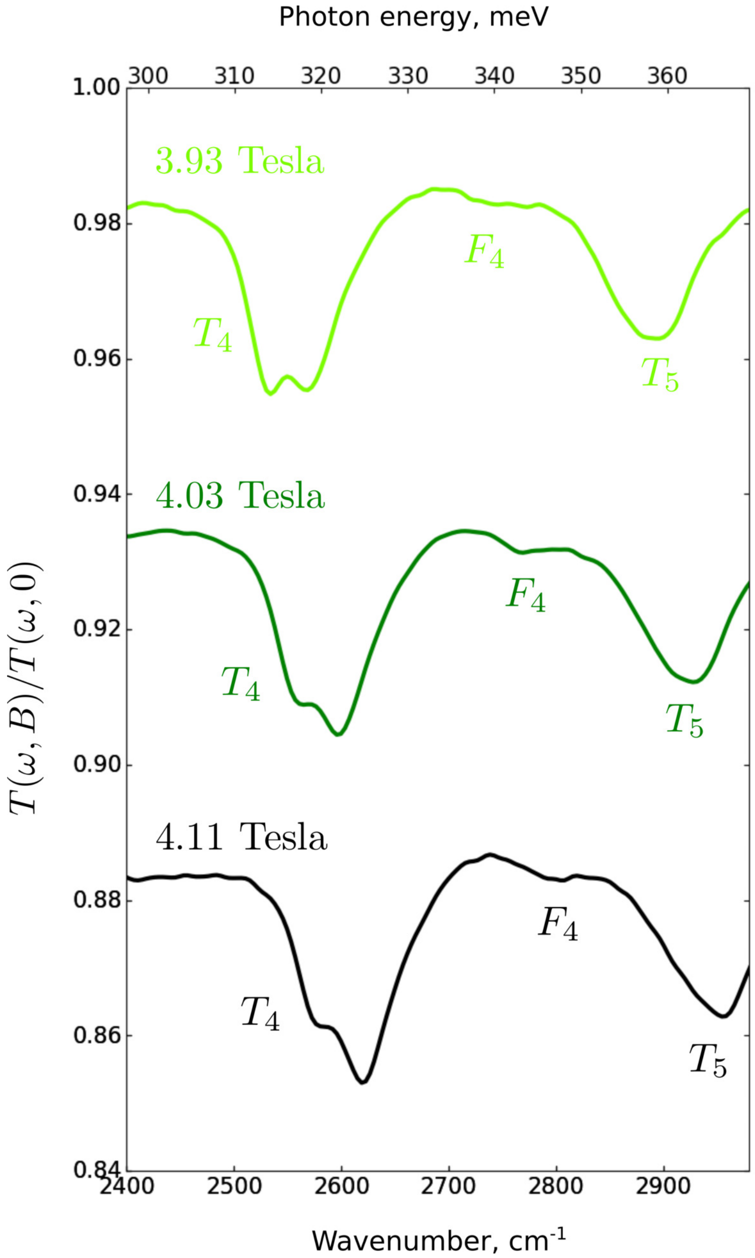

Figure 7.12 – MIR relative transmission spectra $T(\omega, B)/T(\omega, 0)$ of the 30 μm hBN/Gr/hBN membrane, measurements performed on 2015 Aug 29, resolution 8 cm^{-1}. T_4 line has an anomalous two-humped shape.

hBN phonon induced magneto-optical splitting of absorption lines

As the magnetic field increases, the absorption lines move to higher energies and eventually many of them cross the energy of the hBN phonon $\hbar\omega_{\text{ph}} = 169.5$ meV. An interesting effect is observed in the relative transmission spectra whenever T_i or F_i energy approaches $\hbar\omega_{\text{ph}}$: first there forms an asymmetric spectral feature and when the energy of the line and phonon coincide the line acquires a symmetric two humped shape, see Figure 7.13. In the range of magnetic fields accessible with our setup, such phonon induced magneto-optical splitting has been observed for T_2, T_3, T_4, F_2, F_3 absorption lines. This splitting is also visible in the colorplots presented before, see Figures 7.5, 7.6, 7.7. Here we would like to point out that at the phonon's energy, very little light is transmitted through the hBN/Gr/hBN stack. As a result, the signal-to-noise ratio is much worse than in the other parts of the MIR spectrum. Signatures of higher noise at the phonon's energy are visible for example in Figure 7.6 as a dappled horizontal line.

Phonon induced magneto-optical splitting could be clarified to some extent already in the framework of the simple modeling presented in the previous chapter. Colorplots in the 2nd column of Figure 6.4 show that for energies of photons $\hbar\omega_{\text{ph}}$, optical properties of any conducting film encapsulated in hBN remain almost constant in a very large range of σ_+ and σ_- values. Therefore transmission of a hBN/Gr/hBN stack is supposed to remain almost constant at energy $\hbar\omega_{\text{ph}}$ even if both $\sigma_\pm(\omega_{\text{ph}}, B)$ are substantially modified by external magnetic field. This means that the relative transmission which we measure in our experiments must obey

$$\frac{T(\omega_{\text{ph}}, B)}{T(\omega_{\text{ph}}, 0)} \approx 1. \tag{7.5}$$

If there are not any intense magneto-optical absorption lines in the vicinity to ω_{ph}, the statement (7.5) seems to be obvious and even trivial. Indeed, one does not expect a significant difference between $T(\omega_{\text{ph}}, B)$ and $T(\omega_{\text{ph}}, 0)$ if there is not any significant redistribution of spectral weight in $\hat{\sigma}_\pm(\omega, B)$ at ω_{ph} compared to the case of zero field. However the situation changes when intense T_i lines approach ω_{ph}, i.e. the formula (7.5) acquires a less trivial meaning. Importantly, the width of the hBN phonon absorption line is only 1.5 meV which is smaller than the line width of T_i transitions in graphene. As a result, absorption lines T_i are split in two whenever they cross the phonon's frequency so that relative transmission of a hBN/Gr/hBN stack would always remain constant and reach unity *form below*.

A similar interesting effect is observed when the value of the relative transmission is larger than unity in the vicinity to the hBN phonon's energy. In this case, there forms a little dip in the relative transmission which reaches unity *from above*, see panel a of Figure 7.2 and Figure 7.4. This effect is also explained by the formula (7.5), however now influence of the hBN phonon modifies the transmittance of the hBN/Gr/hBN stack in the opposite direction compared to the case of absorption lines.

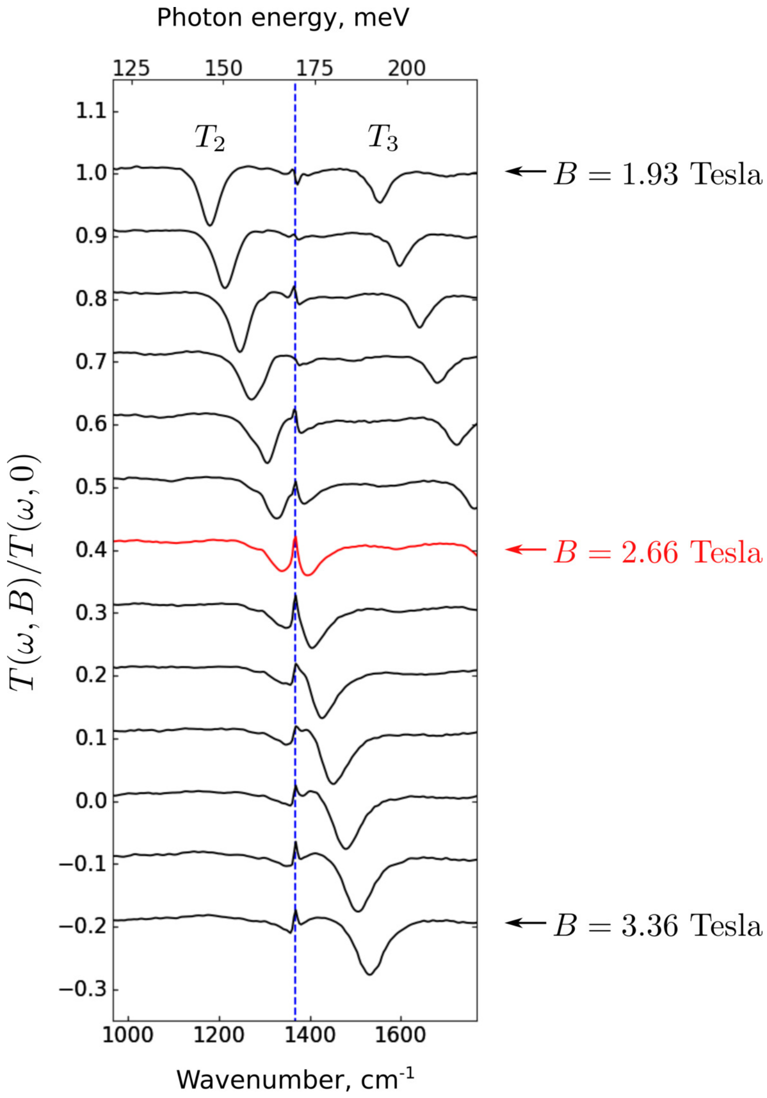

Figure 7.13 – Phonon induced magneto-optical splitting with the example of the T_2 absorption line. Vertical blue dotted line designates the energy of the optically active hBN phonon $\hbar\omega_{\text{ph}} = 169.5$ meV. Relative transmission curves presented in the figure were measured with a step of 0.12 Tesla in magnetic field. As magnetic field grows T_2 line moves to higher energies, crosses energy of the optically active hBN phonon and moves further. The relative transmission curve is marked out by the red color for the case when T_2 energy approaches the closest to $\hbar\omega_{\text{ph}}$. Measurements performed on the 30 μm hBN/Gr/hBN membrane on 2015 Nov 10 and 12, resolution 8 cm^{-1} (the same data as in Figure 7.6).

7.3 Far infrared transmission: mixed and intraband transitions

We performed relative transmission measurements in the FIR region of wavelengths with unpolarized light on our biggest 50 μm hBN/Gr/hBN membrane as described in Section 5.1. In total, three series of measurements have been done with intervals of many months in between, see Table 7.1. The results are show in Figure 7.14.

At low energies we observed spectral features due to the intraband transitions. T_2' line becomes active for photon energies $\hbar\omega < 35$ meV. It has a peculiar asymmetric shape which is clearly visible in the panel a of Figure 7.14. T_3' line becomes active for photon energies $\hbar\omega < 20$ meV, see panel b of Figure 7.14. In our experiment the T_2' and T_3' lines are closely packed and not very well resolved. In the region of high energies, another spectral feature due to the T_1 mixed transition becomes active. For magnetic fields of $>$ 2 Tesla, both T_2' and T_1 coexist together.

It is remarkable that even at comparatively low magnetic fields, < 1.5 Tesla, the relative transmission drops down to $\sim$ 0.6, see the panel b of Figure 7.14. This indicates that the magneto-optical absorption due to intraband transitions is also very high, in fact it has values close to those which we obtained in the MIR region at a magnetic field three times higher for the T_1 mixed magneto-optical transition. For comparison, spectral features due to T_2' and T_3' have been also registered in the relative transmission spectra measured on epitaxial graphene on SiC [79], however they are much less sharp than in our case which could be attributed to the lower mobility of the charge carriers in the above mentioned pitaxial graphene on SiC.

Charge carrier concentration and temperature

Spectral signatures of intraband magneto-optical transitions are direct evidence that our 50 μm graphene sample is doped. In order to understand emergence and exact shape of all features in the FIR transmission spectra presented in Figure 7.14, one should take into account that in our samples the position of the chemical potential changes with magnetic field, see the Figure 2.6. Presumably, it is the charge carrier concentration which remains constant as has been explained in formula (2.10). In the case of p-doping (or n-doping), at low magnetic fields the Landau level $n = -1$ stays above (or submerges below) the lowest well populated Landau level, see panel a of Figure 7.15. As a result, neither $-1 \to 0$ nor $0 \to +1$ magneto-optical transitions are possible because all the levels $n = -1,\ 0,\ +1$ are empty (or completely filled) therefore we do not observe T_1 at low magnetic fields. However at higher magnetic fields, chemical potential reaches $n = -1$ Landau level from below (or $n = +1$ Landau level from above) and this level becomes partially filled, see panel c in Figure 7.15. Therefore mixed magneto-optical transition $-1 \to 0$ (or $0 \to +1$) becomes active and one can observe a T_1 line in the spectra. Next, as magnetic fields grows, occupation of the $n = -1$ Landau levels grows (or occupation of the $n = +1$ Landau levels decreases), thus transition T_2' becomes less

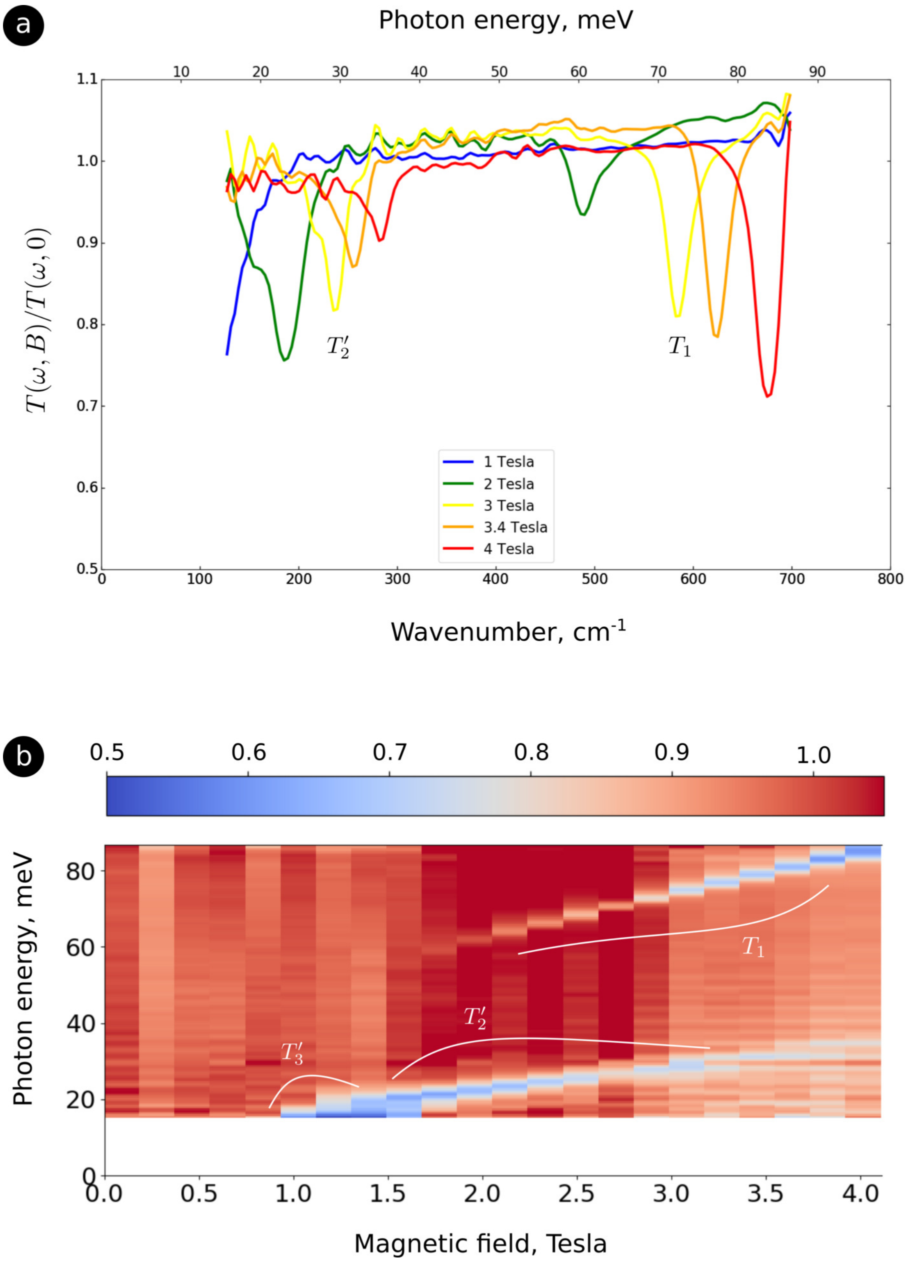

Figure 7.14 – Far infrared relative transmission spectra $T(\omega, B)/T(\omega, B)$ of the 50 μm hBN/Gr/hBN membrane. Resolution in energy is 1 meV (8 cm^{-1}). **Panel a:** Measurements performed on 2015 Dec 11. **Panel b:** Measurements performed on 2016 Nov 7 and 8; step in magnetic field is 0.19 Tesla.

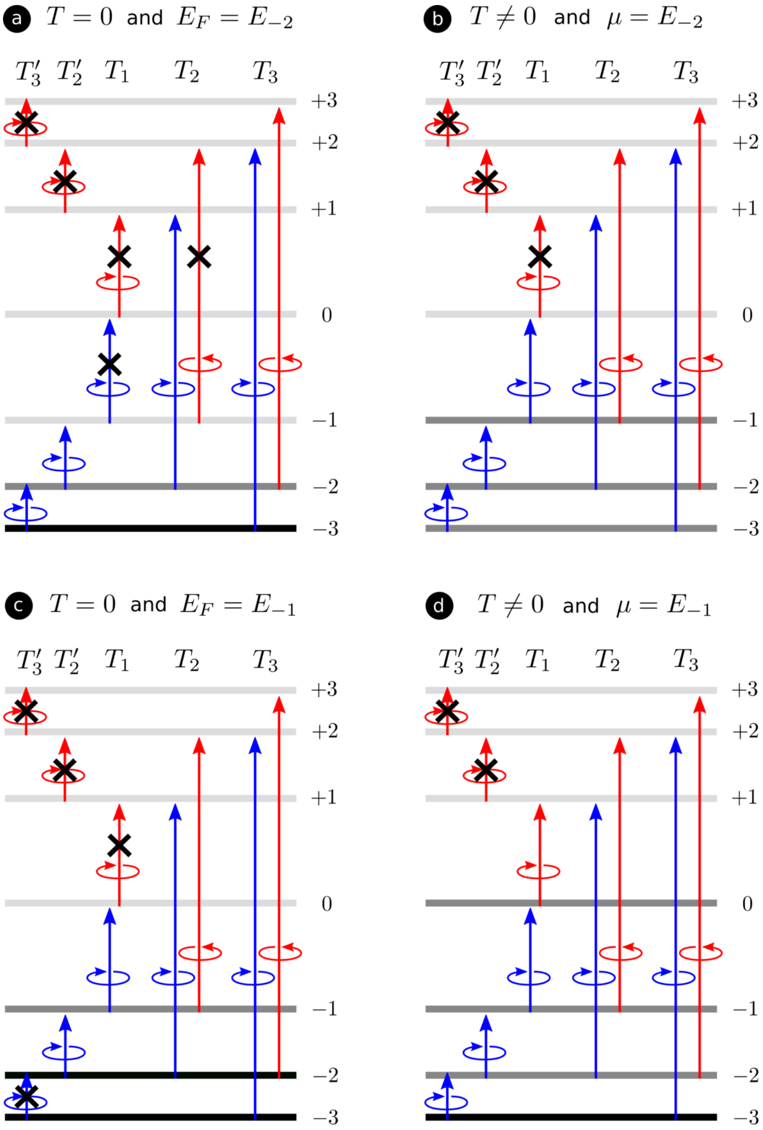

Figure 7.15 – Magneto-optical transitions between the Landau levels in the p-doped graphene. Black, dark gray and light gray horizontal lines depict fully filled, partially filled and empty Landau levels correspondingly. Red and blue vertical arrows depict electronic excitations accompanied by absorption of photons with right and left circular polarizations correspondingly. **Panels a and c:** Hypothetical case of zero temperature for two different positions of the Fermi energy. It is clear that when $T'_{3,-}$ transitions is active then T_1 transition cannot be activated and vice versa. **Panels b and d:** Non-zero temperature, position of the chemical potential μ is the same as in the panels a and b correspondingly. Landau levels near to μ acquire some noticeable partial filling, as a result some transition become "thermally unlocked".

intense at higher magnetic fields.

The lowest magnetic field at which the T_1 line is visible in the spectra is $B_{T_1} = 1.9$ Tesla, see panel b of Figure 7.14. This number allows identifying the absolute value of concentration N of charge carriers in graphene. T_1 line is not active when Landau level $n = -1$ is completely empty (or $n = +1$ is completely filled) and corresponding filling factor is $|\nu| = 6$, see Section 2.2. Therefore we find that $|N| = |\nu| \cdot eB_{T_1}/h \approx (2.8 \pm 0.1) \cdot 10^{11}$ cm^{-2} for the 50 μm hBN/Gr/hBN membrane. In our work, the main error in finding $|N|$ comes from the fact that we measured the transmission spectra with some finite step in magnetic field. Due to the electron-hole symmetry, the sign of the charge carriers cannot be extracted solely for from the relative transmission spectra measured with unpolarized light. Later we found out that the 50 μm sample is p-doped with the help of Faraday rotation curve, see the next section.

A finite temperature modifies the occupation of the Landau levels compared to the zero temperature. As a result, more magneto-optical transitions become unlocked, see panels b and d of Figure 7.15. The "thermally unlocked" lines are much less intense compared to the main ones. At the same time the main lines become a bit less intense than in the case of zero temperature because of the spectral weight redistribution in favor of the "thermally unlocked" spectral lines.

Thus in the spectra presented Figure 7.14, optical signature of T_1 extends to a bit lower energies and optical signatures of T_2' and T_3' also extend in both directions to the higher and lower energies. We performed the measurements only at liquid helium temperatures, as a result these effects are not pronounced enough to find the exact value of the hBN/Gr/hBN membrane temperature and they are not supposed to induce a large error in our estimate of the charge carrier concentration in graphene.

Properties of the T_1 absorption line and charge carriers mobility

We extracted energies of the T_1 line with the help of Lorentzian fit (7.1) the same way as described in the previous section. Figure 7.16 shows how these energies change with the magnetic field. As one can see there is high reproducibility of the line energies on different days of measurements. Just as in the MIR region, the energies of the T_1 line do not coincide with the ones predicted in a framework of a single-electron theory, see formula (7.2) for $i = 1$. It is remarkable that the values of the reduced energies grow nonlinearly as the natural logarithm of the magnetic field goes down, see panel c of Figure 7.16. This could be partly related to the fact that interaction effects and Landau level renormalization depend a lot on the filling factor. Importantly, in our system Landau level fillings change with magnetic field. Around ~ 2 Tesla the chemical potential jumps form the $n = -2$ to the $n = -1$ Landau level and then the $n = -1$ Landau level is slowly populated as magnetic field grows.

Apart from that, we extracted the widths and intensities of the T_1 line with the help of the same Lorentzian fit (7.1). Figure 7.17 shows how these characteris-

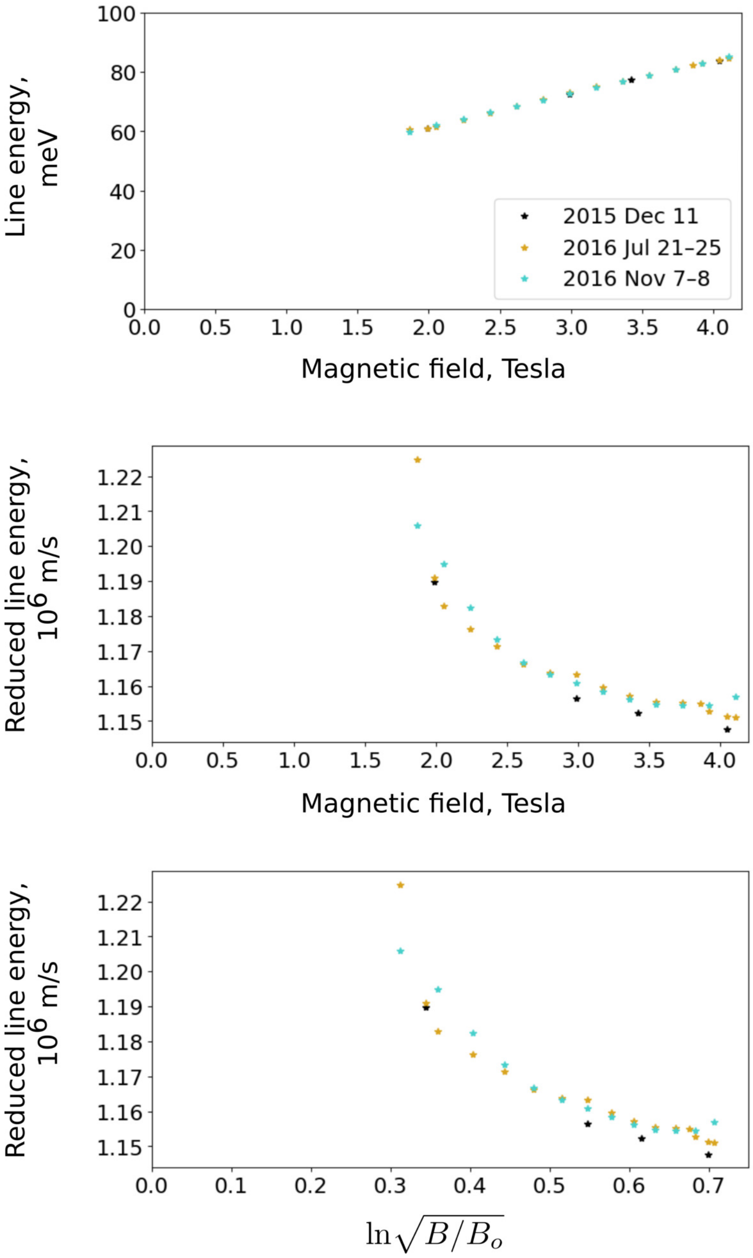

Figure 7.16 – Energies of the T_1 absorption line in the FIR region observed in the 50 μm hBN/Gr/hBN sample during three different series of measurements. The three panels present the same data about line energies in three different ways. Definition of the reduced energy is given in the formula (7.3). In the lowest panel $B_o = 1$ Tesla. All three panels have the same color code.

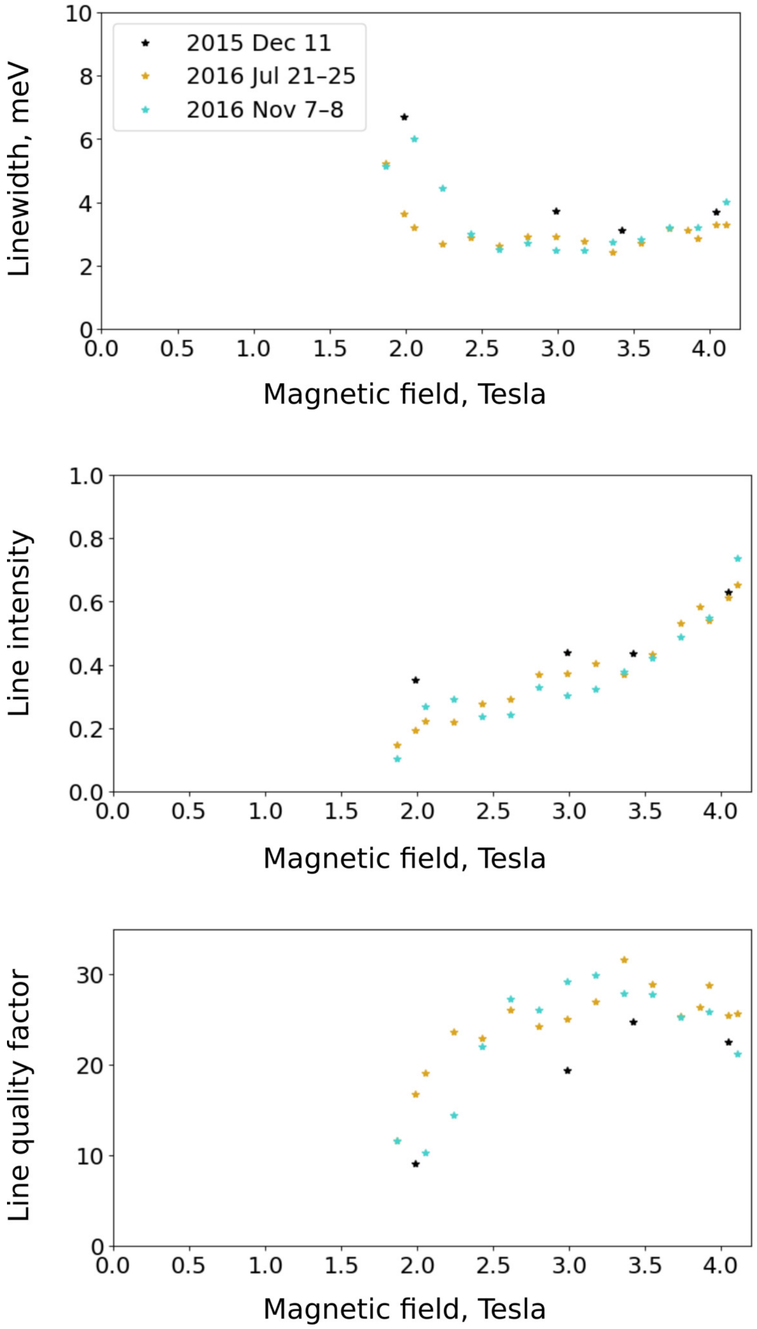

Figure 7.17 – Width, intensity and quality-factor of the T_1 absorption line in the FIR region observed in the 50 μm hBN/Gr/hBN sample during three different series of measurements. All three panels have the same color code.

tics change with the magnetic field. As one can see there is a plausible agreement between the result for the linewidth and its intensity on different days of measurements. Value of the linewidth γ_1 is related to the scattering rate τ and mobility μ of the charge carriers in graphene the following way:

$$\mu = \tau \frac{ev_F^2}{E_F}, \quad \tau = \frac{2\hbar}{\gamma_1}.$$

In order to estimate the charge carrier mobility in the 50 μm hBN/Gr/hBN membrane we consider the T_1 line at $B_{T_1} = 1.9$ Tesla and neglect the nonzero temperature in our samples. In this case, the Fermi energy $E_F = T_1$, the reduced line energy gives effective value of v_F, linewidth γ_1 was also found in the fit, thus all the necessary numbers are presented in Figure 7.17. This leads to the mobility of $\mu \sim 100\ 000$ cm^{2}V^{-1}s^{-1} at charge carrier concentration $|N| \sim 10^{11}$ cm^{-2} and *base* temperature ~ 5 Kelvin. Such a large value for mobility demonstrates the high quality of our graphene samples. Our value of mobility coincides with those reported in the transport measurements [83] on hBN-encapsulated graphene samples which were assembled with the dry transfer method similar to ours.

Robust linewidth indicates that the charge carrier mobility does not deteriorate on the course of 11 months. As one can see from Figure 7.17, the linewidths are the narrowest for in the middle values of the magnetic field around 3 Tesla. The highest quality-factors are observed at somewhat higher magnetic fields of $\sim$ 4 Tesla. The constant intensity of the line suggests that doping of the 50 μm hBN/Gr/hBN membrane remained almost the same on the course of 11 months otherwise some redistribution of the spectral weight between the intraband transitions and T_1 transition would be expected. Intensity of the T_1 line steadily grows with the magnetic field. This is partly attributed to the growing occupation of the $n = -1$ Landau level and partly to the increase of the cyclotron energy E_c at higher magnetic fields.

Band gap opening?

The possibility of the band gap opening in graphene on hBN substrate is currently widely discussed in scientific community. Therefore here we give a comment on the band gap signatures in spectra presented in Figure 7.14 and point out that there are not any pronounced signatures of the band gap opening in the 50 μm encapsulated graphene membrane.

The presence of the band gap Δ modifies positions of the Landau levels, see the formula (2.22). As a result, energies of all magneto-optical absorption lines must be shifted compared to the case of zero gap. However such shifts are not pronounced for the interband absorption lines $T_n,\ n \geq 2$ observed in the MIR region because presumable values of the gap are much smaller compared to the MIR energy scale. As it has been mentioned in the previous section, renormalization of the Fermi velocity also shifts the energies of the $T_n,\ n \geq 2$ lines. Therefore identifying the value of the gap from signatures of the interband transitions is difficult and inconclusive[3]. In contrast, spectral signatures of the mixed transitions T_1 observed in the FIR region carry much less ambiguous information about the gap [240]. Indeed, in the FIR region, the energy scale is lower therefore the ratio Δ/T_1 and presumable shift of T_1 due to the band gap is more pronounced than in the MIR region. What is even more important, presence of the gap *splits* the T_1 absorption line in two lines. As it has been already mentioned at the end of Section 2.2, a band gap opening leads to the splitting of the zeroth Landau level into $+0$ and -0 levels. Selection rules for the magneto-optical transitions remain the same, as a result there are four transitions which involve either $n = +0$ or $n = -0$ Landau level, see panels (i)$-$(iii) of Figure 7.18:

- transition $-0 \to +1$ with energy $T_{1,+} = \sqrt{2e\hbar B v_F^2 + (\Delta/2)^2} + \Delta/2$,
- transition $+0 \to +1$ with energy $T'_{1,+} = \sqrt{2e\hbar B v_F^2 + (\Delta/2)^2}$,
- transition $-1 \to +0$ with energy $T_{1,-} = \sqrt{2e\hbar B v_F^2 + (\Delta/2)^2} + \Delta/2$,
- transition $-1 \to -0$ with energy $T'_{1,-} = \sqrt{2e\hbar B v_F^2 + (\Delta/2)^2}$.

Just as before, transitions between the levels in one band are labeled with a prime i.e. T'_1; transitions between the levels in different bands are denoted T_1 just as the mixed transitions in the absence of the band gap; indices “plus” and “minus” label the handedness of the absorbed light. As one can see, when the gap is zero, energies of T_1 and T'_1 coincide. However when the gap is not zero, energies of T_1 and T'_1 differ, as a result there are two magneto-optical absorption lines separated by Δ. Whether the lines T_1 and T'_1 could be simultaneously observed depends on the filling of the Landau levels. Figure 7.18 illustrates different important scenarios for the case of p-doping (a similar symmetric situation is also observed for the case of n-doping i.e. magneto-optical transitions have the same energies but opposite handedness).

(i) $\Delta \neq 0$, Landau levels $n = -1,\ -0,\ +0,\ +1$ are all completely empty (in the case of n-doped graphene, completely occupied). As a result, neither T_1 nor T'_1 lines are present in the magneto-optical spectra.

(ii) $\Delta \neq 0$, Landau level $n = -1$ is partially or fully occupied, at the same time all higher levels are either empty or partially filled (in the case of n-doped graphene, Landau level $n = +0$ is partially or fully occupied and all higher levels are either empty or partially occupied). As a result, both T_1 and T'_1 lines are simultaneously present in the magneto-optical spectra.

(iii) $\Delta \neq 0$, both $n = -1,\ -0$ Landau levels are fully occupied, all higher Landau levels are either empty of partially occupied (in the case of n-doped graphene, both Landau level $n = +0,\ +1$ are fully occupied and all higher levels are either

---

[3] Nevertheless, such attempts have been reported, see [141].

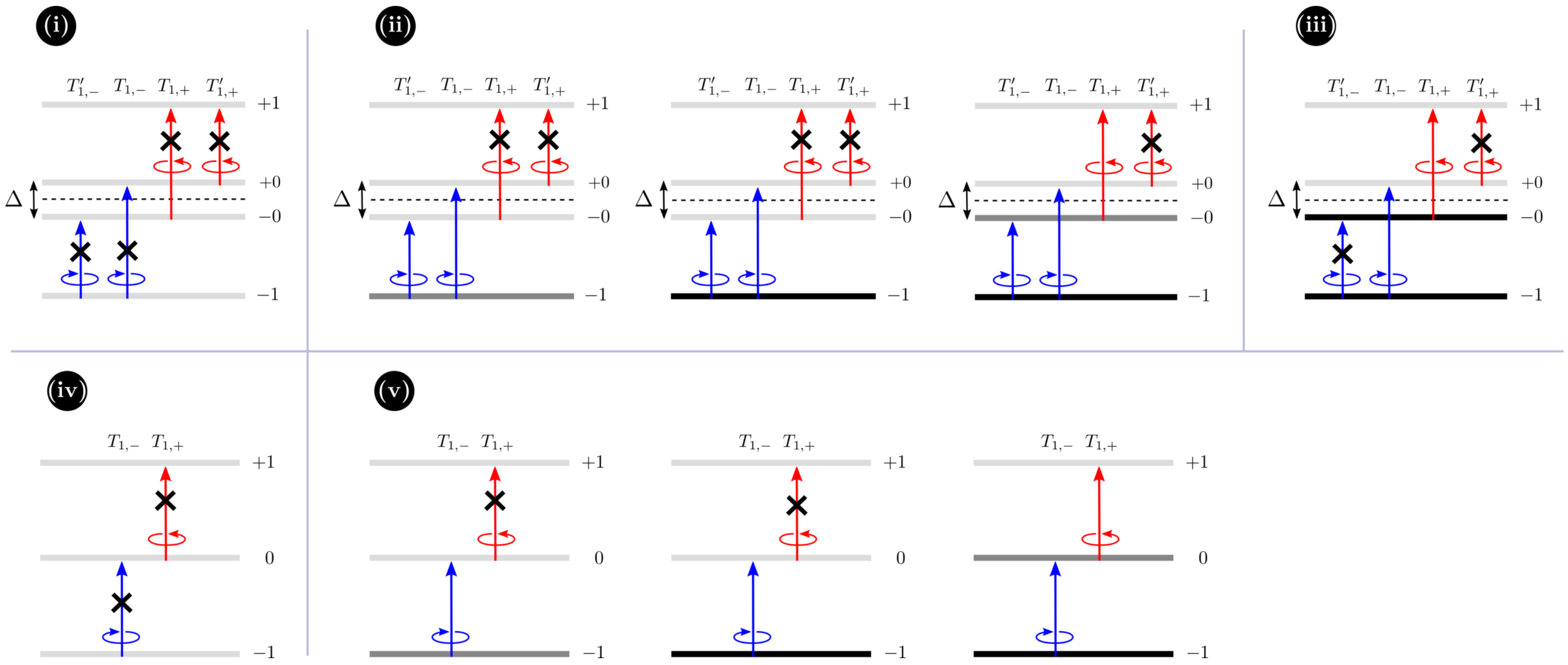

Figure 7.18 – Magneto-optical signatures of the band gap in graphene. Panels from left to right show which spectral lines emerge or disappear as the Fermi level raises. Black, dark gray and light gray horizontal lines depict fully filled, partially filled and empty Landau levels correspondingly. Red and blue vertical arrows depict electronic excitations accompanied by absorption of photons with right and left circular polarizations correspondingly. More details in the text. **Panels (i)−(iii):** Hypothetical band gap Δ is present. **Panels (iv)−(v):** Band gap is absent.

empty or partially occupied). As a result, only a single T_1 line is present in the magneto-optical spectra and T_1' is not active.

(iv) $\Delta = 0$, Landau levels $n = -1,\ 0,\ +1$ are all completely empty (in the case of n-doped graphene, Landau levels $n = -1,\ 0,\ +1$ are all fully occupied). As a result, the T_1 line is not active, and the T_1' line does not exist at all.

(v) $\Delta = 0$, Landau level $n = -1$ is partially or fully occupied, at the same time all higher levels are either empty or partially occupied (in the case of n-doped graphene, Landau level $n = 0$ is partially or fully occupied and all higher levels are either empty or partially occupied). In this case, only a single T_1 line is present in the magneto-optical spectra. The T_1' line does not exist as a separate entity and always coincides with T_1.

In our experiments we observe a single pronounced feature due to T_1 which has a quasi-Lorentzian shape. Such a spectral signature fits both scenario (iii) with a band gap and scenario (v) without a band gap. However we can easily rule out the scenario (iii) because in our system the doping changes gradually with the magnetic field therefore one cannot switch from regime (i) directly to regime (iii) without passing through regime (ii). In the region $\lesssim 2$ Tesla the $n = -1$ Landau level is empty. In the region ~ 2 Tesla the $n = -1$ Landau level is only partially filled, such filling of the Landau levels is depicted in the first scheme in the panel (ii) of Figure 7.18 for the case when a band gap is present in graphene. In this case both $T_{1,-}'$ and $T_{1,-}$ lines must be simultaneously observed. However we see only one line in our spectra. If the size of the band gap Δ is small and comparable to the linewidth of T_1 one would observe two closely packed $T_{1,-}'$ and $T_{1,-}$ absorption lines which merge together. This would give rise to a peculiar two-humped or a non-symmetric spectral feature. Thus we can only estimate the upper limit of the gap value based of the T_1 linewidth. All above mentioned reasoning about the splitting of the T_1 line and the signatures of the band gap also remain valid in the MIR region when T_1 line moves to higher energies in higher magnetic fied. Magneto-optical spectra of the 50 μm hBN/Gr/hBN membrane measured in the MIR region, see Figure 7.5, are consistent with the FIR spectra presented in this section and do not show any signatures of the band gap either. We conclude that if the band gap is present in the 50 μm hBN/Gr/hBN sample, then its value should not be larger than the T_1 half-width therefore $\Delta < 3$ meV.

7.4 Faraday rotation angle

Doped graphene, in contrast to pristine graphene, exhibits the Faraday rotation effect and magnetic circular dichroism. In order to investigate these phenomena, we performed several series of magneto-optical measurements with linearly polarized light on our 50 and 30 μm hBN/Gr/hBN membranes as described in Section 5.2. In the end, we obtained the optical quantities $\Phi(\omega, B)$ and $\Theta(\omega, B)$ defined in formulas (5.6) and (5.9) correspondingly. We remind the physical meaning of these quantities: $\Phi(\omega, B)$ is approximately equal to the Faraday rotation angle, see formula 5.7, and $\Theta(\omega, B)$ is approximately equal to the relative transmission of graphene i.e. transmission normalized by zero field transmission, see formula 5.10. The quantitative deviations of $\Phi(\omega, B)$ from $\theta_F(\omega, B)$ and $\Theta(\omega, B)$ from $\widetilde{T}(\omega, B)$ are discussed in Section 5.4.

Far infrared region, 50 μm hBN/Gr/hBN membrane

$\Phi(\omega, B)$ and $\Theta(\omega, B)$ were measured in the FIR region for 3 Tesla on the 50 μm hBN/Gr/hBN membrane, the result is plotted in Figure 7.19. This value of the magnetic field was chosen because for our doping of the graphene membrane both T_1 and T_2' spectral features have energies accessible to our setup in the FIR region. The scheme of both magneto-optical transitions T_1 and T_2' is shown in the panel c of Figure 7.15. The filling factor corresponding to this magnetic field is $\nu = -3.9$. In order to find the value of the filling factor, we profited from the charge carrier concentration $N = -2.8 \cdot 10^{11}$ cm^{-2} found from measurements performed the other day on 2016 Nov 7 and 8, see the previous section. Both T_1 and T_2' spectral features are accompanied by a noticeable Faraday rotation angle $\sim 5°$, at the same time the Faraday rotation is almost zero in between the two features. At high frequencies, the $\Phi = \Phi(\omega)$ curve has a clear zig-zag shape with a downward inflection at the frequency corresponding to the T_1 absorption line. At low frequencies, the onset of noise and instability of the signal due to atmospheric H_2O distort the experimental curve. Thus only a general character of the downward inflections is visible around the energy of the T_2' transition. Thus for both magneto-optical transitions

$$\frac{d\Phi(\omega)}{d\omega}\bigg|_{\hbar\omega\,=\,T_1,\,T_2'} < 0.$$

Downward inflections of the $\Phi = \Phi(\omega)$ curve at the frequencies of the absorption lines allow us to identify the sign of charge carriers in graphene and we conclude that our 50 μm hBN/Gr/hBN membrane is p-doped, see Figure 2.14.

Middle infrared region, 50 μm hBN/Gr/hBN membrane

$\Phi(\omega, B)$ and $\Theta(\omega, B)$ curves were measured in the MIR region for three different values of magnetic field on the 50 μm hBN/Gr/hBN membrane, the result is plotted in different scales in Figures 7.20 and 7.21. At 3 Tesla (the same value of magnetic field as in the FIR measurements), the T_1 line is not fully visible in the MIR region, T_2 line is situated near to the hBN phonon frequency and is accompanied with some noticeable Faraday rotation angle with a downward inflection, T_3 is accompanied with barely discernible Faraday rotation, meanwhile higher interband transitions $T_4 - T_7$ have signatures in the transmission spectrum and zero Faraday rotation. At the highest magnetic field, 4.1 Tesla, accessible with our setup the absorption lines $T_1 - T_4$ are all accompanied by a noticeable Faraday rotation angle. In between the lines and at high frequencies of light $\hbar\omega > T_4$ the Faraday rotation is almost zero.

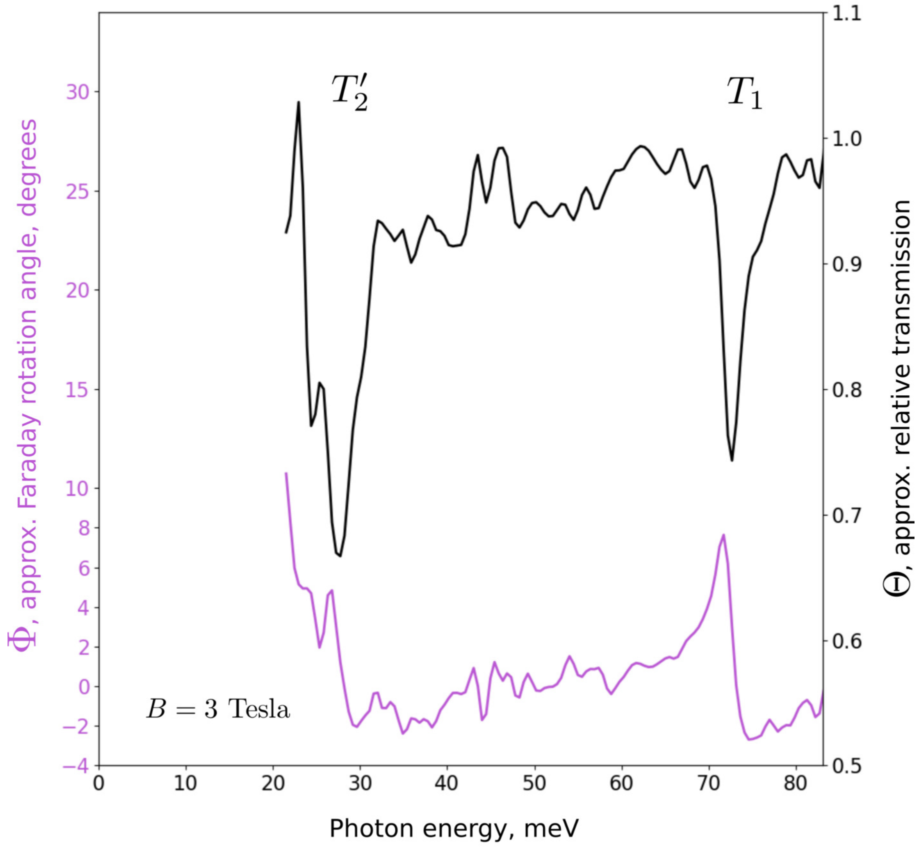

Figure 7.19 – Optical quantities $\Phi(\omega, B)$, approximately equal to the Faraday rotation angle, and $\Theta(\omega, B)$, approximately equal to the relative transmission, measured at the 50 μm hBN/GR/hBN membrane in the FIR region on 2016 Nov 09.

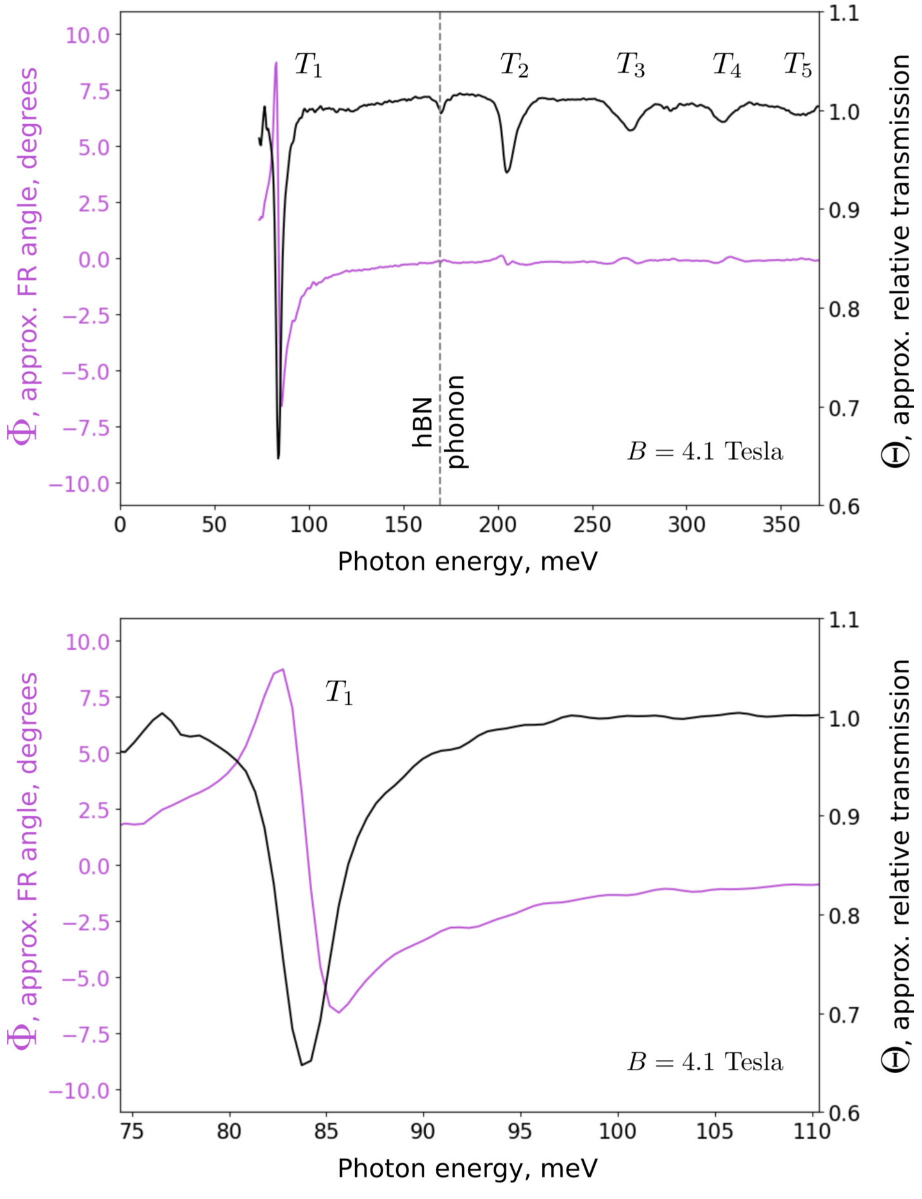

Figure 7.20 – Optical quantities $\Phi(\omega, B)$, approximately equal to the Faraday rotation angle, and $\Theta(\omega, B)$, approximately equal to the relative transmission, measured at the 50 μm hBN/GR/hBN membrane in the MIR region on 2016 Dec 20. Lower panel is zoom to the T_1 region of the upper panel.

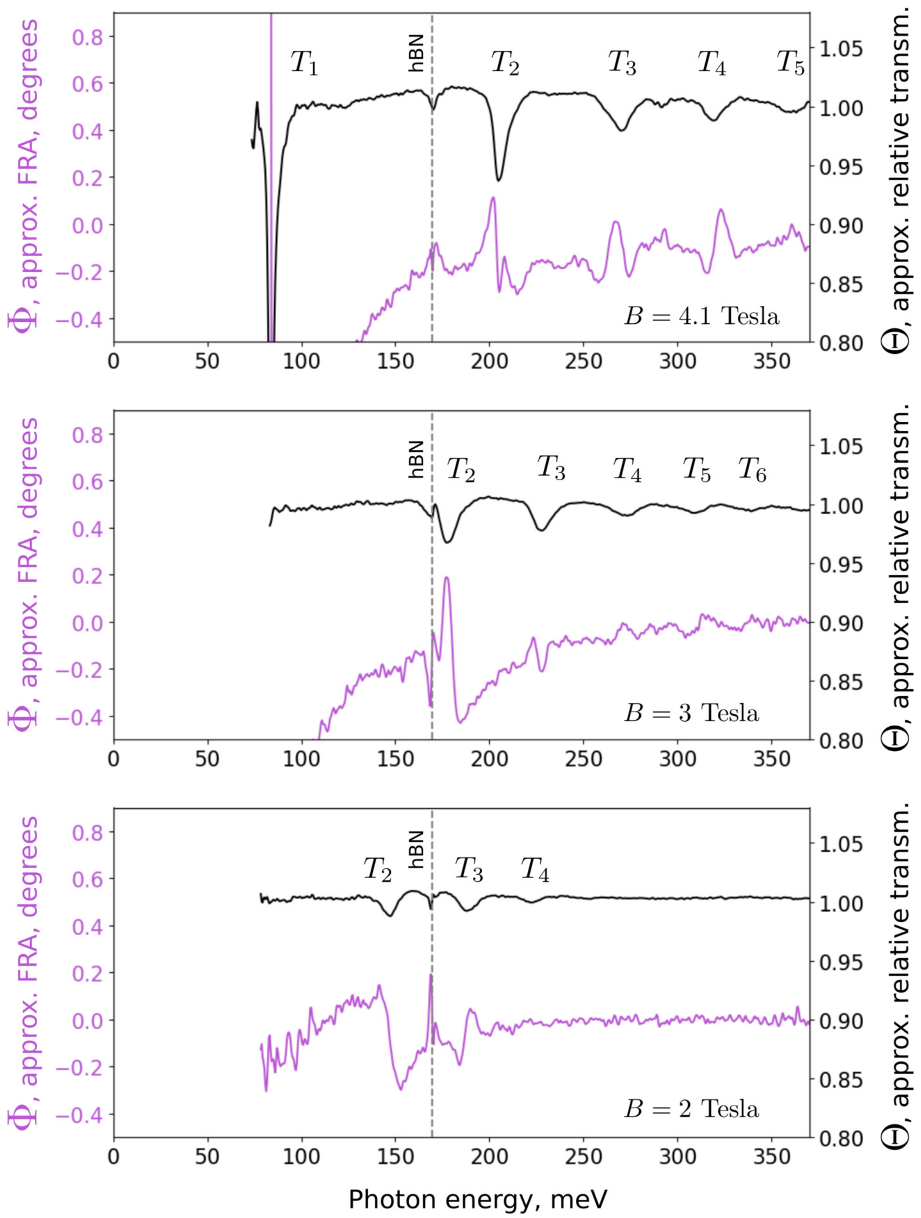

Figure 7.21 – Optical quantities $\Phi(\omega, B)$, approximately equal to the Faraday rotation angle, and $\Theta(\omega, B)$, approximately equal to the relative transmission, measured at the 50 μm hBN/GR/hBN membrane in the MIR region on 2016 Dec 20. Upper panel is zoom to the T_2, T_3, T_4, T_5 region of the upper panel of Figure 7.20.

It is remarkable that T_1 absorption line has a very large value of the Faraday rotation angle of 9° which exceeds the values of Faraday rotation in graphene reported so far at any magnetic field and at any photon energy. We attribute such a large magnitude primarily to the small width of the T_1 line which is in turn related to the high purity and quality of our graphene membrane. For comparison, the largest values of the Faraday rotation $\sim 6^\circ$ reported before were observed in highly doped graphene samples with charge carrier concentration $|N| \sim 10^{13}$ cm^2 in the classical cyclotron regime at frequencies within the FIR region, at the same time the Faraday rotation angle of the T_1 line was reported to be $< 0.5^\circ$ even in magnetic fields much higher than 4 Tesla, see [79]. By the contrast we observed large values of the Faraday rotation angle in the quantum regime of the sample with two-orders of magnitude lower doping at much higher frequencies within the MIR region.

Anomalous inflections of the Faraday rotation curve

Another interesting finding in the spectra of the 50 μm hBN/Gr/hBN membrane is that the Faraday rotation curve $\Phi(\omega, B)$ has nonzero features for several interband transitions, these features coexist with a pronounced "zig-zag" due to the T_1, moreover, they have anomalous inflections dissimilar to the regular zig-zag shapes predicted in the frame work of the simple nearest neighbor single electron theory described in Section 2.2 and illustrated in Figure 2.14. The anomalous inflections are very well visible for the T_3 and T_4 lines in Figure 7.21 at our highest magnetic field of 4.1 Tesla when the Faraday rotation angle is the largest. However at 3 and 2 Tesla, the shape of the $\Phi(\omega, B)$ curve is not clearly discernible at the energy of the T_4 line. In contrast, lower energy lines T_1, T_2, and T_2' always have an ordinary downward inflection of the $\Phi(\omega, B)$ curve which is a hallmark signature of p-doping in graphene.

To our knowledge, such anomalous inflection of the Faraday rotation curve has not been observed in monolayer graphene nor described in theoretical works published so far. At the same time, an unusual inflection has been reported in an experiment performed on turbostratic multilayer graphene on SiC [241]. According to the authors of this work, the anomalous inflection could be attributed to the different values of doping in different layers of graphene. However such an explanation is not valid in our case because we deal with a graphene monolayer.

Phenomenon of Faraday rotation is caused by imbalance between the magneto-optical conductivities of opposite handedness i.e. $\sigma_+(\omega, B) \neq \sigma_-(\omega, B)$, see formulas (6.20) and (6.21). Therefore the anomalous inflection which we observed in the 50 μm hBN/Gr/hBN membrane could be attributed to some nontrivial redistribution of the spectral weight in the magneto-optical conductivities $\sigma_-(\omega, B)$ and $\sigma_+(\omega, B)$. Unfortunately, the data presented in this work is not enough to clarify the microscopic origin of the anomalous inflections of the Faraday rotation curve. Thus here we briefly describe several scenarios which lead to two different anomalies in $\Phi(\omega, B)$ form a purely phenomenological point of view.

(i) An intraband spectral line T_i may acquire an anomalous inflection of the Faraday rotation curve $\Phi(\omega, B)$ if there is a *pronounced mismatch between the linewidths* of $T_{i,-}$ and $T_{i,+}$ or if there is some *nontrivial redistribution of their spectral weight*. The simple theory predicts that $\sigma_-(\omega, B) \geq \sigma_+(\omega, B)$ in p-doped graphene if the linewidths are the same in each pair of $T_{i,-}$ and $T_{i,+}$. However if broadening mechanisms are stronger for $T_{i,-}$ than for $T_{i,+}$ then the resulting values of conductivities may change so much that in the end $\mathrm{Re}\,\sigma_-(T_i/\hbar, B) < \mathrm{Re}\,\sigma_+(T_i/\hbar, B)$ despite of p-doping. In addition, if the $T_{i,-}$ spectral weight is reduced compared to the $T_{i,+}$ spectral weight by some microscopic mechanism which is not taken into account in the simple theory then one may also achieve $\mathrm{Re}\,\sigma_-(T_i/\hbar, B) < \mathrm{Re}\,\sigma_+(T_i/\hbar, B)$. Thus the resulting Faraday rotation curve

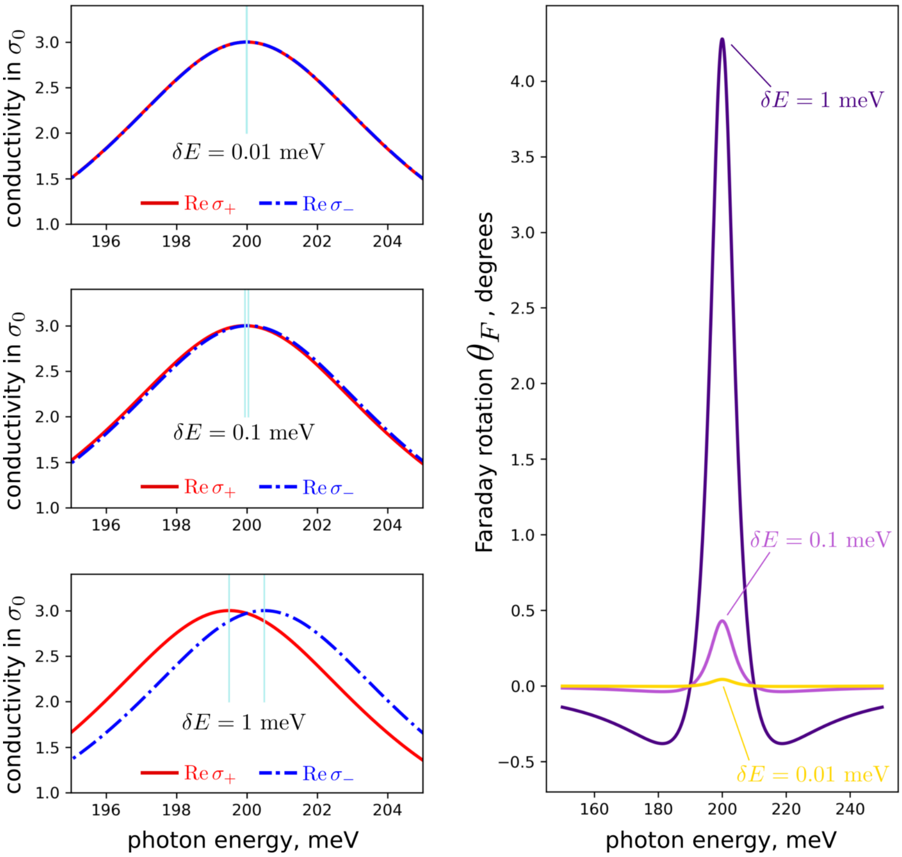

Figure 7.22 – Simulation of the Faraday rotation curve with anomalous inflection for an arbitrary well separated spectral line T_i due to interband transitions. Panels at the left show MO conductivities approximated by Lorentzian functions of the same widths and intensities for three hypothetical cases when $\delta E \equiv T_{i,-} - T_{i,+} \neq 0$. Panel at the right shows three corresponding Faraday rotation curves calculated with formula (6.21) for a bare (non-encapsulated) ultrathin conducting film.

also has a zig-zag feature centered at T_i energy but inflection of this zig-zag is inversed compared to the usual case of p-doping:

$$\left.\frac{d\Phi(\omega)}{d\omega}\right|_{\hbar\omega\,=\,T_i} > 0.$$

(ii) An interband spectral line T_i may acquire an anomalous inflection of the Faraday rotation curve $\Phi(\omega, B)$ if there is even a *little mismatch between the energies* of the $T_{i,-}$ and $T_{i,+}$ lines i.e. $\delta E \equiv T_{i,-} - T_{i,+} \neq 0$, see Figure 7.22. Such a mismatch may have different microscopic origin as Coulomb interaction effects, electron-hole asymmetry relative to the Dirac point, etc. The resulting Faraday rotation curve has a perfectly symmetric pointy feature centered between the $T_{i,-}$ and $T_{i,+}$ provided the $T_{i,-}$ and $T_{i,+}$ transitions have the same intensities and linewidths. Direction of the pointy feature (upwards or downwards) depends on the sign of δE. Magnitude of the pointy feature is very sensitive to the value of the energy mismatch $|\delta E|$: There could be some noticeable Faraday rotation angle of $\sim 0.5^\circ$ even if $|\delta E|$ is two orders of magnitude smaller than the linewidths so that $|\delta E|$ is not resolved in the transmission spectra, see Figure 7.22. However if there is some mismatch in the linewidths or intensities of the $T_{i,-}$ and $T_{i,+}$ then the pointy feature becomes asymmetric and quickly turns into a zig-zag.

Figure 7.24 shows the magneto-optical conductivities $\sigma_\pm(\omega, B)$ of the 50 μm hBN/Gr/hBN membrane which we restored from the $\Phi(\omega, B)$ and $\Theta(\omega, B)$ experimental data. It is clearly visible that at 4 Tesla $\mathrm{Re}\,\sigma_-(T_4/\hbar, B) < \mathrm{Re}\,\sigma_+(T_4/\hbar, B)$ and at 2 Tesla $\mathrm{Re}\,\sigma_-(T_3/\hbar, B) < \mathrm{Re}\,\sigma_+(T_3/\hbar, B)$ despite of p-doping.

7.5 Restoring the magneto-optical conductivity and absorption

The magneto-optical conductivity tensor $\hat{\sigma}(\omega, B)$ of encapsulated graphene could be restored using the experimental curves $\Phi(\omega, B)$ and $\Theta(\omega, B)$ which have been presented in the previous section. This could be done with the help of the Kramers-Kronig constrained fitting described in Section 6.4.

Before applying the fitting routine we have to make some model assumptions about transmission of a hBN/Gr/hBN stack in zero magnetic field $T(\omega, 0)$ because in our experiments quantity $\Theta(\omega, B)$ relies on normalization by zero field transmission. First we find the zero field optical conductivity of doped graphene $\sigma(\omega)$ with the help of the simple model (2.15) in the limit when $B \to 0$. In this model we assume the value of the sample's doping $|N| = (2.8 \pm 0.1) \cdot 10^{11}$ cm^{-2} found in Section 7.3. We also assume a low scattering rate for the charge carriers which is typical for high quality graphene. The result for $\sigma(\omega)$ is plotted in Figures 7.24 and 7.25. The $\mathrm{Re}\,\sigma(\omega)$ curve has a "step" centered at 2μ where μ is position of the chemical potential in graphene at zero magnetic field. Next, formulas (6.11) which relate the optical conductivity to the transmission of the hBN/Gr/hBN stack

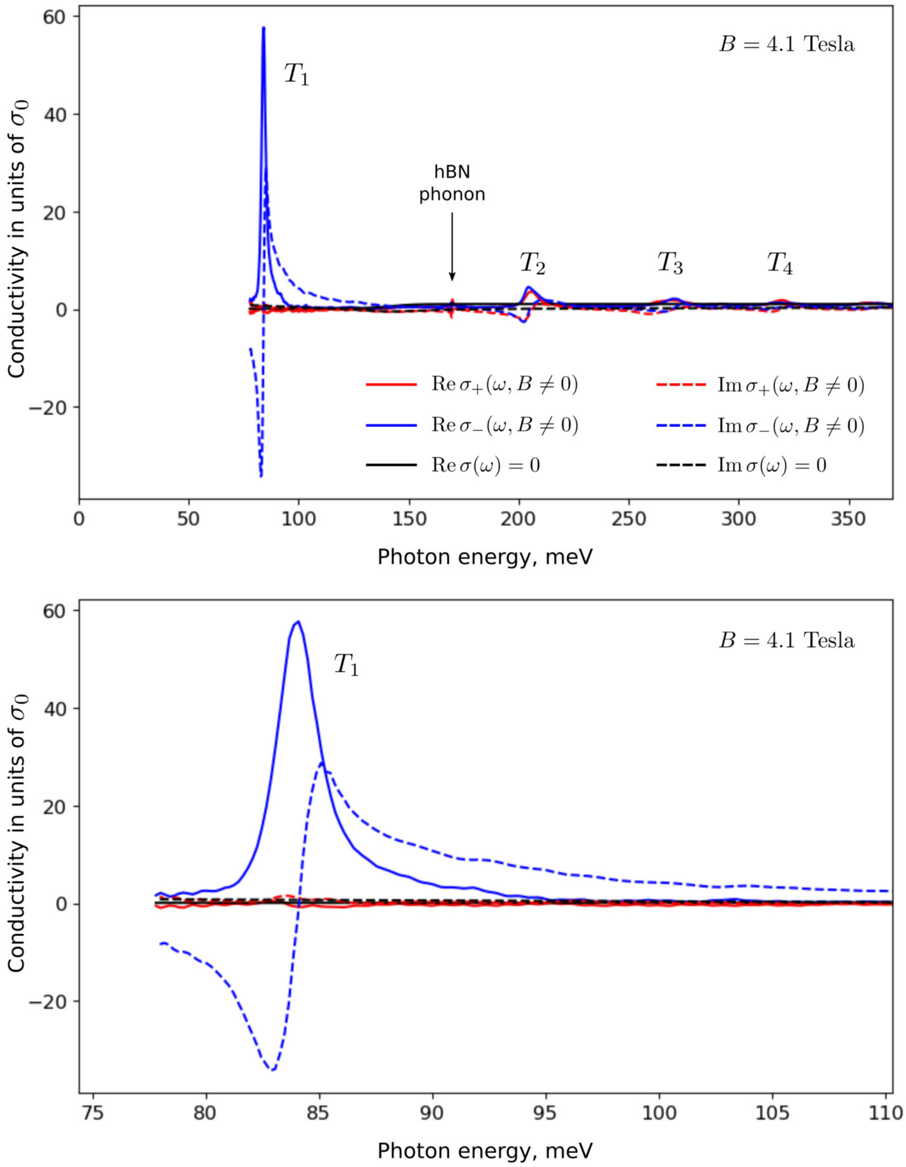

Figure 7.23 – Real and imaginary parts of the magneto-optical conductivities $\sigma_\pm(\omega, B)$ found from the KK constrained fitting for the 50 μm hBN/Gr/hBN sample. Real and imaginary parts of zero field conductivity $\sigma(\omega)$ of doped graphene calculated in the framework of the simple model. All conductivities are expressed in units of the universal conductivity of graphene σ_0. Lower panel is zoom to the T_1 region of the upper panel.

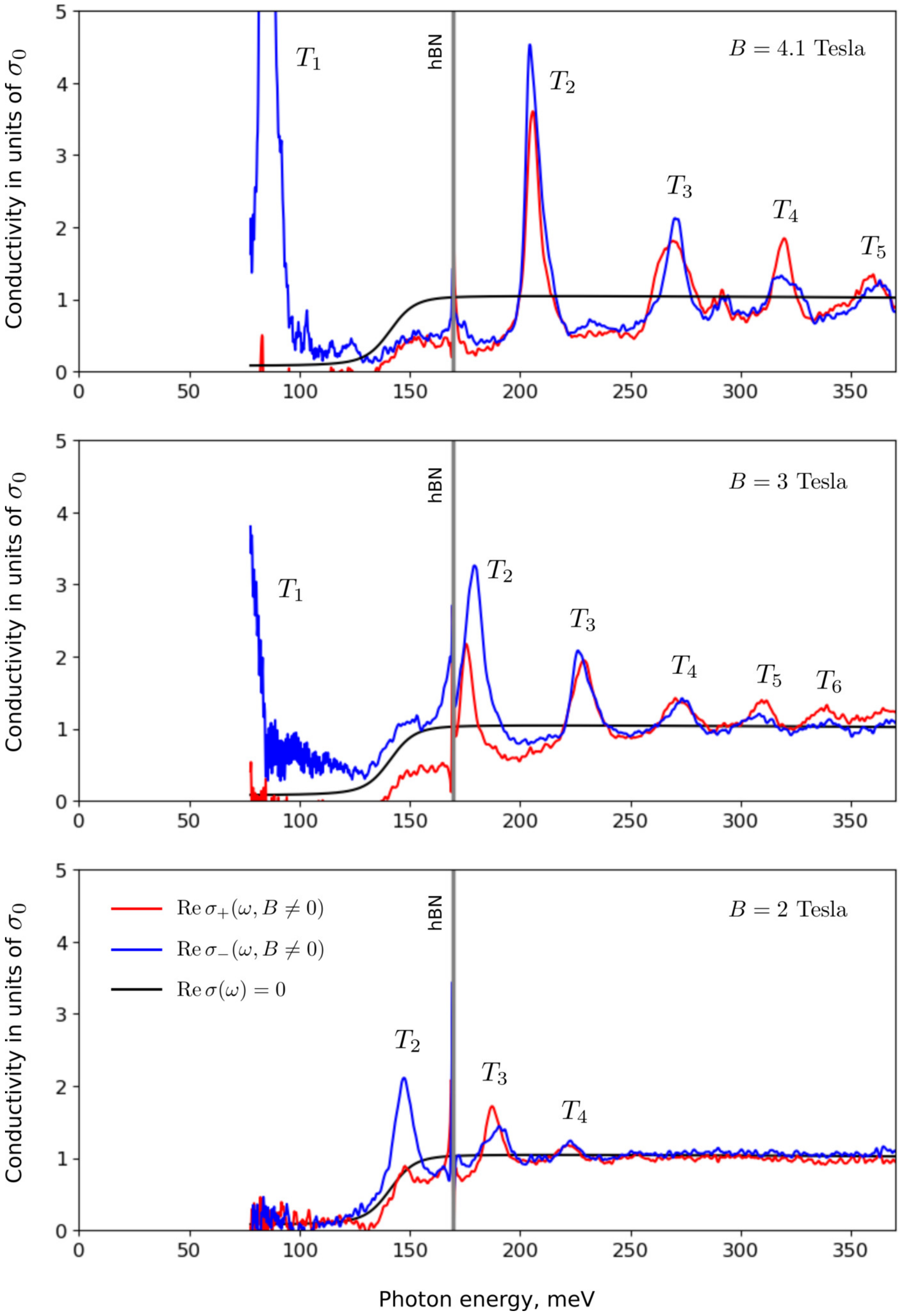

Figure 7.24 – Real parts of the magneto-optical conductivities $\sigma_\pm(\omega, B)$ found from the KK constrained fitting for the 50 μm hBN/Gr/hBN sample at three different values of the magnetic field (and chemical potential). Real part of zero field conductivity $\sigma(\omega)$ of doped graphene calculated in the framework of the simple model. All conductivities are expressed in units of the universal conductivity of graphene σ_0. Upper panel is zoom to the T_2, T_3, T_4, T_5 region of the upper panel of Figure 7.23.

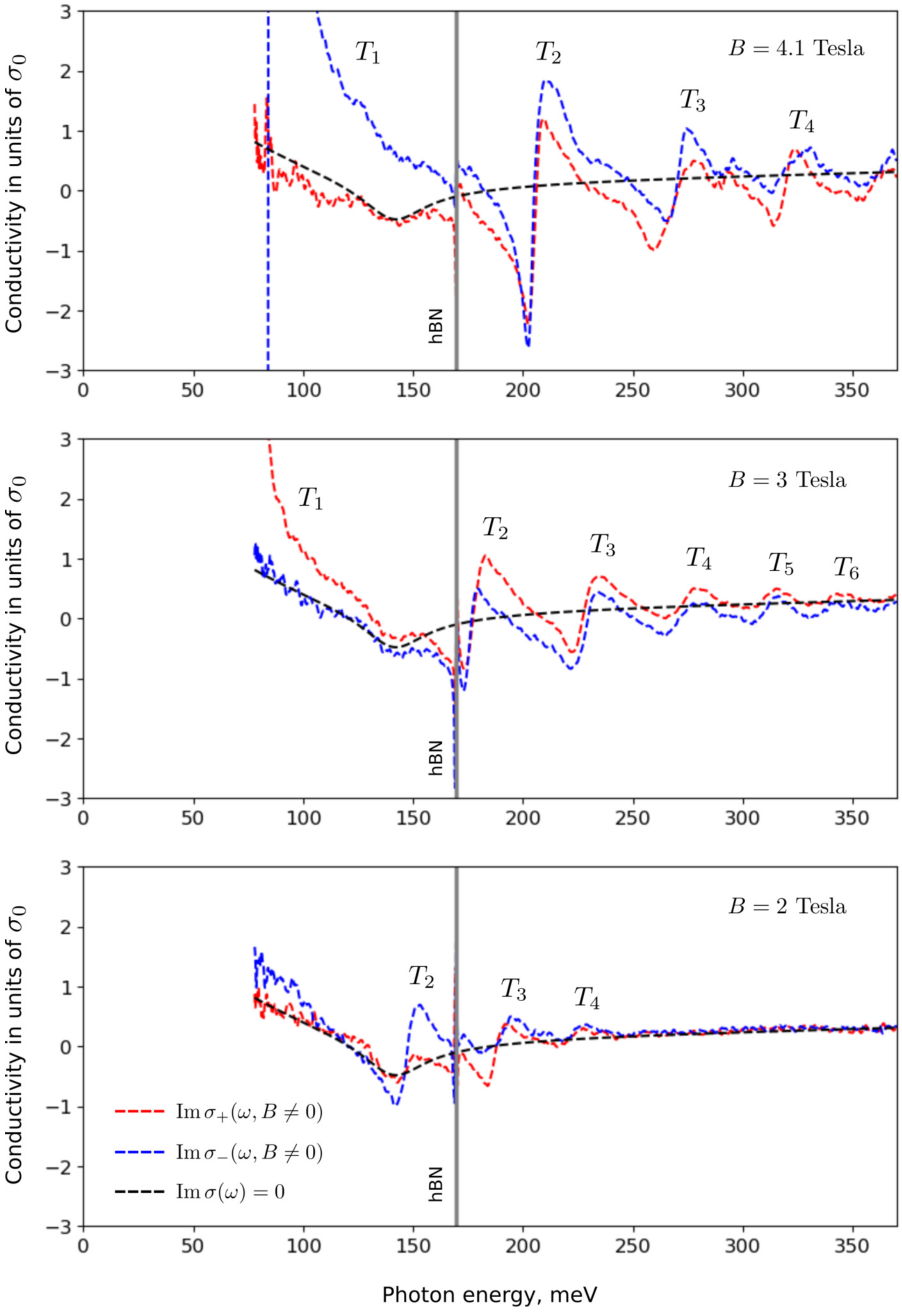

Figure 7.25 – Imaginary parts of the magneto-optical conductivities $\sigma_\pm(\omega, B)$ found from the KK constrained fitting for the 50 μm hBN/Gr/hBN sample at three different values of the magnetic field (and chemical potential). Imaginary part of zero field conductivity $\sigma(\omega)$ of doped graphene calculated in the framework of the simple model. All conductivities are expressed in units of the universal conductivity of graphene σ_0. Upper panel is zoom to the T_2, T_3, T_4, T_5 region of the upper panel of Figure 7.23.

allow us finding $T(\omega, 0)$ and incorporating its value into the expression (5.9) for $\Theta(\omega, B)$.

We calculated both optical conductivities $\sigma_+(\omega, B)$ and $\sigma_-(\omega, B)$ for three values of an external magnetic field. We remind that in our samples position of chemical potential depends on the magnetic field. The result is plotted in different scales in Figures 7.23, 7.24, and 7.25. As one can see in Figure 7.23, the left-handed optical conductivity $\mathrm{Re}\,\sigma_-(\omega, B)$ is equal to 58 σ_0 or 1.33 Y_0 at the energy of the T_1 magneto-optical transition. Whereas $\mathrm{Re}\,\sigma_+(\omega, B)$ is almost zero at the same energy. This proves that magnetic field together with doping may lead to a very pronounced redistribution of the spectral weight at a given frequency of infrared light. At the energies of the higher transitions i.e. T_2, T_3, etc the values of the $\mathrm{Re}\,\sigma_-(\omega, B)$ are much lower and are equal to several σ_0, see Figure 7.24. At higher energies both $\sigma_\pm(\omega, B)$ approach the values of the universal conductivity of graphene σ_0.

Now knowledge of the optical conductivities $\sigma_+(\omega, B)$ and $\sigma_-(\omega, B)$ allows calculating different optical quantities which have not been directly measured in the experiment. Of special interest is how much circularly polarized light is absorbed in the graphene monolayer which makes part of the hBN/Gr/hBN stack. Therefore we calculate the magneto-optical absorption $A_{\text{Gr}+}(\omega, B)$ and $A_{\text{Gr}-}(\omega, B)$ using our model of light propagation in the hBN/Gr/hBN stacks, see formula (6.17), the result is plotted in Figure 7.26. As one can see, absorption of the left-handed circularly polarized light $A_{\text{Gr}-}(\omega, B)$ approaches 48 % at the energy of the T_1 magneto-optical transition. For comparison, the maximal possible absorption of a bare ultrathin conducting film is $A_{\text{max}} = 50$ %. This maximum is achieved when the real part of the optical conductivity is equal to $2Y_0$, see Section 6.1. In our experiments, we closely approach the maximally allowed value of absorption because at our highest magnetic field of 4.1 Tesla, magneto-optical conductivity becomes $\mathrm{Re}\,\sigma_-(T_1/\hbar, B) \approx 1.33Y_0$ which is much closer to the prerequisite of the maximal absorption compared to the case of zero magnetic field conductivity.

Another remarkable effect is strong magnetic circular dichroism. Indeed, at 4.1 Tesla for the T_1 energy $A_{\text{Gr}+}(T_1, B) \approx 0$ within the error of experiment which results into the maximal circular dichroism $\Delta_A = +1$, see formula (6.18). Higher magneto-optical transitions T_2, T_3, etc show a smaller yet quite noticeable magnitude of absorption. Importantly, the level of dichroism significantly decreases for the interband transitions which is explained by the fact that in our sample the chemical potential is very close to the $n = -1$ Landau level at 4.1 Tesla, see panel c of Figure 7.15. Left-handed circularly polarized light is absorbed due to the mixed magneto-optical transition $T_{1,-}$ and right-handed circularly polarized light is almost fully transmitted through graphene because the $T_{1,+}$ transition is not active. Meanwhile interband transitions $T_{i,+}$ and $T_{i,-}$ where $i \geq 2$ have almost the same amplitudes which results in much lower circular dichroism. At high energies the two absorptions $A_{\text{Gr}\pm}(\omega, B)$ together approach the value of graphene's absorption in the absence of a magnetic field. At 2 Tesla, the chemical potential

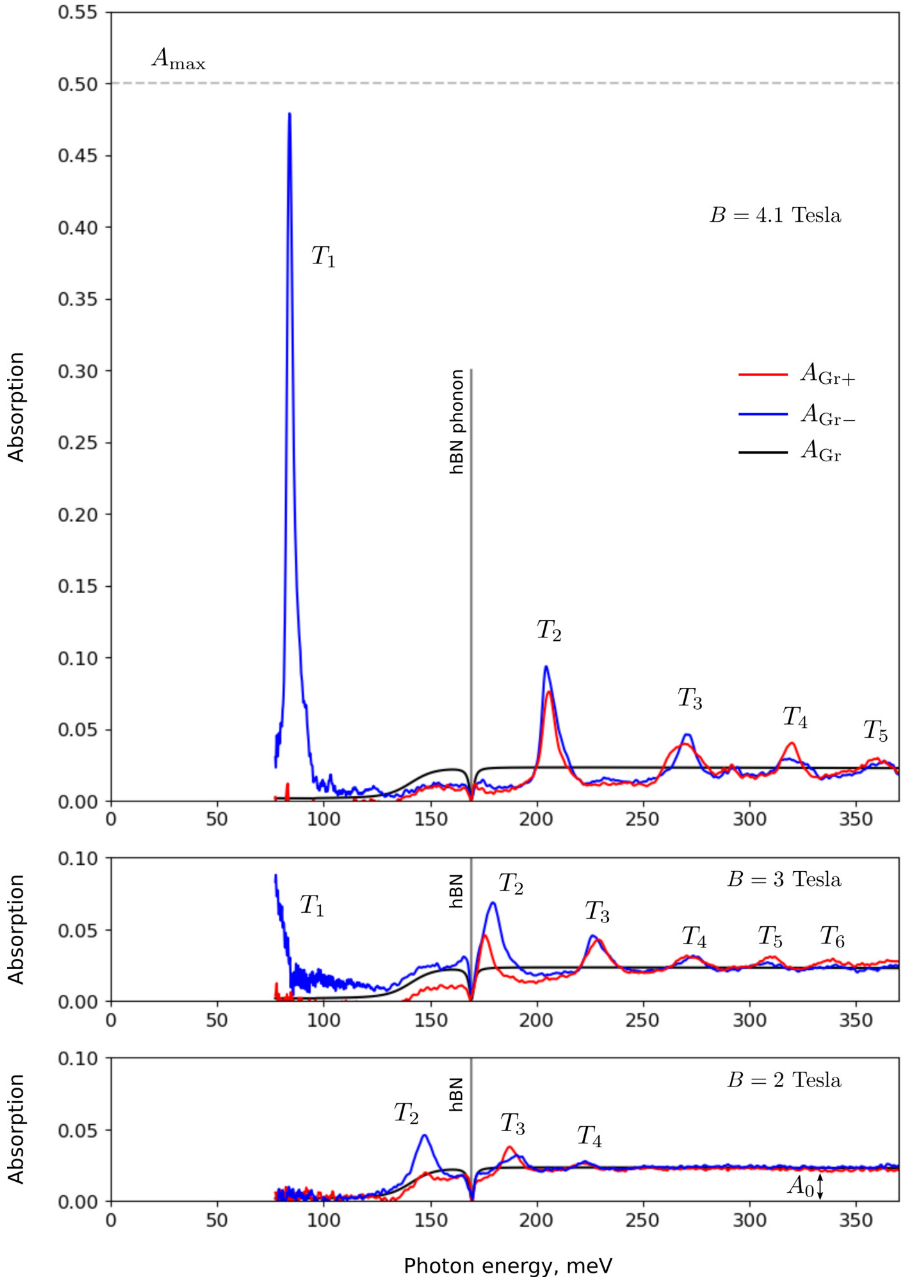

Figure 7.26 – Magneto-optical absorptions $A_{\mathrm{Gr}\pm}$ of graphene monolayer which makes part of the 50 μm hBN/Gr/hBN stack for three different values of the magnetic field (and chemical potential). Absorption A_{Gr} of doped graphene monolayer which makes part of the 50 μm hBN/Gr/hBN stack in the absence of magnetic field calculated in the framework of the simple model. A_0 is absorption of pristine graphene in the absence of magnetic field.

resides almost in the middle between the $n = -1$ and $n = -2$ Landau levels in our sample. This creates some noticeable imbalance in the amplitudes of the $T_{2,+}$ and $T_{2,-}$ transitions and circular dichroism at the T_2 energy becomes much more pronounced $\Delta_A = +0.4$ compared to what is observed at 4.1 Tesla for the same magneto-optical absorption line.

7.6 Technical issues and errors

Temperature of hBN/Gr/hBN membranes

Direct measurement of temperature of a hBN/Gr/hBN membrane is a formidable task because its mass is very small. Therefore we have to rely on the values of the base temperature of the cryostat in order to estimate the temperature of the hBN/Gr/hBN membranes. The base temperature in our experimental setup was monitored on the surface of the SC magnet with a Cernox temperature sensor which was chosen for its low magnetic field-induced errors. The base temperature was different on different days $\sim 5.2 \pm 0.3$ Kelvin[4]. Within one day of measurements the base temperature indicated by the sensor varied no more than $\sim \pm 0.05$ Kelvin.

Real temperature of a hBN/Gr/hBN membranes is supposed to be higher than the base temperature in the cryostat because the membrane is suspended in vacuum and constantly heated by the infrared radiation coming from the spectrometer and the room. Only the edges of the membrane rest on the colder $\mathrm{SiN_x}$/Si support. Thus there forms a complicated gradients of temperature in the membrane and in the various parts of the cryostat, see Figures 3.4 and 5.1. Modeling of the heat propagation and temperature distribution is a formidable task even in the case of a perfectly circular membrane because values of the most important parameters of the problem cannot be precisely identified. These parameters include the quality of the thermal contact between different parts of the system, values of thermal conductivity coefficients of hBN and graphene, etc. Moreover, the thermal conductivity coefficient of hBN strongly depends on temperature. The final result for the membrane's temperature is very sensitive to small variations in the values of the above mentioned parameters. We solved a differential equation in partial derivatives which describes the temperature distribution in a perfectly circular membrane assuming that the temperature of its border is exactly 5 Kelvin, the whole membrane is homogeneously illuminated with the IR light, and thermal conductivity coefficient of hBN is a parameter which does not depend on temperature nor coordinate. This calculation shows that the temperature of the hBN/Gr/hBN membranes could be up to several tens Kelvin higher than the base temperature.

---

[4] We could not reproduce the base temperature on different days of measurements. Moreover, each day our primary goal was to achieve the lowest possible temperature in the SC magnet because decreasing temperature by several decimals of a degree allows producing higher magnetic fields. Lowest possible temperature in the cryostat is influenced by many factors as pressure in the liquid Helium dewar, proper assembly of the cold shield, etc. Another important factor is that the Janis cold finger was used horizontally and not vertically as recommended by the manufacturer.

Importantly, in our experiments optical spectra of hBN/Gr/hBN membranes did not changes when the membranes were illuminated with higher or lower intensity IR light, see Section 5.3. This observation indicates that IR radiation from the spectrometer does not influence the temperature of the membranes in a significant way. Presumably the real temperature of our hBN/Gr/hBN samples is very close to the base temperature of the cryostat.

Systematic errors in the optical spectra

Mechanical stability of the setup is very important for reproducibility of optical spectra. We had to fine-tune pressure and rate at which liquid helium was evaporated at the cold finger in order to remove high frequency vibrations of the cold finger. Apart from that, we constantly monitored the sample's position. For this purpose we created a computer program which allowed easy comparison of the sample's pictures taken during magneto-optical measurement. If the sample drifted out of focus or shifted more than $\sim 2\ \mu$m away from the axis of the Cassegrain reflectors just during the measurements then its spectrum data was discarded, the position of the sample was readjusted and measurement of spectrum was repeated again.

Nevertheless, there remained signatures of such chaotic drifts in the optical spectra. We could estimate them simply by measuring the "100% line" i.e. taking a ratio between a pair of spectra measured in the same conditions. In the MIR spectra, the drifts manifested as equal at all frequencies deviations from unity. On the short time scales of several minutes, such systematic drifts were caused primarily by the lack of mechanical stability in our setup. To reduce the presence of such drifts in the final data, usually we discarded the spectra as outliers if they deviated by more than 5% from the other spectra measured in the same conditions. Next, in order to minimize the effect of systematic drifts on the optical spectra, we applied a baseline correction procedure to the remaining spectra which were not discarded as outliers. Here we made a reasonable assumption that a high frequencies > 4000 cm^{-1} magneto-optical spectra of hBN/Gr/hBN stacks do not have any peculiar spectral features and relative transmission spectra $\widetilde{T}(\omega, B)$ must be equal to unity. However because of the above mentioned drifts, actual high-frequency $\widetilde{T}(\omega, B)$ often deviated from unity by some value Δ which presumably does not depend on the frequency. We estimated the value of Δ in the high-frequency region and then rescaled the spectra with a constant prefactor for all frequencies:

$$\widetilde{T}(\omega, B) \rightarrow \frac{1}{1+\Delta} \cdot \widetilde{T}(\omega, B).$$

Unfortunately, we could not apply a similar procedure in the FIR region because at low energies there is not any extended part of $\widetilde{T}(\omega, B)$ which is supposed to approach unity therefore we were not able to estimate the systematic drift Δ and perform rescaling.

On the longer time scales of several hours, there was yet another inevitable cause of systematic drifts: the detector's sensitivity changed slowly as cryogenic liquids evaporated from the detector's dewar. These slow changes are important for comparison of the spectra measured long time apart as well as for adequate normalization of the spectra. Therefore we measured the reference spectra several times per day and then compared only the normalized spectra.

Statistical error in the optical spectra

Our spectra contain noise related to the IR detectors. Thus relative transmission and Faraday rotation have error $\sim 0.2\%$ in the MIR region below 5000 cm^{-1}. However at frequencies of light in the direct vicinity to the hBN phonon $\omega_{\text{ph}} = 1367$ cm^{-1} amount of light transmitted through the hBN/Gr/hBN membrane is low. As a result, the error is several times higher at 1367 cm^{-1} compared to the other regions of the MIR. This manifests as a dappled horizontal line in the colorplots 7.5, 7.6, and 7.7. In the FIR region the signal-to-noise ratio was always inferior compared to the MIR region and the error amounted up to $\sim 1\%$. Optical measurements could be implemented only on our largest 50 μm membrane because in the FIR region the sizes of our samples are comparable to the wavelengths of the IR light (as an example, 50 μm is 200 cm^{-1} or 25 meV).

Optical signatures of atmospheric gases

The Bruker IR microscope is supposed to be covered with a hood and purged with pure nitrogen during measurement of IR spectra. This allows avoiding optical signatures of atmospheric gases CO_2 and H_2O. This procedure is especially important in the far infrared region of spectrum. However we constantly needed a direct access to the IR microscope and cryostat because we had to monitor and readjust the samples position during the measurements. Therefore we purged the microscope with nitrogen without the hood. This allowed lowering and stabilizing the concentration of the atmospheric CO_2 and H_2O. However there still remained some signatures of atmospheric gases in the spectra of the hBN/Gr/hBN membranes.

IR absorption spectra of CO_2 and H_2O are well known. In the MIR region of spectrum, CO_2 has relatively narrow absorption lines at 667 cm^{-1} and 2350 cm^{-1}, and H_2O has broader absorption bands at 1300 – 2000 cm^{-1} and 3500 – 3900 cm^{-1}. In MIR region, we could significantly reduce the optical signatures of both CO_2 and H_2O in the spectra of hBN/Gr/hBN membrane's through a special data treatment algorithm. Nonetheless, some artefacts of atmospheric gases remained in the MIR spectra. In the FIR region of spectrum, both CO_2 and H_2O have extended absorption bands below 450 cm^{-1}. Therefore we could not apply the same algorithm to remove the signatures of the atmospheric gases and their artefacts are to some extent present in all FIR spectra which we present here.

Values of magnetic field

In our experiments the magnetic field was highly homogeneous across the samples under investigation. According to our magnetic field simulation, variation of the absolute value of magnetic field in the biggest, 50 μm, sample from one edge of the membrane to another is supposed to be < 0.01 %. Such high homogeneity is due to the fact that our samples are three order of magnitude smaller than the bore of the magnet.

However the values of magnetic field could not be reproduced with 0.01 % precision on different days of measurements. There were two sources of systematic errors. 1) On different days of measurements, the sample holder could not be mounted at exactly the same height in the bore of the SC magnet. Therefore the values of magnetic field to which the samples were exposed could vary because of vertical gradient of magnetic field on the axis of the SC magnet, see the upper panel of Figure 4.10. 2) It was difficult to glue our three samples precisely in the centers of their sample holders. Thus position of each hBN/Gr/hBN stack was slightly off center from the axis of the magnet, and the deviation was different for each sample. Therefore the values of magnetic field to which the samples were exposed could also vary because of the horizontal gradient of magnetic field in the SC magnet, see the lower panel of Figure 4.10. Therefore the upper limit for variation of the magnetic field from one day to another is 0.7 % which is magnetic field inhomogeneity in the optically accessible region of the magnet's bore, see Figure 5.2.

Chapter 8

Summary and outlook

Summary of the work and results

This work is devoted to experimental investigation of magneto-optical spectra of suspended hBN-encapsulated graphene membranes. Graphene and hBN flakes were scotch-tape exfoliated, assembled together in hBN/Gr/hBN stacks and suspended using dry transfer only[1], see Section 3.2. Currently these procedures yield the best quality graphene which has low concentration of impurities and defects, high charge carrier mobility, high spatial homogeneity of doping. We had three circular hBN/Gr/hBN membranes with diameters of 50 μm, 30 μm, and 20 μm.

When exposed to an external magnetic field, graphene absorbs electro-magnetic radiation due to the dipole transitions of electrons between the Landau levels. As a result, magneto-optical spectra of graphene have peculiar features in the middle and far infrared regions of wavelengths: absorption lines, magnetic circular dichroism, and Faraday rotation. The magnitude of these effects largely depends on graphene's quality, doping, and temperature. Currently, the highest quality graphene samples can be produced only in small size < 1 mm. Meanwhile bigger graphene samples in most cases have inferior quality which leads to much less pronounced magneto-optical effects. Infrared spectra of graphene were investigated with the FTIR spectroscopy in many research groups predominantly on big graphene samples of $\sim$ 5 mm in size, see Section 2.5. There have been also a few magneto-optical experiments performed on smaller graphene samples < 1 mm. However these experiments had a number of limitations and technical issues despite the efforts of researchers who performed them. Unfortunately, currently no commercially available experimental setup provides ample opportunities for typical magneto-optical experiments when working with small samples, see Section 4.1.

Therefore we developed new experimental setup which enables various magneto-optical experiments on small graphene samples even ~ 10 μm in size, see

---

[1] Sample fabrication has been done in the University of Manchester in Condensed matter physics group by Sheng Hu and Marcelo Lozada Hidalgo in collaboration with Andre K. Geim.

Chapter 4. Our new setup comprises a compact superconducting magnet and its cryostat which were both developed in order to complement a commercial FTIR spectrometer connected to a commercial infrared microscope. Magnetic field in the sample compartment of the magnet can be varied from 0 to ± 4.1 Tesla. Thus our setup provides many new opportunities for magneto-optical experiments which were not feasible before: magneto-optical measurements on small samples both in reflection and transmission regimes, adequate normalization of spectra without overfilling, measurement of Faraday rotation angle, magnetic circular dichroism, and restoring magneto-optical conductivity tensor. On the downside, in our setup temperature in the sample compartment cannot be changed and the base temperature must be ~ 5 Kelvin during operation; mechanical stability is inferior compared to commercially available cryostats dedicated to microscopy measurements.

We performed several types of magneto-optical measurements in the linear response regime on our hBN-encapsulated graphene membranes in the far, middle and near infrared regions of wavelengths, see Chapter 5. We registered very large magnitudes of magneto-optical effects predicted in the framework of a simple single-electron theory. Apart form that we also observed several new subtle effects which to our knowledge have not been reported yet. We also created a simple model of light propagation in the hBN/Gr/hBN stacks in order to better understand the optical signatures due to hBN, see Chapter 6. In the same chapter we also comment on the origin of high tunability of graphene's optical properties.

First hBN/Gr/hBN stacks were illuminated with unpolarized infrared light in order to measure their relative transmission i.e. transmission in a nonzero magnetic field normalized by transmission in zero magnetic field, see Section 5.1. These spectra had pronounced signatures of intraband, mixed and interband magneto-optical transitions between the Landau levels. The absorption lines were narrow $\sim$ 5 meV which indicates low scattering rate of the charge carriers and corresponds to high mobility of $\sim$ 100 000 cm^{2}V^{-1}s^{-1}. The absorption lines were well resolved, in fact we could discern up to 10 absorption lines due to the interband magneto-optical transitions. Remarkably, there was pronounced magneto-optical absorption due to the intraband transitions in the far infrared region already at magnetic fields as low as 1 Tesla, see Section 7.3. At the same time spectra of graphene did not have any distinguishable features within the error of experiment in the near infrared region of wavelengths. In general energies of the lines were slightly shifted compared to the prediction of the single electron theory. Such shifts have been reported before and are usually attributed to the renormalizations due to the Coulomb interactions.

Ordinary dipole magneto-optical absorption lines due to the transitions between the Landau levels obey the selection rule $|n_\mathrm{f}| - |n_\mathrm{in}| = \pm 1$. However in addition to these lines we also registered new "forbidden" absorption lines of lower intensity which presumably satisfy the $|n_\mathrm{f}| - |n_\mathrm{in}| = 0$ selection rule, see Section 7.2. Another puzzling phenomenon which we registered in the transmission spectra of one of our samples at high magnetic field is splitting of the T_4 absorption line due to the interband transition. We also observed an interesting phenomenon which is related to the phonon in the hBN. Whenever a graphene's absorption line approached and crossed the hBN phonon's frequency the absorption line split into two lines of asymmetric shape, see Section 7.2. This phenomenon is well explained in the framework of wave optics within our simple model of hBN/Gr/hBN stacks, see Section 6.2.

Next, we performed experiments with linearly polarized infrared light. These experiments yield optical quantities Φ and Θ which could be approximated as the Faraday rotation angle and the relative transmission, see Section 5.2. Kramers-Kronig constraint fitting of Φ and Θ as well as model assumptions about graphene's behaviour in zero magnetic field allowed us to find the magneto-optical conductivity tensor of graphene, calculate the magnetic circular dichroism, and identify the sign of graphene's doping. In our highest magnetic field of 4.1 Tesla at the energy of the mixed i.e. T_1 magneto-optical transition we registered that absorption of left-handed light is 48 % at the same time no right-handed light is absorbed and the circular dichroism is $\Delta_A = +1$ within the error of the experiment. Such a large value of dichroism is accompanied by a large value of the Faraday rotation angle of $\sim 9^\circ$. For comparison, the highest possible absorption of an ultrathin conducting film of any nature is 50 %, and the largest possible Faraday rotation for graphene monolayer is 45°, see Chapter 6. In addition, we have also observed a new puzzling effect: the Faraday rotation curve had anomalous for p-doping inflections for the T_3 and T_4 interband transitions.

Importantly, in our case the large magnitude of the magneto-optical effects is an intrinsic property of graphene i.e. it is achieved without any kind of photonic structures nor optical resonators. We attribute this large magnitude to the narrow linewidths which is in turn caused by the low scattering rate in high quality samples. Another important prerequisite for efficient absorption is homogeneous chemical potential across the whole surface of the sample which in our case is ensured by the hBN-encapsulation. Indeed, each spot of the sample's surface absorbs the same amount of incoming IR light because there are not any deep electron-hole puddles which would otherwise cause Pauli blocking of electron transitions and consequent reduction in absorption at some random spots of the sample's surface.

The results are largely reproducible in all three hBN/Gr/hBN samples. Moreover, the spectra were measured several times on the same samples with intervals of several months in between the measurements. The total period of monitoring i.e. time which elapsed from the fabrication of samples until the last measurement is 19 months. The samples proved to be robust and survived many thermal cycles. At the same time we also registered some minor signs of degradation, in particular less absorption lines could be resolved at high energies (7 instead of 10). We also noticed optical signatures which indicate increase of graphene's doping with time: presumably the doping was $\sim 10^{10}$ cm^{-2} just after the sample were fabricated and later it became $\approx 2.8 \cdot 10^{11}$ cm^{-2}. Such a change of doping could be attributed to accumulation of some polar carbohydrates at the surface of hBN after many thermal cycles and short moments of exposure to ambient air when the hBN/Gr/hBN samples were mounted and unmounded form the cryostat.

Open question and future experiments

There still remain a lot of open questions, moreover our experimental results have posed new ones: Splitting of the T_4 absorption line, anomalous inflections of the Faraday rotation curve, and emergence of additional "forbidden" absorption lines in the magneto-optical spectra must be fully clarified. Broadening and shape of lines, as well as shifts of the line energies should be considered with more attention and carefully compared to existing theoretical predictions.

Unfortunately, our experimental setup did not allow measuring magneto-optical spectra at different temperatures. Such measurements require modification of experimental setup and could be done in future experiments which continue our endeavors. In particular, temperature dependence of linewidths gives important information about the line broadening mechanisms and dominant charge carrier scattering mechanisms. Our graphene samples do not have a gate electrode attached therefore we did not have the opportunity to control the position of chemical potential in graphene. However manufacturing encapsulated graphene devices with a gate does not pose any technological problems. Thus in future experiments, one may observe how the magnitudes of both Faraday rotation and magnetic circular dichroism depend on the level of doping and how their signs change when chemical potential in graphene crosses the Dirac point. Precise control of doping also allows one to investigate more subtle phenomena as Coulomb interaction effects. Gradually populating a Landau level and measuring the magneto-optical spectra at each step would allow monitoring how the interaction effects manifest for different values of filling factor. Hopefully this would help to clarify the origin of the anomalous inflections of the Faraday rotation curve and splitting of the T_4 absorption line.

More attention may be given to the phonon induced magneto-optical splitting of graphene absorption lines which we registered. Encapsulated graphene could be an interesting playground for different experiments because there are several parameters which could be easily varied or tuned independently from one another: magnetic field tunes the difference between the phonon's energy and graphene's absorption line energy, gate voltage may tune the intensity of graphene's absorption line, hBN thickness and angle of light incidence can vary the local electric field to which graphene is exposed. As we worked in the regime of nearly normal incidence of light, hyperbolicity of hBN is not supposed to be pronounced. However illuminating a hBN/Gr/hBN stack at larger angles requires modification of experimental setup which could be also addressed in future experiments. Hyperbolic property of hBN around its phonon's frequency requires a more elaborate theoretical description compared to the simple model presented in this manuscript.

Special care should be devoted to a better normalization of the optical spectra so that absolute transmission and not relative transmission would be measured. This would allow avoiding any model assumptions about behaviour of graphene in zero magnetic field during analysis of spectra.

A comment on possible applications

This work showed that magneto-optical effects are very strong and pronounced in high quality graphene monolayers which naturally raises the question as to whether these effects could be harnessed for applications in modern technology. An external magnetic field could be viewed as a “knob” which allows one to tune and redistribute spectral weight of graphene’s optical conductivity across a very broad range of wavelengths which includes both the far infrared and the middle infrared regions. Therefore magnetic field allows one to efficiently tune the magnitude of graphene’s magneto-optical absorption and Faraday rotation angle. Potentially, applying a gate voltage to graphene would give yet another “tuning knob” which would allow one to control magnitude and even sign of magnetic circular dichroism as well as the sign of Faraday rotation angle in graphene. All these considerations make high quality graphene a very appealing material for magneto-optical devices [242] including magneto-optical modulators, Faraday rotators, non-reciprocal magneto-optical elements as optical isolators (also called optical diodes), etc. Finding new materials with useful magneto-optical properties is especially important for the far infrared region because for this region of wavelengths there are not as many efficient magneto-optical devices as for the other regions of wavelengths.

Currently, there is a very high demand for lasers which operate in the infrared especially terahertz region of wavelengths. For this reason we would like to mark out the long speculated Landau level lasers among the rest of hypothetical magneto-optical applications of graphene. An idea of a Landau level laser was first proposed for 2D electron systems in 1986 by H. Aoki [243]. The main advantage and peculiar feature of such a laser is its tunable wavelength which could be set to any value from a broad spectral range in the infrared region. Such tuning of the laser’s wavelength is done by tuning the spacing between the Landau levels with the help of the external magnetic field. However it turned out that long-lived population inversion of Landau levels is difficult to achieve in conventional semiconductors because of strong Coulomb scattering between the charge carriers with equidistant Landau levels. In contrast, graphene has non-equidistant Landau levels which cover energies below and above the Dirac point. This unique property makes graphene a promising material for development of a Landau level laser. Different design schemes of such a laser have been proposed in [244, 245]. Our experiments have demonstrated that in high quality hBN/Gr/hBN stacks the absorption lines can be very sharp and narrow, in addition, a lot of absorption lines could be clearly discerned because many scattering mechanisms are mitigated. Both findings are important for better estimates of feasibility, modeling and design of graphene Landau level lasers. The next step needed in order to develop a laser would be further experiments which shed light on nonequilibrium dynamics of electrons and photons in optically pumped graphene.

I would like to mark out yet another field of potential applications which however has not been proposed before and is inspired by the phenomena observed in this work. Section 7.5 talks about maximally strong magneto-absorption and circular dichroism allowed in an ultrathin conducting film which we registered for the T_1 absorption line. This property could be employed in order to create polarization sensitive infrared light detectors with highly tunable characteristics. Such detectors may largely simplify analysis of light polarization for infrared spectra. This would be especially useful for applications in life sciences, pharmaceutics, medicine, forensic science, industrial quality control. As an example, many biological molecules may have symmetric isomers, these isomers have absolutely the same absorption spectra of unpolarized light, however they could be distinguished by different spectral signatures which they in for circularly polarized light of opposite handedness.

At the same time, there are a number of obvious problems which would hinder or even render many potential applications impossible. The first problem is related to the size of high quality graphene crystals. Real life applications require big crystals of at least several millimeters, or even better several centimeters in size. Whereas our scotch-tape exfoliated and manually encapsulated samples are three orders of magnitude smaller than the latter number. Thus it is essentially important to develop new methods of manufacturing high quality graphene crystals (charge carrier mobility $\mu \geq 100\,000\ \mathrm{cm^2V^{-1}s^{-1}}$) which have sufficiently big size as well as new methods of preserving graphene's quality from degradation when the device is assembled and later during routine operation of the device. The second problem is related to the temperature range in which hypothetical graphene based devices would operate. In our work, the magneto-optical effects were measured at liquid helium temperatures, however these effects are supposed to be smaller at room temperature because all mechanisms which cause broadening of graphene's absorption lines become much more pronounced as temperature grows. In principle, there are many devices in modern technology which operate with cryogenic liquids. However their cost, maintenance and operation are expensive, apart from that they are bulky. Thus temperature dependency of the magneto-optical effects in graphene must be investigated in order to assess the feasibility of room temperature applications and economical expedience of applications with different cryogenic liquids. The third problem is related to the generation of magnetic field which induces all the magneto-optical effects in graphene: the field must be high enough; highly homogeneous; in addition, the magnet must not block the optical pass to other devices nor disrupt their work. Some applications as magneto-optical modulators also require opportunity of changing the value of magnetic field, preferably with high speed and reproducibility. Thus room temperature applications would rely on permanent magnets which may produce up to $\sim$ 1 Tesla. Higher magnetic fields could be achieved with superconducting magnets which have several well-known disadvantages: they are more bulky, require cryogenic cooling and supplementary costs.

Appendices

A Suspended non-encapsulated graphene membranes

In our magneto-optical experiments, we also used two non-encapsulated suspended graphene membranes. Both membranes were suspended over scaffolding of the same geometry, see Figure 1. This scaffolding had similar structure but different dimensions compared to the scaffolding created for our hBN-encapsulated graphene membranes, see Figure 3.4. At the same time, scaffolding for non-encapsulated membranes had an additional circular hole in the Si/SiN$_x$ wafer. This hole was created especially for proper normalization of optical spectra during the measurements and in general such scaffolding with an additional hole creates more opportunities for optical experiments, see Appendix E for more details. The non-encapsulated graphene samples were created with the same method as the encapsulated ones, see Section 3.2.

Unfortunately, MIR spectra of the non-encapsulated graphene membranes did not contain any spectral features discernible within the error of our experimental setup even at our highest magnetic field of ~ 4 Tesla. In fact the samples seemed to be absolutely transparent. Most probably the non-encapsulated graphene membranes did not survive ambient conditions and/or were damaged during the first magneto-optical experiments at low temperature.

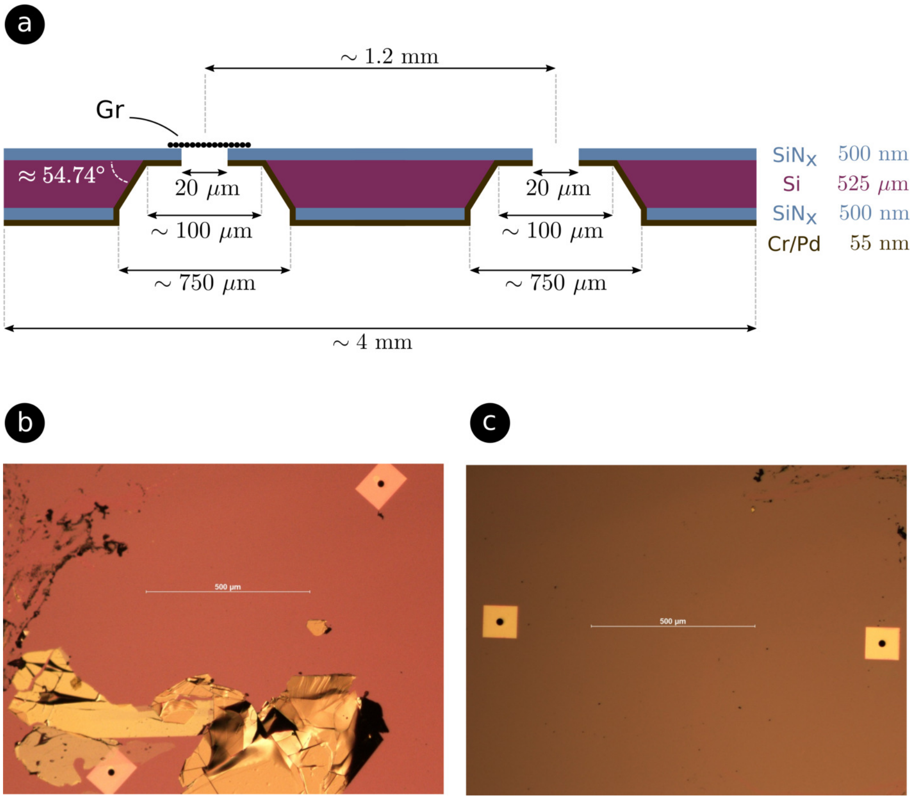

Figure 1 – Panel a: Cross section of the suspended non-encapsulated graphene membrane and scaffolding, the scheme does not show real proportions. **Panels b and c:** Photographs of the non-encapsulated membranes taken with an optical microscope, both scale bars are 500 μm. Light rectangles are the top faces of the truncated square pyramids etched in the scaffolding.

B Schemes of the FTIR spectrometer and the IR microscope

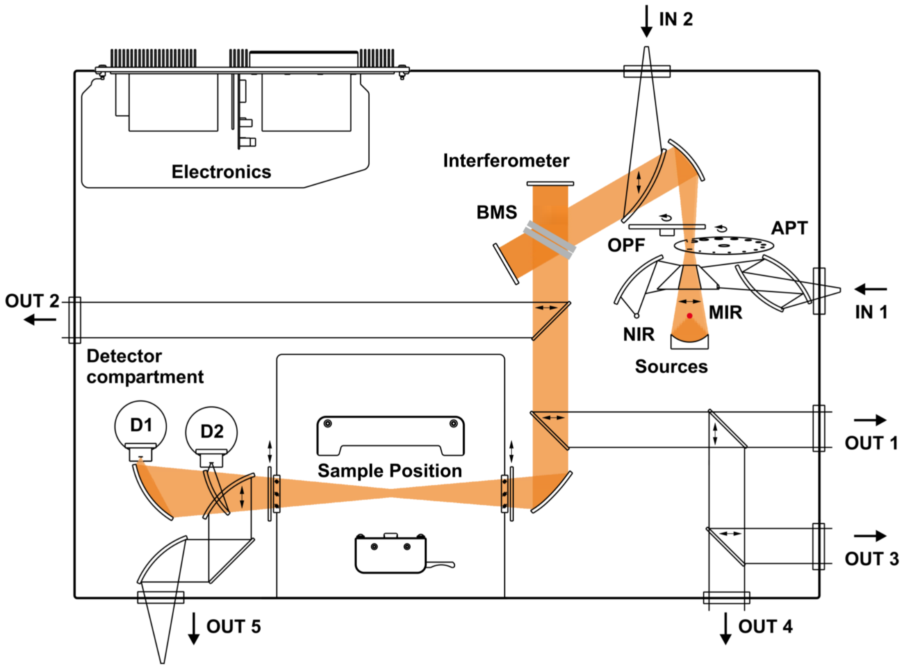

Figure 2 – Bruker FTIR spectrometer “Vertex 70v”. The figure is based on the official Bruker illustration. During our experiments the beam of light was redirected to the OUT2 which led to the IR microscope.

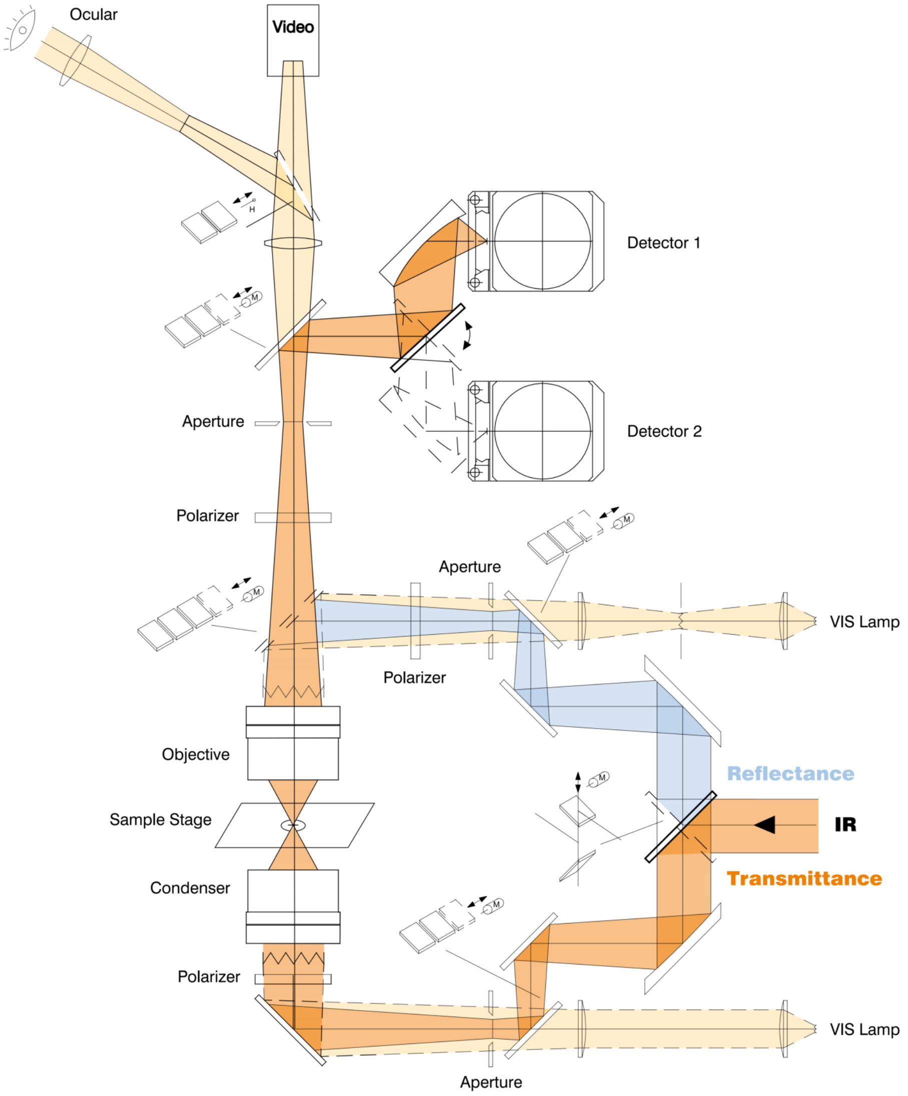

Figure 3 – Bruker IR microscope “Hyperion 2000”. The figure is based on the official Bruker illustration.

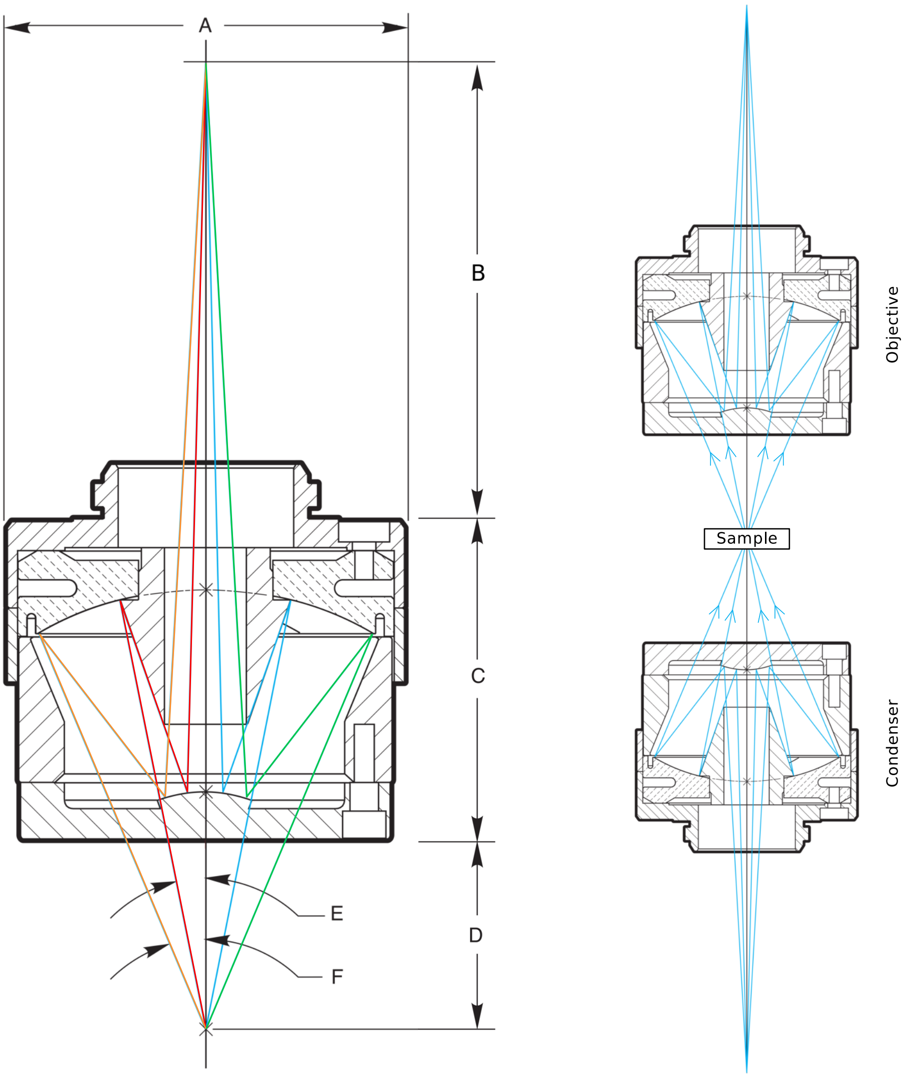

Figure 4 – Optical scheme of the Cassgrain reflectors manufactured by Newport, model 50105-01. A = 49.3 mm, back focal length B = 160.0 mm (dimension of B is not to scale in this figure), C = 38.6 mm, working distance D = 24.0 mm, E = 12.0°, F = 23.6°, magnification 15×, numerical aperture 0.4, field of view 1.2 mm, focal length 13 mm, obscuration 27%, secondary mirror diameter 10.5 mm. The figure is based on the official Newport illustration.

C Computer simulation of magnetic field

The goal of this simulation is to find magnetic field distribution $\mathbf{B}(r, z)$ inside and around an electromagnet of any given shape with axial symmetry, given values of the wire's diameter D, and the current I fed into the magnet.

We use the cylindrical coordinate system (r, φ, z), see Figure 4.8. In our electromagnet the wire spirals around a cylindric spool. The wire's diameter is ~ 100 times smaller than the inner radius of the spool. Therefore we approximated our magnet as a set of perfectly round loops with the same current I circulating in each loop. In this case magnetic field $\mathbf{B}(r, z)$ produced by the magnet could be calculated as a sum of magnetic fields produced by all loops in the magnet. Finding magnetic field $\mathbf{B}_0(r, z, a)$ produced by a single round loop of radius a with current I is a classical problem and its solution could be found in [246].In contrast to the big SC magnet, the small SC magnet is mounted directly the the cold finger without need of a connector. Here we provide the final result for three projections of the magnetic field vector $\mathbf{B}_0(r, z, a)$ in SI units, the center of the loop coincides with the beginning of coordinates, and the loop lays in the $z = 0$ plain.

$$B_{0r} = 2I\,\frac{\mu_0}{4\pi}\frac{z/r}{\sqrt{(a+r)^2+z^2}}\left(\frac{a^2+r^2+z^2}{(a-r)^2+z^2}E - K\right), \quad B_{0\varphi} = 0,$$

$$B_{0z} = 2I\,\frac{\mu_0}{4\pi}\frac{1}{\sqrt{(a+r)^2+z^2}}\left(\frac{a^2-r^2-z^2}{(a-r)^2+z^2}E + K\right),$$

where K and E are complete elliptic integrals of the first and second kinds:

$$K = \int\limits_0^{\pi/2} \frac{d\theta}{\sqrt{1-k^2\sin^2\theta}}, \quad E = \int\limits_0^{\pi/2} \sqrt{1-k^2\sin^2\theta}\,d\theta,$$

$$\text{where} \quad k^2 \equiv \frac{4ar}{(a+r)^2+z^2}.$$

Distribution of magnetic field $\mathbf{B}(r, z)$ does not depend on the angle φ because our magnet has axial symmetry. Therefore we introduced a two-dimensional rectangular grid which lays in any arbitrary plane $\varphi = \text{const}$ in order to proceed with the calculations. Vertical separation δ_z between the nods of the grid was chosen to be the same or several times smaller than the vertical separation between the neighboring loops of the wire Δ_z i.e.

$$n \cdot \delta_z = \Delta_z, \ n = 1, 2, 3, \ldots . \tag{1}$$

In our simulation we allowed $\Delta_z \neq D$ in order to have more flexibility. Horizontal separation δ_r between the nods did not have any specific restrictions and was chosen regarding the desired spatial resolution for the final result. Magnetic field distribution $\mathbf{B}_0(r, z, a)$ was evaluated in the nods of the grid for different values of the loops' radii a. Next, the obtained distributions $\mathbf{B}_0(r, z, a)$ were translated in parallel upwards and downwards by Δ_z, $2\Delta_z$, $3\Delta_z$, etc in order to obtain magnetic field distributions produced by neighboring loops situated higher and lower relative to the former loops. Such parallel translation of the field is enabled by the proper choice of the grid 1 and allows significantly reducing the run time of the code. The final result for the magnetic field distribution $\mathbf{B}(r, z)$ was constructed as a superposition of the above mentioned distributions of single loops $\mathbf{B}_0(r, z, a)$.

The computed code was written in Python language and we used functionality offered by NumPy and SciPy packages. Typically calculating one configuration of magnetic field distribution inside and around the magnet $\mathbf{B}(r, z)$ took only several minutes. Thus we had an opportunity to try many different shapes (not only the cylindrical ones) and dimensions of the magnet as well as different diameters of the wire D and spacing between the wires Δ_z.

D Small superconducting electromagnet

The small SC magnet is made of the same materials as the big SC magnet, and has a similar structure but different dimensions, see Figure 5. The small SC magnet produces fields comparable to those of rare earth permanent magnets ~ 0.8 Tesla. Space dedicated to the loops of SC wire is encompassed between two cylindric surfaces with radii $R_{\text{in}} = 14$ mm and $R_{\text{out}} = 19$ mm and has height $H = 10$ mm. Bore of the small magnet has the same radius and thread as the one in the big magnet. Thus all the sample holders which are supposed to be mounted inside the bore are compatible with both SC magnets. We used a thinner SC wire in the small magnet. According to the magnetic field simulation, the optimal SC wire turned out to be monofilamentary NbTi T48B-M wire in a copper matrix provided by Supercon Inc (product number T48B-M). Its diameter with Formvar insulation is $D = 178$ μm and bare diameter is 152 μm.

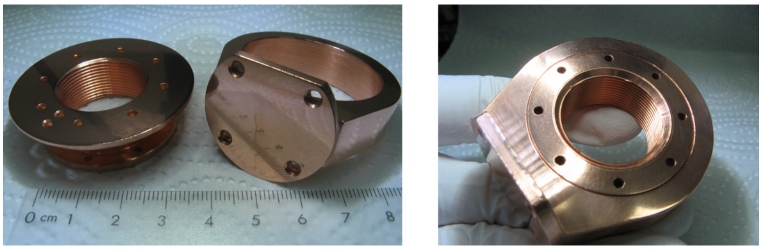

Figure 5 – The small SC magnet. Spool and casing milled from OFHC copper.

E Normalization of detector's signal in optical measurements

Transmission of a medium is defined as $T(\omega, B) = I_{\text{tr}}(\omega, B)/I_{\text{in}}(\omega)$ where $I_{\text{in}}(\omega)$ is intensity of incident light and $I_{\text{tr}}(\omega, B)$ is intensity of transmitted light. Usually one does not measure the quantities $I_{\text{in}}(\omega)$ and $I_{\text{tr}}(\omega, B)$ directly in order to find $T(\omega, B)$ because in FTIRS it is much easier to measure their ratio. The same is true for circular transmission dichroism ratio $D(\omega, B) = T_{-}(\omega, B)/T_{+}(\omega, B)$ which could be extracted from experimental data without direct measurement of $T_{-}(\omega, B)$ and $T_{+}(\omega, B)$ and without any use of circularly polarized light. Here we give a simplified explanation of how different physical quantities are obtained with FTIRS method without going into details about actual Fourier transform of the signal.

Transmission

A scheme of a typical transmission measurement experiment is shown in panel a of Figure 6. The optical path begins at a source which emits IR light of spectrum I_{s}. This light goes through many subsidiary optical elements as windows, mirrors, apertures, beamsplitter, etc. Thus intensity of the light which impinges on the sample under investigation is lower than it was in the beginning $I_{\text{s}}(\omega) \cdot \kappa_1(\omega) = I_{\text{in}}(\omega)$, where $\kappa_1(\omega)$ is a coefficient which characterizes cumulative effect of all intermediate optical elements between the IR source and the sample. From the above mentioned definition intensity of IR light transmitted through the sample is $I_{\text{tr}}(\omega) = T(\omega, B) I_{\text{in}}(\omega)$. Next, IR light has to pass through yet another chain of subsidiary optical elements therefore its intensity is decreases by a factor of $\kappa_2(\omega)$ when the light finally arrives at the IR detector $I_{\text{d}}(\omega) = \kappa_1(\omega) \cdot I_{\text{tr}}(\omega)$. When detector operates in the linear response regime its signal could be expressed as $\kappa_{\text{d}} \cdot I_{\text{d}}(\omega)$ where κ_{d} is a coefficient which describes how detector's sensitivity depends on the frequency of light. Now one can write down a final expression for the detector's signal for the configuration when light passes through a sample under investigation, see panel a of Figure 7:

$$S_{\text{SUI}}(\omega, B) = I_{\text{s}}(\omega)\kappa_1 \cdot T(\omega, B) \cdot \kappa_2 \kappa_{\text{d}}. \tag{2}$$

A priori coefficients κ_1, κ_2, and κ_{d} are considered to be unknown. Therefore detector's signal must be normalized. This could be done by measuring detector's signal in exactly the same optical configuration but without the sample under investigation. Here we make a reasonable assumption that coefficients κ_1, κ_2, and κ_{d} do not depend on the intensity of IR light. In our case the sample under investigation must be substituted by a circular aperture (hole) of exactly the same shape as the one over which the sample under investigation is suspended, see Figure 1 and panel b of Figure 7. Detector's signal when the light passes through the hole without the sample is

$$S_{\text{h}}(\omega) = I_{\text{s}}(\omega)\kappa_1 \cdot \kappa_2 \kappa_{\text{d}}. \tag{3}$$

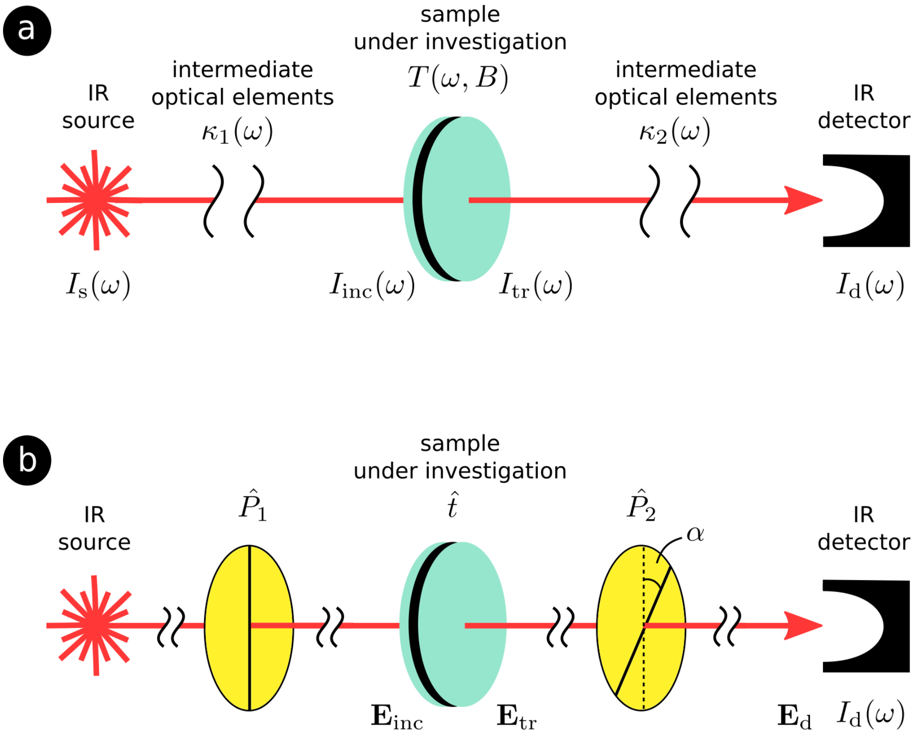

Figure 6 – Schematic illustration of the optical path in typical FTIRS experiments. **Panel a:** Transmission measurement. **Panel b:** Faraday rotation and magnetic circular dichroism measurement. Yellow circles designate two linear polarizers, solid black lines designate orientation of polarizers' axes.

Now one can find transmission of the sample under investigation dividing formula (2) by formula (3):

$$T(\omega, B) = S_{SUI}(\omega, B)/S_h(\omega). \tag{4}$$

Our experimental setup allows performing such a procedure of normalization and we had an opportunity to measure transmission of our non-encapsulated suspended graphene membranes, see Appendix A. However, unfortunately, we did not have circular apertures of exactly the same shape as the ones over which our encapsulated graphene membranes were suspended. Therefore we had to normalize detector's signal in a different way. For this purpose we measured transmission of the sample under investigation in a zero magnetic field, in this case the detector's signal is

$$S_{SUI}(\omega, B=0) = I_s(\omega)\kappa_1 \cdot T(\omega, B=0) \cdot \kappa_2\kappa_d. \tag{5}$$

Now one can find *relative* transmission $\widetilde{T}(\omega, B)$ of the sample under investigation simply dividing formula (2) by formula (5):

$$\widetilde{T}(\omega, B) \equiv \frac{T(\omega, B)}{T(\omega, B=0)} = \frac{S_{SUI}(\omega, B)}{S_{SUI}(\omega, B=0)}. \tag{6}$$

This idea has been already briefly mentioned in Section 5.1 in the formulas (5.1) and (5.2). Here we have made a reasonable assumption that coefficients κ_1, κ_2, and κ_d do not depend on the external magnetic field or magnetic field to which they are exposed is very weak. Another important condition for validity of the signal normalization (6) is that fine alignment of experimental setup must remain the same when magnetic field changes. This was fairly true in our case and did not induce significant systematic errors.

Unfortunately, procedure (6) does not give any meaningful information about transmission of the samples under investigation in zero magnetic field. However it allows one to obtain meaningful physical information about the samples in nonzero magnetic field even without any additional optical element which are needed in order to measure the signal (3). This is the reason why normalization procedure (6) was used in many magneto-optical experiments on graphene (see Section 2.5) including ours.

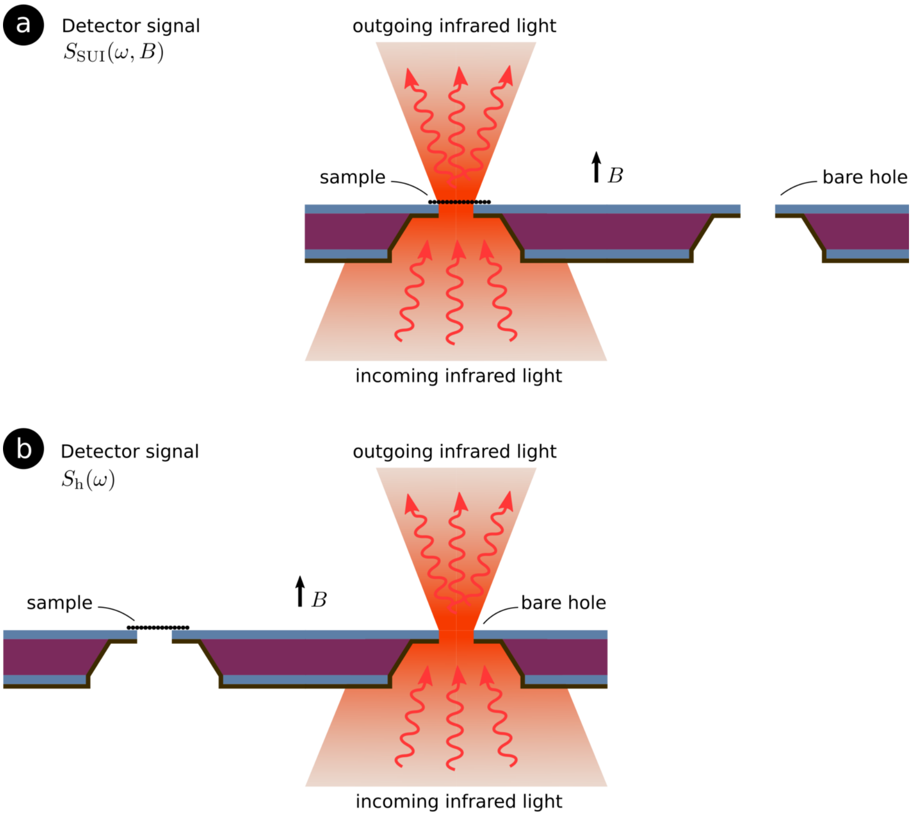

Figure 7 – Optical path for measurement of sample's transmission $T(\omega, B)$ with proper normalization of the detector's signal as described in the formula (4).

Faraday rotation and magnetic circular dichroism

A scheme of a typical Faraday rotation measurement experiment is shown in panel b of Figure 6. As one can see, two broadband linear polarizers are added on the optical path before and after the sample under investigation compared to the scheme of the transmission measurement experiment. In this experiment polarization of light matters therefore we use Jones-matrix formalism to describe propagation of light from one optical element to another. From now on we also omit frequency ω and magnetic field B arguments in order to simply the notation.

Without loss of generality, let us assume that P1 is always fixed and its polarization axis is labeled as x-axis. In such a coordinate system Jones matrix corresponding to P1 is

$$\hat{P}_1 = t_1 \begin{bmatrix} 1 & 0 \\ 0 & 0 \end{bmatrix}, \tag{7}$$

where t_1 is transmission Fresnel coefficient of P1. The IR source emits unpolarized light and after passing through P1, the light acquires linear polarization with amplitude E_0 along the x-axis. Subsidiary optical elements may introduce different parasitic effects to the stream of light: unintended tilts of its Jones vector (depolarization) and some nonzero fraction of unpolarized light. In our calculations we neglect these parasitic effects (except for a full handedness inversion during reflections from mirrors) and considers that subsidiary optical elements can only influence intensity of the light. Moreover, let us omit their effect for a while in order to simply the layout of formulas. Thus the Jones vector of light which impinges on the sample under investigation is

$$\mathbf{E}_{\text{inc}} = t_1 \begin{bmatrix} E_0 \\ 0 \end{bmatrix}. \tag{8}$$

Next, the Jones vector $\mathbf{E}_{\text{tr}}$ of light transmitted through the sample is defined by the sample's Jones matrix $\hat{t}$ and in the simple case of normal incidence of light:

$$\hat{t} = \begin{bmatrix} t_{xx} & t_{xy} \\ -t_{xy} & t_{xx} \end{bmatrix}, \quad \mathbf{E}_{\text{tr}} = \hat{t}\mathbf{E}_{\text{inc}} = t_1 E_0 \begin{bmatrix} t_{xx} \\ -t_{xy} \end{bmatrix}. \tag{9}$$

In nonzero magnetic field $t_{xy} \neq 0$ and the Jones vector $\mathbf{E}_{\text{tr}}$ indicates that light transmitted through the sample acquires elliptical polarization with its major axis tilted relative to the x-axis. The second polarizer P2 is oriented at some angle α relative to the x-axis and has transmission Fresnel coefficient t_2 therefore its Jones matrix is

$$\hat{P}_2 = t_2 \begin{bmatrix} \cos^2\alpha & \cos\alpha\sin\alpha \\ \cos\alpha\sin\alpha & \sin^2\alpha \end{bmatrix}, \tag{10}$$

The Jones vector of light which arrives to the IR detector is

$$\mathbf{E}_{\text{d}} = \hat{P}_2\mathbf{E}_{\text{tr}} = (t_{xx}\cos\alpha - t_{xy}\sin\alpha)t_1 t_2 E_0 \begin{bmatrix} \cos\alpha \\ \sin\alpha \end{bmatrix}. \tag{11}$$

Now we can write down an expression for intensity of light which arrives to the IR detector:

$$I_{\mathrm{d}} = \kappa_1 \kappa_2 |E_{\mathrm{d}}|^2, \tag{12}$$

here we incorporated the coefficients κ_1 and κ_2 in order to take into account the effect of all subsidiary optical elements which we have omitted so far. Signal registered by the IR detector is

$$S_{\mathrm{SUI}} = \kappa_{\mathrm{d}} I_{\mathrm{d}} = \kappa_{\mathrm{d}} \kappa_1 \kappa_2 t_1^2 t_2^2 E_0^2 (t_{xx} \cos\alpha - t_{xy} \sin\alpha)^2. \tag{13}$$

In further formulas we use a shorthand κ for all coefficient which do not characterize the sample under investigation, at the same time κ may depend on the orientation of the polarizers because of imperfections of these devices:

$$\kappa \equiv \kappa_{\mathrm{d}} \kappa_1 \kappa_2 t_1^2 t_2^2 E_0^2.$$

In order to proceed we rewrite Fresnel coefficients t_{xx} and t_{xy} in the basis of circular polarization (see Section 6.3):

$$\begin{aligned} t_{xx} &= \frac{\sqrt{T_+} e^{-i\theta_F} + \sqrt{T_-} e^{i\theta_F}}{2} e^{i(\theta_+ + \theta_F)} \\ t_{xy} &= \frac{\sqrt{T_+} e^{-i\theta_F} - \sqrt{T_-} e^{i\theta_F}}{2i} e^{i(\theta_+ + \theta_F)}. \end{aligned} \tag{14}$$

When expressions (14) are substituted into the formula (13) one should not forget that we have not taken into account the total inversion of polarization handedness after each reflection from the subsidiary mirrors. Such negligence leads to the fact that the sign of the Faraday rotation angle becomes ill-defined. Therefore we introduce a new notation $\theta_F \to \varphi$ where φ is equal to the Faraday rotation angle up to the sign. Thus the signal at the detector is

$$\begin{aligned} S_{\mathrm{SUI}} = \frac{\kappa}{4} \cdot \Big| & \left(\sqrt{T_+} e^{-i\varphi} + \sqrt{T_-} e^{i\varphi} \right) \cos\alpha + \\ & + i \left(\sqrt{T_+} e^{-i\varphi} - \sqrt{T_-} e^{i\varphi} \right) \sin\alpha \Big|^2 = \ldots = \\ & = \frac{\kappa}{2} \left(\frac{T_+ + T_-}{2} + \sqrt{T_+ T_-} \cos\left[2\alpha - 2\varphi\right] \right). \end{aligned} \tag{15}$$

Finally, one can rewrite the above expression in terms of the total transmission $T = (T_+ + T_-)/2$ and the circular transmission dichroism ratio $D = T_-/T_+$:

$$S_{\mathrm{SUI}} = \kappa \cdot T \left(\frac{1}{2} + \frac{\sqrt{D}}{1 + D} \cos\left[2\alpha - 2\varphi\right] \right). \tag{16}$$

Formula (16) coincides with the formula (5.3) presented in Section 5.2 without a proof. A priori the value of coefficient κ is considered to be unknown just like in the transmission measurements described in the previous subsection. When the

Faraday rotation angle is measured as described in the protocol summarized in the formula (5.5) then the unknown coefficient κ is canceled out and it is no longer present in the final formula (5.6) for the optical quantity Φ approximated as the Faraday rotation angle. However other protocols of measurements could potentially require normalization of the detector's signal. This could be done with the help of a reference signal the same way as in the previous subsection: one should measure the detector's signal S_h in exactly the same optical configuration but without the sample under investigation (see Figure 7), alternatively, one should measure detector's signal S_0 when light passes through the sample under investigation in a zero magnetic field. In either case there is not any magneto-optical activity in the sample compartment i.e. $\varphi = 0$ and $T_- = T_+$ therefore the detector's signals are

$$S_\mathrm{h} = \frac{\kappa}{2} \cdot (1 + \cos 2\alpha)\,, \tag{17}$$

$$S_0 = \frac{\kappa}{2} \cdot T(\omega, B \neq 0) \cdot (1 + \cos 2\alpha)\,. \tag{18}$$

F Important scales

Fermi velocity of graphene $v_F = 1.15 \cdot 10^6$ m/s

Admittance of free space $Y_0 = 1/Z_0 = \sqrt{\varepsilon_0/\mu_0} \approx 2.65 \cdot 10^{-3}\ \Omega^{-1}$

Universal conductivity of graphene $\sigma_0 = e^2/(4\hbar) \approx 6.084 \cdot 10^{-5}\ \Omega^{-1}$

Conductivity quantum $G_0 = 2e^2/h \approx 7.748 \cdot 10^{-5}\ \Omega^{-1}$

Optical absorption in undoped graphene at zero magnetic field
$A_0 = \pi\alpha \approx 2.3$ %

Charge carrier concentration in zero magnetic field
$N = (g_s g_v E_F^2)/(4\pi v_F^2 \hbar^2) \approx 7.35 \cdot 10^7 \cdot (E_F/v_F)^2$ cm^{-1}

Magnetic energy $E_B = v_F\sqrt{2e\hbar B} \approx 36.3 v_F \sqrt{B[\text{Tesla}]}$ meV

Magnetic length $l_B = \sqrt{\hbar/(eB)} \approx 25.5/\sqrt{B[\text{Tesla}]}$ nm

Landau level filling factor $\nu = \pm(4|n| + 2)$

Charge carrier concentration in nonzero magnetic field
$N = eB\nu/h \approx 24.1 \cdot 10^9 \cdot \nu B[\text{Tesla}]$ cm^{-2}

G Abbreviations

a. u. – arbitrary units
C-AFM – conductive atomic force microscopy
CVD – chemical vapor deposition
FIR – far infrared
FR – Faraday rotation
FRA – Faraday rotation angle
FT – Fourier transform
FTIR – Fourier transform infrared
FTIRS – Fourier transform infrared spectroscopy/spectrometer
Gr/hBN – graphene on hexagonal boron nitride substrate
OFHC – oxygen-free high thermal conductivity (concerning copper)
IR – infrared
hBN/Gr/hBN – graphene encapsulated in hexagonal boron nitride
KK – Kramers-Kronig
KOH – potassium hydroxide
LL – Landau level
MCD – magnetic circular dichroism
MCT – mercury cadmium telluride (HgCdTe)
MIR – middle infrared
MO – magneto-optical
NIR – near infrared
PE – polyethylene
PMGI – polymethylglutarimide polymer
PMMA – poly-(methyl methacrylate) polymer
PP – polypropylene
RIE – reactive ion etching
RS – Raman spectroscopy/spectrometer
SC – superconducting
STM – scanning tunneling microscopy
STS – scanning tunneling spectroscopy
SUI – sample under investigation
THz-TDS – terahertz time-domain spectroscopy
UV – ultra violet
VIS – visible
2D – two-dimensional
3D – three-dimensional

List of publications

- Ievgeniia O. Nedoliuk, Sheng Hu, Andre K. Geim, and Alexey B. Kuzmenko, “Colossal infrared and terahertz magneto-optical activity in high-mobility graphene”, in preparation.
- Ievgeniia O. Nedoliuk, Damien Stricker, Michaël K. Tran, Ivan P. Levkivskyi, Mehdi P. Brandt, Sheng Hu, Andre K. Geim, and Alexey B. Kuzmenko, “Versatile setup for magneto-optical microspectroscopy at low temperature and magnetic field up to 4 Tesla”, in preparation.
- Pieter J. de Visser, Julien Levallois, Michaël K. Tran, Jean-Marie Poumirol, Ievgeniia O. Nedoliuk, Jérémie Teyssier, Ctirad Uher, Dirk van der Marel, and Alexey B. Kuzmenko, “Suppressed Magnetic Circular Dichroism and Valley-Selective Magnetoabsorption due to the Effective Mass Anisotropy in Bismuth Journal Article”, Physical Review Letters, Volume 117, Issue 1, page 017402, 2016.
- Julien Levallois, Ievgeniia O. Nedoliuk, Iris Crassee, and Alexey B. Kuzmenko, “Magneto-optical Kramers-Kronig analysis”, Review of Scientific Instruments, Volume 86, Issue 3, page 033906, 2015.
- Nicolas Ubrig, Iris Crassee, Julien Levallois, Ievgeniia O. Nedoliuk, Felix Fromm, Michl Kaiser, Thomas Seyller, and Alexey B. Kuzmenko, “Fabry-Perot enhanced Faraday rotation in graphene”, Optics Express, Volume 21, Issue 21, pages 24736−24741, 2013.

Acknowledgements

I would like to express my genuine gratitude to my scientific advisor Alexey B. Kuzmenko for welcoming me in his laboratory. Alexey has been working in the highly competitive field of graphene almost since the discovery of this material. Having knowledge and lot of experience in the infrared optics of graphene, Alexey formulated an interesting, elaborated, and bold project. Thanks to Alexey, I enjoyed a very rare for our days opportunity of participating in an almost textbook scenario of a scientific cycle: I could passed through all stages from the formulation of an initial hypothesis to the joy of obtaining new unexpected results which posed further scientific questions.

I would like to thank to our collaborators from the University of Manchester: Sheng Hu, Marcelo Lozada Hidalgo, and Andre K. Geim. They provided the highest quality graphene membranes assembled and suspended in mid-air with jewelry precision.

I would like to thank our technician Mehdi Brandt who always stood by me in all the ups and downs (especially downs) during my work in the laboratory and during development of the new experimental setup. Mehdi, thank you for sharing your skills, experience, and your infinite sense of humor! I feel special gratitude to Rolland Pellet and his team for their warm welcome in the Mechanical workshop, their meticulous attitude to work and for making all the pieces of experimental setup which were designed in our group on paper real and tangible. I would like to thank Spiros Zanos and his cryogenics team who provided us with galore of liquid helium which is essential for all our superconducting magnets and detectors. I would like to thank Matthias Kuhn and Florent Boudoire for advice about patenting new technologies.

I would like to thank Damien Stricker who passed me his experience of making superconducting magnets: magnetic field simulations, impregnation, winding etc. I would like to thank Lionel Windels for his advice in winding and calibrating the magnets. I would like to thank Michaël Tran who helped me to master "Inventor", design the outer shell of the cryostat and translated the abstract of this thesis into French language. I would like to thank Iris Crassee for introducing me to the infrared microscope and giving some life advice in general. I would like

to thank Adrien Stucky for helping me to anneal our biggest and the most precious graphene membrane when it was in danger of degradation. I would like to thank Benjamin Mc Elfresh for proofreading notes and giving advice about English grammar. Damien, Lionel, Michaël, Iris, Adrien, and Benjamin I am enormously grateful to you for being positive, cheerful, supportive, and always ready to help all these years!

I also would like to thank Nicolas Ubrig, Julien Levallois, Julien Rupen, Davide Valentinis, Gernot Scheerer, Nimrod Bachar, Marco Lopes, Sébastien Müller, Géraldine Cravotto, Bernard Guipet, Christophe Berthod, Didier Jaccard, Basko Denis, Clement Faugeras, Gorbachev Roman, Tobias Wolf, Oded Zilberberg.

I would like to thank communities of Python and Stackoverflow. I would also like to appologize to all authors of scientific publications who were unjustly omited and not cited in this manuscript because nowadays it is very difficult to have a grip on the enormous flux of the information about graphene.

I would like to thank my jury Carmine Senatore and Milan Orlita for scientific discussions and advice, for being patient and attentive when reading the manuscript of my thesis, for useful comments and feedback. I deeply appreciate open-handed help of Thierry Giamarchi and Patrycja Paruch, I thank you both for your support, understanding, and guidance during the most hard times.

I would like to thank Denise Borjon, Dragana Pantelic, Elisabeth Giudicelli, Fabienne Hartmeier, Pierre Bouillot, Patrick Magnin, and Dirk van der Marel for their help with the administrative issues.

I would like to thank my friends Artur, Vladimir, Sandra, Iura, Yuliya, Edvin, Barbara, and Circé. Finally, my special thanks goes to my husband Ivan who helped me in my research work with his scientific advice and sometimes even muscle force, and most importantly I am very grateful to Ivan for his emotional support and understanding.

This work was supported in the framework of the SNSF project 200020-140710, SNSF project 200020-156615, and the DQMP fund of the University of Geneva.

References

[1] H. Boehm, R. Setton, and E. Stumpp, “Nomenclature and terminology of graphite intercalation compounds,” *Carbon*, vol. 24, no. 2, pp. 241 – 245, 1986.

[2] P. R. Wallace, “The band theory of graphite,” *Phys. Rev.*, vol. 71, pp. 622 – 634, May 1947.

[3] R. E. Peierls, “Quelques proprietes typiques des corpses solides,” *Ann. I. H. Poincare*, vol. 5, 1935.

[4] L. D. Landau, “Zur Theorie der phasenumwandlungen II,” *Phys. Z. Sowjetunion*, vol. 11, pp. 26 – 35, 1937.

[5] L. D. Landau and E. M. Lifshitz, *Statistical Physics, Part I.* Pergamon Press, Oxford, 1980.

[6] N. D. Mermin, “Crystalline order in two dimensions,” *Phys. Rev.*, vol. 176, pp. 250 – 254, Dec 1968.

[7] J. A. Venables, G. D. T. Spiller, and M. Hanbucken, “Nucleation and growth of thin films,” *Reports on Progress in Physics*, vol. 47, no. 4, p. 399, 1984.

[8] J. Evans, P. Thiel, and M. Bartelt, “Morphological evolution during epitaxial thin film growth: Formation of 2D islands and 3D mounds,” *Surface Science Reports*, vol. 61, no. 1, pp. 1 – 128, 2006.

[9] A. K. Geim, “Nobel lecture: Random walk to graphene,” *Rev. Mod. Phys.*, vol. 83, pp. 851 – 862, Aug 2011.

[10] H. P. Boehm, A. Clauss, G. O. Fischer, and U. Hofmann, “Das Adsorptionsverhalten sehr dünner Kohlenstoff-Folien,” *Zeitschrift für anorganische und allgemeine Chemie*, vol. 316, no. 34, pp. 119 – 127, 1962. Title in English: The adsorption behavior of very thin carbon films.

[11] K. S. Novoselov, A. K. Geim, S. V. Morozov, D. Jiang, Y. Zhang, S. V. Dubonos, I. V. Grigorieva, and A. A. Firsov, “Electric field effect in atomically thin carbon films,” *Science*, vol. 306, no. 5696, pp. 666 – 669, 2004.

[12] K. S. Novoselov, D. Jiang, F. Schedin, T. J. Booth, V. V. Khotkevich, S. V. Morozov, and A. K. Geim, “Two-dimensional atomic crystals,” *Proceedings of the National Academy of Sciences*, vol. 102, no. 30, pp. 10451 – 10453, 2005.

[13] A. Plume, “Graphene: ten years of the ‘gold rush’,” Sep 2014. *Research Trends*, Issue 38.

[14] A. Barth and W. Marx, “Graphene – a rising star in view of scientometrics,” 2008. Arxiv, arXiv:0808.3320.

[15] K. S. Kim, Y. Zhao, H. Jang, S. Y. Lee, J. M. Kim, K. S. Kim, J.-H. Ahn, P. Kim, J.-Y. Choi, and B. H. Hong, “Large-scale pattern growth of graphene films for stretchable transparent electrodes,” *Nature*, vol. 457, Jan 2009.

[16] A. Reina, X. Jia, J. Ho, D. Nezich, H. Son, V. Bulovic, M. S. Dresselhaus, and J. Kong, “Large area, few-layer graphene films on arbitrary substrates by chemical vapor deposition,” *Nano Letters*, vol. 9, no. 1, pp. 30 – 35, 2009. PMID: 19046078.

[17] J. C. Meyer, A. K. Geim, M. I. Katsnelson, K. S. Novoselov, T. J. Booth, and S. Roth, “The structure of suspended graphene sheets,” *Nature*, vol. 446, 2007.

[18] J. H. Los, K. V. Zakharchenko, M. I. Katsnelson, and A. Fasolino, “Melting temperature of graphene,” *Phys. Rev. B*, vol. 91, p. 045415, Jan 2015.

[19] K. Seibert, G. C. Cho, W. Kütt, H. Kurz, D. H. Reitze, J. I. Dadap, H. Ahn, M. C. Downer, and A. M. Malvezzi, “Femtosecond carrier dynamics in graphite,” *Phys. Rev. B*, vol. 42, pp. 2842 – 2851, Aug 1990.

[20] A. K. Geim, “Graphene: Status and prospects,” *Science*, vol. 324, no. 5934, pp. 1530 – 1534, 2009.

[21] D. D. L. Chung, “Review graphite,” *Journal of Materials Science*, vol. 37, pp. 1475 – 1489, Apr 2002.

[22] J. D. Bernal and W. L. Bragg, “The structure of graphite,” *Proceedings of the Royal Society of London A: Mathematical, Physical and Engineering Sciences*, vol. 106, no. 740, pp. 749 – 773, 1924.

[23] Y. Baskin and L. Meyer, “Lattice constants of graphite at low temperatures,” *Phys. Rev.*, vol. 100, pp. 544 – 544, Oct 1955.

[24] V. Crespi, “Flatland exposed,” *Physics*, vol. 1, p. 15, Aug 2008.

[25] S. V. Dmitriev, J. A. Baimova, A. V. Savin, and Y. S. Kivshar, “Ultimate strength, ripples, sound velocities, and density of phonon states of strained graphene,” *Computational Materials Science*, vol. 53, no. 1, pp. 194 – 203, 2012.

[26] A. H. Castro Neto, F. Guinea, N. M. R. Peres, K. S. Novoselov, and A. K. Geim, “The electronic properties of graphene,” *Rev. Mod. Phys.*, vol. 81, pp. 109 – 162, Jan 2009.

[27] M. Orlita and M. Potemski, “Dirac electronic states in graphene systems: optical spectroscopy studies,” *Semiconductor Science and Technology*, vol. 25, no. 6, p. 063001, 2010.

[28] J. Wang, S. Deng, Z. Liu, and Z. Liu, “The rare two-dimensional materials with Dirac cones,” *National Science Review*, vol. 2, no. 1, pp. 22 – 39, 2015.

[29] Y. Fuseya, M. Ogata, and H. Fukuyama, “Transport properties and diamagnetism of Dirac electrons in bismuth,” *Journal of the Physical Society of Japan*, vol. 84, no. 1, p. 012001, 2015.

[30] H. Fukuyama, Y. Fuseya, M. Ogata, A. Kobayashi, and Y. Suzumura, “Dirac electrons in solids,” *Physica B: Condensed Matter*, vol. 407, no. 11, pp. 1943 – 1947, 2012. Proceedings of the International Workshop on Electronic Crystals (ECRYS-2011).

[31] E. McCann and M. Koshino, “The electronic properties of bilayer graphene,” *Reports on Progress in Physics*, vol. 76, no. 5, p. 056503, 2013.

[32] H. Y. Hwang, Y. Iwasa, M. Kawasaki, B. Keimer, N. Nagaosa, and Y. Tokura, “Emergent phenomena at oxide interfaces,” *Nature Materials*, vol. 11, p. 103, Jan 2012.

[33] T. Stauber, N. M. R. Peres, and A. K. Geim, “Optical conductivity of graphene in the visible region of the spectrum,” *Phys. Rev. B*, vol. 78, p. 085432, Aug 2008.

[34] V. P. Gusynin, S. G. Sharapov, and J. P. Carbotte, “Unusual microwave response of Dirac quasiparticles in graphene,” *Phys. Rev. Lett.*, vol. 96, p. 256802, Jun 2006.

[35] S. A. Mikhailov and K. Ziegler, “New electromagnetic mode in graphene,” *Phys. Rev. Lett.*, vol. 99, p. 016803, Jul 2007.

[36] E. G. Mishchenko, “Effect of electron-electron interactions on the conductivity of clean graphene,” *Phys. Rev. Lett.*, vol. 98, p. 216801, May 2007.

[37] L. A. Falkovsky and S. S. Pershoguba, “Optical far-infrared properties of a graphene monolayer and multilayer,” *Phys. Rev. B*, vol. 76, p. 153410, Oct 2007.

[38] T. Stauber, N. M. R. Peres, and A. H. Castro Neto, “Conductivity of suspended and non-suspended graphene at finite gate voltage,” *Phys. Rev. B*, vol. 78, p. 085418, Aug 2008.

[39] A. G. Grushin, B. Valenzuela, and M. A. H. Vozmediano, “Effect of Coulomb interactions on the optical properties of doped graphene,” *Phys. Rev. B*, vol. 80, p. 155417, Oct 2009.

[40] D. E. Sheehy and J. Schmalian, “Optical transparency of graphene as determined by the fine-structure constant,” *Phys. Rev. B*, vol. 80, p. 193411, Nov 2009.

[41] T. Ando, Y. Zheng, and H. Suzuura, “Dynamical conductivity and zero-mode anomaly in honeycomb lattices,” *Journal of the Physical Society of Japan*, vol. 71, no. 5, pp. 1318 – 1324, 2002.

[42] C. N. Santos, F. Joucken, D. De Sousa Meneses, P. Echegut, J. Campos-Delgado, P. Louette, J.-P. Raskin, and B. Hackens, “Terahertz and mid-infrared reflectance of epitaxial graphene,” *Scientific Reports*, vol. 6, p. 24301, Apr 2016.

[43] L. A. Falkovsky, “Optical properties of graphene,” *Journal of Physics: Conference Series*, vol. 129, no. 1, p. 012004, 2008.

[44] T. Stauber, N. M. R. Peres, and A. K. Geim, “Optical conductivity of graphene in the visible region of the spectrum,” *Phys. Rev. B*, vol. 78, p. 085432, Aug 2008.

[45] Z. Fei, Y. Shi, L. Pu, F. Gao, Y. Liu, L. Sheng, B. Wang, R. Zhang, and Y. Zheng, “High-energy optical conductivity of graphene determined by reflection contrast spectroscopy,” *Phys. Rev. B*, vol. 78, p. 201402, Nov 2008.

[46] E. G. Mishchenko, “Dynamic conductivity in graphene beyond linear response,” *Phys. Rev. Lett.*, vol. 103, p. 246802, Dec 2009.

[47] Q. Bao, H. Zhang, Y. Wang, Z. Ni, Y. Yan, Z. X. Shen, K. P. Loh, and D. Y. Tang, “Atomiclayer graphene as a saturable sbsorber for ultrafast pulsed lasers,” *Advanced Functional Materials*, vol. 19, no. 19, pp. 3077 – 3083, 2009.

[48] D. N. Basov, M. M. Fogler, A. Lanzara, F. Wang, and Y. Zhang, “Colloquium: Graphene spectroscopy,” *Rev. Mod. Phys.*, vol. 86, pp. 959 – 994, Jul 2014.

[49] V. N. Kotov, B. Uchoa, V. M. Pereira, F. Guinea, and A. H. Castro Neto, “Electron-electron interactions in graphene: Current status and perspectives,” *Rev. Mod. Phys.*, vol. 84, pp. 1067 – 1125, Jul 2012.

[50] B. Uchoa, J. P. Reed, Y. Gan, Y. I. Joe, E. Fradkin, P. Abbamonte, and D. Casa, "The electron many-body problem in graphene," *Physica Scripta*, vol. 2012, no. T146, p. 014014, 2012.

[51] M. O. Goerbig, "Electronic properties of graphene in a strong magnetic field," *Rev. Mod. Phys.*, vol. 83, pp. 1193 – 1243, Nov 2011.

[52] F. Chiappini, S. Wiedmann, K. Novoselov, A. Mishchenko, A. K. Geim, J. C. Maan, and U. Zeitler, "Lifting of the Landau level degeneracy in graphene devices in a tilted magnetic field," *Phys. Rev. B*, vol. 92, p. 201412, Nov 2015.

[53] M. V. Berry, "Quantal phase factors accompanying adiabatic changes," *Proceedings of the Royal Society of London. A. Mathematical and Physical Sciences*, vol. 392, no. 1802, pp. 45 – 57, 1984.

[54] G. P. Mikitik and Y. V. Sharlai, "Manifestation of Berry's phase in metal physics," *Phys. Rev. Lett.*, vol. 82, pp. 2147 – 2150, Mar 1999.

[55] G. P. Mikitik and Y. V. Sharlai, "Band-contact lines in the electron energy spectrum of graphite," *Phys. Rev. B*, vol. 73, p. 235112, Jun 2006.

[56] T. Ando, "Magnetic oscillation of optical phonon in graphene," *Journal of the Physical Society of Japan*, vol. 76, no. 2, p. 024712, 2007.

[57] L. Onsager, "Reciprocal relations in irreversible processes. II.," *Phys. Rev.*, vol. 38, pp. 2265 – 2279, Dec 1931.

[58] V. Lucarini, K.-E. Peiponen, J. J. Saarinen, and E. M. Vartiainen, *Kramers-Kronig Relations in Optical Materials Research*. Springer, 2005.

[59] H. Nussenzveig, *Causality and Dispersion Relations*. Academic Press, 1972.

[60] W. P. Healy and E. A. Power, "Dispersion relations for optically active media," *American Journal of Physics*, vol. 42, no. 12, pp. 1070 – 1074, 1974.

[61] V. P. Gusynin, S. G. Sharapov, and J. P. Carbotte, "Magneto-optical conductivity in graphene," *Journal of Physics: Condensed Matter*, vol. 19, no. 2, p. 026222, 2007.

[62] V. P. Gusynin and S. G. Sharapov, "Transport of Dirac quasiparticles in graphene: Hall and optical conductivities," *Phys. Rev. B*, vol. 73, p. 245411, Jun 2006.

[63] L. L. Moseley and T. Lukes, "A simplified derivation of the KuboGreenwood formula," *American Journal of Physics*, vol. 46, no. 6, pp. 676 – 677, 1978.

[64] H. Funk, A. Knorr, F. Wendler, and E. Malic, “Microscopic view on Landau level broadening mechanisms in graphene,” *Phys. Rev. B*, vol. 92, p. 205428, Nov 2015.

[65] W. Kohn, “Cyclotron resonance and de Haas-van Alphen rscillations of an interacting electron gas,” *Phys. Rev.*, vol. 123, pp. 1242 – 1244, Aug 1961.

[66] P. Goswami, X. Jia, and S. Chakravarty, “Quantum oscillations in graphene in the presence of disorder and interactions,” *Phys. Rev. B*, vol. 78, p. 245406, Dec 2008.

[67] G. S. Ranganath, “Faraday rotation tensor-extraction of components,” *Proceedings of the Indian Academy of Sciences - Section A*, vol. 75, pp. 237 – 248, May 1972.

[68] P. S. Pershan, “Magnetooptical effects,” *Journal of Applied Physics*, vol. 38, no. 3, pp. 1482 – 1490, 1967.

[69] H. D. Cornean, G. Nenciu, and T. G. Pedersen, “The Faraday effect revisited: General theory,” *Journal of Mathematical Physics*, vol. 47, no. 1, p. 013511, 2006.

[70] L. M. Roth, “Theory of the Faraday effect in solids,” *Phys. Rev.*, vol. 133, pp. A542 – A553, Jan 1964.

[71] N. P. Barnes and L. B. Petway, “Variation of the Verdet constant with temperature of terbium gallium garnet,” *J. Opt. Soc. Am. B*, vol. 9, pp. 1912 – 1915, Oct 1992.

[72] M. Cardona, *Faraday rotation in semiconductors*, pp. 72 – 88. Berlin, Heidelberg: Springer Berlin Heidelberg, 1962.

[73] M. Suzuki, K. ichi Fujii, T. Ohyama, H. Kobori, and N. Kotera, “Far-infrared resonant Faraday effect in semiconductors,” *Journal of the Physical Society of Japan*, vol. 72, no. 12, pp. 3276 – 3285, 2003.

[74] H. J. Jiménez-González, R. L. Aggarwal, and G. Favrot, “Infrared Faraday rotation of n-type InSb,” *Phys. Rev. B*, vol. 49, pp. 4571 – 4578, Feb 1994.

[75] L. Ohnoutek, M. Hakl, M. Veis, B. A. Piot, C. Faugeras, G. Martinez, M. V. Yakushev, R. W. Martin, Drašar, A. Materna, G. Strzelecka, A. Hruban, M. Potemski, and M. Orlita, “Strong interband Faraday rotation in 3D topological insulator Bi_2Se_3,” *Scientific Reports*, vol. 6, p. 19087, 2016.

[76] K. S. Novoselov, V. I. Falko, L. Colombo, P. R. Gellert, M. G. Schwab, and K. Kim, “A roadmap for graphene,” *Nature*, Oct 2012.

[77] I. Fialkovsky and D. Vassilevich, “Faraday rotation in graphene,” *The European Physical Journal B*, vol. 85, p. 384, Nov 2012.

[78] M. H. Bryniildsen and H. D. Cornean, “On the Verdet constant and Faraday rotation for graphene-like materials,” *Reviews in Mathematical Physics*, vol. 25, no. 04, p. 1350007, 2013.

[79] I. Crassee, J. Levallois, A. L. Walter, M. Ostler, A. Bostwick, E. Rotenberg, T. Seyller, D. van der Marel, and A. B. Kuzmenko, “Giant Faraday rotation in single- and multilayer graphene,” *Nature Physics*, vol. 7, p. 48, Nov 2010.

[80] K. I. Bolotin, K. J. Sikes, J. Hone, H. L. Stormer, and P. Kim, “Temperature-dependent transport in suspended graphene,” *Phys. Rev. Lett.*, vol. 101, p. 096802, Aug 2008.

[81] X. Du, I. Skachko, A. Barker, and E. Y. Andrei, “Approaching ballistic transport in suspended graphene,” *Nature Nanotechnology*, vol. 3, p. 491, Jul 2008.

[82] A. S. Mayorov, D. C. Elias, I. S. Mukhin, S. V. Morozov, L. A. Ponomarenko, K. S. Novoselov, A. K. Geim, and R. V. Gorbachev, “How close can one approach the Dirac point in graphene experimentally?,” *Nano Letters*, vol. 12, no. 9, pp. 4629 – 4634, 2012. PMID: 22935053.

[83] A. S. Mayorov, R. V. Gorbachev, S. V. Morozov, L. Britnell, R. Jalil, L. A. Ponomarenko, P. Blake, K. S. Novoselov, K. Watanabe, T. Taniguchi, and A. K. Geim, “Micrometer-scale ballistic transport in encapsulated graphene at room temperature,” *Nano Letters*, vol. 11, no. 6, pp. 2396 – 2399, 2011. PMID: 21574627.

[84] L. Wang, I. Meric, P. Y. Huang, Q. Gao, Y. Gao, H. Tran, T. Taniguchi, K. Watanabe, L. M. Campos, D. A. Muller, J. Guo, P. Kim, J. Hone, K. L. Shepard, and C. R. Dean, “One-dimensional electrical contact to a two-dimensional material,” *Science*, vol. 342, no. 6158, pp. 614 – 617, 2013.

[85] E. H. Hwang and S. Das Sarma, “Acoustic phonon scattering limited carrier mobility in two-dimensional extrinsic graphene,” *Phys. Rev. B*, vol. 77, p. 115449, Mar 2008.

[86] S. V. Morozov, K. S. Novoselov, M. I. Katsnelson, F. Schedin, D. C. Elias, J. A. Jaszczak, and A. K. Geim, “Giant intrinsic carrier mobilities in graphene and its bilayer,” *Phys. Rev. Lett.*, vol. 100, p. 016602, Jan 2008.

[87] Image library of the "Solid state nanophysics research group" of the Max Planck Institute for Solid State Research in Stuttgart.

[88] H. Vandeparre, M. Piñeirua, F. Brau, B. Roman, J. Bico, C. Gay, W. Bao, C. N. Lau, P. M. Reis, and P. Damman, “Wrinkling hierarchy in constrained thin sheets from suspended graphene to curtains,” *Phys. Rev. Lett.*, vol. 106, p. 224301, Jun 2011.

[89] N. M. R. Peres, “Colloquium: The transport properties of graphene: An introduction,” *Rev. Mod. Phys.*, vol. 82, pp. 2673 – 2700, Sep 2010.

[90] S. Das Sarma, S. Adam, E. H. Hwang, and E. Rossi, “Electronic transport in two-dimensional graphene,” *Rev. Mod. Phys.*, vol. 83, pp. 407 – 470, May 2011.

[91] J.-H. Chen, C. Jang, S. Adam, M. S. Fuhrer, E. D. Williams, and M. Ishigami, “Charged-impurity scattering in graphene,” *Nature Physics*, vol. 4, p. 377, Apr 2008.

[92] A. K. Geim and I. V. Grigorieva, “Van der Waals heterostructures,” *Nature*, vol. 499, pp. 419 – 425, Jul 2013.

[93] Q. H. Wang, Z. Jin, K. K. Kim, A. J. Hilmer, G. L. C. Paulus, C.-J. Shih, M.-H. Ham, J. D. Sanchez-Yamagishi, K. Watanabe, T. Taniguchi, J. Kong, P. Jarillo-Herrero, and M. S. Strano, “Understanding and controlling the substrate effect on graphene electron-transfer chemistry via reactivity imprint lithography,” *Nature Chemistry*, vol. 4, p. 724, Aug 2012.

[94] A. V. Babichev, S. A. Rykov, M. Tchernycheva, A. N. Smirnov, V. Y. Davydov, Y. A. Kumzerov, and V. Y. Butko, “Influence of substrate microstructure on the transport properties of CVD-graphene,” *ACS Applied Materials & Interfaces*, vol. 8, no. 1, pp. 240 – 246, 2016. PMID: 26652757.

[95] S. Fratini and F. Guinea, “Substrate-limited electron dynamics in graphene,” *Phys. Rev. B*, vol. 77, p. 195415, May 2008.

[96] J. Sabio, C. Seoánez, S. Fratini, F. Guinea, A. H. C. Neto, and F. Sols, “Electrostatic interactions between graphene layers and their environment,” *Phys. Rev. B*, vol. 77, p. 195409, May 2008.

[97] I. Calizo, W. Bao, F. Miao, C. N. Lau, and A. A. Balandin, “The effect of substrates on the Raman spectrum of graphene: Graphene-on-sapphire and graphene-on-glass,” *Applied Physics Letters*, vol. 91, no. 20, p. 201904, 2007.

[98] X. Hong, A. Posadas, K. Zou, C. H. Ahn, and J. Zhu, “High-mobility few-layer graphene field effect transistors fabricated on epitaxial ferroelectric gate oxides,” *Phys. Rev. Lett.*, vol. 102, p. 136808, Apr 2009.

[99] C. H. Lui, L. Liu, K. F. Mak, G. W. Flynn, and T. F. Heinz, “Ultraflat graphene,” *Nature*, vol. 462, p. 339, Nov 2009.

[100] E. V. Castro, H. Ochoa, M. I. Katsnelson, R. V. Gorbachev, D. C. Elias, K. S. Novoselov, A. K. Geim, and F. Guinea, “Limits on charge carrier mobility in suspended graphene due to flexural phonons,” *Phys. Rev. Lett.*, vol. 105, p. 266601, Dec 2010.

[101] M. Katsnelson and A. Geim, “Electron scattering on microscopic corrugations in graphene,” *Philosophical Transactions of the Royal Society of London A: Mathematical, Physical and Engineering Sciences*, vol. 366, no. 1863, pp. 195 – 204, 2008.

[102] S. Deng and V. Berry, “Wrinkled, rippled and crumpled graphene: an overview of formation mechanism, electronic properties, and applications,” *Materials Today*, vol. 19, no. 4, pp. 197 – 212, 2016.

[103] E. Mariani and F. von Oppen, “Flexural phonons in free-standing graphene,” *Phys. Rev. Lett.*, vol. 100, p. 076801, Feb 2008.

[104] W. Bao, F. Miao, Z. Chen, H. Zhang, W. Jang, C. Dames, and C. N. Lau, “Controlled ripple texturing of suspended graphene and ultrathin graphite membranes,” *Nature Nanotechnology*, vol. 4, p. 562, Jul 2009.

[105] K. Nomura and A. H. MacDonald, “Quantum transport of massless Dirac fermions,” *Phys. Rev. Lett.*, vol. 98, p. 076602, Feb 2007.

[106] E. H. Hwang, S. Adam, and S. D. Sarma, “Carrier transport in two-dimensional graphene layers,” *Phys. Rev. Lett.*, vol. 98, p. 186806, May 2007.

[107] W. Zhu, T. Low, V. Perebeinos, A. A. Bol, Y. Zhu, H. Yan, J. Tersoff, and P. Avouris, “Structure and electronic transport in graphene wrinkles,” *Nano Letters*, vol. 12, no. 7, pp. 3431–3436, 2012. PMID: 22646513.

[108] Y.-C. Lin, C.-C. Lu, C.-H. Yeh, C. Jin, K. Suenaga, and P.-W. Chiu, “Graphene annealing: How clean can it be?,” *Nano Letters*, vol. 12, no. 1, pp. 414 – 419, 2012. PMID: 22149394.

[109] K. Kumar, Y.-S. Kim, and E.-H. Yang, “The influence of thermal annealing to remove polymeric residue on the electronic doping and morphological characteristics of graphene,” *Carbon*, vol. 65, pp. 35 – 45, 2013.

[110] C. R. Dean, A. F. Young, I. Meric, C. Lee, L. Wang, S. Sorgenfrei, K. Watanabe, T. Taniguchi, P. Kim, K. L. Shepard, and J. Hone, “Boron nitride substrates for high-quality graphene electronics,” *Nature Nanotechnology*, vol. 5, p. 722, Aug 2010.

[111] T. Taychatanapat, K. Watanabe, T. Taniguchi, and P. Jarillo-Herrero, “Electrically tunable transverse magnetic focusing in graphene,” *Nature Physics*, vol. 9, p. 225, Feb 2013.

[112] P. J. Zomer, S. P. Dash, N. Tombros, and B. J. van Wees, “A transfer technique for high mobility graphene devices on commercially available hexagonal boron nitride,” *Applied Physics Letters*, vol. 99, no. 23, p. 232104, 2011.

[113] E. Y. Andrei, G. Li, and X. Du, “Electronic properties of graphene: a perspective from scanning tunneling microscopy and magnetotransport,” *Reports on Progress in Physics*, vol. 75, no. 5, p. 056501, 2012.

[114] J. Martin, N. Akerman, G. Ulbricht, T. Lohmann, J. H. Smet, K. von Klitzing, and A. Yacoby, “Observation of electron-hole puddles in graphene using a scanning single-electron transistor,” *Nature Physics*, vol. 4, p. 144, Nov 2007.

[115] M. Gibertini, A. Tomadin, F. Guinea, M. I. Katsnelson, and M. Polini, “Electron-hole puddles in the absence of charged impurities,” *Phys. Rev. B*, vol. 85, p. 201405, May 2012.

[116] P. Neugebauer, M. Orlita, C. Faugeras, A.-L. Barra, and M. Potemski, “How perfect can graphene be?,” *Phys. Rev. Lett.*, vol. 103, p. 136403, Sep 2009.

[117] D. R. Cooper, B. D’Anjou, N. Ghattamaneni, B. Harack, M. Hilke, A. Horth, N. Majlis, M. Massicotte, L. Vandsburger, E. Whiteway, and V. Yu, “Experimental review of graphene,” *ISRN Condensed Matter Physics*, vol. 2012, p. 56, 2012.

[118] S. Bae, H. Kim, Y. Lee, X. Xu, J.-S. Park, Y. Zheng, J. Balakrishnan, T. Lei, H. Ri Kim, Y. I. Song, Y.-J. Kim, K. S. Kim, B. Özyilmaz, J.-H. Ahn, B. H. Hong, and S. Iijima, “Roll-to-roll production of 30-inch graphene films for transparent electrodes,” *Nature Nanotechnology*, vol. 5, p. 574, Jun 2010.

[119] X. Chen, L. Zhang, and S. Chen, “Large area CVD growth of graphene,” *Synthetic Metals*, vol. 210, pp. 95 – 108, 2015. Reviews of Current Advances in Graphene Science and Technology.

[120] Y. Hao, M. S. Bharathi, L. Wang, Y. Liu, H. Chen, S. Nie, X. Wang, H. Chou, C. Tan, B. Fallahazad, H. Ramanarayan, C. W. Magnuson, E. Tutuc, B. I. Yakobson, K. F. McCarty, Y.-W. Zhang, P. Kim, J. Hone, L. Colombo, and R. S. Ruoff, “The role of surface oxygen in the growth of large single-crystal graphene on copper,” *Science*, vol. 342, no. 6159, pp. 720 – 723, 2013.

[121] “Scientific background on the Nobel Prize in Physics 2010 graphene,” Oct 2010. The Royal Swedish Academy of Science.

[122] Y. Chen, X.-L. Gong, and J.-G. Gai, “Progress and challenges in transfer of large-area graphene films,” *Advanced Science*, vol. 3, no. 8, p. 1500343, 2016.

[123] Q. Wu, W. Wongwiriyapan, J.-H. Park, S. Park, S. J. Jung, T. Jeong, S. Lee, Y. H. Lee, and Y. J. Song, “In situ chemical vapor deposition of graphene and hexagonal boron nitride heterostructures,” *Current Applied Physics*, vol. 16, no. 9, pp. 1175 – 1191, 2016. Special Section on Nanostructure Physics and

Materials Science at Center for Integrated Nanostructure Physics, Institute for Basic Science at Sungkyunkwan University.

[124] R. Kitaura, Y. Miyata, R. Xiang, J. Hone, J. Kong, R. S. Ruoff, and S. Maruyama, “Chemical vapor deposition growth of graphene and related materials,” *Journal of the Physical Society of Japan*, vol. 84, no. 12, p. 121013, 2015.

[125] Y. J. Song, A. F. Otte, Y. Kuk, Y. Hu, D. B. Torrance, P. N. First, W. A. de Heer, H. Min, S. Adam, M. D. Stiles, A. H. MacDonald, and J. A. Stroscio, “High-resolution tunnelling spectroscopy of a graphene quartet,” *Nature*, vol. 467, p. 185, 2010.

[126] J. L. Tedesco, B. L. VanMil, R. L. Myers-Ward, J. M. McCrate, S. A. Kitt, P. M. Campbell, G. G. Jernigan, J. C. Culbertson, C. R. Eddy, and D. K. Gaskill, “Hall effect mobility of epitaxial graphene grown on silicon carbide,” *Applied Physics Letters*, vol. 95, no. 12, p. 122102, 2009.

[127] E. Pallecchi, F. Lafont, V. Cavaliere, F. Schopfer, D. Mailly, W. Poirier, and A. Ouerghi, “High electron mobility in epitaxial graphene on 4H-SiC(0001) via post-growth annealing under hydrogen,” *Scientific Reports*, vol. 4, p. 4558, 2014.

[128] J. D. Caldwell, T. J. Anderson, J. C. Culbertson, G. G. Jernigan, K. D. Hobart, F. J. Kub, M. J. Tadjer, J. L. Tedesco, J. K. Hite, M. A. Mastro, R. L. Myers-Ward, C. R. Eddy, P. M. Campbell, and D. K. Gaskill, “Technique for the dry transfer of epitaxial graphene onto arbitrary substrates,” *ACS Nano*, vol. 4, no. 2, pp. 1108 – 1114, 2010. PMID: 20099904.

[129] S. Maëro, A. Torche, T. Phuphachong, E. Pallecchi, A. Ouerghi, R. Ferreira, L.-A. de Vaulchier, and Y. Guldner, “Disorder-perturbed Landau levels in high-electron-mobility epitaxial graphene,” *Phys. Rev. B*, vol. 90, p. 195433, Nov 2014.

[130] M. Orlita, C. Faugeras, R. Grill, A. Wysmolek, W. Strupinski, C. Berger, W. A. de Heer, G. Martinez, and M. Potemski, “Carrier scattering from dynamical magnetoconductivity in quasineutral epitaxial graphene,” *Phys. Rev. Lett.*, vol. 107, p. 216603, Nov 2011.

[131] M. Orlita, C. Faugeras, P. Plochocka, P. Neugebauer, G. Martinez, D. K. Maude, A.-L. Barra, M. Sprinkle, C. Berger, W. A. de Heer, and M. Potemski, “Approaching the Dirac point in high-mobility multilayer epitaxial graphene,” *Phys. Rev. Lett.*, vol. 101, p. 267601, Dec 2008.

[132] M. N. Wilson, *Superconducting Magnets*. Oxford University Press, 1983.

[133] Y. Iwasa, *Case Studies in Superconducting Magnets Design and Operational Issues*. Springer, 2009. second edition.

[134] Q. Wang, Z. Ni, and C. Cui, *Superconducting Magnet Technology and Applications*. 2012.

[135] P. Griffiths and J. de Haseth, *Fourier Transform Infrared Spectrometry*. John Wiley and Sons, Inc., 2007. second edition.

[136] B. C. Smith, *Fundamentals of Fourier Transform Infrared Spectroscopy*. CRC Press, 2011. second edition.

[137] B. Stuart, *Infrared Spectroscopy: Fundamentals and Applications*. John Wiley and Sons, Ltd, 2004. Series: Analytical Techniques in the Sciences.

[138] G. Grüner, *Millimeter and Submillimeter Wave Spectroscopy of Solids*. Springer, 1998. Topics in Applied Physics 74.

[139] P. Garidel and M. Boese, "Non-invasive fourier transform infrared microspectroscopy and imaging techniques: Basic principles and applications," 2007. Modern Research and Educational Topics in Microscopy. A. Méndez-Vilas and J. Díaz (Eds.), FORMATEX, Series ISBN-13: 978-84-611-9418-6, Vol. 1 ISBN-13: 978-84-611-9419-3., 2007.

[140] Z. Jiang, E. A. Henriksen, L. C. Tung, Y.-J. Wang, M. E. Schwartz, M. Y. Han, P. Kim, and H. L. Stormer, "Infrared spectroscopy of Landau levels of graphene," *Phys. Rev. Lett.*, vol. 98, p. 197403, May 2007.

[141] Z.-G. Chen, Z. Shi, W. Yang, X. Lu, Y. Lai, H. Yan, F. Wang, G. Zhang, and Z. Li, "Observation of an intrinsic bandgap and Landau level renormalization in graphene/boron-nitride heterostructures," *Nature Communications*, vol. 5, p. 4461, Jul 2014.

[142] M. L. Sadowski, G. Martinez, M. Potemski, C. Berger, and W. A. de Heer, "Landau level spectroscopy of ultrathin graphite layers," *Phys. Rev. Lett.*, vol. 97, p. 266405, Dec 2006.

[143] A. M. Witowski, M. Orlita, R. Stępniewski, A. Wysmołek, J. M. Baranowski, W. Strupiński, C. Faugeras, G. Martinez, and M. Potemski, "Quasi-classical cyclotron resonance of Dirac fermions in highly doped graphene," *Phys. Rev. B*, vol. 82, p. 165305, Oct 2010.

[144] M. Orlita, I. Crassee, C. Faugeras, A. B. Kuzmenko, F. Fromm, M. Ostler, T. Seyller, G. Martinez, M. Polini, and M. Potemski, "Classical to quantum crossover of the cyclotron resonance in graphene: a study of the strength of intraband absorption," *New Journal of Physics*, vol. 14, no. 9, p. 095008, 2012.

[145] J. Wang, F. Ma, and M. Sun, "Graphene, hexagonal boron nitride, and their heterostructures: properties and applications," *RSC Adv.*, vol. 7, pp. 16801 – 16822, 2017.

[146] M. Yankowitz, J. Xue, and B. J. LeRoy, "Graphene on hexagonal boron nitride," *Journal of Physics: Condensed Matter*, vol. 26, no. 30, p. 303201, 2014.

[147] M. Petrescu and M.-G. Balint, "Structure and properties modifications in boron nitride. Part I: direct polymorphic transformations mechanisms," *U.P.B. Sci. Bull. Series B*, vol. 69, 2007.

[148] R. S. Pease, "An X-ray study of boron nitride," *Acta Crystallographica*, vol. 5, no. 3, pp. 356 – 361, 1952.

[149] Y. Shi, C. Hamsen, X. Jia, K. K. Kim, A. Reina, M. Hofmann, A. L. Hsu, K. Zhang, H. Li, Z.-Y. Juang, M. S. Dresselhaus, L.-J. Li, and J. Kong, "Synthesis of few-layer hexagonal boron nitride thin film by chemical vapor deposition," *Nano Letters*, vol. 10, no. 10, pp. 4134 – 4139, 2010. PMID: 20812716.

[150] O. Hod, "Graphite and hexagonal boron-nitride have the same interlayer distance. Why?," *Journal of Chemical Theory and Computation*, vol. 8, no. 4, pp. 1360 – 1369, 2012. PMID: 26596751.

[151] V. Solozhenko, G. Will, and F. Elf, "Isothermal compression of hexagonal graphite-like boron nitride up to 12 GPa," *Solid State Communications*, vol. 96, no. 1, pp. 1 – 3, 1995.

[152] R. Geick, C. H. Perry, and G. Rupprecht, "Normal modes in hexagonal boron nitride," *Phys. Rev.*, vol. 146, pp. 543 – 547, Jun 1966.

[153] C. Tarrio and S. E. Schnatterly, "Interband transitions, plasmons, and dispersion in hexagonal boron nitride," *Phys. Rev. B*, vol. 40, pp. 7852 – 7859, Oct 1989.

[154] N. Ooi, V. Rajan, J. Gottlieb, Y. Catherine, and J. B. Adams, "Structural properties of hexagonal boron nitride," *Modelling and Simulation in Materials Science and Engineering*, vol. 14, no. 3, p. 515, 2006.

[155] J. B. MacNaughton, A. Moewes, R. G. Wilks, X. T. Zhou, T. K. Sham, T. Taniguchi, K. Watanabe, C. Y. Chan, W. J. Zhang, I. Bello, S. T. Lee, and H. Hofsäss, "Electronic structure of boron nitride single crystals and films," *Phys. Rev. B*, vol. 72, p. 195113, Nov 2005.

[156] K. Watanabe, T. Taniguchi, and H. Kanda, "Direct-bandgap properties and evidence for ultraviolet lasing of hexagonal boron nitride single crystal," *Nature Materials*, vol. 3, p. 404, May 2004.

[157] F. C. Brown, R. Z. Bachrach, and M. Skibowski, "Effect of X-ray polarization at the boron K edge in hexagonal BN," *Phys. Rev. B*, vol. 13, pp. 2633 – 2635, Mar 1976.

[158] V. Solozhenko, A. Lazarenko, J.-P. Petitet, and A. Kanaev, “Bandgap energy of graphite-like hexagonal boron nitride,” *Journal of Physics and Chemistry of Solids*, vol. 62, no. 7, pp. 1331 – 1334, 2001.

[159] M. J. Rand and J. F. Roberts, “Preparation and properties of thin film boron nitride,” *J. Electrochem. Soc.*, vol. 115, pp. 423 – 429, 1968.

[160] D. M. Hoffman, G. L. Doll, and P. C. Eklund, “Optical properties of pyrolytic boron nitride in the energy range 0.05 – 10 eV,” *Phys. Rev. B*, vol. 30, pp. 6051 – 6056, Nov 1984.

[161] A. Zunger, A. Katzir, and A. Halperin, “Optical properties of hexagonal boron nitride,” *Phys. Rev. B*, vol. 13, pp. 5560 – 5573, Jun 1976.

[162] X. Blase, A. Rubio, S. G. Louie, and M. L. Cohen, “Quasiparticle band structure of bulk hexagonal boron nitride and related systems,” *Phys. Rev. B*, vol. 51, pp. 6868 – 6875, Mar 1995.

[163] R. Dovesi, C. Pisani, and C. Roetti, “Exact-exchange Hartree-Fock calculations for periodic systems. II. Results for graphite and hexagonal boron nitride,” *International Journal of Quantum Chemistry*, vol. 17, no. 3, pp. 517 – 529, 1980.

[164] J. Zupan and D. Kolar, “Optical properties of graphite and boron nitride,” *Journal of Physics C: Solid State Physics*, vol. 5, no. 21, p. 3097, 1972.

[165] G.-H. Lee, Y.-J. Yu, C. Lee, C. Dean, K. L. Shepard, P. Kim, and J. Hone, “Electron tunneling through atomically flat and ultrathin hexagonal boron nitride,” *Applied Physics Letters*, vol. 99, no. 24, p. 243114, 2011.

[166] J. Zupan, M. Komac, and D. Kolar, “Magnetic susceptibility of boron nitride,” *Journal of Applied Physics*, vol. 41, no. 13, pp. 5337 – 5338, 1970.

[167] E. Machado-Charry, P. Boulanger, L. Genovese, N. Mousseau, and P. Pochet, “Tunable magnetic states in hexagonal boron nitride sheets,” *Applied Physics Letters*, vol. 101, no. 13, p. 132405, 2012.

[168] K.-A. N. Duerloo, M. T. Ong, and E. J. Reed, “Intrinsic piezoelectricity in two-dimensional materials,” *The Journal of Physical Chemistry Letters*, vol. 3, no. 19, pp. 2871 – 2876, 2012.

[169] Y. Li, Y. Rao, K. F. Mak, Y. You, S. Wang, C. R. Dean, and T. F. Heinz, “Probing symmetry properties of few-layer MoS_2 and h-BN by optical second-harmonic generation,” *Nano Letters*, vol. 13, no. 7, pp. 3329 – 3333, 2013. PMID: 23718906.

[170] J. Zhang and S. A. Meguid, “Piezoelectricity of 2D nanomaterials: characterization, properties, and applications,” *Semiconductor Science and Technology*, vol. 32, no. 4, p. 043006, 2017.

[171] K. H. Michel and B. Verberck, "Theory of elastic and piezoelectric effects in two-dimensional hexagonal boron nitride," *Phys. Rev. B*, vol. 80, p. 224301, Dec 2009.

[172] K. H. Michel, D. Çak ır, C. Sevik, and F. M. Peeters, "Piezoelectricity in two-dimensional materials: Comparative study between lattice dynamics and ab initio calculations," *Phys. Rev. B*, vol. 95, p. 125415, Mar 2017.

[173] K.-A. N. Duerloo and E. J. Reed, "Flexural electromechanical coupling: A nanoscale emergent property of boron nitride bilayers," *Nano Letters*, vol. 13, no. 4, pp. 1681 – 1686, 2013. PMID: 23484488.

[174] E. K. Sichel, R. E. Miller, M. S. Abrahams, and C. J. Buiocchi, "Heat capacity and thermal conductivity of hexagonal pyrolytic boron nitride," *Phys. Rev. B*, vol. 13, pp. 4607 – 4611, May 1976.

[175] J.-C. Zheng, L. Zhang, A. V. Kretinin, S. V. Morozov, Y. B. Wang, T. Wang, X. Li, F. Ren, J. Zhang, C.-Y. Lu, J.-C. Chen, M. Lu, H.-Q. Wang, A. K. Geim, and K. S. Novoselov, "High thermal conductivity of hexagonal boron nitride laminates," *2D Materials*, vol. 3, no. 1, p. 011004, 2016.

[176] B. Kelly, "The thermal conductivity of hexagonal boron nitride parallel to the basal planes," *Journal of Nuclear Materials*, vol. 68, no. 1, pp. 9 – 12, 1977.

[177] W. Paszkowicz, J. Pelka, M. Knapp, T. Szyszko, and S. Podsiadlo, "Lattice parameters and anisotropic thermal expansion of hexagonal boron nitride in the 10 – 297.5 K temperature range," *Applied Physics A*, vol. 75, pp. 431 – 435, Sep 2002.

[178] A. Poddubny, I. Iorsh, P. Belov, and Y. Kivshar, "Hyperbolic metamaterials," *Nature Photonics*, vol. 7, p. 948, Nov 2013.

[179] M. Xu, T. Liang, M. Shi, and H. Chen, "Graphene-like two-dimensional materials," *Chemical Reviews*, vol. 113, no. 5, pp. 3766 – 3798, 2013. PMID: 23286380.

[180] D. Pacilé, J. C. Meyer, Girit, and A. Zettl, "The two-dimensional phase of boron nitride: Few-atomic-layer sheets and suspended membranes," *Applied Physics Letters*, vol. 92, no. 13, p. 133107, 2008.

[181] A. V. Kretinin, Y. Cao, J. S. Tu, G. L. Yu, R. Jalil, K. S. Novoselov, S. J. Haigh, A. Gholinia, A. Mishchenko, M. Lozada, T. Georgiou, C. R. Woods, F. Withers, P. Blake, G. Eda, A. Wirsig, C. Hucho, K. Watanabe, T. Taniguchi, A. K. Geim, and R. V. Gorbachev, "Electronic properties of graphene encapsulated with different two-dimensional atomic crystals," *Nano Letters*, vol. 14, no. 6, pp. 3270 – 3276, 2014. PMID: 24844319.

[182] R. Decker, Y. Wang, V. W. Brar, W. Regan, H.-Z. Tsai, Q. Wu, W. Gannett, A. Zettl, and M. F. Crommie, “Local electronic properties of graphene on a BN substrate via scanning tunneling microscopy,” *Nano Letters*, vol. 11, no. 6, pp. 2291 – 2295, 2011. PMID: 21553853.

[183] S. J. Haigh, A. Gholinia, R. Jalil, S. Romani, L. Britnell, D. C. Elias, K. S. Novoselov, L. A. Ponomarenko, A. K. Geim, and R. Gorbachev, “Cross-sectional imaging of individual layers and buried interfaces of graphene-based heterostructures and superlattices,” *Nature Materials*, vol. 11, p. 764, Jul 2012.

[184] J. R. Wallbank, M. MuchaKruczyński, X. Chen, and V. I. Fal’ko, “Moiré superlattice effects in graphene/boronnitride van der Waals heterostructures,” *Annalen der Physik*, vol. 527, no. 5-6, pp. 359 – 376.

[185] G. Giovannetti, P. A. Khomyakov, G. Brocks, P. J. Kelly, and J. van den Brink, “Substrate-induced band gap in graphene on hexagonal boron nitride: Ab initio density functional calculations,” *Phys. Rev. B*, vol. 76, p. 073103, Aug 2007.

[186] M. Kindermann, B. Uchoa, and D. L. Miller, “Zero-energy modes and gate-tunable gap in graphene on hexagonal boron nitride,” *Phys. Rev. B*, vol. 86, p. 115415, Sep 2012.

[187] A. H. MacDonald and R. Bistritzer, “Graphene moiré mystery solved?,” *Nature*, vol. 474, p. 453, Jun 2011.

[188] M. Kuwabara, D. R. Clarke, and D. A. Smith, “Anomalous superperiodicity in scanning tunneling microscope images of graphite,” *Applied Physics Letters*, vol. 56, no. 24, pp. 2396 – 2398, 1990.

[189] W.-T. Pong and C. Durkan, “A review and outlook for an anomaly of scanning tunnelling microscopy (STM): superlattices on graphite,” *Journal of Physics D: Applied Physics*, vol. 38, no. 21, p. R329, 2005.

[190] M. Yankowitz, J. Xue, D. Cormode, J. D. Sanchez-Yamagishi, K. Watanabe, T. Taniguchi, P. Jarillo-Herrero, P. Jacquod, and B. J. LeRoy, “Emergence of superlattice Dirac points in graphene on hexagonal boron nitride,” *Nature Physics*, vol. 8, p. 382, Mar 2012.

[191] C. R. Woods, L. Britnell, A. Eckmann, R. S. Ma, J. C. Lu, H. M. Guo, X. Lin, G. L. Yu, Y. Cao, R. Gorbachev, A. V. Kretinin, J. Park, L. A. Ponomarenko, M. I. Katsnelson, Y. Gornostyrev, K. Watanabe, T. Taniguchi, C. Casiraghi, H.-J. Gao, A. K. Geim, and K. Novoselov, “Commensurate-incommensurate transition in graphene on hexagonal boron nitride,” *Nature Physics*, vol. 10, p. 451, Apr 2014.

[192] J. Xue, J. Sanchez-Yamagishi, D. Bulmash, P. Jacquod, A. Deshpande, K. Watanabe, T. Taniguchi, P. Jarillo-Herrero, and B. J. LeRoy, “Scanning tunnelling microscopy and spectroscopy of ultra-flat graphene on hexagonal boron nitride,” *Nature Materials*, vol. 10, p. 282, Feb 2011.

[193] D. S. L. Abergel and M. Mucha-Kruczyński, “Infrared absorption of closely aligned heterostructures of monolayer and bilayer graphene with hexagonal boron nitride,” *Phys. Rev. B*, vol. 92, p. 115430, Sep 2015.

[194] T. M. R. Wolf, “Optical characterization of graphene superlattice structures,” Feb 2016. Master thesis, Institute for Theoretical Physics, ETH Zürich.

[195] P. Moon and M. Koshino, “Optical properties of the Hofstadter butterfly in the moiré superlattice,” *Phys. Rev. B*, vol. 88, p. 241412, Dec 2013.

[196] E. Kan, H. Ren, F. Wu, Z. Li, R. Lu, C. Xiao, K. Deng, and J. Yang, “Why the band gap of graphene is tunable on hexagonal boron nitride,” *The Journal of Physical Chemistry C*, vol. 116, no. 4, pp. 3142 – 3146, 2012.

[197] T. M. R. Wolf, O. Zilberberg, I. Levkivskyi, and G. Blatter, “Substrate-induced topological minibands in graphene,” *Phys. Rev. B*, vol. 98, p. 125408, Sep 2018.

[198] B. Sachs, T. O. Wehling, M. I. Katsnelson, and A. I. Lichtenstein, “Midgap states and band gap modification in defective graphene/h-BN heterostructures,” *Phys. Rev. B*, vol. 94, p. 224105, Dec 2016.

[199] E. Wang, X. Lu, S. Ding, W. Yao, M. Yan, G. Wan, K. Deng, S. Wang, G. Chen, L. Ma, J. Jung, A. V. Fedorov, Y. Zhang, G. Zhang, and S. Zhou, “Gaps induced by inversion symmetry breaking and second-generation Dirac cones in graphene/hexagonal boron nitride,” *Nature Physics*, vol. 12, p. 1111, Aug 2016.

[200] J. R. Wallbank, A. A. Patel, M. Mucha-Kruczyński, A. K. Geim, and V. I. Fal’ko, “Generic miniband structure of graphene on a hexagonal substrate,” *Phys. Rev. B*, vol. 87, p. 245408, Jun 2013.

[201] F. Guinea and T. Low, “Band structure and gaps of triangular graphene superlattices,” *Philosophical Transactions of the Royal Society of London A: Mathematical, Physical and Engineering Sciences*, vol. 368, no. 1932, pp. 5391–5402, 2010.

[202] L. Brey and H. A. Fertig, “Emerging zero modes for graphene in a periodic potential,” *Phys. Rev. Lett.*, vol. 103, p. 046809, Jul 2009.

[203] C.-H. Park, L. Yang, Y.-W. Son, M. L. Cohen, and S. G. Louie, “New generation of massless Dirac fermions in graphene under external periodic potentials,” *Phys. Rev. Lett.*, vol. 101, p. 126804, Sep 2008.

[204] T. Jiao, D. Wei, X. Song, T. Sun, J. Yang, L. Yu, Y. Feng, W. Sun, W. Wei, H. Shi, C. Hu, and C. Du, "High-efficiency, stable and non-chemically doped graphene-Si solar cells through interface engineering and PMMA antireflection," *RSC Adv.*, vol. 6, pp. 10175 – 10179, 2016.

[205] C. Xie, X. Zhang, K. Ruan, Z. Shao, S. S. Dhaliwal, L. Wang, Q. Zhang, X. Zhang, and J. Jie, "High-efficiency, air stable graphene/Si micro-hole array Schottky junction solar cells," *J. Mater. Chem. A*, vol. 1, pp. 15348 – 15354, 2013.

[206] E. Singh and H. S. Nalwa, "Stability of graphene-based heterojunction solar cells," *RSC Adv.*, vol. 5, pp. 73575 – 73600, 2015.

[207] Y. J. Kim, S. Lee, Y. G. Lee, C. G. Kang, and B. H. Lee, "Optimized integration processes to achieve highly stable CVD graphene FETs," in *2014 Silicon Nanoelectronics Workshop (SNW)*, pp. 1 – 2, June 2014.

[208] M. Schriver, W. Regan, W. J. Gannett, A. M. Zaniewski, M. F. Crommie, and A. Zettl, "Graphene as a long-term metal oxidation barrier: Worse than nothing," *ACS Nano*, vol. 7, no. 7, pp. 5763 – 5768, 2013. PMID: 23755733.

[209] S. Hu, M. Lozada-Hidalgo, F. C. Wang, A. Mishchenko, F. Schedin, R. R. Nair, E. W. Hill, D. W. Boukhvalov, M. I. Katsnelson, R. A. W. Dryfe, I. V. Grigorieva, H. A. Wu, and A. K. Geim, "Proton transport through one-atom-thick crystals," *Nature*, vol. 516, p. 227, Nov 2014.

[210] L. Wang, I. Meric, P. Y. Huang, Q. Gao, Y. Gao, H. Tran, T. Taniguchi, K. Watanabe, L. M. Campos, D. A. Muller, J. Guo, P. Kim, J. Hone, K. L. Shepard, and C. R. Dean, "One-dimensional electrical contact to a two-dimensional material," *Science*, vol. 342, no. 6158, pp. 614 – 617, 2013.

[211] "Microstat MO2," 2017. Oxford Instruments plc, Technical note.

[212] "Magneto-optic module for cryostation," 2017. Montana Instruments, Technical note.

[213] E. A. Henriksen, P. Cadden-Zimansky, Z. Jiang, Z. Q. Li, L.-C. Tung, M. E. Schwartz, M. Takita, Y.-J. Wang, P. Kim, and H. L. Stormer, "Interaction-induced shift of the cyclotron resonance of graphene using infrared spectroscopy," *Phys. Rev. Lett.*, vol. 104, p. 067404, Feb 2010.

[214] J. A. Harrington, *Infrared fibers and their applications*, vol. PM135 of *Monograph*. SPIE Press, 2003. The International Society for Optical Engineering.

[215] J. A. Harrington, "Infrared fiber optics." Specialty Fiber Optics Handbook (2007).

[216] “The Bruker Rocksolid TM Interferometer.” Bruker, Technical note.

[217] F. E. Terman, *Radio Engineer’s Handbook*. McGraw-Hill Book Company, Inc., 1943.

[218] Y. S. Ang, Q. Chen, and C. Zhang, “Nonlinear optical response of graphene in terahertz and near-infrared frequency regime,” *Frontiers of Optoelectronics*, vol. 8, pp. 3 – 26, Mar 2015.

[219] C. Klingshirn, “Non-linear optical properties of semiconductors,” *Semiconductor Science and Technology*, vol. 5, no. 6, p. 457, 1990.

[220] O. Heavens, *Optical properties of thin solid films*. Dover Publications, Inc., 1955.

[221] J. Peatross and M. Ware, *Physics of Light and Optics*. 2012. Brigham Young University.

[222] L. N. Hadley and D. M. Dennison, “Reflection and transmission interference filters Part I. Theory,” *J. Opt. Soc. Am.*, vol. 37, pp. 451 – 465, Jun 1947.

[223] C. Hilsum, “Infrared absorption of thin metal films,” *J. Opt. Soc. Am.*, vol. 44, pp. 188 – 191, Mar 1954.

[224] A. Ferreira, N. M. R. Peres, R. M. Ribeiro, and T. Stauber, “Graphene-based photodetector with two cavities,” *Phys. Rev. B*, vol. 85, p. 115438, Mar 2012.

[225] Y. Cai, J. Zhu, and Q. H. Liu, “Tunable enhanced optical absorption of graphene using plasmonic perfect absorbers,” *Applied Physics Letters*, vol. 106, no. 4, p. 043105, 2015.

[226] Q. Pan, J. Hong, G. Zhang, Y. Shuai, and H. Tan, “Graphene plasmonics for surface enhancement near-infrared absorptivity,” *Opt. Express*, vol. 25, pp. 16400 – 16408, Jul 2017.

[227] C. Hilsum, “Infrared absorption of thin metal films at non-normal incidence,” *J. Opt. Soc. Am.*, vol. 45, pp. 135 – 136, Feb 1955.

[228] N. Ubrig, I. Crassee, J. Levallois, I. O. Nedoliuk, F. Fromm, M. Kaiser, T. Seyller, and A. B. Kuzmenko, “Fabry-Perot enhanced Faraday rotation in graphene,” *Opt. Express*, vol. 21, pp. 24736 – 24741, Oct 2013.

[229] F. C. Jahoda, “Fundamental absorption of barium oxide from its reflectivity spectrum,” *Phys. Rev.*, vol. 107, pp. 1261 – 1265, Sep 1957.

[230] H. Bode, *Network Analysis and Feedback Amplifier Design*. D. Van Nostrand Company, Inc., 1945.

[231] J. Levallois, I. O. Nedoliuk, I. Crassee, and A. B. Kuzmenko, "Magneto-optical Kramers-Kronig analysis," *Review of Scientific Instruments*, vol. 86, no. 3, p. 033906, 2015.

[232] A. B. Kuzmenko, "Kramers-Kronig constrained variational analysis of optical spectra," *Review of Scientific Instruments*, vol. 76, no. 8, p. 083108, 2005.

[233] A. Dienstfrey and L. Greengard, "Analytic continuation, singular-value expansions, and Kramers-Kronig analysis," *Inverse Problems*, vol. 17, no. 5, p. 1307, 2001.

[234] M. Orlita, C. Faugeras, R. Grill, A. Wysmolek, W. Strupinski, C. Berger, W. A. de Heer, G. Martinez, and M. Potemski, "Carrier scattering from dynamical magnetoconductivity in quasineutral epitaxial graphene," *Phys. Rev. Lett.*, vol. 107, p. 216603, Nov 2011.

[235] C. Faugeras, S. Berciaud, P. Leszczynski, Y. Henni, K. Nogajewski, M. Orlita, T. Taniguchi, K. Watanabe, C. Forsythe, P. Kim, R. Jalil, A. K. Geim, D. M. Basko, and M. Potemski, "Landau level spectroscopy of electron-electron interactions in graphene," *Phys. Rev. Lett.*, vol. 114, p. 126804, Mar 2015.

[236] L. A. Falkovsky, "Quantum magneto-optics of the graphite family," *Journal of Experimental and Theoretical Physics*, vol. 115, pp. 1151 – 1164, Dec 2012.

[237] U. Briskot, I. A. Dmitriev, and A. D. Mirlin, "Quantum magneto-oscillations in the ac conductivity of disordered graphene," *Phys. Rev. B*, vol. 87, p. 195432, May 2013.

[238] O. Kashuba and V. I. Fal'ko, "Signature of electronic excitations in the Raman spectrum of graphene," *Phys. Rev. B*, vol. 80, p. 241404, Dec 2009.

[239] C. Faugeras, M. Amado, P. Kossacki, M. Orlita, M. Kühne, A. A. L. Nicolet, Y. I. Latyshev, and M. Potemski, "Magneto-Raman scattering of graphene on graphite: Electronic and phonon excitations," *Phys. Rev. Lett.*, vol. 107, p. 036807, Jul 2011.

[240] V. P. Gusynin, S. G. Sharapov, and J. P. Carbotte, "Anomalous absorption line in the magneto-optical response of graphene," *Phys. Rev. Lett.*, vol. 98, p. 157402, Apr 2007.

[241] I. Crassee, J. Levallois, D. van der Marel, A. L. Walter, T. Seyller, and A. B. Kuzmenko, "Multicomponent magneto-optical conductivity of multilayer graphene on SiC," *Phys. Rev. B*, vol. 84, p. 035103, Jul 2011.

[242] A. K. Zvezdin and V. A. Kotov, *Modern Magnetooptics and Magnetooptical Materials*. Taylor and Francis, 1997. Studies in Condensed Matter Physics.

[243] H. Aoki, "Novel Landau level laser in the quantum Hall regime," *Applied Physics Letters*, vol. 48, no. 9, pp. 559 – 560, 1986.

[244] S. Brem, F. Wendler, and E. Malic, "Microscopic modeling of tunable graphene-based terahertz Landau-level lasers," *Phys. Rev. B*, vol. 96, p. 045427, Jul 2017.

[245] F. Wendler and E. Malic, "Towards a tunable graphene-based Landau level laser in the terahertz regime," *Scientific Reports*, vol. 5, p. 12646, Jul 2015.

[246] L. D. Landau and E. M. Lifshitz, *Electrodynamics of Continuous Media*. Pergamon Press, 1984. Volume 8 of Course of Theoretical Physics, 2nd Edition revised and enlarged by E. M. Lifshitz and L. P. Pitaevskii.